# Individual studies of newly (re-) discovered galactic sources : a study with INTEGRAL and XMM-Newton

Zurita Heras, Juan Antonio

**UNIVERSITÉ DE GENÈVE**
**Département d'astronomie**

**FACULTÉ DES SCIENCES**
**Professeur T. J.-L. Courvoisier**

# Individual studies of newly (re-)discovered Galactic Sources: a Study with *INTEGRAL* and *XMM-NEWTON*

# THÈSE

**présentée à la Faculté des sciences de l'Université de Genève**
**pour obtenir le grade de Docteur ès sciences,**
**mention astronomie et astrophysique**

**par**

**Juan Antonio ZURITA HERAS**

**de**

**La Coronada (CÓRDOBA - ESPAÑA)**

**Thèse N° 3724**

**GENÈVE**
**Atelier de reproduction de la Section de physique**
**2006**

.

**CETTE THÈSE A FAIT L'OBJET DES PUBLICATIONS SUIVANTES:**
**voir Appendice A.**

*Para mis abuelos*

# Résumé En Français

Le travail présenté dans cette thèse a été entièrement effectué au centre de données spatiales *INTEGRAL* (*INTEGRAL* Science Data Centre - ISDC) entre janvier 2002 et décembre 2005. Le thème principal de cette thèse est l'étude d'objets émettant dans la partie à haute énergie du spectre électromagnétique, et plus particulièrement dans le domaine des rayons X et rayons X durs. Le moteur principal de cette émission est l'accrétion de matière sur des sources compactes.

La première année de ma thèse a été consacrée d'une part à l'apprentissage des outils d'analyse concernant les données de la mission *INTEGRAL*, et d'autre part à l'étude à grande échelle de l'accrétion dans l'Univers. Nous avons comparé celle-ci aux deux autres sources d'énergies principales dans l'Univers que sont le fond de rayonnement cosmique (*Cosmic Microwave Background* - CMB) et la nucléosynthèse au sein des étoiles. La deuxième année a été consacrée plus particulièrement au programme de suivi par *INTEGRAL* des binaires X de faible masse (*Low Mass X-ray Binary* - LMXB) situées dans notre Galaxie. Les troisième et quatrième années ont été consacrées à l'étude de nouvelles sources découvertes par *INTEGRAL*. C'est dans ce cadre que j'ai appris à analyser les données d'une nouvelle mission dédiée aux rayons X, *XMM-Newton*, ainsi que les outils d'analyse couramment utilisés en astrophysique des hautes énergies.

## Accrétion et binaires X

Avant la découverte au début des années 1960 de la première source X en-dehors du système solaire (Sco X-1 par Giacconi et al. (1962)), la principale source d'énergie considérée en astrophysique était l'énergie nucléaire. En effet, si on compare l'énergie gravitationnelle à l'énergie au repos, on peut définir le rendement gravitationnel comme étant : $\eta_{\rm G} \equiv \frac{GM}{Rc^2}$ où $G$ est la constante gravitationnelle, $M$ et $R$ la masse et le rayon de l'étoile respectivement, et $c$ la vitesse de la lumière. Pour une étoile de type solaire, le rendement gravitationnel sera de $\eta_{\rm G_*} = 2\,10^{-6}$ en comparaison avec le rendement nucléaire qui est de $\eta_{\rm N} = 7\,10^{-3}$. La fusion nucléaire au sein des étoiles est donc la principale source d'énergie. Cependant, dans certaines conditions, l'énergie gravitationnelle peut jouer un rôle majeur. En particulier, pour une étoile à neutron (*Neutron Star* - NS, rayon$\sim$10 km et masse$\sim$1.4 $M_\odot$), le rendement gravitationnel est de $\eta_{\rm G_{NS}} = 10^{-1}$. L'accrétion de matière sur des objets compacts peut donc être une source importante d'énergie en astrophysique. La zoologie d'objets compacts comprend les étoiles à neutron, les naines blanches (*White Dwarf* - WD), les trous noirs (*Black Hole* - BH) et les trous noirs supermassifs (Super Massive BH - SMBH).

La luminosité des objects compacts accrétant de la matière dépend du taux de masse accrétée $\dot{M}$ :

$$L_{\rm accr} = \eta_{\rm G}\,\dot{M}\,c^2. \tag{0.1}$$

Cette luminosité est maximale lorsque la gravité attirant la matière est contrebalancée par la pression radiative due à la source X. Cette luminosité maximale est appelée *luminosité*

*d'Eddington* et est égale à :

$$L_{\rm Edd} = 1.3\,10^{38}\,(\frac{M}{\rm M_\odot})\ {\rm ergs\,s^{-1}}. \tag{0.2}$$

Pour une étoile à neutron, le taux maximal d'accrétion de matière est $\dot{M}_{\rm NS} \leq 10^{-8}\ {\rm M_\odot\,yr^{-1}}$. Au-dessus de cette valeur, la matière est repoussée et la source n'émet plus de photons X.

Les trois mécanismes principaux responsables de l'accrétion sont :

1. le transfert par Lobe de Roche : quand le compagnon remplit son volume de Roche, un transfert de matière a lieu au point de Lagrange $L_1$. La matière se distribue sous la forme d'un disque autour de l'objet compact, à cause de son moment cinétique trop grand pour que l'accrétion ait lieu directement. Lorsque la matière a perdu suffisamment de moment cinétique, elle tombe sur la source centrale;

2. le mécanisme Be : une étoile Be est une étoile de type spectral B présentant une rotation très rapide et un vent stellaire anisotrope avec une plus forte densité à l'équateur. L'objet compact, placé sur une orbite excentrique, va accréter de la matière (à travers la formation d'un disque) quand il passe à proximité de l'étoile Be et traverse sa région équatoriale dense. La source montre alors une forte éruption de rayons X, qui peut se prolonger au-delà du passage du périastre tant que le disque d'accrétion existe. Une fois que toute la matière accrétée a été consommée, le flux X diminue à nouveau à son niveau minimum (ou disparaît si le flux minimum est trop faible pour être détecté). Les sources accrétant à travers le mécanisme Be sont appelées sources transitoires; et

3. le vent stellaire : quand le compagnon est une étoile massive de type spectral O ou B, il présente un important vent stellaire. Ces étoiles ont une forte perte de masse ($\dot{M} \sim 10^{-4}\ {\rm M_\odot\,yr^{-1}}$) qui est suffisante pour que des objets compacts rayonnent à une fraction significative de la luminosité d'Eddington.

Parmi les différents types de sources de rayons X, il y a la catégorie des binaires X (*X-ray binaries* - XRB). Une binaire X est un système composé de deux étoiles : une étoile normale de la séquence principale (*Main Sequence* - MS) et un objet compact (WD, NS, ou BH) qui est le produit final de l'évolution stellaire quand une étoile a fini de brûler son propre combustible et/ou se débarasse de son enveloppe externe (par exemple suite a une supernova pour les NS ou BH). Les binaires X (NS ou BH) peuvent être divisées en deux catégories selon la masse de leur compagnon :

**Les binaires X de grande masse (*High mass X-ray Binaries* - HMXB)** pour lesquelles la masse du compagnon est supérieure à 10 $\rm M_\odot$. Il y a 2 types de HMXB :

- Certaines HMXB montrent une émission X persistante. Le compagnon est une supergéante massive de type spectral OB. Ces étoiles massives ont un fort vent stellaire dont une fraction est accrétée par l'objet compact. Ces systèmes montrent une orbite quasi-circulaire avec une période orbitale inférieure à 15 jours. Elles possèdent un fort champ magnétique ($B \sim 10^{12} - 10^{14}$ G) qui influence la géométrie de l'accrétion et provoque une modulation de l'émission X. La période des pulsations est de l'ordre de 10–1000 s. Une dizaine de HMXB avec supergéante étaient connues (Liu et al. 2000) avant que de nouvelles sources de ce type soient découvertes par *INTEGRAL*; et

- La deuxième famille, composée de sources transitoires, comprend la majorité des HMXB observées à ce jour (Liu et al. 2000). Elles ont des orbites excentriques et des périodes orbitales supérieures à 20 jours (pouvant aller jusqu'à quelques centaines de jours). Ces systèmes sont formés d'une étoile Be dont la particularité est d'avoir un fort vent équatorial dû à la rotation rapide de l'étoile. Ces binaires X sont le théâtre d'éruptions récurrentes dont la durée varie entre quelques jours et plusieurs mois.

Les HMXB présentant une pulsation sont nommées des pulsars X accrétants. Dans ces objets, l'accrétion est anisotrope puisque le puissant champ magnétique domine l'environnement immédiat de la NS, donc la matière est dirigée vers les pôles magnétiques où l'accrétion a lieu par instabilité magnéto-hydrodynamique. L'émission des pulsars est principalement due à la diffusion Compton et le spectre observé peut être modélisé par une loi de puissance dure avec une coupure à haute énergie. Parfois, le spectre est fortement absorbé à basse énergie (1–2 keV) et une raie en émission à 6.4 keV est observée. Elle correspond à la fluorescence de fer froid présent dans l'environnement de la HMXB. Les HMXB sont plutôt distribuées dans le plan galactique, en particulier dans les régions riches en étoiles OB.

**Les binaires X de petite masse (*Low mass X-ray Binaries* - LMXB)** pour lesquelles la masse du compagnon est $\lesssim 1$ $M_\odot$. Leur période orbitale est de l'ordre de quelques minutes à quelques jours. L'objet compact accrète à partir d'un disque chaud qui est la principale source d'émission dans les domaines optique et infrarouge (IR). Le champ magnétique est plutôt faible ($B \sim 10^9 - 10^{11}$ G). Peu de LMXB montrent des pulsations, p.ex. X 1822-371 avec $P_{\rm spin} = 0.59$ s (Jonker & van der Klis 2001). La variabilité de ces sources est importante et prend plusieurs formes :

- éruptions X fréquentes dont l'origine est un flash thermonucléaire dû à l'accumulation de suffisamment de matière à la surface de la NS pour provoquer une explosion nucléosynthétique;
- les éclipses sont rares, mais suivant l'inclinaison de certaines sources par rapport à l'observateur, elles peuvent montrer une brusque diminution de leur émission X due à l'absorption de la lumière par la matière éjectée au-dessus du disque à l'endroit où le flot de matière du compagnon touche le disque (ce phénomène est nommé "dip" en anglais); et
- des oscillations quasi-périodiques (*Quasi-Periodic Oscillations* - QPO) dues à l'interaction du disque d'accrétion avec le champs magnétique de la NS.

L'émission des LMXB peut être caractérisée par une loi de corps noir (*Black Body* - BB) à basse énergie (rayons X mous) et par un modèle de Comptonisation à plus haute énergie (rayons X). Parfois, une loi de puissance doit être appliquée pour tenir compte d'une émission importante dans les rayons X durs. Une raie en émission à 6.7 keV est aussi souvent observée dans le spectre d'une LMXB correspondant à la présence de fer fortement ionisé. Les LMXB sont principalement situées dans le bulbe galactique et les amas d'étoiles, et elles correspondent à une population d'étoiles vieilles.

## *INTEGRAL* et *XMM-Newton* : Deux missions pour l'astronomie des hautes énergies

(a) *INTEGRAL*

(b) *XMM-Newton*

**Figure** *0.1: Visions d'artistes des deux satellites de l'ESA dédiés à l'observation des sources émettant à haute énergie. Sources: (a) ESA - D. Ducros et (b) ESA/*XMM-Newton.

*INTEGRAL* (INTErnational Gamma-Ray Astrophysics Laboratory) est une mission de l'Agence Spatiale Européenne (ESA) dédiée à l'observation des rayons X et gamma dans l'Univers (voir Fig. 0.1). Lancé en 2002, ce satellite transporte quatre instruments dont les 2 principaux sont un imageur, IBIS (composé de 2 plans de détection : ISGRI (20–1000 keV) et PICsIT (200 keV–8 MeV), et un spectromètre, SPI. Ces deux instruments sont sensibles aux rayons X durs et rayons $\gamma$ (20 keV–10 MeV) et possèdent un grand champs de vue (diamètre $\sim 30^{o}$). Ils sont complétés par deux moniteurs, un pour les rayons X, JEM-X (3–30 keV, diamètre $\sim 13^{o}$), et un autre pour le domaine optique, OMC (utilisant un filtre V de Jonhson). La technologie utilisée pour les 2 instruments à haute énergie est basée sur le principe des masques codés. La lumière du ciel (S) est modulée par un masque (M) installé devant les détecteurs qui enregistrent l'ombre projetée dessus (D). Le ciel est reconstruit (S') à partir de l'ombre et de propriétés connues du masque, en particulier il a été choisi tel qu'il existe une matrice G vérifiant M*G=$\delta$ :

$$\mathrm{D} = \mathrm{S} * \mathrm{M} + \mathrm{B} \Rightarrow \mathrm{S}' = \mathrm{D} * \mathrm{G} = \mathrm{S} * \mathrm{M} * \mathrm{G} + \mathrm{B} * \mathrm{G} = \mathrm{S} + \mathrm{B} * \mathrm{G}, \tag{0.3}$$

où B représente le bruit de fond. Le ciel est donc retrouvé à une constante près (B*G) qui est liée au bruit de fond. Cette technique permet de faire de l'imagerie à haute énergie, en remplacement de la méthode plus classique consistant à focaliser les photons mais qui est inopérante dans les rayons X et $\gamma$ étant donné qu'ils sont soit absorbés par l'optique elle-même, soit ils la traversent sans interaction. C'est une méthode indirecte et complexe dont les 2 principaux avantages sont la possibilité d'avoir un énorme champ de vue et la possibilité de mesurer simultanément le signal des sources et le bruit de fond. Les principaux objectifs d'*INTEGRAL* sont :

- l'étude des objets compacts galactiques (WD, NS, BH) dans des systèmes binaires;
- l'étude de sources extra-galactiques, telles que les noyaux actifs de galaxies (*Active Galactic Nuclei* - AGN), ou encore les amas de galaxies;

- l'étude des raies d'émission d'origine nucléosynthétique telles que l'$^{26}$Al ou le $^{44}$Ti; et
- l'étude de la raie d'annihilation électron-positron détectée au centre de notre Galaxie.

Ces études sont effectuées soit dans des programmes d'observations pointées, soit dans le cadre de grands programmes visant à couvrir l'ensemble du plan galactique.

*XMM-Newton* (X-ray Multi-Mirror mission) est également une mission de l'ESA lancée en 1999 (voir Fig. 0.1). Le satellite transporte 2 instruments pour l'étude des rayons X (EPIC & RGS) et une caméra optique (OM). Les instruments dans ce domaine d'énergie utilisent la technique de l'incidence rasante pour focaliser les photons X grâce à leur faible angle d'incidence. Ainsi le télescope X consiste en 58 miroirs dit de Wolter type I (qui sont une combinaison d'un miroir parabolique et d'un miroir hyperbolique). Le premier instrument X est l'imageur EPIC qui permet de créer des images et des spectres entre 0.15–15 keV. Le deuxième instrument X est un spectromètre nommé RGS (Reflection Grating Spectrometer) qui fonctionne entre 6–35 Å(0.33–2.5 keV). Il permet d'obtenir des spectres à très haute résolution à basse énergie, dans un domaine où l'on trouve potentiellement plusieurs raies dues aux transitions K et L d'éléments légers et lourds.

## Les sources galactiques découvertes par *INTEGRAL*

*INTEGRAL* observe régulièrement le plan galactique et le centre galactique. Depuis le début de la mission, une centaine de nouvelles sources ont été découvertes grâce à l'imageur IBIS/ISGRI. La liste complète de ces nouvelles sources peut être trouvée à :

`http://isdc.unige.ch/~rodrigue/html/igrsources.html`.

Par convention, elles reçoivent le nom IGR JHHMMm±DDMM, où IGR identifie que la source a été découverte avec la mission *INTEGRAL* , suivi par sa position en coordonnées équatoriales avec l'époque J2000 donnée en heures minutes pour l'ascencion droite et en degrés arc-minutes pour la déclinaison. La plupart de ces sources sont situées dans la direction de notre Galaxie. ISGRI permet de connaître leur spectre dans les rayons X durs (>20 keV). Cependant, pour mieux comprendre la nature de ces objets, il est nécessaire d'étendre le spectre jusqu'à des énergies plus basses (*i.e.* 0.2 keV). Pour ce travail, nous avons sélectionné un échantillon de sources pour lesquelles nous avons accès à des données à basse énergie grâce à *XMM-Newton* et *Chandra* (mission X de la NASA, 0.08–10 keV). L'échantillon complet est présenté dans le tableau 0.1.

L'ensemble des données publiques et des données privées à disposition au début de janvier 2005 concernant *INTEGRAL* a été utilisé pour l'analyse de l'émission X dure de ces sources. Des images, des courbes de lumière et des spectres ont été extraits dans plusieurs bandes d'énergie pour l'instrument IBIS/ISGRI. Les 2 autres instruments SPI et JEM-X n'ont pas été utilisés puisque les sources étant faibles et situées dans des régions très peuplées du ciel, les résolutions spatiales et/ou énergétique ne sont pas suffisantes pour pertmettre une analyse correcte de ces sources avec SPI et JEM-X. L'échantillon de sources concerne la même portion du ciel. Donc, vu que le champs de vue de l'instrument IBIS/ISGRI est grand, l'analyse de l'ensemble des sources peut être effectuée en même temps en sélectionnant de grandes listes de données regroupant tous les pointages où l'on retrouve une de nos sources dans le champs de vue. Cela représente environ 6–7 Ms de temps d'exposition total

**Table** 0.1: Échantillon des sources *INTEGRAL* étudiées dans le cadre de cette thèse et résumé des caractéristiques découvertes au cours de l'analyse.

| Source | Position X (error) hh mm ss dd mm ss ($''$) |
|---|---|
| IGR J16318−4848 | 16 31 48.6 -48 49 00 (4)[a] |
| IGR J16320−4751 | 16 32 01.9 -47 52 27 (4)[b] |
| IGR J16358−4726 | 16 35 53.8 -47 25 41 (0.6)[c] |
| IGR J16393−4643 | 16 39 05.4 -46 42 12 (4)[d] |
| IGR J16418−4532 | 16 41 51.0 -45 32 25 (4) |
| IGR J16479−4514 | 16 48 06.6 -45 12 08 (4) |
| IGR J16465−4507 | 16 46 35.5 -45 07 05 (4)[e] |
| IGR J17252−3616 | 17 25 11.3 -36 16 58 (4)[f] |
| IGR J17544−2619 | 17 54 25.4 -26 19 53 (4)[g] |
| IGR J17597−2201 | 17 59 45.7 -22 01 39 (4) |
| IGR J18027−2016 | 18 02 42.0 -20 17 18 (4) |

[a]Schartel et al. (2003)
[b]Rodriguez et al. (2006)
[c]Kouveliotou et al. (2003)
[d]Bodaghee et al. (2005)
[e]Zurita Heras & Walter (2004)
[f]Zurita Heras et al. (2005)
[g]Gonzalez-Riestra et al. (2003)

**Table** 0.2: Résumé des caractéristiques des sources IGR découvertes au cours de l'analyse. Les 2 types s'idenfitie comme source Persistente (P) ou Transitoire (T).

| Source | $N_{\rm H}$ $10^{22}$ cm$^{-2}$ | $F_{2-100\rm keV}$ $10^{-10}$ ergs cm$^{-2}$ s$^{-1}$ | $P_{\rm spin}$ s | $P_{\rm orb}$ j | EW(Fe K$\alpha$ ) eV | Type |
|---|---|---|---|---|---|---|
| IGR J16318−4848 | 193 | 3.5 | | | 82 | P |
| IGR J16320−4751 | 18.3 | 2.5 | 1302 | 8.99 | 85 | P |
| IGR J16358−4726 | 27.9 | 13 | 5880 | | ?? | T |
| IGR J16393−4643 | 23.7 | 1.7 | 912 | | 60 | P |
| IGR J16418−4532 | 10.0 | 1.1 | 1246 | | | P |
| IGR J16479−4514 | 7.7 | 1.4 | | | | P |
| IGR J16465−4507 | 60 | 2.1 | 228 | | $<$60 | T |
| IGR J17252−3616 | 14.9 | 1.8 | 414 | 9.72 | 84 | P |
| IGR J17544−2619 | 1.8 | 5.5 | | 165 | | T |
| IGR J17597−2201 | 4.5 | 3.0 | | | | P |
| IGR J18027−2016 | 9.1 | 1.0 | 139 | 4.57 | 33 | P |

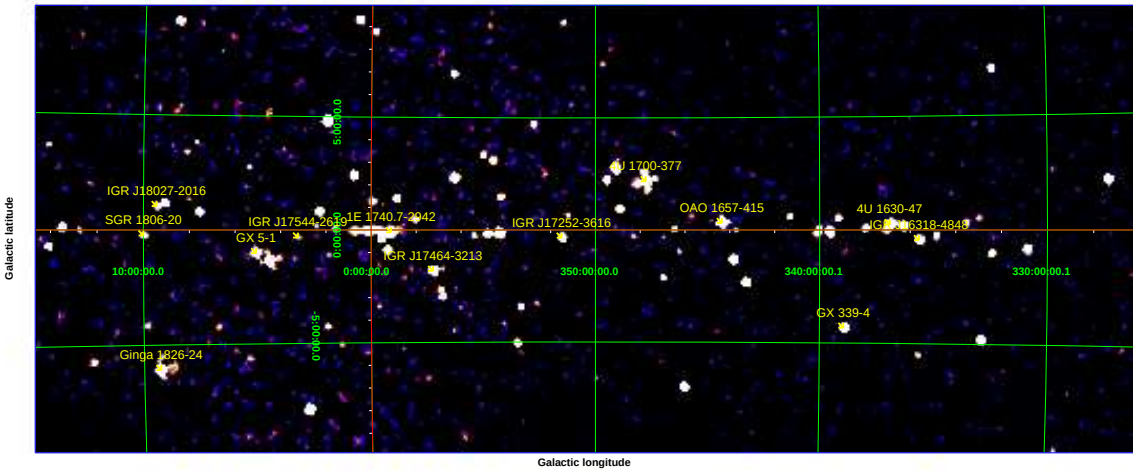


**Figure** *0.2: Image du signal sur bruit (ISGRI, 20–60 keV) du plan galactique comprise entre l=[-35°;+15°] et b=[-10°;+10°]. L'image est centrée sur IGR J17252−3616.*

à analyser (environ 70 révolutions réparties sur 2 ans de mission). Une bonne centaine de sources est détectée dans la bande d'énergie 20–60 keV (voir Fig. 0.2).

Pour six sources de l'échantillon, nous avons eu des observations pointées avec *XMM-Newton* (programme 020638, chercheur principal : Walter R.). Le temps d'exposition était de l'ordre de 10–20 ks pour chaque observation. Trois des observations ont été fortement affectées par le bruit de fond (IGR J16418−4532, IGR J16479−4514 et IGR J17597−2201). L'analyse combinée des données *XMM-Newton* (ou *Chandra*) et *INTEGRAL* a permis d'étudier les propriétés à haute énergie des 11 sources de notre échantillon. Les faits suivant ont pu être déterminés (voir aussi tableau 0.2) :

1. Pour les 6 sources du programme d'observation *XMM-Newton*, nous avons déterminé des positions X précises à $4''$ (compatible avec les positions *INTEGRAL*). Ceci permet la recherche des contreparties optique/IR (en utilisant les catalogues IR 2MASS ou optique USNO, ou encore en effectuant de nouvelles observations spectroscopiques). Les observations multi-longueurs d'onde sont un puissant outil pour déterminer la nature du compagnon (décisive concernant les HMXB);

2. Sept sources ont une émission persistante et montrent une absorption locale forte. Quand les données sont d'assez bonne qualité, une raie en émission à 6.4 keV due à la fluorescence de fer froid dans l'environnement de la source X est également detectée. Pour 5 d'entre elles, une pulsation est également détectée allant de 139 s à 1302 s. Nous connaissons également les périodes orbitales pour 3 systèmes qui varient entre 5–10 j. Ces systèmes sont apparemment des HMXB accrétant de la matière du vent stellaire du compagnon dans lequel l'objet compact se trouve profondément englouti. La distribution de la matière est compatible avec une géométrie sphérique et la région d'émission du fer se situerait à $\sim 10^8$ km;

3. Trois sources sont transitoires. IGR J17544−2619 est sûrement un système Be avec une longue période de 165 j et sans absorption intrinsèque. IGR J16465−4507 est

une HMXB hautement absorbée avec un compagnon supergéant sgB (Negueruela et al. 2005a). La nature de IGR J16358−4726 est encore un mystère. Cependant, la plupart de ces caractéristiques tende à la classer comme une HMXB transitoire avec une forte absorption. Sa pulsation de 5880 s serait la pulsation la plus longue connue pour des pulsars accrétant;

4. IGR J17597−2201 est sûrement une LMXB non absorbée, ce qui est aussi confirmé par Lutovinov et al. (2005a);

5. Un excès à basse énergie est également observé dans les HMXB hautement absorbées, ce qui semble une caractéristique commune de cette catégorie de sources (Hickox et al. 2004), p.ex. Vela X-1 ou 4U 1700-377;

6. IGR J17252−3616 et IGR J18027−2016 montrent une éclipse dans la courbe de lumière repliée sur la période orbitale; et

7. la population des HMXB avec supergéante vient d'augmenter considérablement étant donné que seulement une dizaine de HMXB situées dans notre Galaxie étaient connues auparavant.

Ces études sont présentés dans les articles suivants : Zurita Heras et al. (2005), Bodaghee et al. (2005), Walter et al. (2005), et Patel et al. (2006).

## Le programme de suivi des binaires X de faible masse par *INTEGRAL*

Étant donné que notre Galaxie est régulièrement observée par *INTEGRAL*, des programmes pour étudier différentes catégories de sources X ont été mis en place. Tous les instituts ayant collaborés à la mission *INTEGRAL* participent à cet effort scientifique. L'une des catégories concerne les LMXB dont l'objet compact peut soit être une NS ou un BH. 78 sources ont été sélectionnées pour faire partie de l'échantillon. Le but de cette investigation est d'étudier les LMXB et leurs propriétés sur une longue échelle de temps.

Dans ce cadre, j'ai développé des outils permettant la visualisation de l'émission dans plusieurs bandes d'énergie pour les instruments IBIS/ISGRI et JEM-X. Des résultats préliminaires ont été publiés dans Paizis et al. (2003) et Paizis et al. (2004). Un exemple est montré dans la Fig. 0.4 où l'on présente la courbe de lumière de GX 339-4, une LMXB transitoire avec un trou noir (voir p.ex. Belloni et al. 2005).

## L'accrétion à l'échelle de l'Univers

Les trois sources d'énergie principale dans l'Univers sont : le fond de rayonnement cosmique (CMB, l'émission résiduelle du Big Bang), la fusion nucléaire au sein des étoiles et la gravitation par accrétion de matière sur des objets compacts supermassifs (SMBH) au coeur de galaxies actives (les AGN). Il a été démontré que l'énergie d'origine nucléosynthétique varie sur une échelle cosmologique et montre un pic à $z \sim 1.5-2$ ($z$ est le décalage spectral, ou *redshift*) (Madau et al. 1996; Somerville et al. 2001). Cette évolution de la formation stellaire est apparemment équivalente à l'évolution de l'énergie rayonnée par l'accrétion

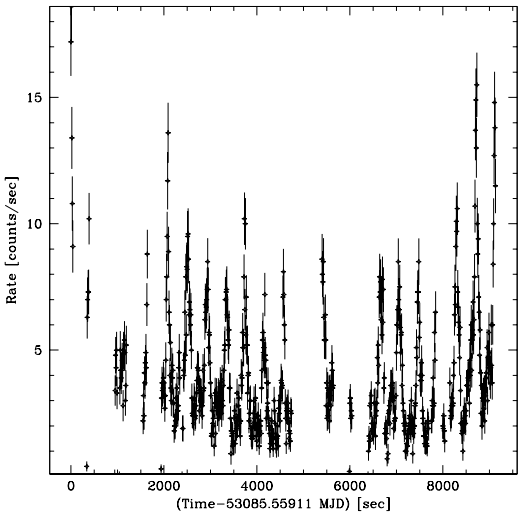


(a) courbe de lumière entre 0.4–10 keV.

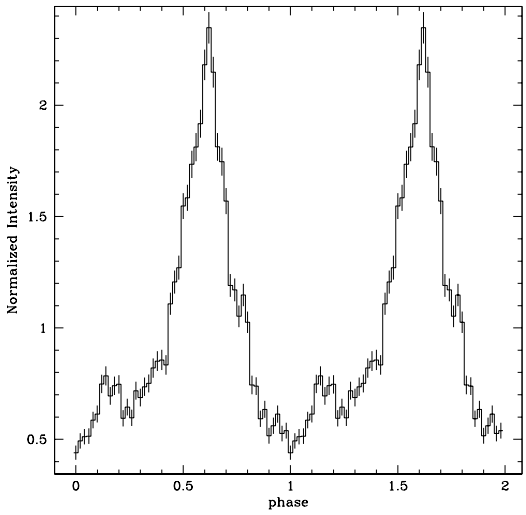


(b) courbe de lumière repliée (0.4–10 keV) sur la pulsation de 414 s.

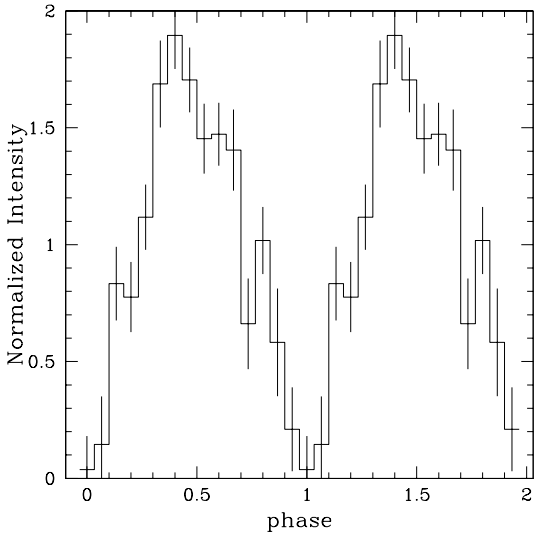


(c) courbe de lumière repliée (20–40 keV) sur la période orbitale 9.72 j.

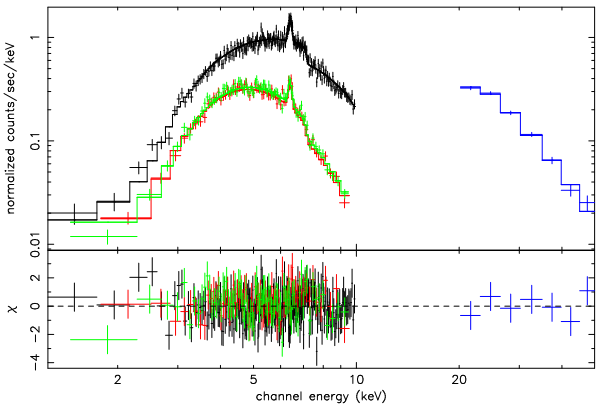


(d) spectre combiné *XMM-Newton* et *INTEGRAL*

**Figure** *0.3: Analyse de IGR J17252−3616(Zurita Heras et al. 2005). Ces figures illustrent ce qui est décrit dans la partie sur les sources IGR.*

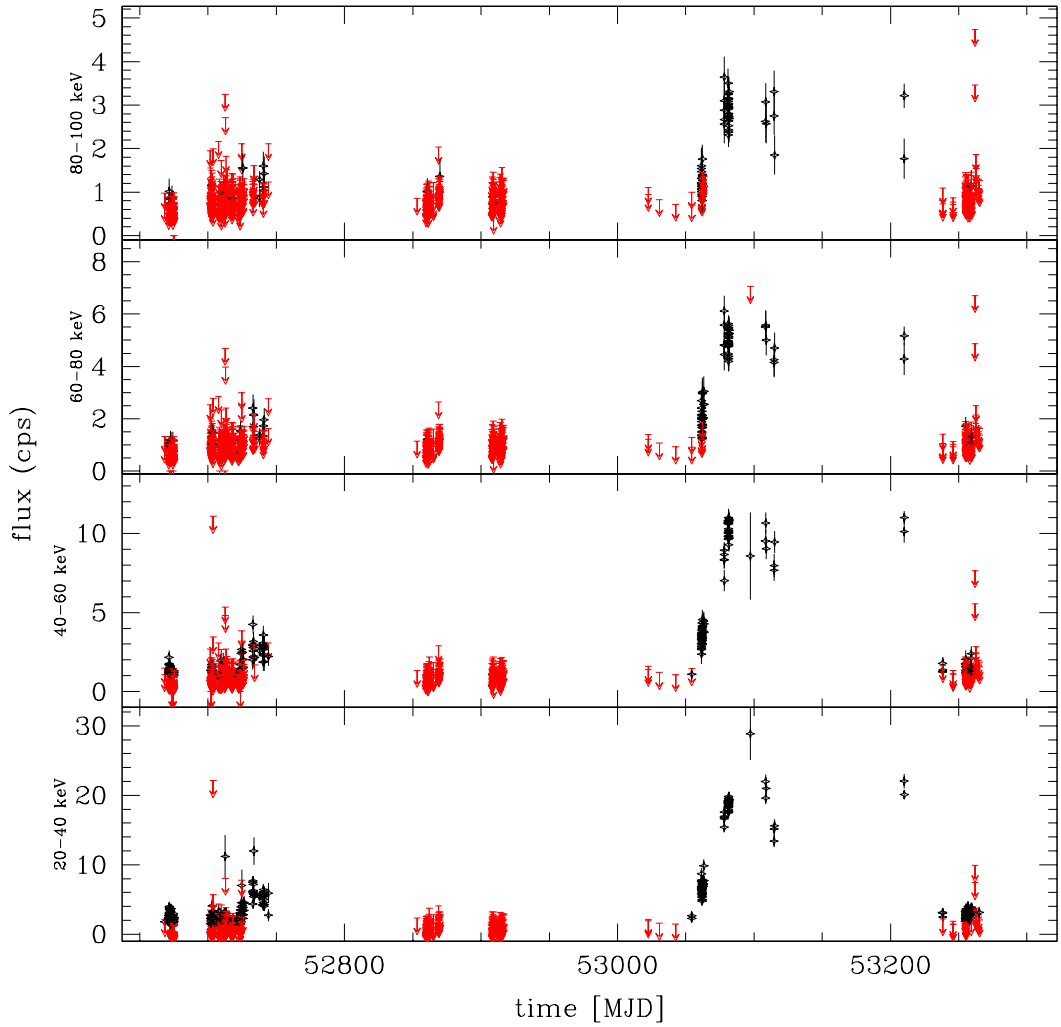


**Figure** *0.4: Courbes de lumière de GX 339-4 (une LMXB transitoire avec BH) dans différentes bandes d'énergies créées à partir de données de IBIS/ISGRI accummulées pendant les premières 1.5 années d'*INTEGRAL.

sur des SMBH qui montre également un pic à $z \sim 1.5-2$ (Dunlop 1998; Franceschini et al. 1999). Par conséquent, on peut supposer que les deux phénomènes sont liés et donc, le rapport des énergies rayonnées par chacun peut être dérivé. Cette question a déjà reçu l'attention de plusieurs auteurs par le passé (Fabian & Iwasawa 1999; Franceschini et al. 1999; Courvoisier 2001; Elvis et al. 2002) avec des résultats pouvant varier par des facteurs importants.

A partir des modèles d'évolution stellaire de Leitherer et al. (1999) et de l'histoire de la formation stellaire (Somerville et al. 2001,Tableau 2 et les références présentées), nous avons dérivé la densité d'énergie stellaire pour différentes métallicités et 2 fonctions de masses initiales ($\alpha$=2.35 ou 3.3, Salpeter ou Scalo) (*Initial Mass Function* - IMF). En considérant l'émission combinée de toutes les AGN, on peut reproduire l'émission du fond diffus des rayons X (*X-ray background* - XRB) (Comastri et al. 1995; Gilli et al. 1999, 2001). Donc, la densité d'énergie rayonnée par les AGN peut être déduite à partir du XRB.

En effectuant tous ces calculs et en considérant les travaux précédents, nous remarquons que tous les travaux convergent vers un rapport équivalent une fois que toutes les valeurs considérées au départ sont uniformisées :

$$\frac{E_{\rm AGN}}{E_{\rm stars}} = 0.02 - 0.07 \tag{0.4}$$

Personnellement, pour une IMF de Salpeter et une métallicité solaire, nous trouvons un rapport de 0.04. Les différentes densités d'énergie sont : CMB $\sim$0.2 eV cm$^{-3}$, nucléosynthèse $\sim$0.02 eV cm$^{-3}$ et la gravitation/accrétion $\sim$0.0008 eV cm$^{-3}$.

Par ailleurs, nous avons estimé que les quasars radio-bruyants contribuent 3400 fois moins que l'ensemble des AGN à l'émission due à l'accrétion. Le total de masse accumulée en moyenne par un SMBH est de $\sim 6.5\,10^7$ M$_\odot$.

Ces résultats sont présentés dans l'article Zurita Heras et al. (2003).

# Table of contents

# List of figures

# List of tables

# List of acronyms and terminology

- *ADC* Accretion Disc Corona
- *AGN* Active Galactic Nucleus
- *ATel* Astronomer's TELegram
- *BH* Black Hole
- *BHC* Black Hole Candidate
- *CCF* Current Calibration Files, the calibration files specific to the *XMM-Newton* mission
- *CE* Common Envelope
- *CIF* Calibration Index File, file listing the default calibration files used for an *XMM-Newton* observation at a specific epoch
- *CMB* Cosmic Microwave Background
- *CO* Compact Object
- *CV* Cataclysmic Variable
- *CRF* Cyclotron Resonant Features
- *DITHERING* In order to improve an instrument with coded mask spatial resolution, it is possible to use the 'dithering' technique. Dithering consists in obtaining multiple images of the same field of view, with an attitude shift between each image.
- *EPIC* European Photon Imaging Camera
- *FCFOV* Fully Coded Field Of View
- *FITS* Flexible Image Transport System, a standard astronomical data format
- *FOV* Field Of View
- *FTOOLS* FITS based software utilities
- *GCDE* Galactic Centre Deep Exposure
- *GCN* Gamma-ray Coordinates Network
- *CP* Core Programme
- *GPS* Galactic Plane Scan

- *GRB* Gamma Ray Burst
- *GUI* Graphical User Interface
- *HMXB* High Mass X-Ray Binary
- *IAUC* International Astronomical Union Circulars
- *IBAS INTEGRAL* Burst Alert System
- *IBIS* Imager on Board *INTEGRAL* Satellite
- *IMF* Initial Mass Function
- *INTEGRAL* INTErnational Gamma Ray Astrophysics Laboratory
- *IOSM* Interactive Operations Status Monitoring
- *IPN* InterPlanetary Network
- *IQLA* Interactive Quick Look Analysis
- *IREM INTEGRAL* Radiation Environment Monitor
- *ISGRI INTEGRAL* Soft Gamma Ray Instrument
- *ISDC INTEGRAL* Science Data Center
- *ISOC INTEGRAL* Science Operations Center
- *JEM-X* Joint European Monitor for X-Rays
- *LMXB* Low Mass X-Ray Binary
- *MOC* Mission Operations Center
- *MS* Main Sequence
- *NRT* Near Real Time
- *ODF* Observation Data Files, basic science packet for *XMM-Newton*
- *OSA* Off-line Scientific Analysis
- *OG* Observation Group defined as a collection of Science Window Groups plus observation level results.
- *OMC* Optical Monitoring Camera
- *PCFOV* Partially Coded Field Of View
- *PICsIT* Pixellated Imaging Caesium Iodide Telescope
- *POINTING* A specific commanded location on the Celestial sphere. It is also the period of time during which the spacecraft reference axis (X axis) is held at a commanded location.

- *QLA* Quick Look Analysis
- *RGA* Reflection Grating Array, the gratings for the *XMM-Newton*/RGS spectrometer intrument
- *RGS* Reflection Grating Spectrometer
- *RLO* Roche Lobe Overflow
- *RXTE* Rossi X-ray Timing Explorer
- *SAS* Scientific Analysis Subsystem, the *XMM-Newton* data reduction package
- *Scody* Scientist On Duty
- *S/C* SpaceCraft
- *S/W* Software
- *ScW* Science Window, a unit of continuous observing time used by the ISDC system to archive and process data. It is the basic unit of *INTEGRAL* observations. Under normal dithering operations one science window shall correspond to one S/C pointing or slew manoeuver. In the OSIM it refers only to pointings as slews are not simulated.
- *SLEW* The movement of the S/C between 2 pointings. Also the period of time covered by this.
- *SMBH* Super Massive Black Hole
- *SPI* SPectrometer on board *INTEGRAL* satellite
- *SFXT* Supergiant Fast X-ray Transient
- *SXT* Soft X-ray Transient
- *TM* TeleMetry
- *ToO* Target Of Opportunity
- *XMM* X-ray Multi-Mirror, the *XMM-Newton* space observatory
- *XRB* X-Ray Binary
- *XRB* X-Ray Background, indeed this acronym is used in both cases
- *WD* White Dwarf

xxx

# First part

# Introduction

# Chapter 1
# INTRODUCTION

This thesis has been done at the *INTEGRAL* Science Data Centre from January 2002 to December 2005. The topic of this thesis is the study of high energy radiations, mainly from galactic sources in the X-ray and hard X-ray domains. These sources are powered by accretion onto compact objects.

The sources studied here are X-ray binaries. They are double-stars systems hosting one compact object that can be either a white dwarf, a neutron star or a black hole. They are powerful sources of X-rays fuelled by the accretion of matter from the companion star onto the compact object. They can reach luminosities up to $10^{38}$ ergs s$^{-1}$. X-ray binaries are classified in several categories depending on the mass of the companion star : high mass X-ray binaries ($\geq 10$ M$_\odot$), low mass X-ray binaries ($\leq 1$ M$_\odot$), or intermediate mass X-ray binaries ($\sim 1 - 10$ M$_\odot$). There are a few hundreds of X-ray binaries located in our Galaxy. These categories show different features in terms of variability, spectral behaviour, and spatial distribution.

There are several spatial high energy missions studying these sources that are currently flying. For my thesis, I have used data of two space missions : *INTEGRAL* and *XMM-Newton*. *INTEGRAL* is an X-ray and $\gamma$-ray space observatory launched on October 17, 2002. It has the capability to create images and spectra in a wide energy range with fine spatial and spectral resolutions in the hard X/$\gamma$-ray ranges. *XMM-Newton* is also a European space observatory launched earlier on 1999. It has imaging and spectral capabilities in the soft X-ray and X-ray domains. Both missions also have an optical camera to cover simultaneously the optical and high energy spectral domains. We concentrated our work in the study of the new X-ray galactic sources discovered by *INTEGRAL* during its first 2 years of mission.

The first year of my thesis was used to learn the data analysis tools related to each *INTEGRAL* instruments. Meanwhile, we also studied the accretion in a frame as large as the Universe comparing its radiation to the stellar radiation and the Cosmic Microwave Background emission. During the second year, I mainly participated to the Low-Mass X-ray binaries monitoring programme with *INTEGRAL*. The third and fourth years of my thesis were focused on the study of the new X-ray sources discovered by *INTEGRAL*. In this frame, I learnt to use the data of another high energy mission, *XMM-Newton*.

This thesis is organised into four different parts.

Firstly, we briefly review the accretion mechanisms as the main engine of high energy emission and we give a short review of X-ray binaries. We also present the Fourier transform

method as a tool to study the variability detected in the X-ray binaries. The first part ends with the presentation of the *INTEGRAL* and the *XMM-Newton* missions.

The second part is the core of this thesis. We present the analysis of 11 IGR sources of which 3 are presented in more detail : IGR J17252−3616, IGR J16358−4726 and IGR J16393−4643.

In the third part, we present other contributions to the science with *INTEGRAL*. We describe our participation to the LMXB monitoring programme in its first years. We also present our contribution to the daily monitoring of *INTEGRAL* observations.

The fourth part is also linked to accretion but not with *INTEGRAL*. Based on the fact that the star formation rate and the evolution of the luminosity due to accretion processes in the Universe are similar, we calculate the global contributions from each category in the Universe.

All the work done in this thesis is summarised in the conclusion.

# Chapter 2
# ACCRETION

In this chapter, we describe the basic concept underlying the powerful X/$\gamma$-ray emission. This is only meant to be a basic introduction to high energy astrophysics. Detailed explanations can be found in recent reviews (Nagase 1989; Bildsten et al. 1997; King 1995; Tauris & van den Heuvel 2005).

## 2.1 Energy radiated in the Universe

There are three main mechanisms producing photons in the Universe : the Big Bang, which is the source of the cosmic micro-wave background (CMB), the nucleosynthesis in the heart of stars mainly emitting in the ultra-violet (UV) and optical energy bands, and the gravitation through accretion processes that emits photons mainly in the X-ray and $\gamma$-ray energy domains. These domains correspond to wavelengths lower than 100 Å. In X-ray astronomy, the wavelength terminology is not used and is replaced by the energy expressed in electron-volt (eV). The energy range ($E = h\,c/\lambda$) is 0.1–100 keV for X-rays and, is higher than 100 keV for $\gamma$-rays.

The importance of gravitation compared to nuclear energy can be well understood when considering the different energetic efficiencies. The energy gained by a particle of mass $m$ accreted from infinity onto a star of mass $M_*$ and radius $R_*$ is :

$$E_{\rm acc} = \frac{GM_*m}{R_*}, \tag{2.1}$$

where $G$ is the gravitational constant. When considering Einstein's equation :

$$E = mc^2, \tag{2.2}$$

where $c$ is the speed of light, the gravitational efficiency $\eta_{\rm G}$ can be defined as :

$$\eta_{\rm G} = \frac{GM}{Rc^2}. \tag{2.3}$$

If we consider a normal star such as the Sun ($M = 1\,{\rm M}_\odot$,$R = 1\,{\rm R}_\odot$), the efficiency is equal to :

$$\eta_{\rm G_*} = 2\,10^{-6}, \tag{2.4}$$

which is much less efficient than the nuclear fusion efficiency $\eta_{\rm N}$ :

$$\eta_{\rm N} = 7\,10^{-3}. \tag{2.5}$$

The nuclear fusion inside a normal star is thus the main source of energy.

Nevertheless, under special conditions, the gravitational energy can be a very powerful and efficient source of energy. If we consider a neutron star (NS) with $R_{\rm NS} = 10\,{\rm km}$ and $M_{\rm NS} = 1.4\,{\rm M}_\odot$, its gravitational efficiency $\eta_{\rm G_{NS}}$ is :

$$\eta_{\rm G_{NS}} = 0.1, \tag{2.6}$$

*i.e.* a factor ∼15 better than nuclear fusion. Therefore, accretion under special circumstances is the most powerful source of energy, and it critically depends on the mass and size of the accreting object. Thus, the accretion is not of interest for normal stars, but for neutron stars, black holes, supermassive black holes, and in some cases white dwarfs, it is the main source of radiated energy. Indeed, soon after the discovery of X-ray objects in the 1960's, the accretion of matter onto compact objects (CO) quickly became the most reliable scenario in order to explain the huge amounts of radiated energy.

The luminosity in an accreting compact objects can be defined as :

$$L_{\rm accr} = \eta_{\rm G}\,\dot{M}\,c^2, \tag{2.7}$$

so the main factor driving the luminosity is the mass accretion rate $\dot{M}$ factor. The luminosity increases proportionally to $\dot{M}$. However, there is a limit to the mass accretion rate. If the accreting material is spherically distributed around the compact object, the pressure of the radiated luminosity on the infalling matter becomes more important as the luminosity increases. At some point, it becomes powerful enough to stop the accretion; it happens when the radiation expelling the matter counterbalances the gravity pulling at the matter. This limit is called the Eddington luminosity and is defined as :

$$\frac{\sigma_{\rm T}\,L_{\rm accr}}{4\pi R^2 c} = \frac{GMm}{R^2} \tag{2.8}$$

$$\Rightarrow L_{\rm Edd} = \frac{4\pi GMmc}{\sigma_{\rm T}} = 1.3\,10^{38}\,(\frac{M}{{\rm M}_\odot})\ {\rm ergs\,s^{-1}} \tag{2.9}$$

where $\sigma_{\rm T}$ is the Thomson cross-section, and $m = m_{\rm e}+m_{\rm p} \simeq m_{\rm p}$ the mass of a proton. In the case of a NS, this implies an upper limit for the mass accretion rate of $\dot{M}_{\rm NS} \leq 10^{-8}\ {\rm M}_\odot\,{\rm yr}^{-1}$.

## 2.2 Accretion mechanisms

However, reality is more complex and accretion can occur in an asymmetric scenario. The accretion flow geometry depends on its origin, *i.e.* , in X-ray binaries, it depends on the companion star. There are 3 main mechanisms are responsible of the accretion onto CO, namely the Roche Lobe overflow, the Be binary mechanism, and the accretion from the stellar wind.

### 2.2.1 Roche Lobe overflow

A binary system composed of two stars has a particular gravitational potential, called the Roche potential, which is the combination of both individual potentials. It contains two gravitational wells (corresponding to the two stars) and five points of equilibrium (*i.e.* where all the forces counterbalance each other), the so-called Lagrange points $L_1$–$L_5$ (see Fig. 2.1). The innermost equipotential surface englobing both stars is defined as the Roche surface and it has a major role. Indeed, if a star starts growing and fills all its Roche volume (or the *Roche Lobe*), the matter can escape from the star through the $L_1$ point since the matter located further than the Roche Lobe will not be gravitationally bound to the star anymore. The expelled matter can then be captured by the other star. This phenomenon is called the Roche Lobe Overflow (RLO).

However, accretion will not happen immediately. Indeed, due to the rotation of the companion star, the matter has a significant angular momentum $J$, so it will first form a disk around the compact object (of mass $M_1$). The circular radius $R_{\rm circ}$ is defined as :

$$R_{\rm circ} = \frac{J^2}{GM_1}. \tag{2.10}$$

The matter will then lose angular momentum and move towards the central source of X/$\gamma$-rays, and, at some point, it will fall onto the compact object.

#### The standard $\alpha$-disk model

The $\alpha$-disk model was proposed by Shakura & Sunyaev (1973). The disk is geometrically thin and optically thick. The matter composing the disk can be cut in different rings, and each of them follows a Keplerian orbit. Due to friction between the different rings, the gravitational energy of particles heats the disk that starts radiating. The matter loses angular momentum who is transferred towards the outer rings, while the material moves towards the centre and accretes on the compact object.

A simple combination of black body functions is sufficient to model the spectrum of an accreting disk. However, the geometry and the radiation mechanism can be far more complicated.

### 2.2.2 Be-mechanism

In some systems, the companion star is a *Be-star*, *i.e.* a B star rotating very rapidly. This rotation provokes the appearance of a *decretion torus*. This region will be the source of many emission lines, hence the *e* in the name.

In such systems, the compact object is in a very eccentric orbit. While it is orbiting far away from the Be-star, the compact object (NS or BH) cannot accrete any matter from the torus of material surrounding the star, so it will not emit any X-rays or $\gamma$-rays. When passing the periastron, the compact object will cross the decretion torus and will accrete matter after the formation of a disk around the CO. An X-ray outburst will thus be observable. Once the periastron passage is over, the mass accretion rate will rapidly decrease and soon the disk will stop feeding the compact object. The X-ray emission becomes fainter and stays at a low level until the next periastron passage. In some cases, the Be binary system

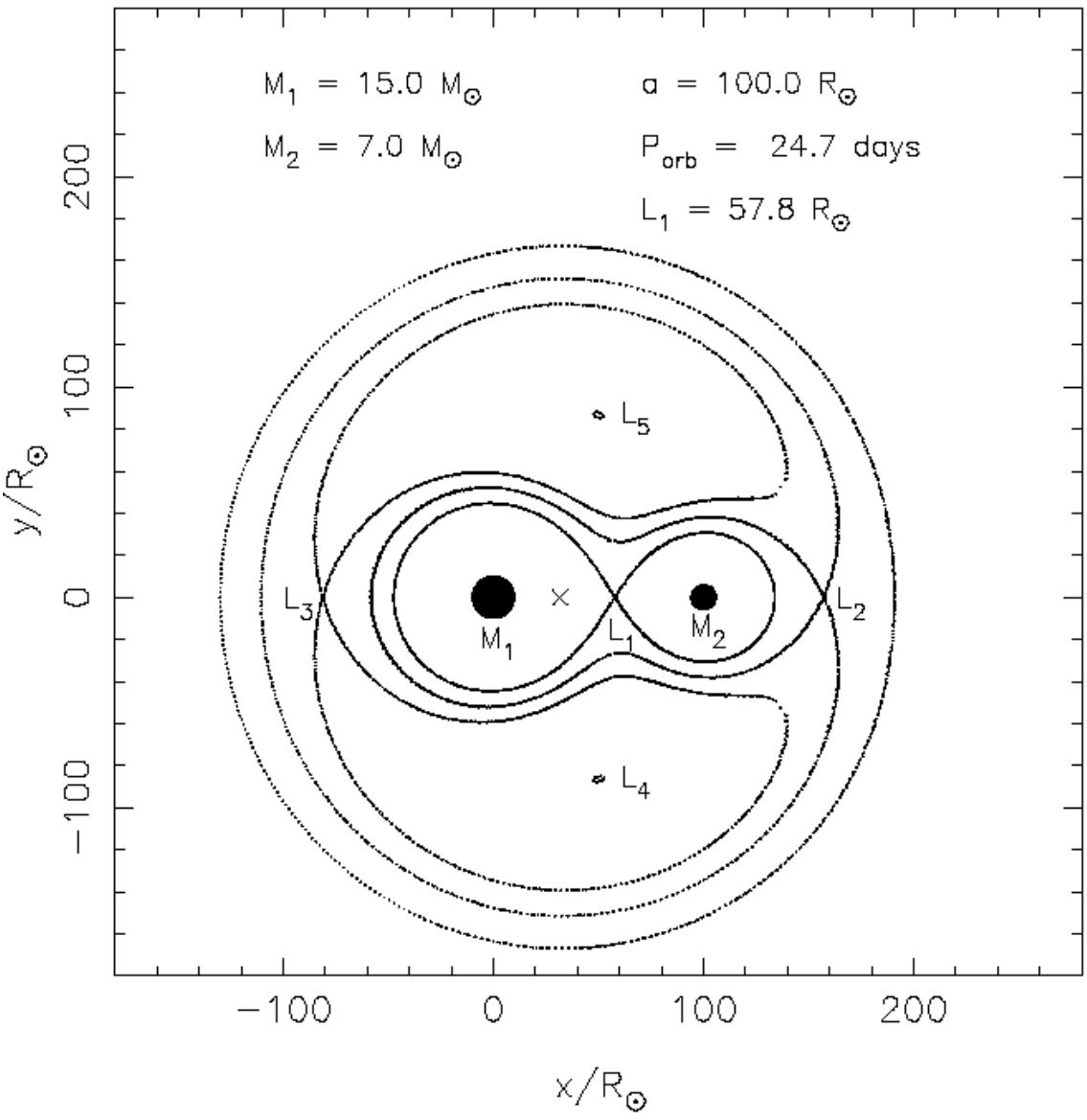


**Figure** *2.1: Equipotential surfaces of the Roche potential. The points $L_1 - L_5$ are the Lagrangian points. The surface crossing the $L_1$ point is the Roche Lobe. Credits: Tauris & van den Heuvel (2005).*

in a low level is unobservable : these sources are then among the transient sources which are detected only episodically.

### 2.2.3 Stellar wind

If the companion star of the compact object is an O or B star, the mass loss through stellar wind plays a key role in accretion. Indeed, the amount of matter expelled by the companion star can reach up to $10^{-4}$ $\mathrm{M_\odot\,yr^{-1}}$. In such systems, the compact object orbits not too far away from the massive star, thus it is deeply embedded in the stellar wind. The stellar wind does not carry a significant angular momentum, so the compact object can accrete matter directly from the dense stellar wind. As the wind angular momentum is not strictly null, a disk might also form. Besides, the released X-rays will also ionise the wind.

This accretion mechanism is very complex and depends much on the dense stellar wind geometry. Also, this method is not very efficient since the material is expelled in all directions and only a small part will be accreted onto the compact object. The accretion will take place in a cylindrical region above the compact object with a radius $r_{\mathrm{accr}}$ of :

$$r_{\mathrm{accr}} = \frac{2GM_{\mathrm{CO}}}{v_{\mathrm{wind}}^2 + v_{\mathrm{CO}}^2} \tag{2.11}$$

where $M_{\mathrm{CO}}$ and $v_{\mathrm{CO}}$ are the mass and velocity of the compact object, respectively, and $v_{\mathrm{wind}}$ the stellar wind velocity. With a wind emitted over a solid angle $\Omega$ and a mass-loss rate $\dot{M}_{\mathrm{wind}}$, the mass accretion rate is thus :

$$\dot{M} \sim \frac{\pi r_{\mathrm{accr}}^2}{\Omega a^2}\dot{M}_{\mathrm{wind}}, \tag{2.12}$$

where $a$ is the binary separation. Considering an isotropic wind ($\Omega = 4\pi$) with typical velocities of $\sim 10^3$ $\mathrm{km\,s^{-1}}$ and a binary separation $a \sim 10^{12}$ cm, the accretion radius $r_{\mathrm{accr}}$ is $\sim 10^{10}$ cm, so the accreted fraction is $\sim 10^{-4}$. As the mass-loss rate of the companion star is important, there is enough accreted matter ($\dot{M} \leq 10^{-8}$ $\mathrm{M_\odot\,yr^{-1}}$) to radiate at a significant fraction of the Eddington luminosity, even if the process is very inefficient compared to Roche Lobe overflow where all the matter falls onto the compact object.

# Chapter 3
# X-RAY BINARIES

In this chapter, we briefly review the family of X-ray binaries. These objects have been the central topic of this thesis. There are several reviews on them in the literature giving full explanations about their emission properties and their evolution : Nagase (1989); White et al. (1995); Verbunt & van den Heuvel (1995); Bildsten et al. (1997); Orlandini (2004); Tauris & van den Heuvel (2005). These reviews (and references therein) have been used throughout this chapter.

## 3.1 Introduction

X-ray binaries (XRB) are systems formed of two stars hosting one compact object. There are several possibilities for the the two stars and, depending on the composition of the system, this will give rise to different physical emission mechanisms. These are the brightest X-ray sources in the sky. The first source serendipitously discovered was Sco X-1 during an observation of the Moon (Giacconi et al. 1962).

There are three types of compact object that can be part of an X-ray binary system : a white dwarf (WD), a neutron star (NS) or a black hole (BH). The binaries with a WD form a particular sub-family that will not be described here.

The factors determining the emission properties depend on the central engine (NS or BH) and the geometrical distribution of the accreting matter, disk versus spherical accretion. If the central object is a neutron star, the presence of a strong magnetic field also influences the X-ray emission. This determines the emission region location and size. The radiated luminosity and the spectral shape depend on the mass accretion rate and the mass of the central object. These sources are highly variable.

X-ray binaries with either a NS or a BH can be divided into different sub-families. The mass of the companion star is used to distinguish between them. There are three categories (as stated by Tauris & van den Heuvel (2005)) :

- the High Mass X-ray Binary (HMXB) with the companion star mass $M_{\rm C}$ higher than 10 $\rm M_{\odot}$;
- the Low Mass X-ray binary (LMXB) with $M_{\rm C} \leq 1$ $\rm M_{\odot}$; and
- the Intermediate Mass X-ray Binary (IMXB) with $M_{\rm C} \sim 1 - 10$ $\rm M_{\odot}$.

## 3.2 Properties of X-ray binaries

The different categories of XRB display different observable properties. We give a short review of them for each subfamily : first the HMXB, next the LMXB, and finally the less common IMXB.

### 3.2.1 High Mass X-ray binary

The mass of the companion star is higher than $10M_{\odot}$. There are two categories of HMXB, one being X-ray persistent sources and the other X-ray transients. The compact object can be either a NS or a BH.

The standard HMXB has a massive supergiant companion of spectral type OB. These stars expel huge quantities of matter through stellar winds that partly feed the compact object. They are mainly in almost-circular orbits with an orbital period between 1–15 days. These systems are persistent. Ten HMXB with a supergiant companion were known previously to the *INTEGRAL* mission and its discoveries (e.g. see catalogue of Liu et al. (2000) or Bildsten et al. (1997)). They possess a strong magnetic field ($B \sim 10^{12-14}$ G). Some of these sources display pulsations in their light curve and are called pulsars. The observed pulsation periods are between ∼10–1000 s.

Another category of HMXB is composed of transient sources. They have an eccentric orbit and an orbital period between ∼20–300 d. These systems are formed with a Be star which is a highly rotating B star that possesses a strong equatorial wind. They show strong variability going from complete absence of emission to giant outbursts. The durations of the outbursts range from days to months.

The HMXB are principally located along the galactic plane among the OB stars regions.

### 3.2.2 Low Mass X-ray binary

The mass of the companion star is around $\leq 1M_{\odot}$. They show orbital periods ranging from a few minutes to many days. The observed optical spectrum corresponds to the hot accretion disk. The companion star emission is totally dominated by the disk one. Their magnetic field is lower than for HMXB ($B \sim 10^{9-11}$ G), so they do not show pulsations except in a few cases, e.g. 4U 1822-371. They often show X-ray flares due to thermonuclear flashes. Indeed, accretion on the surface of the NS can accumulate enough matter to produce nucleosynthetic explosions. They also show quasi-periodic oscillations (QPO) in their power spectrum that is the signature of the interaction of the accretion disk with the magnetic field of the NS.

Depending on the inclination of the system, different emission features can be observed. In most cases, no eclipse is observable. For low angles, the accreting source is observable. For high angles ($\sim 90^{o}$), the accreting source emission is blocked by the thick accretion disk. However, X-ray emission is still detected through scattering in the hot corona. With an angle comprised between $\alpha \sim 70 - 80^{o}$, dips and, in some cases, eclipses are observable in the source light curve. Dips are related to material ejected above the disk plane where the gas stream of the companion star hits the accretion disk.

Two families of LMXB can be described from their spectral emission properties when the compact object is a neutron star. In colour-colour diagrams, the highly luminous LMXB

show a Z pattern and the low luminous LMXB show an Atoll pattern. The movement of the source in both patterns would be due to the evolution of the mass accretion rate $\dot{M}$. The spectrum is often described in two parts. The soft spectrum is either fitted with a single temperature black body or by a multi-colour disc black body. The hard spectrum is described with a Comptonisation model. In some cases, there is another component. For a few sources, hard X-ray tails are observed and need an additional power law component in order to describe the broad band spectrum. Observations of iron K line emission at 6.7 keV are also often reported.

Most of the LMXB are located in the galactic bulge and in globular clusters. They are an old population of stars.

### 3.2.3 Intermediate Mass X-ray Binary

The mass of the companion star is comprised between $\geq 1\mathrm{M}_\odot$ and $\leq 10\ \mathrm{M}_\odot$. These systems are very uncommon. Indeed, the companion star is not massive enough to produce a strong stellar wind that would be able to fuel long enough an X-ray source as for HMXB. Their X-ray emission is due to Roche Lobe overflow from the companion star. This phase is very short since the mass ratio between both stars is large. The mass transfer rate would be large enough to obscure the X-ray source as it would exceed the Eddington luminosity. However, their presence is necessary to help to explain the formation of binaries with a heavy white dwarf.

This category will not be discussed again in this thesis.

## 3.3 Formation and evolution

The formation of a binary system needs the formation of two stars in the same molecular cloud where the two proto-stars would not merge. Other possibilities (capture of a low-mass star by a high mass star or the fragmentation of a high-mass stars due to a very high rotation) are highly improbable. The two newly formed stars will normally evolve along the Hayashi line and pass most of their life in the main sequence (MS) phase. The more massive star of the system will evolve faster and quit the MS earlier. At this point, the evolution of both stars will differ from normal single stars. There are many possible scenarios depending on the initial masses of both stars.

The two main categories of X-ray binaries (HMXB and LMXB) differ in many points in their evolution. We briefly review their evolution separately. Even if the formation of white dwarf binaries is the most common scenario, we will not discuss it here.

### 3.3.1 Evolution of HMXB

Two massive stars ($M > 12\,\mathrm{M}_\odot$) are required at the beginning. At least, the secondary star (that will feed the compact object once it is formed) must be massive enough to reach the critical mass necessary to end in a supernova after the mass transfer from the other one.

The more massive star evolves first from the MS. It fills its Roche Lobe (see Sect. 2.2.1) and thus transfers its mass to the secondary star. Meanwhile, the core continues its evolution. If the mass is sufficient ($M \geq 3\ \mathrm{M}_\odot$), the star explodes as a supernova leaving a neutron

star behind (or eventually a black hole in more massive cases when the initial mass of the primary star is higher than 40 $M_\odot$). The explosion expels an important quantity of matter out of the system if not transferred to the other star. This causes a change of the orbit. If the mass loss is too important (more than half of the initial mass), the system is disrupted. Therefore, the mass transfer to the other star is vital to keep a binary system after the supernova. Observations revealed an important number of HMXB with a Be companion star in an eccentric orbit. Due to the mass transfer, *i.e.* also the angular momentum carried by the matter, the B star gets an important rotation that gives rise to the decretion torus.

At this stage, the system is formed of a compact object, either a NS or a BH, and a massive companion star (more massive than at the beginning). This system emits X/$\gamma$-rays if the NS or BH captures matter from its companion. As Be-star loses matter in two ways, a strong equatorial wind and a lighter spherical stellar wind, the Be-HMXB shows a low level emission with important outbursts when the compact object crosses the strong equatorial wind region. The other persistent HMXB are close binaries with an evolved supergiant secondary star. The supergiant star has a strong stellar wind from which the compact object accretes matter.

Due to the mass gained, the secondary star evolves faster and it will expand. At some point, it reaches its Roche Lobe. Part of the matter is transferred on the compact object while most of the envelope is lost. During this Common Envelope (CE) phase, the compact object spirals into the envelope of its companion. The evolved core of the secondary star finally explodes in a second supernova in the system. The final product is a combination of NS and/or BH depending on the initial masses of both stars. The evolutionary stages of a HMXB are illustrated in Fig. 3.1.

## 3.4 Evolution of LMXB

The formation of LMXB needs the presence of a massive star at the beginning in order to get a compact object and a MS star with mass $\sim 1$ $M_\odot$.

The massive star evolves, fills its Roche Lobe and engulfs the MS star in its envelope as seen previously for the HMXB case due to mass transfer. Once the envelope expelled, the core of the massive star continues its evolution and, eventually, it ends as a supernova. That forms a compact object, either a NS or BH. This phenomenon is dramatic in many cases, except if the mass of the core is not too massive before the explosion. Otherwise, the binary system is disrupted.

The newly formed NS or BH starts to accrete from the MS star once the separation between both stars has shortened enough due to loss of angular momentum, so the MS star reaches its Roche Lobe. Due to RLO, an accretion disk is formed and the LMXB emits X-rays. The loss of angular momentum is due to gravitational waves and/or magnetic braking (see Sect. 11.3.2 of Verbunt & van den Heuvel (1995) for a detailed explanation of this process). The MS star naturally evolves as a giant and continues to fuel the XRB source as long as it fills its Roche Lobe. This ends once the mass of the envelope is lower than 0.01 $M_\odot$.

The binary system now consists of the evolved core of a giant and a compact object. In the case of a NS, the transfer of mass leads to an increase in the rotation. In that case, the NS can show up as a radio pulsar once the mass transfer stops. Even, the mass transfer phase is long enough to produce millisecond pulsars with weakly magnetised NS ($B \sim 10^9$ G).

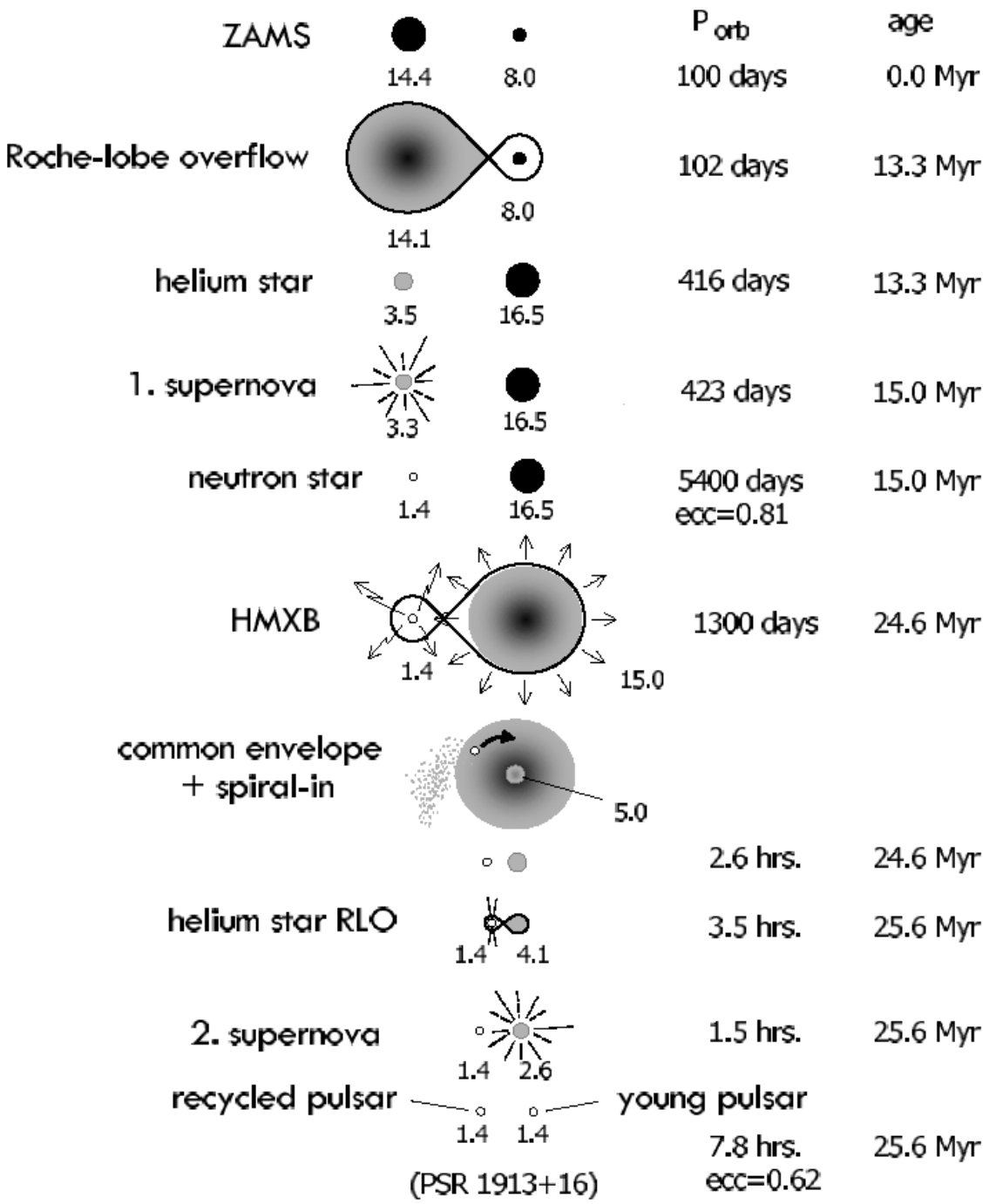


**Figure** *3.1: Sketch presenting the formation and evolution of a high mass X-ray binary. A Be-accreting system is formed in this case. The stellar masses are in solar units. Credits: Tauris & van den Heuvel (2005).*

The companion star can either finish as a cool WD or the strong X-ray emission of the compact object can evaporate it.

The evolutionary stages of a LMXB are illustrated in Fig. 3.2.

## 3.5 Pulsars

The discovery of pulsed emission in XRB defined a new category of X-ray sources : the accreting X-ray pulsar[1]. The presence of a strong magnetic field ($B \sim 10^{11-14}$ G) plays a key role in the X-ray emission. The basic picture of a pulsar is a strongly magnetised neutron star accreting matter from its companion star. The matter is funnelled onto the NS polar cap along the magnetic field lines. The pulsed emission is easily understood as the misalignment of the NS rotation axis and the magnetic axis. When the $B$-axis is directed towards the Earth, an enhancement of the radiated energy is observed.

The formation of the strong magnetic field is independent of the single star evolution. Its formation would happen during the carbon burning phase where the core is very convective.

### 3.5.1 Accretion geometry

A full magneto-hydrodynamic treatment is necessary to explain the complex emission of pulsars. However, some analytical consideration concerning the geometry of the accretion are possible.

The matter driven towards the NS (wind-fed or RLO) is subject to the magnetic pressure and the ram pressure of the infalling gas. When both pressures are equal, the matter is driven by the $B$-field lines. This point is defined as the magnetospheric radius or the Alfvén radius :

$$r_{\rm m} = 2.9\,10^8\, M_{\rm X}^{1/7}\, R_6^{-2/7}\, L_{37}^{-2/7}\, \mu_{30}^{4/7}\ {\rm cm} \tag{3.1}$$

where $M_{\rm X}$ is the mass of the X-ray source in solar units, $R_6$ is the NS radius in units of $10^6$ cm, $L_{37}$ is the X-ray luminosity in units of $10^{37}$ ergs s$^{-1}$, and $\mu_{30}$ is the dipolar magnetic moment in units of $10^{30}$ G cm$^3$. At this distance, the matter accretes due to magneto-hydrodynamical instabilities. This transition region between the infalling gas stream and its disruption where the gas follows the $B$-field lines is also called the boundary layer.

In order to have accretion onto the NS, its rotation should not be fast enough to expel the matter through centrifugal forces, *i.e.* the pulsar magnetosphere should rotate slower than the Keplerian velocity at the boundary layer. The balance between both forces is achieved at the co-rotation radius :

$$r_{\rm c} = 1.5\,10^8\, P^{2/3}\, M_{\rm X}^{1/3}\ {\rm cm} \tag{3.2}$$

where $P$ is the rotational period in seconds. Thus, the magnetic radius $r_{\rm m}$ must lie inside the co-rotation radius $r_{\rm c}$ in order to get accretion onto the NS. This is the *accretor regime*. When $r_{\rm c} \leq r_{\rm m}$, the centrifugal force inhibits the matter to be funnelled onto the NS and it

[1]Here, we concentrate on HMXB pulsars. There are other categories of pulsars : the radio pulsars whose pulsation mechanism comes the rotation and not the accretion and the millisecond pulsars that are very rapidly rotating NS with a weak magnetic field of the order of $10^9$ G formed in LMXB systems.

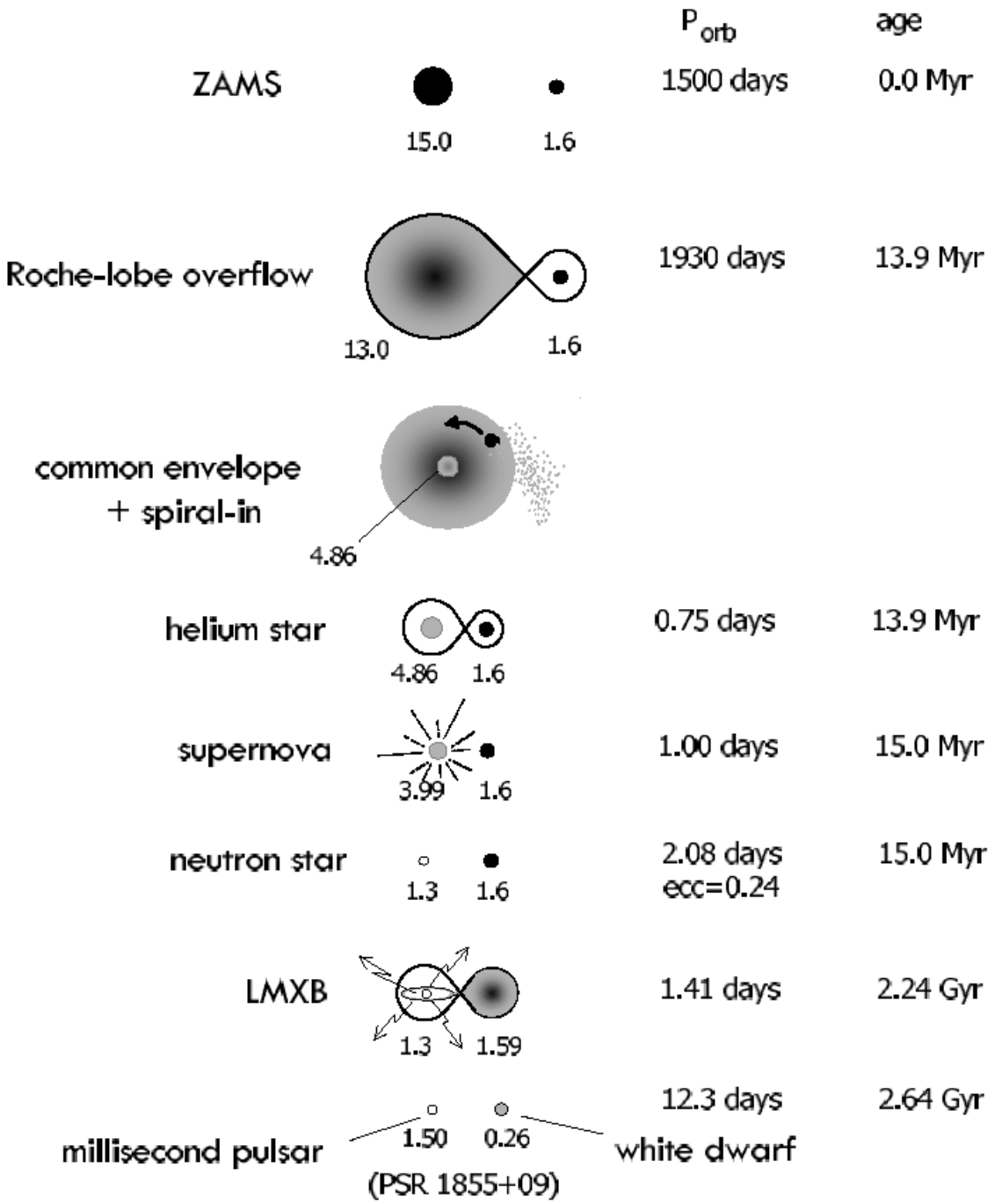


**Figure** *3.2: Sketch presenting the formation and evolution of a low mass X-ray binary. A millisecond pulsar is formed at the end. The stellar masses are in solar units. Credits: Tauris & van den Heuvel (2005).*

is swept away. This is known as the *propeller effect*. These two regimes will cause the NS spin to vary.

Once the matter has penetrated the magnetosphere, it follows the $B$-field lines until the magnetic polar caps whose size is rather small, $\sim$1 km. Depending on the amount of matter accreted onto the NS, two kinds of emission can be distinguished. If the luminosity is greater than $10^{37}$ ergs s$^{-1}$, a radiative shock is formed at a certain radius of the NS surface. Thus, an accretion column just above the polar cap is formed. It is optically thick to X-rays. Therefore, the infalling plasma radiates perpendicularly to the direction of the $B$-field lines. This results in a broad emission geometry and it is called the *fan beam emission pattern*. If $L_{\rm X} < 10^{37}$ ergs s$^{-1}$, there is no shock front formation. The matter reaches the NS surface. There, X-ray photons due to thermal bremsstrahlung and Compton cooling are emitted in a parallel direction. This narrow emission geometry is called the *pencil beam*.

In these scenarios, the observed pulse profile depends on the inclination of the magnetic axis respect to the line of sight. If both polar caps are visible, the folded light curve displays a double peak pulse profile. If only one polar cap is visible, only one peak is visible.

### 3.5.2 Cyclotron lines

The X-ray radiation interacts with the surrounding matter before escaping the system. Due to the strong $B$-field, the electrons moving inside the magnetosphere are quantified at certain energy levels determined by the Larmor frequency. Therefore, photons are scattered at specific energy levels. A non-relativistic treatment gives :

$$E_{\rm cyc} = 11.6\, B_{12} \text{ keV}. \tag{3.3}$$

Even if the observed feature looks like an absorption line in the spectrum, the phenomenon is more likely a scattering process as a photon is quickly re-emitted. This *absorption* process is more likely called *Cyclotron Resonant Features* (CRF). This topic will not be discuss anymore as no CRF were detected in the objects studied in this thesis (at least, to date).

### 3.5.3 Energy spectra

#### Continuum

The main mechanism operating in a pulsar is Compton scattering. The X-ray continuum spectra of the pulsars can be easily modelled with a hard power law modified by a high-energy cut off. This phenomenological analytical function is written as :

$$f(E) = A\, E^{-\Gamma} \times e^{\frac{E_{\rm cut}-E}{E_{\rm fol}}} \tag{3.4}$$

where $E_{\rm cut}$ and $E_{\rm fol}$ are the high-energy cutoff and the $e$-folding energy, respectively. Typical values are a hard power law energy index $\Gamma \sim 0.0 - 1.0$, and a high-energy cutoff between 5–25 keV.

Other models can also reproduce the observed spectra as, for example, a broken power law. A broad band energy spectrum is important to constrain the possible models as for example, the high-energy cutoff lies at energies higher than classical X-ray missions (e.g. *XMM-Newton*).

### Fluorescence Iron line

An emission line at 6.4 keV is often visible in the spectra of highly absorbed HMXB. This line correspond to the fluorescence emission of less ionised iron present in the cool matter surrounding the XRB system. This differs from LMXB that show an iron emission line at 6.7 keV that corresponds to highly ionised iron.

The precise determination of the line centroid helps to determine the level of ionisation of the iron. House (1969) computed the wavelengths of K$\alpha$-type X-ray transition for a series of heavy particles like iron (see Table 2, p.30). The ionisation parameter is defined as :

$$\xi = \frac{L}{nR^2} \tag{3.5}$$

where $L$ is the source luminosity, $n$ the gas density, and $R$ the distance between the radiating source and the ionisation region (Kallman et al. 2004). Basically, $nR$ is equal to the column density $N_{\mathrm{H}}$. Kallman et al. (2004) computed the ion fraction vs the ionisation parameter for different ionisation stage of the iron (see Fig. 5 in their paper). Therefore an upper limit $\xi_{\max}$ can be given to $\xi$ once the maximum iron ionisation is known. Knowing the luminosity and the local absorption of a specific source, the minimal distance $R_{\min}$ between the X-ray source and the region where the cold iron is located can be calculated as :

$$R_{\min} = \frac{L}{N_{\mathrm{H}}\xi_{\max}}. \tag{3.6}$$

### Soft X-ray excess

Soft excess at energies below 5 keV have been observed in several highly absorbed HMXB (e.g. Vela X-1). This excess comes above the expected photo-electric absorption. This absorption is not pulsed. The origin of this soft excess would be due to interaction between the X-ray radiation and the companion stellar wind.

Hickox et al. (2004) studied a sample of XRB pulsars. They determined that a soft X-ray excess is very common in pulsars. In the very luminous ones ($L_{\mathrm{X}} \geq 10^{38}$ ergs s$^{-1}$), the soft excess is only due to the reprocessing of hard X-rays emitted by the NS by the inner shell of the accretion disk. In less luminous pulsars ($L_{\mathrm{X}} \leq 10^{36}$ ergs s$^{-1}$), the soft excess is produced either by photo-ionised or collisionally heated diffuse gas or thermal emission from the surface of the NS. In intermediate cases ($L_{\mathrm{X}} \sim 10^{37}$ ergs s$^{-1}$), any combination of processes are possible.

# Chapter 4
# Variability and timing analysis

X-ray binaries show strong variability on different time scales. In some cases, their light curves can display coherent modulations. Therefore, timing analysis in the frequency domain is very helpful. Indeed, a periodic oscillation in a light curve gives a peak in a frequency power spectrum representation.

In this chapter, the timing analysis method through Fourier transform is presented. This chapter is based on papers of Lomb (1976), Scargle (1982), Leahy et al. (1983), Horne & Baliunas (1986) and Press & Rybicki (1989). More information (and all equations) can be found in these papers.

First, the Fourier transform and the definition of the periodogram is presented. Then, a modified periodogram proposed by Lomb (1976) and Scargle (1982) that handles with unevenly spaced timing samples is proposed. Finally, an alternative method using the epoch-folding technique is presented.

## 4.1 Fourier transform : the periodograms

An observable $X$ is observed $N_0$ times, thus forming a data set : $\{X(t_i), i = 1, 2, .., N_0\}$. The discrete Fourier transform (FT) is then written as :

$$\mathrm{FT}_X(\omega) = \sum_{j=1}^{N_0} X(t_j)\, e^{-i\omega t_j} \,. \tag{4.1}$$

The periodogram (or power spectrum) is then defined as :

$$P_X(\omega) = \frac{1}{N_0} \left|\mathrm{FT}_X(\omega)\right|^2 . \tag{4.2}$$

The power spectrum can be evaluated for any frequency $\omega$. If a periodic signal with frequency $\omega_0$ appear in the series $X(t_i)$, $P_X(\omega_0)$ results in a high value because the factors $X(t_j)\, e^{-i\omega t_j}$ are in phase.

The natural binning in frequency for an observation of duration $T$ is :

$$\omega_n = \frac{2\pi}{T}\, n \qquad \left(n = -\frac{N_0}{2}, .., +\frac{N_0}{2}\right) , \tag{4.3}$$

so only half of the frequencies ($n = 0, 1, .., N(= +\frac{N_0}{2})$) needs to be calculated since the periodogram is symmetric : $P_X(-\omega) = P_X(\omega)$. As $\omega = 2\pi\nu$, the lowest (fundamental)

frequency is $\nu_1 = 1/T$, which corresponds to a signal with a period equal to the duration of the observation. The highest frequency is called the Nyquist frequency and is defined as $\nu_{\rm N} = 1/(2\,\delta t) = N_0/(2T)$ where $\delta t (= T/N_0)$ is the shortest time interval available.

## 4.2 The Lomb-Scargle periodogram

The equations presented in the previous section work well for evenly sampled data. However, in astrophysics, this is often not the case. The observations are often unevenly spaced in time. Thus, the power spectrum must be adapted to work also for unevenly spaced data sets.

Lomb (1976) and Scargle (1982) developed a new method to compute the periodogram. For a data set $\{x_i, i = 1, 2, .., N\}$, the mean and variance are computed as :

$$\bar{x} = \frac{1}{N}\sum_1^N x_i \qquad \text{and} \qquad \sigma^2 = \frac{1}{N-1}\sum_1^N (x_i - \bar{x})^2, \text{ respectively.} \tag{4.4}$$

Basically, they modified the periodogram proposed in Eq. 4.2 by introducing a slight offset $\tau$ defined as :

$$\tan 2\omega\tau = \frac{\sum_j \sin 2\omega t_j}{\sum_j \cos 2\omega t_j}. \tag{4.5}$$

The *normalised Lomb-Scargle periodogram* is then :

$$P_N(\omega) = \frac{1}{2\sigma^2}\left\{\frac{[\sum_j (x_j - \bar{x})\cos\omega(t_j - \tau)]^2}{\sum_j \cos^2\omega(t_j - \tau)} + \frac{[\sum_j (x_j - \bar{x})\sin\omega(t_j - \tau)]^2}{\sum_j \sin^2\omega(t_j - \tau)}\right\}. \tag{4.6}$$

The property due to the introduction of the offset is that the power spectrum $P_N(\omega)$ becomes independent to any shifting of each time $t_i$ by a constant. This form is equivalent to the equation that one would obtain by fitting the data points $x_i$ with a sinusoidal model ($x_i = A\cos\omega t + B\sin\omega t$) and minimising with a linear least square method (Lomb 1976). Thus, this periodogram gives better results for unevenly spaced time series as the data are weighted per point, and not per time interval.

A fast computing method of the Lomb-Scargle periodogram is proposed by Press & Rybicki (1989). First, 4 sum factors must defined as :

$$S_x \equiv \sum_{j=1}^N x_j \sin\omega t_j, \qquad C_x \equiv \sum_{j=1}^N x_j \cos\omega t_j, \tag{4.7}$$

$$S_2 \equiv \sum_{j=1}^N \sin 2\omega t_j, \qquad C_2 \equiv \sum_{j=1}^N \cos 2\omega t_j. \tag{4.8}$$

Then, the Lomb-Scargle periodogram can be easily evaluated with :

$$\sum_j x_j \cos \omega(t_j - \tau) = C_x \cos \omega\tau + S_x \sin \omega\tau \qquad \equiv c1, \tag{4.9}$$

$$\sum_j x_j \sin \omega(t_j - \tau) = S_x \cos \omega\tau - C_x \sin \omega\tau \qquad \equiv c2, \tag{4.10}$$

$$\sum_j \cos^2 \omega(t_j - \tau) = \frac{N}{2} + \frac{1}{2}C_2 \cos(2\omega\tau) + \frac{1}{2}S_2 \sin(2\omega\tau) \qquad \equiv c3, \tag{4.11}$$

$$\sum_j \sin^2 \omega(t_j - \tau) = \frac{N}{2} - \frac{1}{2}C_2 \cos(2\omega\tau) - \frac{1}{2}S_2 \sin(2\omega\tau) \qquad \equiv c4, \tag{4.12}$$

and, with :

$$\sum_j \bar{x} \cos \omega(t_j - \tau) \equiv c5, \tag{4.13}$$

$$\sum_j \bar{x} \sin \omega(t_j - \tau) \equiv c6, \tag{4.14}$$

hence, Eq. 4.6 can be written :

$$P_N(\omega) = \frac{1}{2\sigma^2}\left\{\frac{(c1 - c5)^2}{c3} + \frac{(c2 - c6)^2}{c4}\right\}. \tag{4.15}$$

The incertitude on the frequency $\delta\omega$ (Horne & Baliunas 1986) is :

$$\delta\omega = \frac{3\pi\sigma_N}{2\sqrt{N_0}TA}, \tag{4.16}$$

where $\sigma_N^2$ is the variance of the noise after the signal has been subtracted, $T$ the duration of the data set, and $A$ the amplitude of the signal (Hill et al. 2005) given by :

$$A = 2\sqrt{\frac{z_0\sigma_s^2}{N}} \tag{4.17}$$

where $z_0$ is the Lomb-Scargle power and $\sigma_s^2$ is the variance of the light curve. In case the signal is completely dominated by the noise, the variance of the noise is equal to the variance of the data set (*i.e.* $\sigma_N^2 = \sigma_s^2$) (see Appendice A of Scargle (1982) and also Horne & Baliunas (1986) for more detail).

## 4.3 Alternative method : the epoch-folding search technique

The technique based on folding the data with a given epoch is also useful to detect periodicities in X-ray observations. Indeed, it can handle data sets with gaps, something quite common in satellite observations. Moreover, it is more sensitive for period shapes that are not sinusoidal. This feature can be found for example in pulsars (e.g. Bulik et al. (2003)).

A data set of total length $T$ is folded into $n$ phase bins (with a count rate in the $j$th bin of $R_j$) with different trial periods over an arbitrary range. The presence of a signal is determined by the following statistic $S$ :

$$S = \sum_{j=1}^{n} \frac{(R_j - R)^2}{\sigma_j^2} \tag{4.18}$$

where $R = N_\gamma/T'$ ($N_\gamma$ is the total number of photons and $T'$ is equal to the sum of all $T_j$), $\sigma_j^2 = R/T_j$, and $T_j$ is the integration time over the $j$th phase bin. Coherent modulation in the signal is visible when the value of $S$ becomes important. The usual statistic used is the $\chi^2$-statistic when the count rates are important enough.

# Chapter 5
# DESCRIPTION OF TWO SPACE MISSIONS: *INTEGRAL* and *XMM-Newton*

In this chapter, we essentially describe the basic concepts of the two space missions that we have used throughout our work: *INTEGRAL* and *XMM-Newton*. The data accumulated with the high energy instruments on-board the former helped to discover a new family of galactic objects that can be studied jointly with the latter.

We first describe the *INTEGRAL* mission, its instruments, and its data analysis software. Then, we describe the *XMM-Newton* mission with which we performed follow-up observations of the sources that were discovered by *INTEGRAL*. This allowed us to get information on the sources from the soft to hard X-rays. Its dedicated data analysis software is also presented. We put special emphasis on the instruments that were mainly used throughout our studies.

## 5.1 The *INTEGRAL* mission

The INTErnational Gamma-Ray Astrophysics Laboratory, *INTEGRAL* Winkler et al. (2003), is a medium-sized mission of the European Space Agency (ESA). The purpose of this satellite is to look at the hard X- and $\gamma$-ray skies. This mission belongs to ESA's "Horizon 2000" programme. It was successfully launched on October 17, 2002, by a Russian PROTON rocket from the Baikonour space centre in Kazakhztan.

Four scientific instruments were integrated on-board the spacecraft. All together, they cover a large range of the electromagnetic spectrum from the optical band to the $\gamma$-ray band. Their goal is to study the different physical processes producing emission at high energies. The two main instruments have been specifically designed to observe in the hard X-ray and $\gamma$-ray ranges with fine spatial and spectroscopic resolutions.

The main targets for this spatial observatory are $\gamma$-ray sources, either point or diffuse sources, present mainly in our galaxy, but also sometimes in extragalactic fields. Another topic of interest for *INTEGRAL* are the regions where stellar nucleosynthesis takes place.

We first introduce the spacecraft itself and the ground segment. We continue with the instruments where we take the opportunity to describe the coded-mask imaging technique

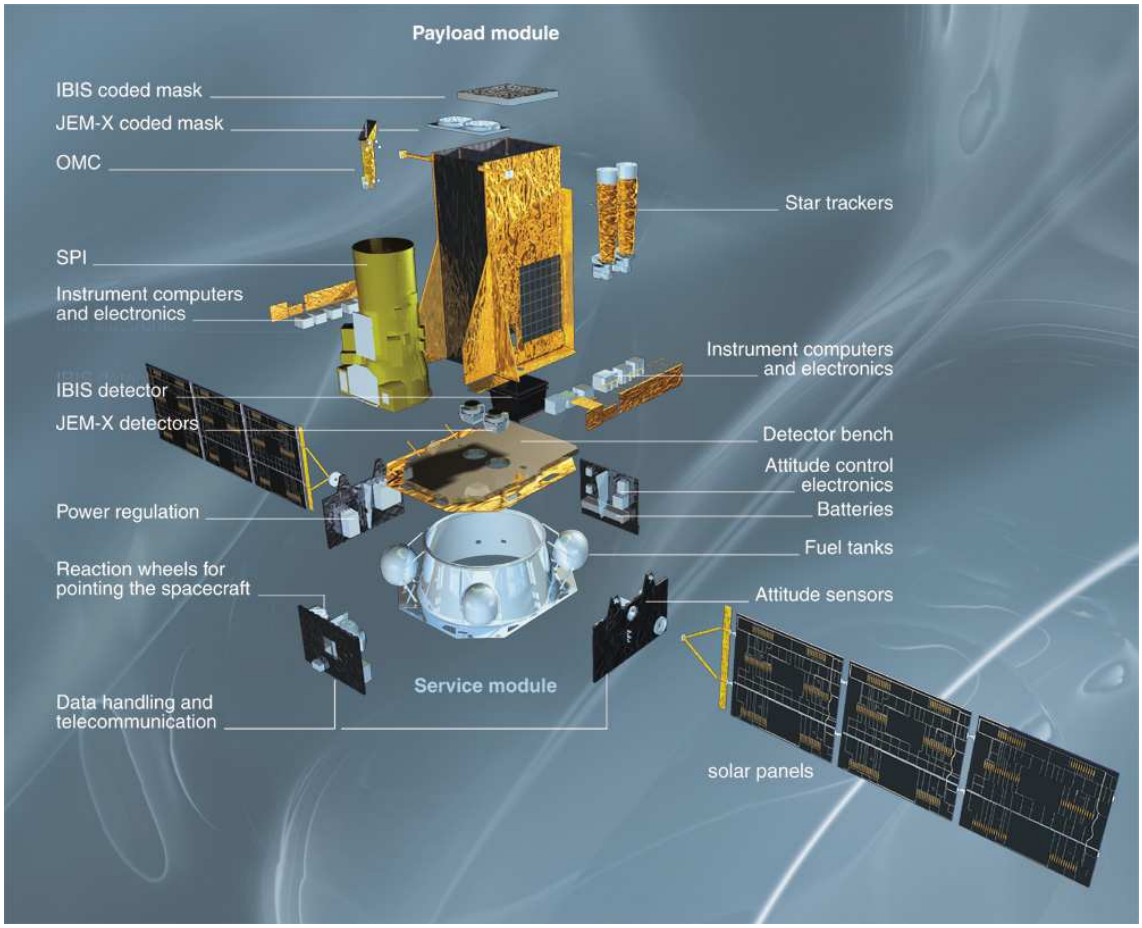


**Figure** *5.1: Exploded view of* INTEGRAL. *The service module at the bottom supports all the technical systems. At the top, there is the payload module with the four instruments : IBIS, SPI, JEM-X, and OMC, plus the star tracker. Credits : ESA 2002.*

as it was the one chosen for the high-energy instruments on-board *INTEGRAL*. We finish with a brief introduction to the offline data analysis software.

### 5.1.1 The spacecraft

The spacecraft (S/C) is made of two big structures. At the bottom, the service module supports the technical systems (e.g. the thermal, attitude, electrical control and orbital ones). The *INTEGRAL* Radiation Environment Monitor (IREM) whose goal is to monitor the radiation activity around the satellite is also mounted on the service module and, in case of an increase of such radiation, an alert is sent to the instruments. The service module is also the part to which the solar panels are fixed. On top of it is located the payload module. It consists of the four instruments, plus the star tracker (see Fig. 5.1).

The S/C flies around the Earth in an elliptical orbit lasting nearly 3 days. An eccentric orbit was chosen to make sure that the S/C spends most of its time far away from the disturbing electronic and hadronic belts located high above the Earth surface. When the S/C crosses the belts, the high energy instruments must be turned off, because they interact with the

particles causing an increase of the detected background activity and possible damage to the detectors. Every revolution, the satellite flies by the Earth at a perigee distance of 9000 km and retreats until it reaches an apogee of 160 000 km. Therefore, the detectors can perform long exposure observations without interruption for nearly 3 days : almost 90% of the revolution can be dedicated to scientific observations. During the rest of the time, the detectors are put in safe mode to ensure that they won't be damaged when crossing the vicinity of the Earth and its radiation belts.

### 5.1.2 The ground segment

Two stations ensure the satellite follow-up : Redu in Belgium and Goldstone in California. Hence, the whole orbit is covered. The telemetry packets are then sent to the Mission Operation Centre (MOC) located in Darmstadt (Germany).

The *INTEGRAL* ground segment is divided in two parts : the operation and the science. The *INTEGRAL* Science Operation Centre (ISOC) (located at ESTEC at the beginning and since 2005 at ESAC) is in charge to call for proposals and to provide an observation plan to the MOC.

The *INTEGRAL* Science Data Centre (ISDC) (located at Versoix near Geneva) receives the telemetry data and process them before releasing the processed data to the community. An archive of all the data is maintained at ISDC. The ISDC also provides the Offline Science Analysis package that allows an interactive analysis of the *INTEGRAL* data.

A Quick-Look Analysis (QLA) is also operated at ISDC that allows to get images per pointing of the X-ray and $\gamma$-ray sky approximately three hours after its observation. Therefore, unexpected interesting events can rapidly be checked and the community alerted (see more in Chapter 11).

### 5.1.3 The instruments on-board INTEGRAL

The four instruments on-board *INTEGRAL* are :

- the hard X-ray and $\gamma$-ray imager IBIS Ubertini et al. (2003) which works in the 20 keV to 10 MeV energy range and has got two detector layers :
  - ISGRI Lebrun et al. (2003) for the 20 keV to 1 MeV energy band;
  - PICsIT Labanti et al. (2003) for the 200 keV to 10 Mev energy band;
- the hard X-ray and $\gamma$-ray spectrometer SPI Vedrenne et al. (2003) which goes from 20 keV to 8 MeV;
- the X-ray monitor JEM-X Lund et al. (2003) that covers the 3–30 keV energy range; and
- the optical camera OMC Mas-Hesse et al. (2003) performing photometry using a Johnson V filter.

All these instruments offer a full coverage in the high energy band from X-rays to $\gamma$-rays (i.e. 3 keV to 10 MeV), and an optical observation in the V band ($\lambda$=5500 Å). They all point in the same direction and are simultaneously operated.

The main characteristic of the three high-energy instruments is that they are based on coded-mask detectors. Indeed, focusing high-energy photons remains a difficult task. The incident X- or $\gamma$-ray photons tend to either be absorbed by the optics built to focus them or to cross it, but they are usually not reflected. Therefore, the common technique based on gathering all the photons at a focal point where the detector is located was discarded during the design of the instruments. Instead of this, masks with specific patterns were placed in front of each detector. The photons coming from a given source in the field of view of the instrument are distributed on the detector following the pattern of the coded-mask and the position of the source. Afterwards, the sky image can be reconstructed provided the mask pattern was carefully chosen. This technique allows to create images of the X- or $\gamma$-ray skies. One advantage of this technique is that both the source and the background are measured simultaneously. The other main advantage is a significantly wider FOV, as its size is of the order of degrees, while classical telescopes are limited to FOV of a few arc-minutes.

### Coded-mask imaging

The goal of coded-mask telescopes is to create images of the X/$\gamma$-ray skies. The use of coded masks follows from the fact that focusing incident X/$\gamma$-ray photons into a focal plane detector (as is done in classical telescopes) is almost impossible. Indeed, the wavelength of X/$\gamma$-ray photons is significantly shorter than the distance between atoms of the focusing material. Therefore, they can go through the lens without any interaction.

A coded mask consists of a planar array of transparent and opaque elements, whose distribution is specifically chosen to get optimal performances. The mask is placed in front of the detector plane. Each source within the FOV projects a shadow of the mask on the detector plane. Every detected X/$\gamma$-ray photon is recorded along with the energy deposited, its arrival time, and its (x,y) position on the detector plane. The photons arriving on the detector plane form the so-called shadowgram image or simply shadowgram ($D$). Once the observation is finished, the original sky ($S$) has to be reconstructed from the shadowgram and the (known) mask geometry ($A$). Additionally, the background activity ($B$) is simultaneously measured. The encoded information can be described as :

$$\mathrm{D} = \mathrm{S} * \mathrm{A} + \mathrm{B} \tag{5.1}$$

where the matrix D represents the two-dimensional shadowgram, S the original sky, A the coded mask, and B the additional background that is not modulated by the mask as there are events coming from the side. It is an indirect and complex method to visualize the sky.

There are many possibilities for the mask pattern such as

- a base pattern which is repeated (known as an Uniformly Redundant Array (URA)). For IBIS, a variant of URA was chosen. The IBIS mask is thus a Modified Uniformly Redundant Array (MURA); or
- a random distribution of the blocking elements, which is the solution chosen for JEM-X.

The best sensitivity is achieved with half of the elements being opaque and the other half transparent in order to reduce the high-energy background effect.

Another important property of coded masks is that their FOV can be divided into two regions: the fully-coded and the partially-coded field of view (FCFOV and PCFOV, respectively). These two regions are defined as the zones for which the source modulated by the mask totally illuminates the detector plane (FCFOV) or only part of the detector plane is covered by the shadow (PCFOV). The significance being higher when the source is located within the FCFOV, a way to increase the FCFOV it is to build a mask larger than the detector. The inconvenience of this method based on masks with a repeated geometry is that sources situated within the PCFOV produce non-perfect coded shadowgrams, so it provokes ghost peaks in the images that must be eliminated during the reconstruction process.

The main advantages of these redundant arrays is that they offer a wide FOV when compared to classical telescopes (FOV of degrees compared to arcminutes) and the background is measured simultaneously to the source.

### The imager IBIS

IBIS stands for Imager on Board (the) *INTEGRAL* Satellite. It is a $\gamma$-ray telescope designed to create images with a high angular resolution. It operates in the 15 keV to 10 MeV energy range. It is made of two detector layers behind a coded mask made of Tungsten. The mask is formed of the coded pattern plus the structure that sustains it. Its angular resolution depends only on the size of the mask element ($c = 11.2$ mm) and on the distance between the mask and the detector plane ($H = 3133$ mm), so the angular accuracy achieved is :

$$d\theta = arctan(c/H) = 12' \,. \tag{5.2}$$

This is the size of the point-spread function (PSF) used when decoding the images. The mask is a parallelipipede of 1064x1064x16 $mm^3$, with 95x95 individual cells. Half of them are opaque in the IBIS energy range. The choice of the mask is based on a cyclic replication array called MURA.

Between the mask and the detectors, there is a collimator made of a passive material that blocks as much as possible of the high energy diffuse background emission. The collimator is opaque up to 200 keV. The FOV achieved for IBIS is of $29° \times 29°$ square.

The top detector is the *INTEGRAL* Soft Gamma-Ray Imager, ISGRI, that operates from 20 keV up to approximately 1 MeV. It is an array of 128x128 independent pixels made of Cadmium-Telluride (CdTe) crystals.

The bottom detector is the Pixellated Imaging Caesium Iodide Telescope, PICsIT, that operates from approximately 200 keV up to 10 MeV. It is composed of Caesium-Iodide (CsI) scintillator crystals divided in an array of 64x64 pixels.

The two detector layers are completely surrounded on five sides (bottom+4 lateral sides) by an anti-coincidence system named VETO. This shielding system is made of BGO crystals. Its goal is to reduce the background by rejecting those events detected by the instruments due to cosmic particles or local environment radiations.

The normal ISGRI science mode records each event, (*i.e.* each photon absorbed in one crystal), and tags it with the (X,Y) position of the detection pixel in the detector plane, the energy deposited in that pixel, and the event time.

Even if the possibility to record each event exists also for PICsIT, this procedure is not used because of the higher background influence. Instead, the PICsIT standard mode is to accumulate images and spectra for 30 minutes and to download them as histograms. The time resolution of PICsIT is thus 30 minutes.

### The spectrometer SPI

The SPectrometer on board the *INTEGRAL* satellite, SPI, is the main instrument for high-resolution spectroscopy at hard X- and $\gamma$-ray energies. Its spectral range goes from 20 keV up to 10 MeV. It also provides low-angular resolution images.

The instrument is made of three main parts: a coded mask, an array of detectors, and a shield. The coded mask (see Sect. 5.1.3 for an explanation of coded-mask detector) is made of tungsten and has a hexagonal geometry. The elements are 60 mm large, and 50% of them are transparent. They are distributed in a 120° rotated symmetric pattern. The mask is located 1710 mm in front of the detector plane, so the angular resolution is $\sim 2.5^{\circ}$ (see Equ. 5.2). The detector is a hexagonal array of 19 high purity Germanium detectors. Two of these detectors are presently dead: #2 and #17, so the effective area and the sensitivity are slightly reduced. In order to minimise the radiation damage on detectors and to bring them back to their nominal state, an annealing is needed every 6–12 months to recuperate perfect crystals. Due to high background contamination, an Anti-Coincidence Shield (ACS) made of BGO crystals surrounds the detectors array and detects all events coming from outside the observed FOV. Its size defines the wide field of view with a diameter of 35°.

The ACS has a scientific impact as it is a multi-directional detector for all $\gamma$-ray photons, so it can detect all random Gamma-Ray Bursts (GRB), but without any spatial information.

SPI has only one operating mode : a photon-by-photon counting mode with a high-temporal resolution. All information for each photon (not coincident with an ACS event) is transmitted to the ground station. The event type can be either :

- a single event (*i.e.* detected in one detector); or
- a multiple event (*i.e.* when the incident photon is Compton scattered and deposits its energy in different locations, within the same detector or different ones.

As there are very few detectors, many pointings are needed in order to reconstruct the image. Therefore, a dithering strategy is adopted; the satellite observes the same field but with a slight offset for each pointing. This also allows a better average (and thus reduction) of the background, which is very interesting because it is very important in the $\gamma$-ray domain when compared to the brightness of the high-energy sources.

### The X-ray monitor JEM-X

The Joint European Monitor for X-rays, JEM-X, is designed to complement the observations taken with the two main instruments described above, thus widening the energy range down to 3 keV. JEM-X can also observe sources with steep spectra that would be well beyond the detection limits of IBIS and SPI.

The instrument consists of two identical coded-mask telescopes co-aligned with the other instruments on-board *INTEGRAL*. Each JEM-X unit is made of three parts: the coded

mask at the top, the detector, and the electronics at the bottom. The detector is a microstrip gas chamber where incident photons are absorbed by photo-electric processes and the resulting ionisation is amplified towards the strip anodes using high voltages. The collimator structure, joining the mask and the detector, fixes the diameter of the FOV to $13^{o}.2$ and helps to reduce the background contamination. The mask pattern is based on a hexagonal uniformly redundant array. Only 25% of the cells are transparent. This value is a compromise between a better sensitivity and telemetry allocation constraints. The distance between the mask and the detector of 3400 mm and the cell size of 3.3 mm determine the angular resolution of $3'$ (see Equ. 5.2).

After the mission started, important degradations of the anodes due to interaction with cosmic rays were noted. Consequently, only one unit is operated at a time. At the beginning of the mission, JEM-X1 was turned off and now it is JEM-X2 that is not operational. The high voltage used after the launch is also reduced to protect the detectors, and this results in a loss of sensitivity.

JEM-X has several operating modes to cope with telemetry constraints. A filtering of the events is also performed on-board with a logical grey filter that randomly rejects photons. Packets can be transmitted with or without image information, and the timing and spectral performances also change.

#### The optical monitor OMC

The optical monitoring camera, OMC, is a wide-field telescope using a large-format CCD detector. It is co-aligned with the other high-energy instruments. The optical system consists of a set of refractive lenses and a Johnson $V$ filter. It has a square FOV of $5^{o} \times 5^{o}$, but only small fractions of it are transmitted to the ground due to telemetry restrictions. In fact, the normal science operation mode consists of a selection of boxes around known sources within the FOV that are observed during short exposures. Reference stars, high-energy sources and good-photometric candidates are good targets for OMC, and are observed in consecutive shots. The window size is $3' \times 3'$ (*i.e.* 11×11 pixels). Another fast monitoring mode is used when highly fast variable targets are expected in the FOV. In this fast mode, the integration time is ∼3 s.

If a GRB is detected in the IBIS FOV and this GRB is located within the OMC FOV, OMC automatically stops its current observation and starts monitoring a $24' \times 24'$ field around the GRB position.

The limiting magnitudes $m_{\mathrm{V}}$ for OMC lie between 7–18.1 magn.

#### Field of view summary

The field of view of the different high energy instruments on-board *INTEGRAL* are of different sizes and the sensitivity also depends on the instrument:

- IBIS has a square FOV of $29^{\circ} \times 29^{\circ}$ ($9^{\circ} \times 9^{\circ}$ for the fully-coded FOV) and its angular resolution is $12'$,
- SPI has an hexagonal FOV with a diameter of $31^{\circ}$ ($16^{\circ}$ for the fully-coded FOV) and its angular resolution is $2^{\circ}$, and

- JEM-X has a circular FOV with a diameter of 13.2° (4.8° for the fully-coded FOV) and its angular resolution is 3.35′.

Due to the SPI instrument, *INTEGRAL* adopts a dithering strategy during observations. There are two dither pattern :

- the 25×25 pointings dithering pattern that ensures a better sensitivity for SPI; and
- the 8 hexagonal pointings dithering pattern that ensures a full coverage with JEM-X of the source located at the centre of the FOV.

*INTEGRAL* can also perform staring observation.

### 5.1.4 The *INTEGRAL* observation time

The observing time of *INTEGRAL* is defined as the time when the instruments are in nominal mode for scientific observations. It is divided in two components :

- the General Programme, which is open to the whole scientific community; and
- the Core Programme (CP), which is guaranteed observation time for the *INTEGRAL* Science Working Team, as a reward for their contribution while developing the mission.

During the first three years, the time has been divided between the two programmes as follows: 65% (year 1), 70% (year 2), 75% (year 2+) for the General Programme, and, consequently, 35% (year 1), 30% (year 2), 25% (year 2+) for the CP.
In order to make the best out of this large amount of guaranteed time, large observational projects have been undertaken. The *INTEGRAL* CP consists of several topics :

- Observations of the Galactic central region :
  - Galactic Centre Deep Exposures (GCDE);
  - Deep exposures of the Scutum and Norma galactic spiral arms (only during AO3);
  - Galactic latitude profile scans (only during AO3);
- Frequent Galactic Plane Scans (GPS);
- Observations of selected sources such as Cyg X-1 or 3C273;
- Deep extragalactic survey (only during AO3); and
- Follow-up observations of Target of Opportunities (ToO).

Only data taken during the GCDE and the GPS were used for this monitoring programme. The GCDE consists of different grids of pointings covering approximately the area defined by $l \sim [-30^o; +30^o]$ and $b \sim [-20^o; +20^o]$. Each pointing lasts ∼1800 s. In order to improve the sensitivity of the main instrument used for this study (IBIS/ISGRI), the observation strategy pattern was changed for the AO3 period. A small offset is now introduced between each grid. Therefore, the residual background structures in the images are averaged and thus better limited. The GPS is based on regular scans along the galactic plane, with an

extension in latitude limited to $[-10^o; +10^o]$. The satellite basically executes a movement of slew and stare, which draws a saw-tooth pattern along the galactic plane. Each pointing lasts 2200 s.

The main scientific goals of these programmes are :

- the study of galactic compact objects (white dwarfs, neutron stars and black hole candidates) in binary systems;
- the detection of diffuse continuum emission;
- mapping the line emission from nucleosynthetic radioisotopes such as $^{26}$Al, $^{44}$Ti; and
- studying the positron-electron annihilation line at 511 keV.

### 5.1.5 The off-line science analysis software

The off-line science analysis software (OSA) is the official software package used to reduce the raw data accumulated by the various instruments on-board *INTEGRAL* and to perform interactive science analysis. OSA is released by the ISDC, and it integrates all the applications developed by the instrument teams in a uniform way.

OSA is currently at version 5.1. However, during the four years of this thesis, we have seen (tested...) all the evolutions of the different versions, from version 1.0 to the present one, and even earlier with the simulator. Evidently, the data presented in further chapters have been processed with the most recent version at the time of the study. Indeed, most of the results shown in the articles were derived with OSA 4.2. A re-processing with OSA 5.0 was conducted in selected cases to confirm previous results. OSA 5.1 was not used as the new software was released long after the writing was started.

OSA provides the step from the raw science, housekeeping, auxiliary and calibration data, to the common analysis tools (such as `Xspec` or `Xronos`). Personal scripts are also possible to manipulate the OSA output files. In short, the goals of OSA are :

- to apply necessary corrections;
- to calculate the dead times and select good-time intervals;
- to perform the image reconstruction from shadowgrams;
- to identify the sources within the FOV;
- to extract spectra; and
- to extract light curves.

The complexity of the mission due to the coded-mask instruments results in a complex data analysis process. Except for the OMC, no true imaging is performed : images are reconstructed through deconvolution. As the FOV of the main instruments are wide and the source signal encoded, sky reconstruction must take into account all the sources together, so the data sets are huge and the algorithms are complex. The procedure is totally different from the one used by other telescopes (such as *XMM-Newton*) that deal with event lists. The basic piece of data is the so-called *Science Window* (ScW) that corresponds to one

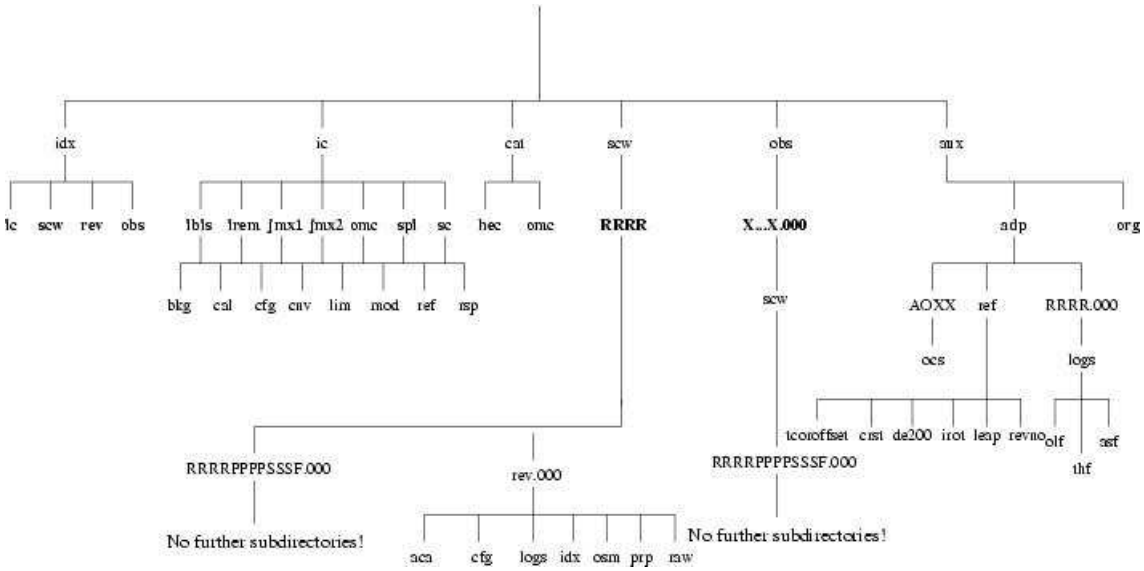


**Figure** *5.2: Hierarchical organisation of* INTEGRAL *data.*

single pointing. All information specific to a single ScW is contained in a *Science Window Group* (SWG). A collection of individual ScW can be arbitrarily grouped together in an *Observation Group* (OG) by the user. The OG consists of one sub-directory created in the directory `obs` by the OSA task `og_create` that contains other sub-directories and index files (e.g. `og_ibis.fits`) linking to files necessary for the analysis, for example the calibration files. The OSA scripts write all the analysis output files in these sub-directories. All the information data needed by OSA is distributed within a specific (ISDC-like) structure of directories containing :

- all the auxiliary files (orbit, attitude) (`aux`);
- the source catalogues (`cat`);
- the instrument calibrations (`ic`);
- the science window data (`scw`); and
- index tables to facilitate the search of files (`idx`).

This represents hundred of files (see Fig. 5.2).

Each instrument has a specific set of scripts to interactively analyse the data. This can be done in two ways: either by using the graphical user interface (GUI), or by passing all the desired parameters through the line command. A real-life example on how to proceed is given throughout Chapter 6.

## 5.2 The *XMM-Newton* mission

The X-ray Multi-Mirror space observatory, *XMM-Newton* Jansen et al. (2001), is also an ESA mission that is part of the "Horizon 2000" programme. The spacecraft was successfully launched on December 10, 1999, by the European launcher Ariane V, and placed in an eccentric orbit lasting 48 hours. The eccentric orbit offers a long continuous coverage of the observed field. The satellite contains two X-ray instruments that provide imaging and spectral capabilities, and one optical monitor for simultaneous optical/UV imaging and grism spectroscopy.

### 5.2.1 The spacecraft

The spacecraft weights 4 tonnes and is 10 m long. It is composed of two payload modules connected by a tube that forms the optical bench. The service module contains the technical systems, the optical monitor, and the three mirror modules. The high-energy detectors are located at the focal plane of the X-ray telescopes. A schematic view of the payload modules is shown in Fig. 5.3.

All the scientific instruments operate simultaneously and are co-aligned. Long continuous observations are possible due to the eccentric orbit (up to 40 hours). The perigee is at 7 000 km and the apogee is at 114 000 km.

As explained in section 5.1, the incident X-ray photons cannot be reflected by classical focusing methods as for optical or infra-red photons. However, *XMM-Newton* still uses mirrors to focalize the incident beam, but it is based on grazing incidence optics. Incident photons with energies around 1 keV can be reflected provided their incidence angle is less than a few degrees. Each X-ray telescope consists of 58 "Wolter type I" mirrors, which are a combination of parabolic and hyperbolic mirrors that reflect highly energetic photons and focus them at a focal distance smaller than if using only parabolic mirrors (see Fig. 5.4). A large effective area over a wide energy band is assured with the selected design. The sensitivity is consequently high. The angular resolution of the point-spread function is of the order of $6''$. Sieve plates were put in front of the mirrors in order to avoid straylight contamination. Indeed, photons coming from powerful X-ray sources located outside the FOV can be reflected only by the hyperbolic mirrors and directly reach the detectors resulting in a background enhancement.

### 5.2.2 Ground operations

Two ground stations (Perth and Kourou) follow the satellite during the whole orbit. The science and housekeeping data, along with the spacecraft telemetry, are transmitted to the ground via these two stations and sent to the Mission Operations Centre (MOC) at the European Space Astronomy Centre (ESAC, located beside Villafranca of Spain, near Madrid). The MOC monitors the satellite performance and provides the data to the Science Operation Centre (SOC), also located at Vilspa.

The SOC processes the data into the *Observation Data Files* (ODF) and puts them at the disposition of the scientific community. A data set with the *Current Calibration Files* (CCF) is also provided together with the ODF, so that further interactive scientific analysis can be performed.

All the ODF are first sent to the Survey Science Centre (SSC) in Leicester where they

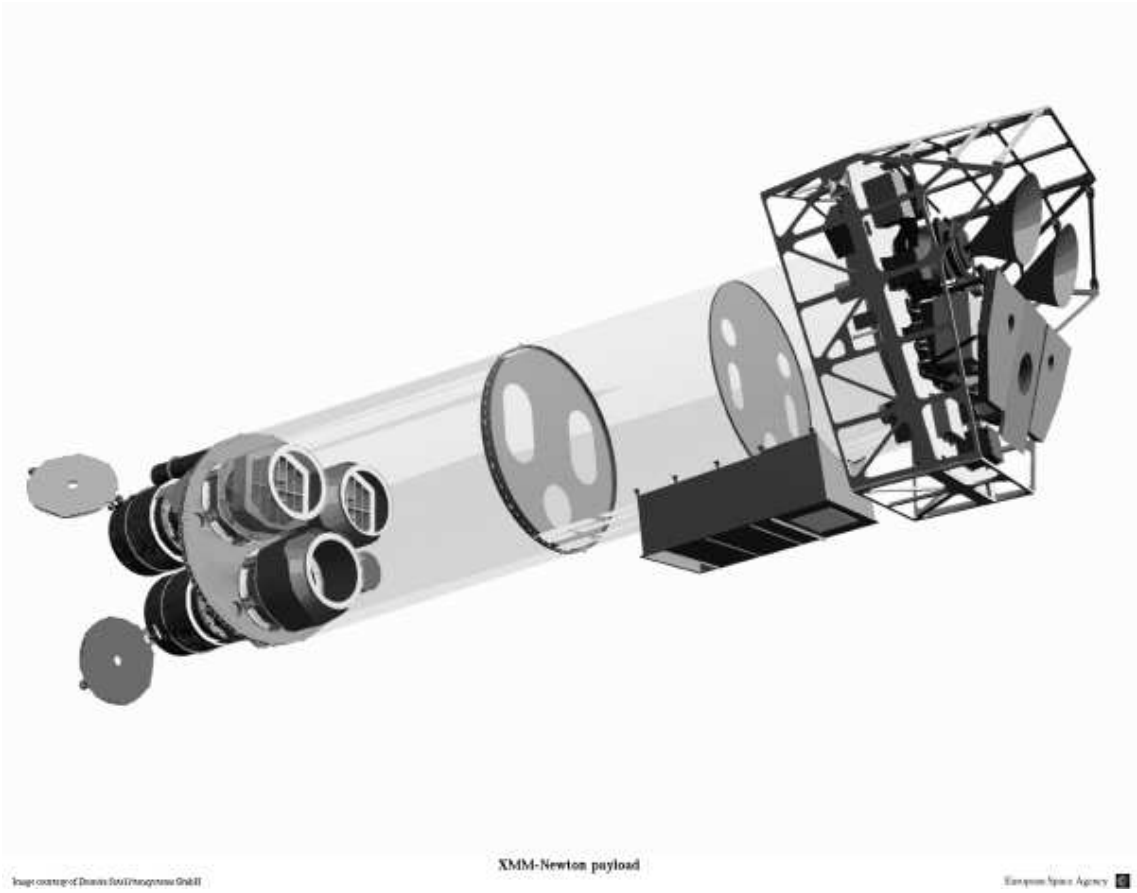


**Figure** *5.3: Sketch of the* XMM-Newton *satellite inside the modules. On the left, there are the three mirror modules, two (top) of which are followed by reflection gratings arrays. Beside the third mirror module, the rear side of the optical camera is visible. On the right, at the focal plane, the detectors are installed: on the top, the two MOS cameras of EPIC and on the bottom, the two RGS detectors surrounding the EPIC/pn camera. Creadits : Image courtesy of Dornier Satellitensysteme GmbH and ESA.*

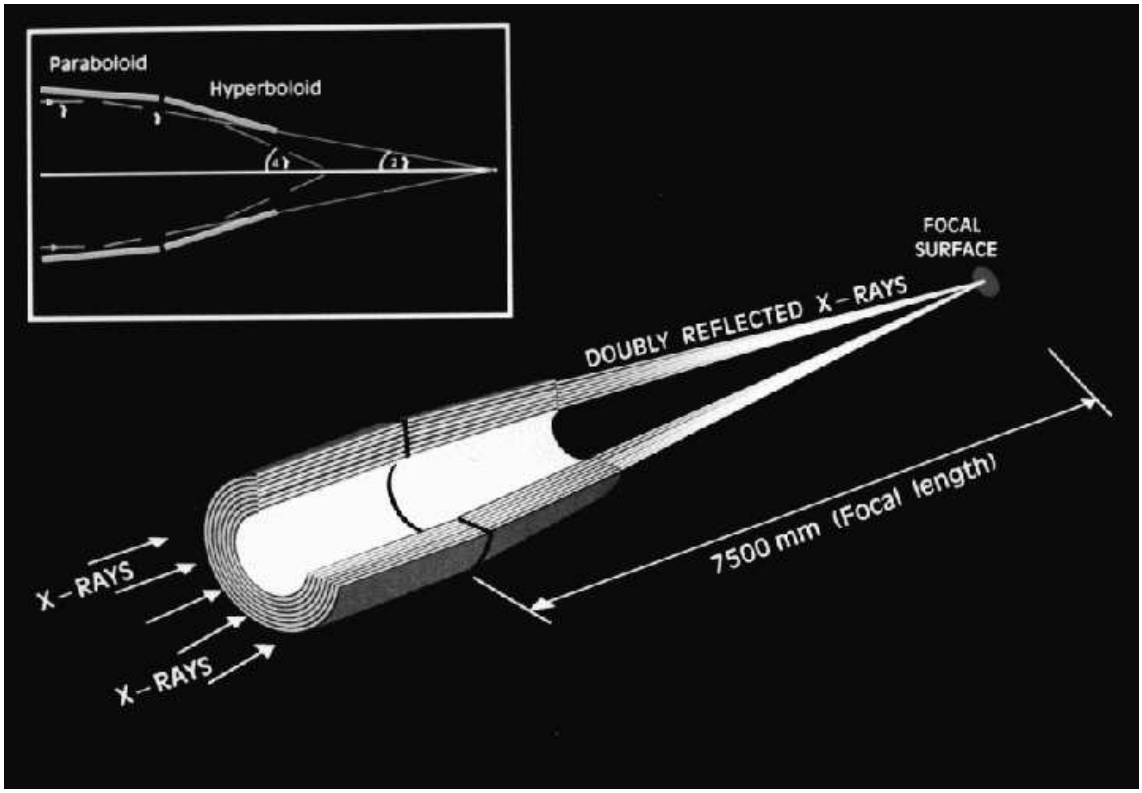


**Figure** *5.4: Grazing incident optics used on-board* XMM-Newton. *Credits : XMM-Newton Users' Handbook.*

are processed through a defined pipeline, in order to create standard products. Cleaned and calibrated event lists, source detection lists, images, spectra and light curves are then proposed to the observers as a starting point for their analysis.

The SSC and SOC provide all the software necessary to analyse *XMM-Newton* data. The applications are gathered together as the *Science Analysis Sub-system* (SAS), and allow observers to perform their own interactive analysis of the data.

### 5.2.3 The instruments

Three scientific instruments are on-board the satellite: the EPIC imager, the RGS spectrometer, and the OM optical monitor.

#### The imager EPIC

The European Photon Imaging Camera, EPIC, is composed of three cameras: two MOS (Metal Oxide Semi-conductor) CCD arrays and a third different CCD camera called pn. The cameras provide highly sensitive imaging performance with a field of view of $30'$, in the energy range 0.15–15 keV, with moderate spectral resolution ($E/\Delta E \sim 20 - 50$) and good angular resolution ($6''$). The chip array geometry is different for both CCD types:

- 7 chips for the MOS, one of which is slightly behind the others to follow the focal plane curvature. Reflection grating arrays are located in front of the detectors, so only 44% of the incident beam reach the MOS cameras, the rest being directed to the RGS. The MOS cameras are shifted by $90^o$ between each other.
- 12 CCD chips (2 rows of 6) for the pn, which are slightly offset with respect to the optical axis, so that the on-axis source fully falls on one CCD (#4) and not at the intersection of 4 of them.

The read-out systems are different for both cameras. The EPIC/pn camera has a read-out node for each column of the CCD, so the information is transmitted faster than for MOS, allowing better timing performance.

All the EPIC CCD work in photon counting mode. There are several science modes depending on the observation type :

**full frame** all the pixels are read out, so the total FOV is covered;

**partial frame** (large window LW, or small window SW) : for MOS, only part of the central CCD is read out, and for pn, in LW only half of each CCD are read out and, in SW, only part of CCD#4 is read out; and,

**timing** (there is also a burst mode specific to pn) : imaging is degraded to one dimension only, but quick read out allows faster timing performances.

As the CCD cameras are able to detect (and in this case affected by) IR, optical and UV photons, blocking filters are used to prevent contamination. The background registered by EPIC has two origins: the Cosmic X-ray Background (CXB) and the instrumental background. The former is partly due to clouds of soft protons populating the Earth's

magnetosphere that interact with the instruments. This creates flares in the light curves that have to be removed when analysing the data. An internal quiescent background is also observed due to the interaction of high energy particles with the structure surrounding the detectors. Spectral features such as fluorescence lines from the detectors and from the S/C structure are visible. All these have been measured. The detector noise in EPIC is negligible.

Another point to be taken into account is the pile-up phenomenon. Photon pile-up is due to the arrival of more than one photon in one pixel before it is read out. Therefore, the information registered would lead to an excess of hard photons. A diagnostic tool is included in the analysis software to check if a list of events is contaminated by pile-up.

### The spectrometer RGS

The Reflection Grating Spectrometer, RGS, is the instrument used for high resolution spectroscopy in the 0.33–2.5 keV (5–38 Å) energy range. This energy range comprises many potential lines of light and heavy elements, due e.g. to K- or L-shell transitions.

The instrument consists of two identical units: RGS1 and RGS2. Each of these units is made of one Reflection Grating Array (RGA) located in the light path of one focusing mirror module and of one CCD camera located at the focal plane of the diffracted beam. The EPIC/MOS cameras are placed at the prime focus plane of the mirror module. 58% of the focused beam is reflected towards the RGS Focal Camera (RFC). The dispersion of the instrument is a function of the dispersion angle. The RFC consists of a linear array of 9 CCD equivalent to those of the MOS and placed along the dispersion direction. The CCD width determines the FOV in the cross-dispersion direction: $5'$ in the case of RGS. Both RFC are slightly offset with respect to each other in order to fill all the dispersion directions and to avoid gaps between the CCD chips. Both RGS lost one of their CCD chips during the early period of the mission : CCD#7 for RGS1 and CCD#4 for RGS2 (see Fig. 6.20).

The diffraction geometry on the grating arrays is shown in Fig. 5.5. The light beam has an incident angle $\alpha$ when reaching the gratings and is reflected with a dispersion angle $\beta$. The dispersion equation is as follow :

$$cos(\beta) = cos(\alpha) + \frac{m\,\lambda}{d} \tag{5.3}$$

where $\lambda$ is the incoming photon wavelength, $d$ the grating spacing, and $m$ the spectral order. Due to the size of the RGA, the first and second orders of the incident radiation can be detected. Higher orders are only detected for very bright sources. The 1st and 2nd orders are easily separated when plotting the CCD energy versus the dispersion angle (see bottom of Fig. 6.20 for an example : the boxes show the theoretical location of the different orders).

The standard operating mode of RGS is called spectroscopy : all CCD are read out. The way the CCD work is that half of each CCD is exposed to the sky and the other half stores the information transmitted by the first half before the read out process. A special mode exists for very bright sources : the spectroscopy High Count Rate (HCR) mode works as the standard one, except it does not make diagnostic images.

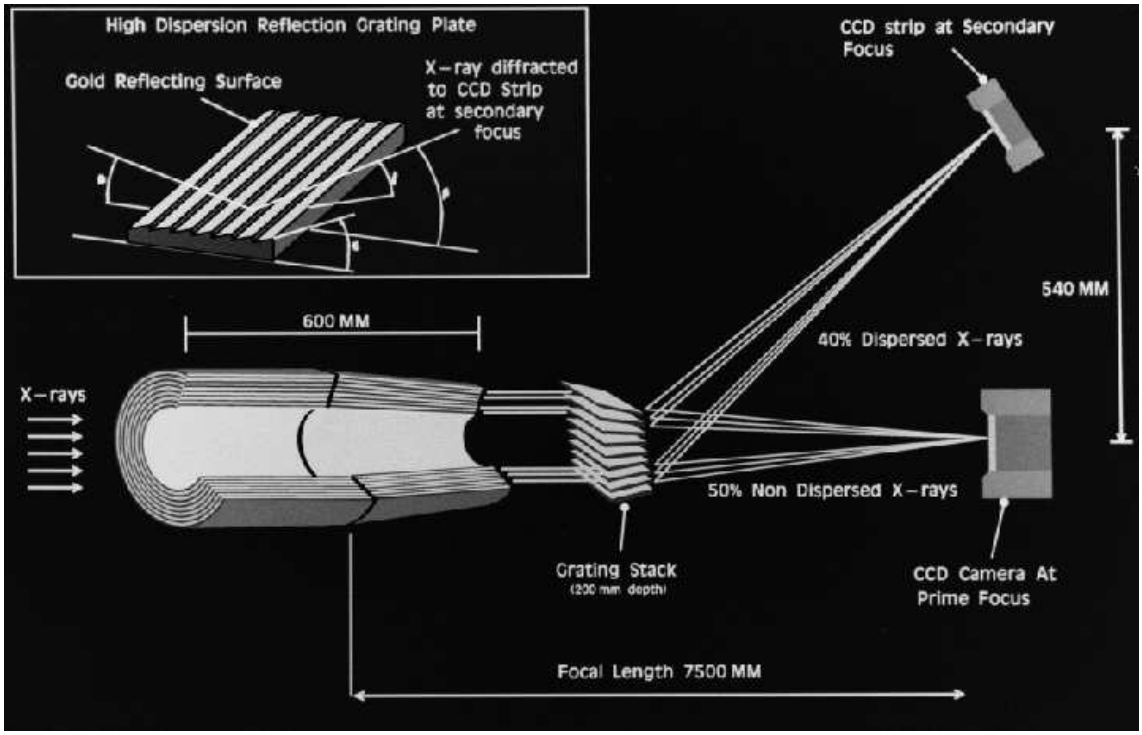


**Figure** *5.5: Illustrative Schema of the diffraction in the RGA. Credits : XMM-Newton Users' Handbook.*

### The optical monitor OM

Besides the high-energy instruments, *XMM-Newton* has on-board an optical/UV telescope that is co-aligned with the other telescopes, so the space observatory simultaneously observes the X-ray and optical/UV skies. Its wavelength range goes from 180 to 600 nm. High-time resolution photometry or low resolution spectroscopy are both possible.

The optical monitor, OM, consists of a Ritchey-Chrétien telescope where the incoming light is first reflected by a primary mirror towards a secondary mirror placed in front of it that reflects the light to a flat mirror located behind the primary one. This last one is placed on a rotatable support that directs the light to one of the two redundant detectors. The telescope is 30 cm long. The OM detectors consist of a micro-channel plate intensified CCD. The field of view is $17' \times 17'$.

The OM works in a photon-counting mode. However, not all the detected photons can be transmitted due to limitations such as memory space and telemetry available. A choice has to be done between images and time resolution. Two operating modes exist:

**imaging mode** images are accumulated in short exposures (less than 5 ks maximum). No timing information is collected for individual photons; and

**fast mode** produces event lists. No images are created.

Different filters are available and cover the UV/optical wavelength band: U, B, V, UVW1, UVM2, UVW2 and a white one. Their wavebands are displayed in Fig. 5.6. Moreover,

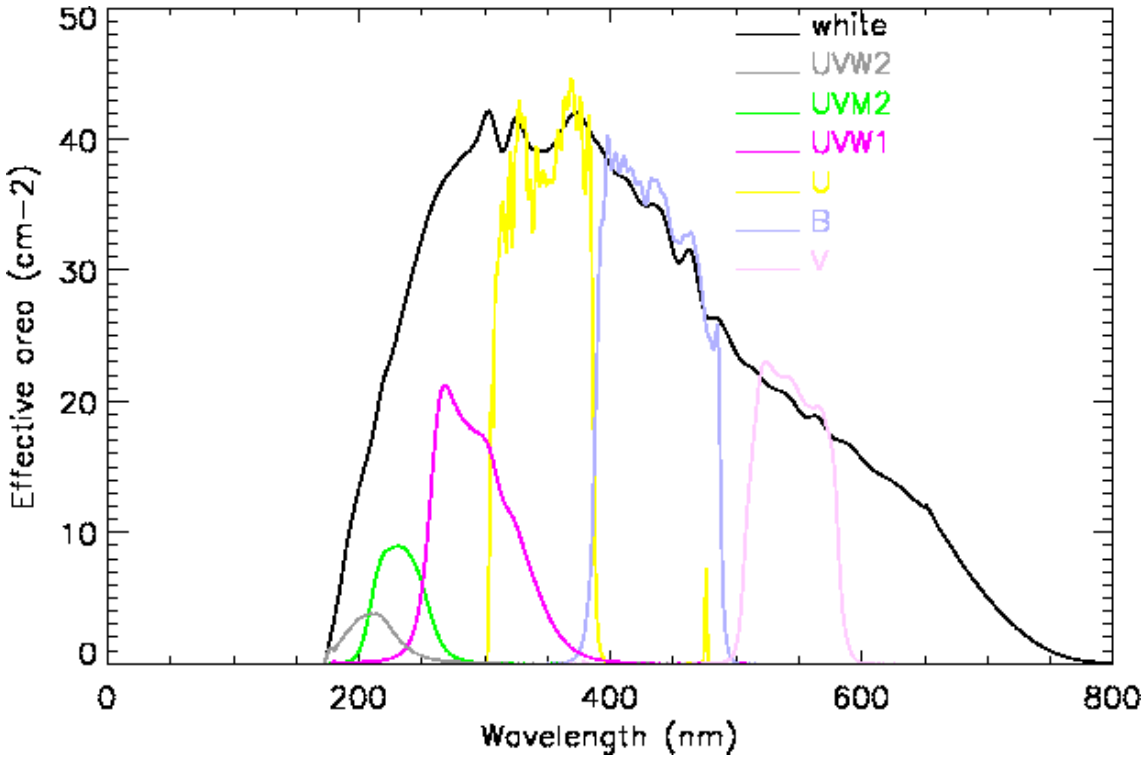


**Figure** *5.6: The throughput curves of the different filters of the optical monitor OM on-board* XMM-Newton. *Credits : XMM-Newton Users' Handbook.*

the filter wheel also holds two grisms. The OM can be used either for UV or optical spectroscopy.

### 5.2.4 The Science Analysis Software

The *XMM-Newton* Scientific Analysis Subsystem (SAS) is the analysis tool to process the *XMM-Newton* data for each instrument on-board the S/C. The package is accessible at :

`http://xmm.vilspa.esa.es/external/xmm_sw_cal/sas_frame.shtml`

The SAS current version is 6.5.0 with an additional patch concerning the usage of calibration files for the MOS cameras. The first version used during this thesis was 6.0.0. Almost all the results presented in this thesis comes from the SAS 6.1.0 version.

The SAS is the tool that processes the ODF. The output files are in FITS format (Flexible Image Transport System format) who is a standard format widely used in astronomy. Then, the common analysis tools (such as `FTOOLS` or `Xspec`) or personal scripts can be used to go further in the science analysis and interpretation.

The steps to perform an *XMM-Newton* analysis are :

1. The user must prepare the SAS environment :

```
setenv SAS_DIR /path_to/xmmsas_version
```

```
setenv SAS_PATH $SAS_DIR
source $SAS_DIR/sas-setup.csh
```

and other packages necessary within SAS as for example `GRACE`;

2. give the link to the Current Calibration Files (CCF) and the ODF :

```
setenv SAS_CCFPATH /path_to/ccf_location
setenv SAS_ODF /path_to/odf_location
```

and prepare the Calibration Index File (CIF) and the link to SAS :

```
cifbuild
setenv SAS_CCF ccf.cif
```

that selects a sub-set of CCF that are correlated to the time of the observation; and

3. prepare the summary file of the ODF and the link to SAS :

```
odfingest
setenv SAS_ODF `\ls -1 *SUM.SAS`
```

that contains the information necessary to run SAS on the data

At this point, the user can perform the analysis for each instrument. Every instrument possesses its own task to process the data and to create concatenated event lists. The user can either use command lines or the graphical interface (`xmmselect`) in order to create images, light curves and spectra. A real-life example is described in Chapter 6.

Threads on how to proceed with the *XMM-Newton* analysis is available on-line :

```
http://xmm.vilspa.esa.es/external/xmm_sw_cal/sas_frame.shtml
and click on Data analysis threads.
```

They are well described.

# Second part

# Galactic Sources discovered by *INTEGRAL*

# Chapter 6
# IGR J17252−3616 OBSERVED BY *INTEGRAL* AND *XMM-Newton*

In this chapter we describe in full detail the analysis of IGR J17252−3616. This source was extensively observed by the *INTEGRAL* satellite during the core programme dedicated to the study of the Galactic Centre and of the galactic plane. This object was also observed by *XMM-Newton* for three hours.

We first describe the discovery of this source. We continue presenting the whole observation performed on this field. Afterwards, the analysis is presented step-by-step: imaging, timing and spectral aspects. The careful study of these different features allows us to speculate on the nature of the object. We give the probable type of IGR J17252−3616. We finally present the future studies on this source.

## 6.1 Introduction

One of the main goals of the *INTEGRAL* mission was to observe the galactic plane and Galactic Centre, and to catalogue all the point sources present in the Galaxy. Evidently, the satellite would also seek for new $\gamma$-ray galactic sources. The imager IBIS has the best spatial resolution ever achieved in the hard X-ray and $\gamma$-ray energy bands : $12'$ . It is therefore an excellent tool for this prospect.

The first new source discovered by *INTEGRAL* was IGR J16318−4848. It happened on January 29, 2003, with the help of the IBIS/ISGRI imager (Courvoisier et al. 2003b). The source is located in the Norma Arm direction, one of the inner arms of our spiral Galaxy. This part of the sky is regularly monitored by *INTEGRAL* through the GCDE and the GPS (see Sect. 5.1.4 for explanations and details of the core program). IGR J16318−4848 is a binary system composed of a compact object, a neutron star or a black hole, and a super-giant star that are gravitationally bound. This source showed a highly absorbed spectrum at soft X-rays. This huge absorption is intrinsic to the system. Moreover, strong fluorescence emission lines of cold material were also observed. The source intensity displays big variations, but it is continuously detected. The mass donor is an early-type supergiant star, with a dense and absorbing circumstellar material surrounding the compact object (Filliatre & Chaty 2004).

This discovery was the first one, soon followed by many other new X/$\gamma$-ray sources that were unnoticed in previous X-rays surveys. X-ray counterparts were found for a few of

them in *ASCA*, ROSAT (e.g. Stephen et al. 2005) and other X-ray missions. Most of the time, even when some of them were previously detected, the information gathered on them was quite poor. The re-discovery of these sources motivated scientists to go have a look at archival data.

All the galactic sources detected by IBIS are catalogued by the *INTEGRAL* survey team and other teams interested in this topic. Around 100 X/$\gamma$-ray sources were discovered or re-discovered by *INTEGRAL*. Complete information on them can be found on the web at:

`http://isdc.unige.ch/~rodrigue/html/igrsources.html`.

One of those new sources is IGR J17252−3616. This source was observed by *INTEGRAL* and *XMM-Newton*. In this chapter, we follow the chronology of events that led us to a better understanding of this source. As we started studying this source as something unknown, we adopt an observational approach and we are going to put, piece by piece, each element of the puzzle as we found it ourselves. We are going to describe step-by-step the analysis we have performed. First, we briefly review the discovery of this source. We continue describing all the data sets that were at our disposition. After, we explain our choice on how to proceed with the huge amount of data from *INTEGRAL*. At this point, we successively show the results we got: images, light curves and spectra, stressing on what we found interesting in each of them. From this information, we could go further in understanding the source. We present the paper that resulted from this detailed analysis. We finish with some speculations about questions that this source could help solve.

## 6.2 Discovery of IGR J17252−3616

The *INTEGRAL* survey team is composed of many different institutes involved in the mission spread across Europe: Bologna, Geneva, Paris, Rome and Southampton. They constantly look for new sources in the galactic field. Due to its unique sensitivity, the IBIS imager is the main tool for this. They try to lower systematic effects on order to reach the theoretical limit of sensitivity and detect the faintest sources.

Most of the new sources were discovered after the satellite performed an observation on a given field and the data were analysed by a scientist. Afterwards, they were announced through an astronomical telegram[2], an *ATel*, so that interested people can be warned and conduct new observations at other wavelengths. Indeed, a multi-wavelength study of a source is a powerful tool to investigate the nature of a new bright object in the sky.

However, IGR J17252−3616 was found in all-sky mosaic images built from ISGRI data accumulated between February 27 and October 19, 2003. It was announced on February 9, 2004, in the ATel #229 (Walter et al. 2004). The given position at that time was R.A. (2000.0)=17h25m.2 and Dec.=$-36°\,16'$ with an accuracy of $2'$, and a significance of 39 in the 20–40 keV energy band.

The source was also present in the first IBIS catalogue published by Bird et al. (2004) (label #53), and located at R.A. (2000.0)=261.309° and Dec.=−36.274° (R.A. (2000.0)=17h25m14.2s and Dec.=$-36°\,16'\,26''.4$). The 20–40 keV average count rate is 1.13±0.03 counts $s^{-1}$ (when

[2] `http://www.astronomerstelegram.org/`

the Crab intensity[3] is 93.64±0.07 counts s$^{-1}$, giving a flux of ∼12 mCrab), and the 40–100 keV average count rate is 0.27±0.03 counts s$^{-1}$ (Crab flux is ∼ 69.12 counts s$^{-1}$, so ∼3.9 mCrab) with a significance of 20.3 for an exposure time of 801 ks (corrected for vignetting). The mean location uncertainty of their technique is 0.72′. However, the systematic error when reconstructing the image for a source with a significance of 20 is of ∼ 1.4′ (Gros et al. 2003). They give no indication about the source type. Data of the first year of operations were used.

## 6.3 Observations of IGR J17252−3616

As the source is located near the Galactic Centre and almost in the galactic plane ($l, b = 351.5^{\circ}, -0.3^{\circ}$), it is regularly monitored by *INTEGRAL*. This leads to a huge amount of data after two years of operations. By the time of this analysis, four GCDE and GPS were completed. Moreover, we could also add all the data that became public for January 2005. In number, the INTEGRAL data set consists of all public data accumulated until MJD 52928.3 (*i.e.* 2003-10-16T07:10:55.8 UTC or revolution 123) and core programme data accumulated until MJD 53341.1 (*i.e.* 2004-12-02T02:22:55.8 UTC or revolution 261), for a total exposure time of 6.5 Ms[4].

The basic scientific product of *INTEGRAL* is a science window (ScW), which consists of one uninterrupted pointing of the satellite towards a given direction. A selection of ScW that populate the archive has to be made. For this, we need to consider what kind of sky field we are looking at. Almost all observations of the satellite are executed in the dithering mode because of SPI. Therefore, due to the big FOV of SPI and IBIS, the sources of interest can appear in many ScW for these two instruments and in much fewer ScW for JEM-X (see Sect. 5.1.3). Another point to be considered is the crowdedness of the targeted region. Indeed, SPI has a worse angular resolution than IBIS, so contamination could occur between sources. In the case of IGR J17252−3616, if you select all sources within a radius of 20° centred on its position, you get tens of sources from the *INTEGRAL* reference catalogue (Ebisawa et al. 2003). Therefore, the analysis was focused on IBIS/ISGRI. We selected all the ScW for which the position of IGR J17252−3616 is within the 29° × 29° FOV of IBIS. A summary is presented in Tables 6.1 and 6.2 for public and CP data, respectively. The whole data set is formed of 70 revolutions, composed of 3029 pointings with a total exposure on the target location of 6.7 Ms. For JEM-X, the data set is reduced to 649 ScW of which only 110 have the source within 3° of the FOV centre. This is just 4% of the ISGRI total.

IGR J17252−3616 was also observed by *XMM-Newton* for three hours. This follow-up is part of the accepted proposal programme 020638 (PI: Walter R.). More information is given in Sect. 9.2. The observation started on March 21, 2004, at 13h02m45s UTC and finished at 16h04m45s UTC during the revolution 784, so the total exposure time is 10.92 ks. The science mode of the different instruments on-board *XMM-Newton* are listed

[3]The Crab count rates comes from the catalogue of Bird et al. (2004). Its label is #3. Their data take into account the first year of the *INTEGRAL* CP.

[4]The GCDE performed during 2005 are not considered in this thesis as they were completed after our investigation. Indeed, the large ISGRI analysis was done in January 2005 and the next GCDE started in March.

**Table** 6.1: Journal of IGR J17252−3616 observations with *INTEGRAL*. The data set is composed of public data.

| Revolution | ScW | Start time MJD | Exposure ks | Off-axis angle $^{o}$ | JEM-X |
|---|---|---|---|---|---|
| 0037 | 77 | 52671.08 | 171.5 | 14.1 | 0 |
| 0038 | 36 | 52674.07 | 79.4 | 13.7 | 0 |
| 0046 | 75 | 52698.00 | 173.7 | 5.5 | 44 (15) |
| 0047 | 27 | 52700.99 | 50.0 | 15.9 | 0 |
| 0049 | 47 | 52706.97 | 82.2 | 12.3 | 0 |
| 0050 | 16 | 52709.96 | 31.6 | 13.7 | 2 (1) |
| 0051 | 45 | 52712.95 | 81.3 | 6.3 | 25 (5) |
| 0052 | 58 | 52715.94 | 104.1 | 7.9 | 15 (4) |
| 0053 | 82 | 52718.93 | 149.0 | 7.5 | 30 (4) |
| 0054 | 57 | 52721.92 | 107.1 | 10.7 | 6 (0) |
| 0055 | 13 | 52724.91 | 22.5 | 8.4 | 5 (2) |
| 0056 | 30 | 52727.90 | 53.4 | 11.7 | 1 (1) |
| 0057 | 8 | 52730.89 | 11.1 | 10.0 | 0 |
| 0058 | 35 | 52733.89 | 79.8 | 6.4 | 18 (5) |
| 0059 | 6 | 52736.88 | 12.6 | 9.8 | 2 (0) |
| 0060 | 28 | 52739.87 | 51.3 | 6.5 | 13 (5) |
| 0061 | 100 | 52742.86 | 203.7 | 9.5 | 25 (6) |
| 0062 | 15 | 52745.85 | 28.3 | 14.7 | 0 |
| 0063 | 59 | 52748.84 | 126.1 | 8.4 | 24 (6) |
| 0100 | 101 | 52859.48 | 188.2 | 10.8 | 9 (0) |
| 0101 | 5 | 52862.47 | 9.9 | 14.7 | 0 |
| 0103 | 94 | 52868.45 | 171.9 | 5.9 | 50 (13) |
| 0104 | 2 | 52871.44 | 4.2 | 7.2 | 0 |
| 0105 | 59 | 52874.43 | 204.1 | 8.4 | 17 (0) |
| 0106 | 61 | 52877.42 | 210.7 | 9.3 | 10 (0) |
| 0107 | 57 | 52880.41 | 194.1 | 8.8 | 10 (0) |
| 0108 | 56 | 52883.40 | 197.4 | 9.2 | 9 (0) |
| 0109 | 23 | 52886.39 | 76.7 | 16.3 | 0 |
| 0110 | 62 | 52889.38 | 210.2 | 9.3 | 11 (0) |
| 0111 | 62 | 52892.38 | 214.1 | 9.2 | 11 (0) |
| 0112 | 62 | 52895.37 | 214.0 | 9.2 | 10 (0) |
| 0113 | 62 | 52898.36 | 214.0 | 9.1 | 11 (0) |
| 0114 | 61 | 52901.35 | 213.6 | 8.4 | 15 (0) |
| 0115 | 64 | 52904.34 | 208.3 | 9.1 | 8 (0) |
| 0116 | 24 | 52907.33 | 43.3 | 15.8 | 0 |
| 0118 | 54 | 52913.32 | 100.6 | 11.5 | 8 (0) |
| 0119 | 79 | 52916.31 | 145.8 | 10.2 | 17 (6) |
| 0120 | 96 | 52919.30 | 174.4 | 11.9 | 0 |
| 0121 | 5 | 52922.29 | 9.0 | 16.8 | 0 |
| 0122 | 8 | 52925.29 | 14.4 | 18.1 | 0 |

**Table** 6.2: Journal of IGR J17252−3616 observations with *INTEGRAL*. The data set is composed of CP data.

| Revolution | ScW | Start time MJD | Exposure ks | Off-axis angle $^{o}$ | JEM-X |
|---|---|---|---|---|---|
| 0157 | 1 | 53030.04 | 1.2 | 16.7 | 0 |
| 0164 | 53 | 53050.99 | 97.8 | 9.3 | 17 (5) |
| 0165 | 59 | 53053.98 | 108.9 | 9.6 | 17 (4) |
| 0167 | 42 | 53059.96 | 77.3 | 8.5 | 20 (6) |
| 0168 | 60 | 53062.96 | 110.7 | 9.5 | 14 (0) |
| 0169 | 114 | 53065.95 | 211.2 | 9.1 | 28 (0) |
| 0171 | 96 | 53071.93 | 174.9 | 9.4 | 23 (0) |
| 0173 | 14 | 53077.91 | 25.2 | 11.4 | 1 (0) |
| 0174 | 27 | 53080.90 | 48.8 | 10.6 | 1 (0) |
| 0175 | 15 | 53083.90 | 29.4 | 12.4 | 0 |
| 0179 | 18 | 53095.86 | 33.7 | 9.0 | 7 (2) |
| 0181 | 10 | 53101.84 | 18.0 | 8.5 | 3 (0) |
| 0183 | 57 | 53107.82 | 102.8 | 10.6 | 10 (2) |
| 0185 | 38 | 53113.81 | 72.8 | 11.0 | 6 (2) |
| 0217 | 1 | 53209.49 | 2.2 | 15.3 | 0 |
| 0226 | 6 | 53236.40 | 15.3 | 9.3 | 2 (1) |
| 0228 | 12 | 53242.38 | 21.6 | 17.1 | 0 |
| 0229 | 6 | 53245.37 | 13.2 | 9.9 | 1 (0) |
| 0231 | 20 | 53251.36 | 34.8 | 11.3 | 1 (0) |
| 0232 | 85 | 53254.35 | 159.3 | 7.6 | 42 (12) |
| 0233 | 27 | 53257.34 | 52.5 | 13.1 | 1 (0) |
| 0234 | 18 | 53260.33 | 33.6 | 4.2 | 3 (0) |
| 0235 | 69 | 53263.32 | 132.1 | 10.4 | 7 (0) |
| 0237 | 3 | 53269.30 | 6.6 | 13.2 | 0 |
| 0240 | 112 | 53278.27 | 206.3 | 10.1 | 18 (0) |
| 0241 | 77 | 53281.27 | 142.5 | 10.0 | 12 (1) |
| 0242 | 2 | 53284.26 | 3.6 | 15.9 | 0 |
| 0243 | 32 | 53287.25 | 59.0 | 11.1 | 6 (2) |
| 0244 | 41 | 53290.24 | 74.7 | 12.3 | 2 (0) |
| 0249 | 3 | 53305.20 | 6.6 | 12.6 | 1 (0) |

below :

**EPIC** medium filter and large window science mode;

**RGS** no filter and HCR science mode; and

**OMC** imaging mode.

The observation was simultaneous with three pointings of *INTEGRAL* during revolution 175. The ScW are: 017500660010, 017500670010 and 017500680010.

## 6.4 Detailed analysis of IGR J17252−3616

At this point, all we know about IGR J17252−3616 is its position and its 20–40 keV and 40–100 keV average fluxes. Its nature is still unknown. Looking at the images, studying its light curve and possible coherent structures, and investigating its spectral state and possible evolution, can help to elucidate part of the mystery of this source.

The analysis software packages of both missions, OSA for *INTEGRAL* and SAS for *XMM-Newton*, were used. In this chapter, we give examples of the command lines used to perform the analysis in order to illustrate the explanations. For full detailed explanations on how to proceed to analyse *INTEGRAL* data or *XMM-Newton* data, the user can find *online* cookbooks with everything that is necessary :

**INTEGRAL** `http://isdc.unige.ch/?Support+documents`

**XMM** `http://xmm.vilspa.esa.es/external/xmm_sw_cal/sas_frame.shtml`

In terms of exposure, the *XMM-Newton* observation corresponds to a the wink of an eye compared to *INTEGRAL*.

We start by producing images and improving the source position. We continue investigating its general behaviour through light curves. Finally, we study its spectrum. In every part, we first start with a general view and then, we go further into details.

Another remark before starting this *trip to the unknown* is that during this analysis, many versions of both packages have been released and used: five for OSA (3.0, 4.0, 4.1, 4.2 and 5.0) and two for SAS (6.0.0 and 6.1.0)[5]. Due to the huge amount of data concerning *INTEGRAL*, the difficulty of the analysis in terms of CPU time and disk space (without even considering questions of stability), some steps of the OSA analysis were hardly feasible or repeatable between different versions.

Finally, we put in parenthesis some OSA and SAS specific keywords in the text that illustrate what we explain for those that are familiar with OSA and SAS.

The `HEAsoft` (HEASARC software) utilities (like `XRONOS`, `Xspec`) are used throughout our analysis.

[5]At the time of writing this thesis, SAS version was implemented to 6.5.0.

### *XMM-Newton*/EPIC

Some brief comments concerning EPIC are needed before entering the imaging section. As it was described in Sect. 5.2.4, the scientific data are stored as lists of events. Some screening is needed before creating images, light curves or spectra. Some action can be undertaken to filter bad events and to reduce the background influence. First, as EPIC is less sensitive at energies higher than 10 keV[6], large structures in the light curve when selecting only single events above 10 keV are due to local charged particle. The basic line command to manipulate XMM data is the `evselect` tool. It selects the events following the indication given in the `expression` keyword and creates images, light curves and spectra files. In this case, we create a light curve (`withrateset, rateset, maketimecolumn, timebinsize, makeratecolumn`) of the background.

```
evselect \
  table=file_pn_EventList.fits \
  withrateset=Y rateset=pnlc_highBkgd.fits \
  maketimecolumn=Y timebinsize=50 makeratecolumn=Y \
  expression='\#XMMEA_EP && (PI>10000) && (PATTERN==0)'}
```

The place where the cut should go in order to eliminate lapses of time with enhanced background activity is open to the user's decision. These cuts for EPIC MOS[12] and pn are illustrated in Fig. 6.1.

The values are: 1 counts $s^{-1}$ for MOS1 and MOS2, and 4 counts $s^{-1}$ for pn.

```
tabgtigen table=pnlc_highBkgd.fits \
  expression='RATE<=1.0' gtiset=pnlc_gti.fits
```

Afterwards, all events within the time intervals where the >10 keV count rate exceeds these cuts values are discarded. Moreover, events tagged as bad (`#XMMEP` for pn and `#XMMEM` for MOS[12]) by internal processes were also eliminated from the cleaned event lists that are the starting point to create images, light curves and spectra.

```
evselect table=file_pn_EventList.fits \
  withfilteredset=Y filteredset=pnCleanEventList.fits \
  destruct=Y keepfilteroutput=T \
  expression='#XMMEA_EP && gti(pnlc_gti.fits,TIME)'
```

In the calibration document `XMM-SOC-CAL-TN-0018`[7], instructions on selecting low energy threshold and event types are given for the specific tasks.

## 6.4.1 Images and source position

### IBIS/ISGRI

We have four periods of continuous observations corresponding to the four GCDE. The Galactic Centre can be observed twice per year for a few months due to technical constraints

[6] Indeed, the effective area at energies higher than 10 keV are insignificant for the three cameras, see p.39–40 of the *XMM-Newton* User Handbook.

[7] `http://xmm.vilspa.esa.es/external/xmm_sw_cal/calib/documentation/index.shtml#EPIC`

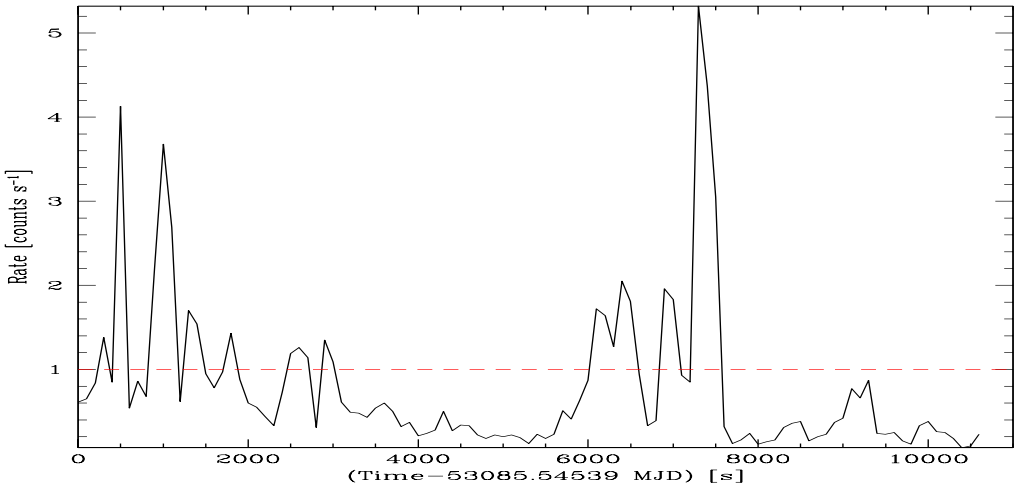


(a) MOS1

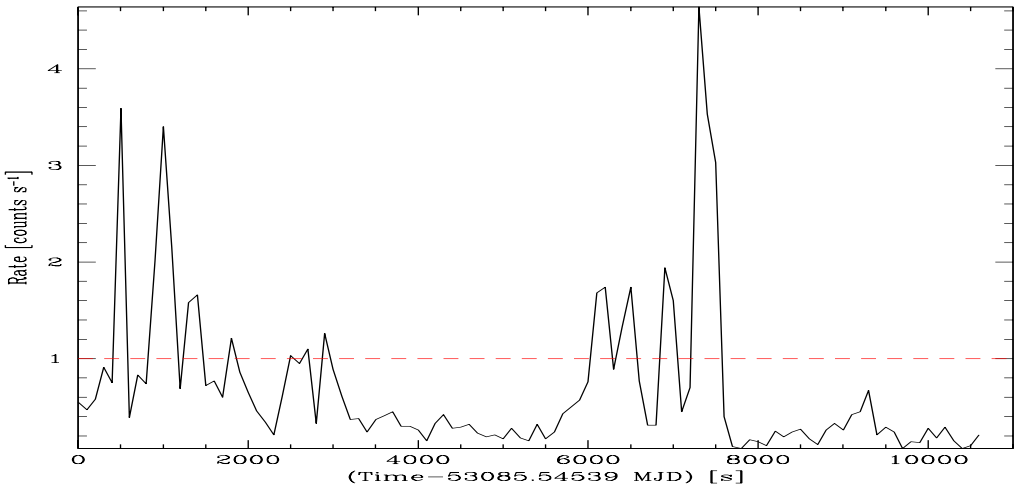


(b) MOS2

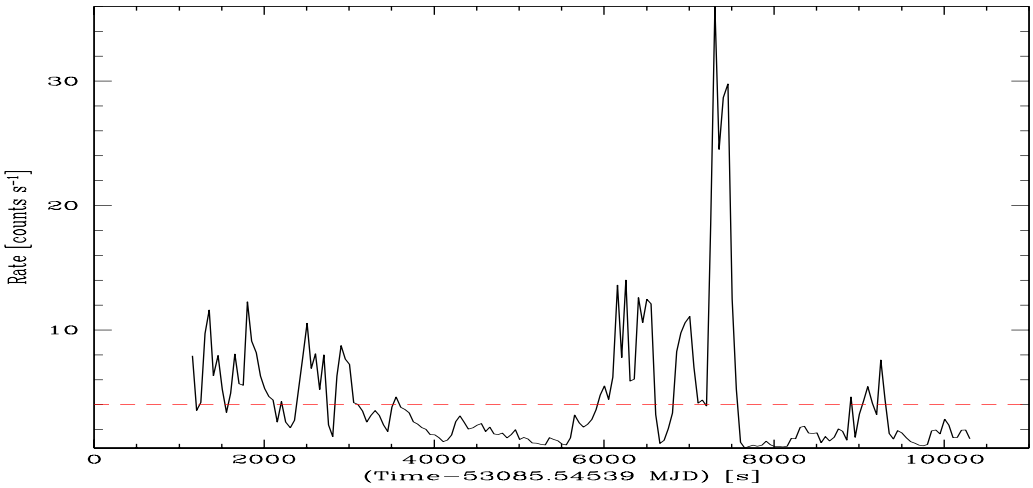


(c) pn

**Figure** *6.1: EPIC count rates at energies higher than 10 keV. The red dotted lines represent the cut for each detector: 1 counts* $s^{-1}$ *for MOS1 and MOS2, and 4 counts* $s^{-1}$ *for pn.*

such as avoiding the sun.

We first started with IBIS/ISGRI. We built a database analysing all the ScW from the correction step (`startLevel=COR`) until the image step (`endLevel=IMA`). A subcatalogue was created from the general reference catalogue with all the sources detected by ISGRI as they appear in the literature (`ISGRI_FLAG==0`), plus adding all the sources for which detections in the daily follow-up in the barn, where the near-real time data are processed and analyzed by the IQLA system, were obtained (for more details, proceed to Chapter 11). We finally ended with 241 sources. We asked the programme to extract the flux for all the sources in the subcatalogue located within the observed FOV (`OBS1_SearchMode=3`) if the significance level was higher than 3 (`OBS1_MinCatSouSnr=3`), plus we left opened the possibility that new sources could be present in the observed field (`OBS1_ToSearch=3`) with a significance level higher than 6 (`OBS1_MinNewSouSnr=6`). These conservative values came from the four-year experience of handling OSA. The deconvolution procedure is sensible to these values and we can finish with spurious detections with lower significance threshold. The data were analyzed per revolution, *i.e.* one observation group (`ogid=revRRRR_ima`) was created per revolution.

```
og_create \
  idxSwg=ScW.list \
  ogid=our_OGID baseDir=REP_BASE_PROD instrument=IBIS
```

The `idxSwg` parameter refers to an ascii file listing all the ScW that have to be analysed. The `baseDir` parameter corresponds to the path where the analysis is going to take place.

Each ScW was individually analyzed. Afterwards, all the individual ScW images of one observation group were mosaicked[8] together (`OBS1_DoPart2=1`). Two energy bands were selected for this first step: 20–60 keV and 60–150 keV.

```
  ibis_science_analysis \
    ogDOL="./og_ibis.fits[1]" \
    startLevel="COR" endLevel="IMA2" \
    SWITCH_disablePICsIT=yes \
    CAT_refCat="file_catalogue.fits[1]" \
    IBIS_II_ChanNum=2 \
    IBIS_II_E_band_min="19.7018  59.9126" \
    IBIS_II_E_band_max="59.9126 149.9082" \
    OBS1_SearchMode=3 OBS1_ToSearch=3 \
    OBS1_MinCatSouSnr=3 OBS1_MinNewSouSnr=6 \
    OBS1_DoPart2=1
```

We get at the end 3500 individual pointing images and 77 mosaics.

The first intuitive step is to take all the data together and check what happens: where is the source, who are the neighbours, how bright is the source. Therefore, all the revolution

[8]The mosaic process consists in adding different images together. This increases the exposure time and helps reducing the background level. This process is not trivial, as images cover slightly different regions of the sky (depending on the attitude of the satellite). The counts in every pixel of the images must be correctly re-distributed in the mosaic image.

mosaics were added together to build one image with two years of data. The significance maps of both energy bands are displayed in Fig. 6.2. The source is clearly visible in the

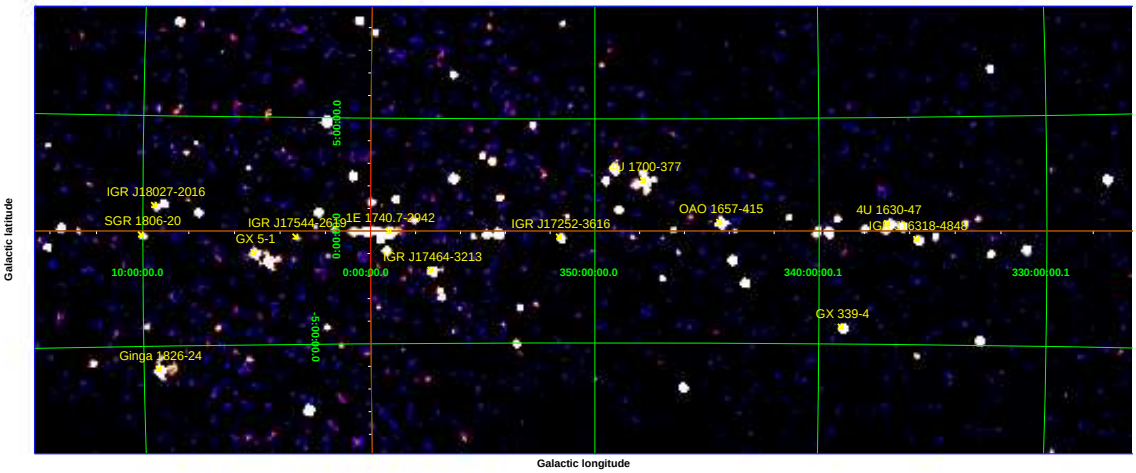


(a) 20–60 keV significance map

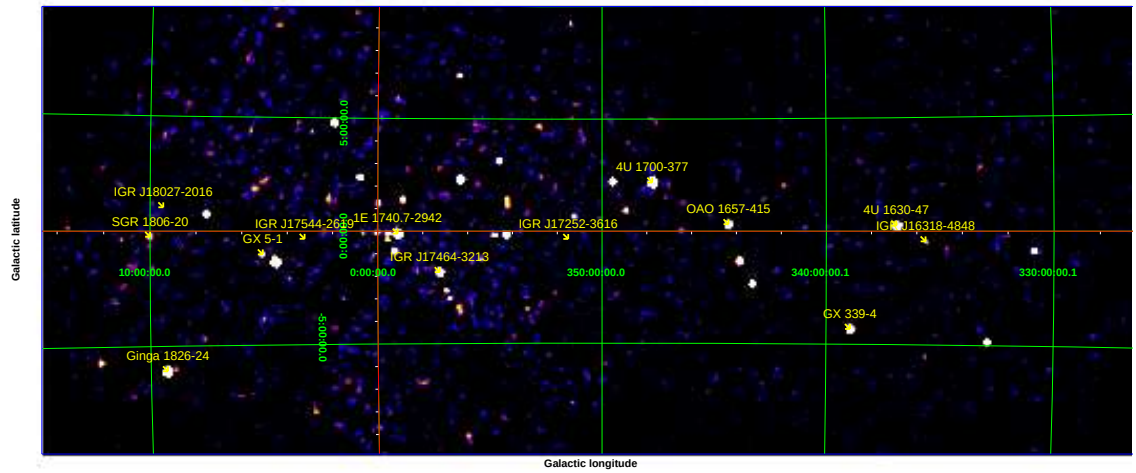


(b) 60–150 keV significance map

**Figure** *6.2: ISGRI significance mosaic images with an exposure of 2 years of observations. The image is centered on IGR J17252−3616 position and displayed a large portion of the galactic plane : l=[-35°;+15°] and b=[-10°;+10°].*

20–60 keV significance map with $\sigma \sim 70$, but it has completely faded in the 60–150 keV significance map. The maps are presented with other known sources belonging to different classes : LMXB with a NS (Sco X-1, GX 5-1), LMXB with a BH (GX 339-4, 4U 1630-47, Ginga 1826-24), supergiant HMXB with a NS (4U 1700-377, OAO 1657-415), and also a few IGR sources that are studied in this thesis (IGR J16318−4848, IGR J17252−3616, IGR J17544−2619, IGR J18027−2016). In these images, the extreme variability of the high energy sky is clearly visible. There are sources appearing and disappearing, or showing

high flux variability.

Second step, second question: is the source always present? The four GCDE were considered separately. The four significance maps are shown in Fig. 6.3 and 6.4.

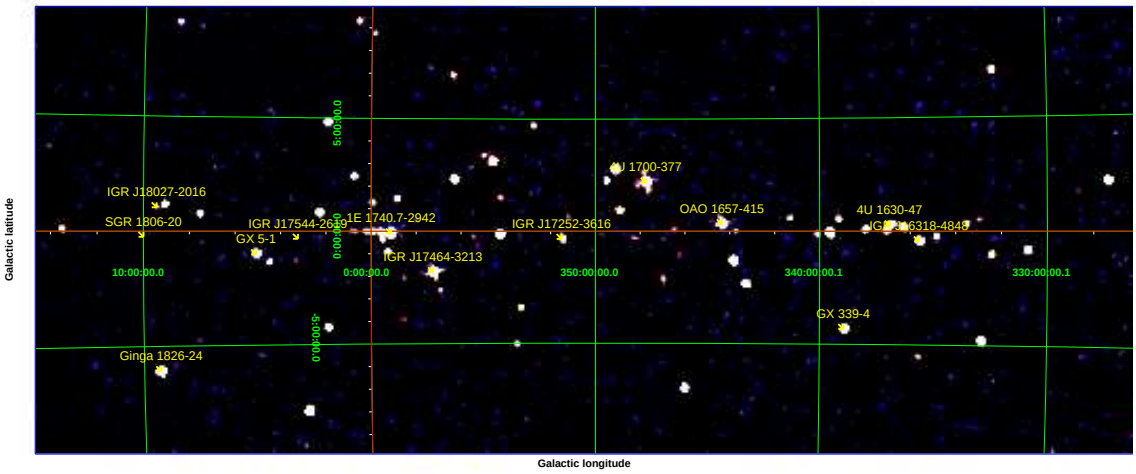


(a) GCDE#1

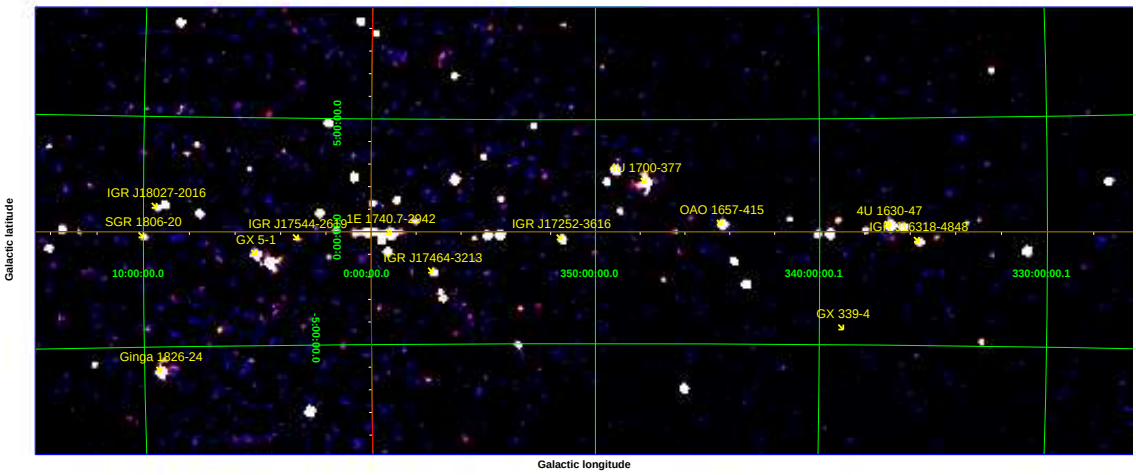


(b) GCDE#2

**Figure** *6.3: ISGRI 20–60 keV significance mosaic images. The image is centered on IGR J17252−3616 position and displayed a large portion of the galactic plane : l=[-35°;+15°] and b=[-10°;+10°].*

IGR J17252−3616 is detected in each GCDE. The source does not disappear for a period longer than 6 months as some galactic sources do.

A step further is to check if the source is detected in each revolution. As the exposure is variable between each revolution, only those with an effective exposure higher than 1 ks were kept. The limiting significance to discriminate between detection and non-detection

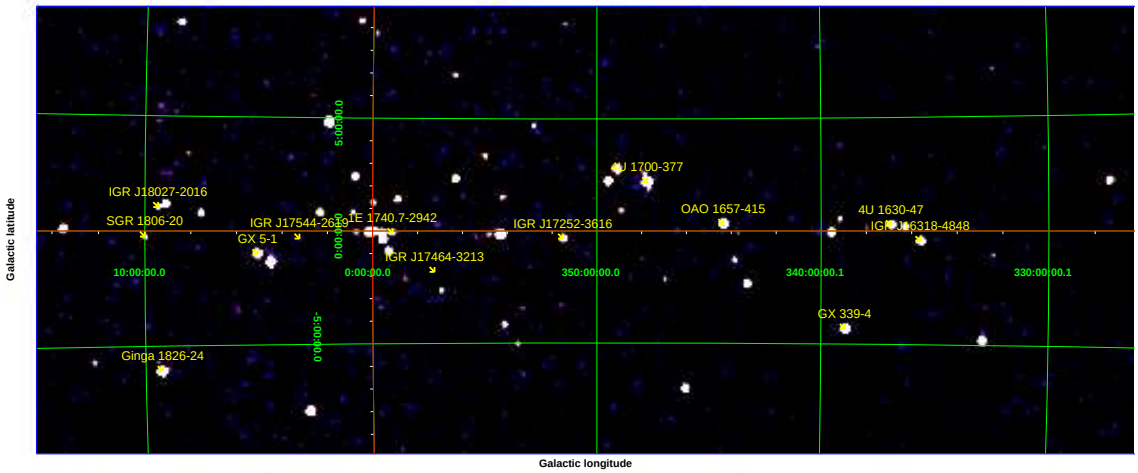


(a) GCDE#3

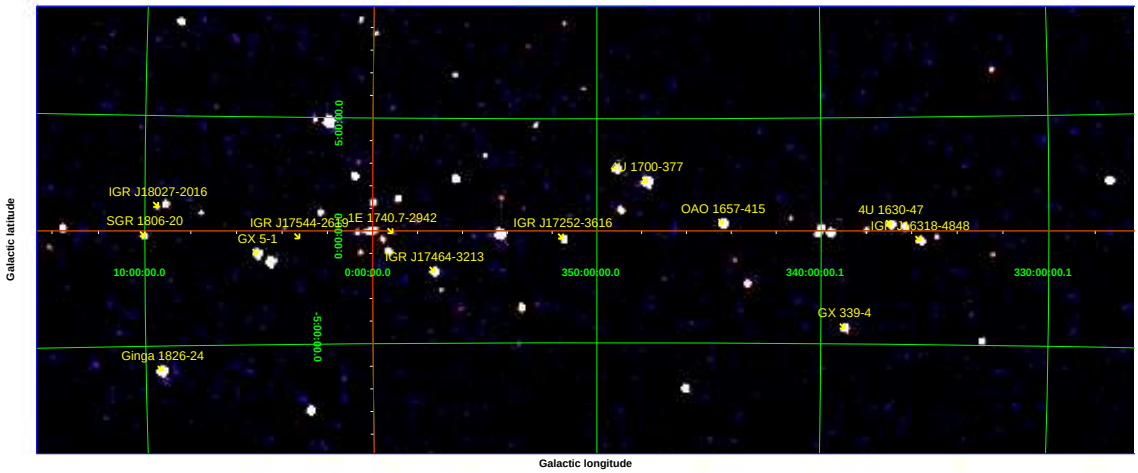


(b) GCDE#4

**Figure** *6.4: ISGRI 20–60 keV significance mosaic images. The image is centered on IGR J17252−3616 position and displayed a large portion of the galactic plane : l=[-35°;+15°] and b=[-10°;+10°].*

is set at 4. This results in 50 revolution mosaic images for which we have 36 detections and 14 non-detections (see Table 6.3). The non-detection cases are often linked to short exposures except in a few cases as revolution 46 where the source is not detected with an exposure of 90 ks which is the revolution with the longest exposure.

**Table** 6.3: Journal of IGR J17252−3616 detections with *INTEGRAL*. When IGR J17252−3616 is not detected within one revolution, the $1\sigma$ upper limit is reported.

| Revolution | 20–60 keV Flux counts $s^{-1}$ | Flux error counts $s^{-1}$ | Significance | Effective exposure s |
|---|---|---|---|---|
| 0037 | 1.1 | 0.2 | 7.3 | 21976 |
| 0038 | 2.4 | 0.2 | 10.6 | 9862 |
| 0046 | <0.07 | | 3.5 | 90120 |
| 0047 | <0.5 | | 1.4 | 2349 |
| 0049 | <0.2 | | 2.8 | 13579 |
| 0050 | <0.3 | | 0.9 | 6130 |
| 0051 | 1.6 | 0.1 | 16.3 | 40713 |
| 0052 | 0.65 | 0.09 | 6.9 | 43672 |
| 0054 | 1.1 | 0.1 | 7.8 | 22400 |
| 0055 | 1.1 | 0.2 | 4.7 | 6639 |
| 0056 | <0.3 | | 1.7 | 5932 |
| 0057 | <0.4 | | 2.1 | 3022 |
| 0058 | 0.63 | 0.09 | 7.1 | 45910 |
| 0059 | <0.7 | | 2.0 | 1143 |
| 0060 | 1.3 | 0.1 | 10.7 | 25680 |
| 0061 | 1.17 | 0.07 | 16.0 | 73430 |
| 0062 | <0.6 | | 0.4 | 1638 |
| 0063 | 0.7 | 0.1 | 6.5 | 39420 |
| 0100 | 1.3 | 0.1 | 11.4 | 33769 |
| 0103 | 2.23 | 0.07 | 32.1 | 78027 |
| 0105 | 0.93 | 0.07 | 12.6 | 73155 |
| 0106 | 4.06 | 0.09 | 46.4 | 64535 |
| 0107 | 1.54 | 0.09 | 17.7 | 58505 |
| 0110 | 1.1 | 0.1 | 10.7 | 43586 |
| 0111 | 0.44 | 0.09 | 5.1 | 53955 |
| 0113 | 2.19 | 0.08 | 28.2 | 64421 |
| 0115 | 0.88 | 0.09 | 9.8 | 55596 |
| 0116 | <0.5 | | 3.9 | 2294 |
| 0118 | <0.1 | | 3.8 | 20655 |
| 0119 | 1.2 | 0.1 | 11.3 | 38995 |
| 0120 | 1.1 | 0.1 | 10.1 | 36889 |
| 0164 | 0.9 | 0.1 | 7.0 | 27683 |
| 0167 | 1.4 | 0.1 | 10.9 | 25716 |
| 0168 | 1.6 | 0.1 | 13.4 | 29413 |
| 0169 | 0.75 | 0.09 | 8.7 | 61295 |
| 0173 | 1.3 | 0.3 | 4.8 | 5704 |

**Table** 6.3: *continued.*

| Revolution | 20–60 keV Flux counts $s^{-1}$ | Flux error counts $s^{-1}$ | Significance | Effective exposure s |
|---|---|---|---|---|
| 0174 | 1.5 | 0.2 | 6.6 | 10505 |
| 0179 | 2.5 | 0.3 | 9.4 | 4951 |
| 0181 | <0.3 | | 3.4 | 3266 |
| 0183 | <0.1 | | 1.2 | 23306 |
| 0226 | <0.4 | | 3.8 | 2007 |
| 0229 | <0.7 | | 0.0 | 1009 |
| 0231 | 1.2 | 0.2 | 4.9 | 8581 |
| 0232 | 0.70 | 0.09 | 7.9 | 57787 |
| 0233 | 1.4 | 0.2 | 6.2 | 8475 |
| 0234 | 1.3 | 0.2 | 7.4 | 14180 |
| 0240 | 2.2 | 0.1 | 22.3 | 56448 |
| 0241 | 0.6 | 0.1 | 5.3 | 34824 |
| 0243 | 2.1 | 0.2 | 11.4 | 13302 |
| 0244 | 2.0 | 0.2 | 10.7 | 12691 |

The detection with the highest significance happens during revolution 106. Thanks to `mosaic_spec`, we extracted the best hard X-ray position : (R.A. (2000.0)=17h25m10s and Dec.=$-36^{o}\,17'\,18''$ with a statistic uncertainty of $23''$. However, the systematics for a detection of $\sigma \sim 47$ is $\sim 36''$.

### JEM-X

The JEM-X data set is much sparser than ISGRI. In Tables 6.1 and 6.2, we see that only 110 ScW where IGR J17252−3616 is located within $3^{o}$ of the centre FOV would be worth analysing. This off-axis angle limit comes from the experience with the JEM-X analysis (JEM-X specialists' private communication).

However, the JEM-X analysis did not give any significant result. The source is not detected in a single pointing. We analysed the 15 good ScW of revolution 103 (see Table 6.1). At the position of IGR J17252−3616for an exposure of ∼14 ks, none X-ray source is detected (see Fig. 6.5). The source is too faint to be detected with JEM-X.

### EPIC

Images with $2''$ (MOS[12]) and $4''$ (pn) resolution were built. Only events until the quadruple level were considered, so the low energy treshold was put at 0.8 keV.

```
evselect table=pnCleanEventList.fits \
  imagebinning=binSize imageset=pnImg.fits withimageset=yes \
  xcolumn=X ycolumn=Y ximagebinsize=80 yimagebinsize=80 \
  expression='(PATTERN<=12) && (PI IN [800:10000])'
```

The MOS1 and pn images are shown in Fig. 6.6. The ISGRI position with its error box (derived from our mosaics, see previous subsection on ISGRI) are reported. Only one X-ray source detected by EPIC corresponds to the ISGRI position.

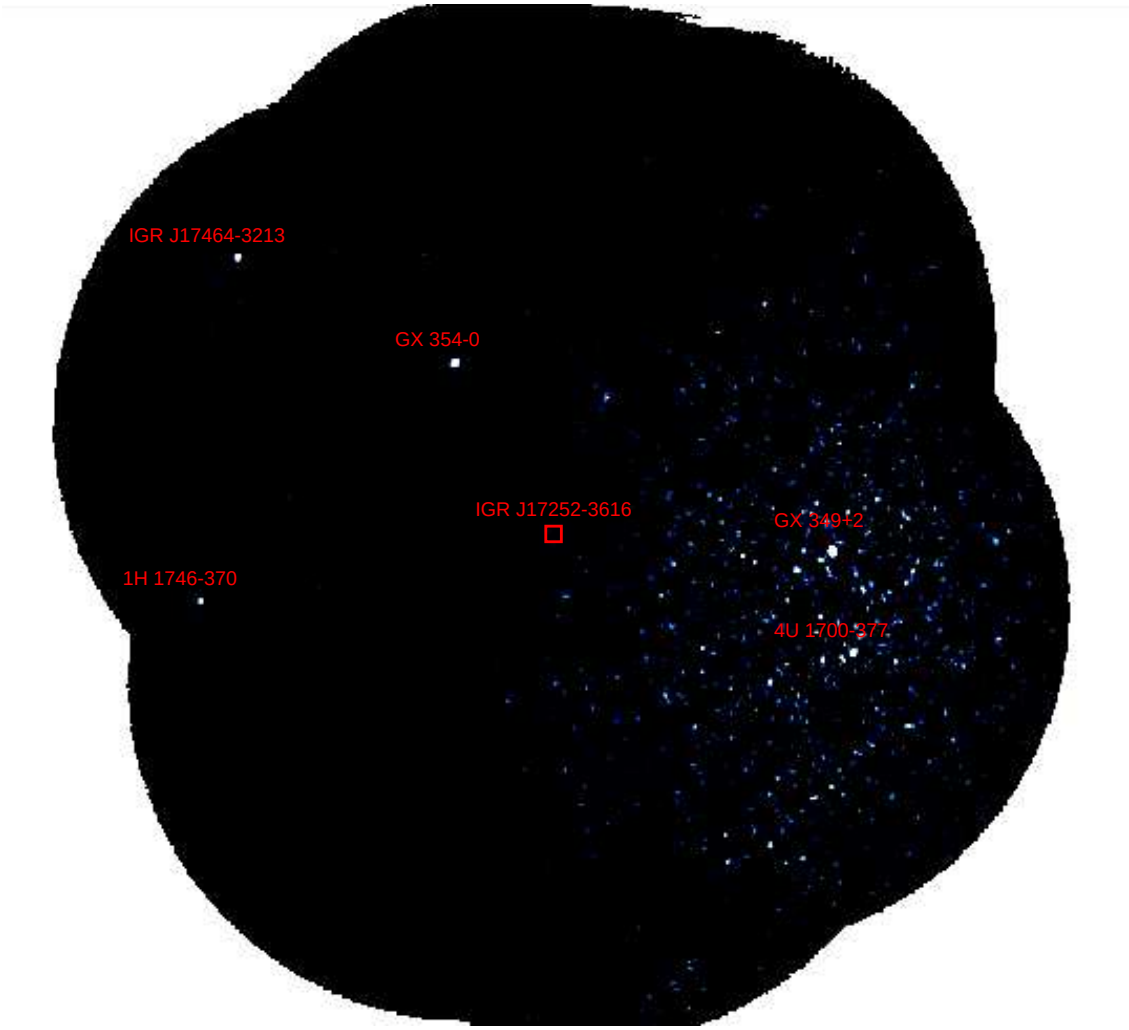


**Figure** *6.5: JEM-X2 3–10 keV significance map for 15 ScW during revolution 103. IGR J17252−3616 is not detected for an exposure of 14 ks.*

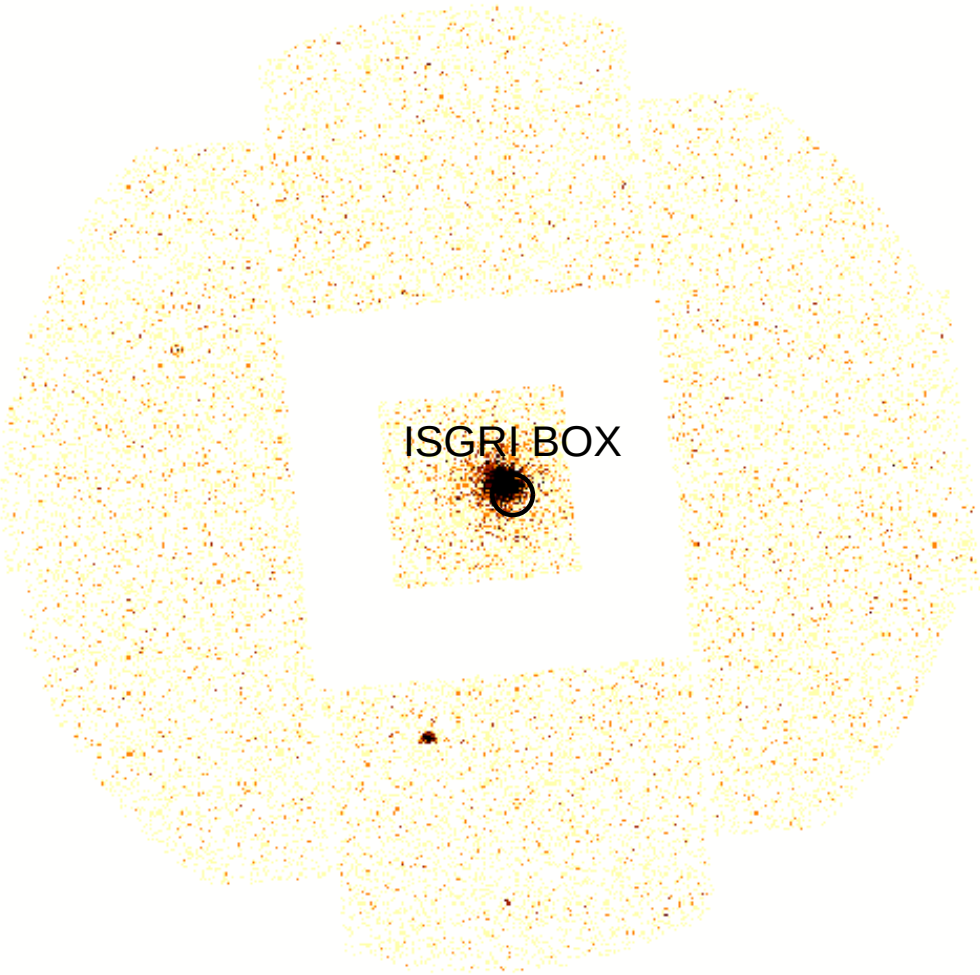


(a) MOS1

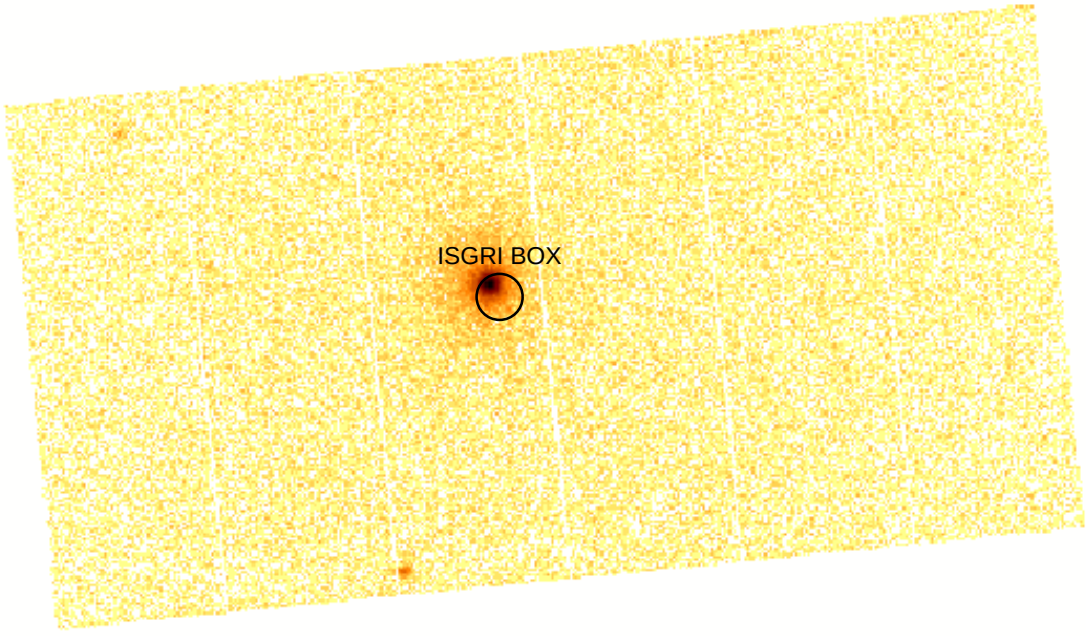


(b) pn

**Figure** *6.6: 0.8-10 keV EPIC images. Only one source is detected. The ISGRI error box is shown.*

**Table** 6.4: Summary of the found position with the EPIC cameras.

| EPIC Camera | R.A. (2000) | Dec. |
|---|---|---|
| MOS1 | 261.297263633449 | -36.2828327163658 |
| MOS2 | 261.297472617505 | -36.2829319220529 |
| pn | 261.297239799224 | -36.2830517998260 |
| average | 261.2973254 | -36.28293881 |
| | 17:25:11.358 | -36:16:58.58 |

The source location was better determined with the help of the three EPIC cameras. Four images with energy ranges of 0.5–2, 2–4.5, 4.5–7.5 and 7.5–12 keV were created and the source position was individually determined with each camera (using `evselect` as previously seen : pnImg_b*num*.fits, *num*=1,2,3,4). This step was done with the `edetect_chain` tool.

```
edetect_chain eventsets=pnCleanEventList.fits \
  attitudeset=file_attittude.fits \
  imagesets='"pnImg_b1.fits" "pnImg_b2.fits" "pnImg_b3.fits" "pnImg_b4.fits"' \
  pimin='500 2000 4500 7500' pimax='2000 4500 7500 12000' \
  ecf='6.442 1.930 0.9394 0.2400' \
  eboxl_list='pn_eboxlist_l.fits' eboxm_list='pn_eboxlist_m.fits' \
  esp_nsplinenodes=16 eml_list='pn_emllist.fits' esen_mlmin=15
```

The individual positions are listed in Table 6.4.

The bottom line corresponds to the average location between each measurement. The spatial error is dominated by systematics in the satellite astrometry and it is well superior to the statistical instrument error. Therefore, the conservative uncertainty on the position error is $4''$ for *XMM-Newton*.

**Conclusion**

IGR J17252−3616 is a persistent source that is detected by *INTEGRAL* in almost each individual revolution. The source is not detected at energies higher than 60 keV. Therefore, PICsIT analysis is worthless.

An X-ray counterpart was found in the *XMM-Newton* data. The most accurate position of IGR J17252−3616 is (R.A. (2000.0)=17h25m11.4s and Dec.=$-36^{\circ}\,16'\,58''.6$ with an uncertainty of $4''$.

### 6.4.2 Timing analysis

In the same way we proceeded with the images, the light curve of IGR J17252−3616 can be studied from the longest time scales to the shortest ones.

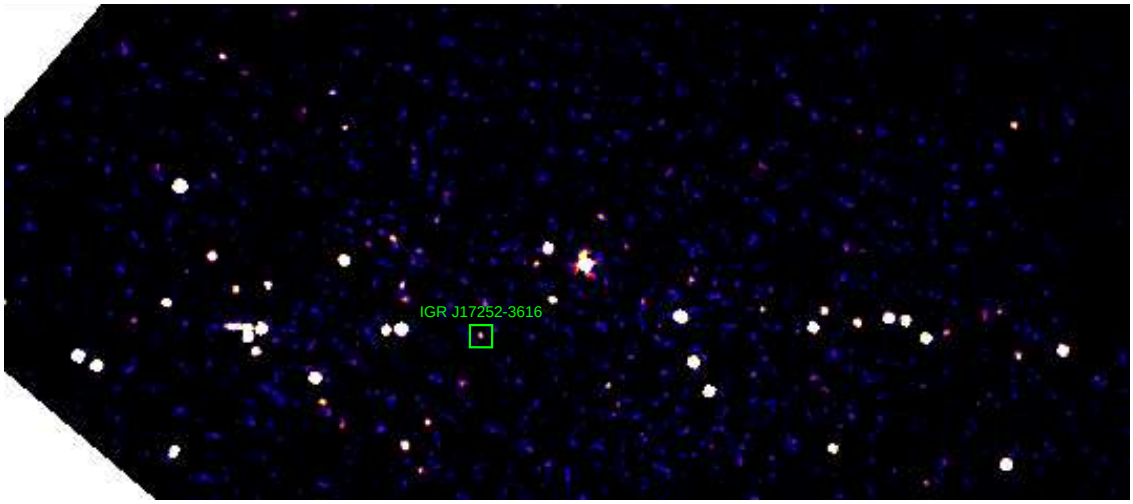


**Figure** *6.7: 20–06 keV significance mosaic map of revolution 46, 49, 50, 56, 118 and 183. IGR J17252−3616 is clearly detected with a significance of 5.*

### Light curves over two years

The long-term light curve over the two years of observations comes directly from the mosaic images per revolution (see Table 6.3). It is shown in Zurita Heras et al. (2005) (see Sect. 6.6). The revolutions with an exposure less than 5 ks are discarded. When the source is not detected within one revolution, the $3\sigma$ upper limit is reported in the plot. When the source is detected within one revolution, the 20–60 keV average flux lies between 0.4 counts $s^{-1}$ and 2.4 counts $s^{-1}$. Only on one occasion, the source flux increases until 4 counts $s^{-1}$ (in revolution 106). Moreover, IGR J17252−3616 is not detected in six revolutions: 46, 49, 50, 56, 118 and 183. Gathering the data of the six revolutions and building a mosaic image, we get a clear detection (see Fig. 6.7) for a 165 ks exposure. The extracted flux is very low: 0.19±0.04 counts $s^{-1}$ (significance=5). This flux lies a bit higher than the sensitivity limit of the detector that is ∼1 mCrab (∼0.16 counts $s^{-1}$). The average 20–60 keV count rate of the whole data set is 0.96±0.01 counts $s^{-1}$.

The source is thus persistent, but requires a sufficient exposure time to be detected. IGR J17252−3616 already shows strong variations in term of intensity on the revolution time scale.

Going a step further into the details, we built a light curve with a time step based on pointings. Therefore, new time features shorter than days could be discovered. The 20–60 keV count rate per ScW is shown in Fig. 6.8, 6.9 and 6.10. The typical exposure time is around 2 ks. Therefore, the source is often not detected by ISGRI. However, strong flares are observed in the 2nd (see Fig. 6.9) and the 4th GCDE (see Fig. 6.10).

In Fig. 6.11, the four flares are shown in more detail. They are variable within the own flare. They are different in brightness and time scale. The 1st and 3rd ones are more similar with an average intensity of ≤6.0 counts $s^{-1}$ and they last ≤0.5 d. The 2nd and 4th ones are also more similar with an average intensity of >6.0 counts $s^{-1}$ and they last >0.5 d. The 2nd flare is the brightest with one pointing reaching 10 counts $s^{-1}$ and lasts the longest, 0.9 d. They are listed in Table 6.5. Apparently, they are randomly distributed.

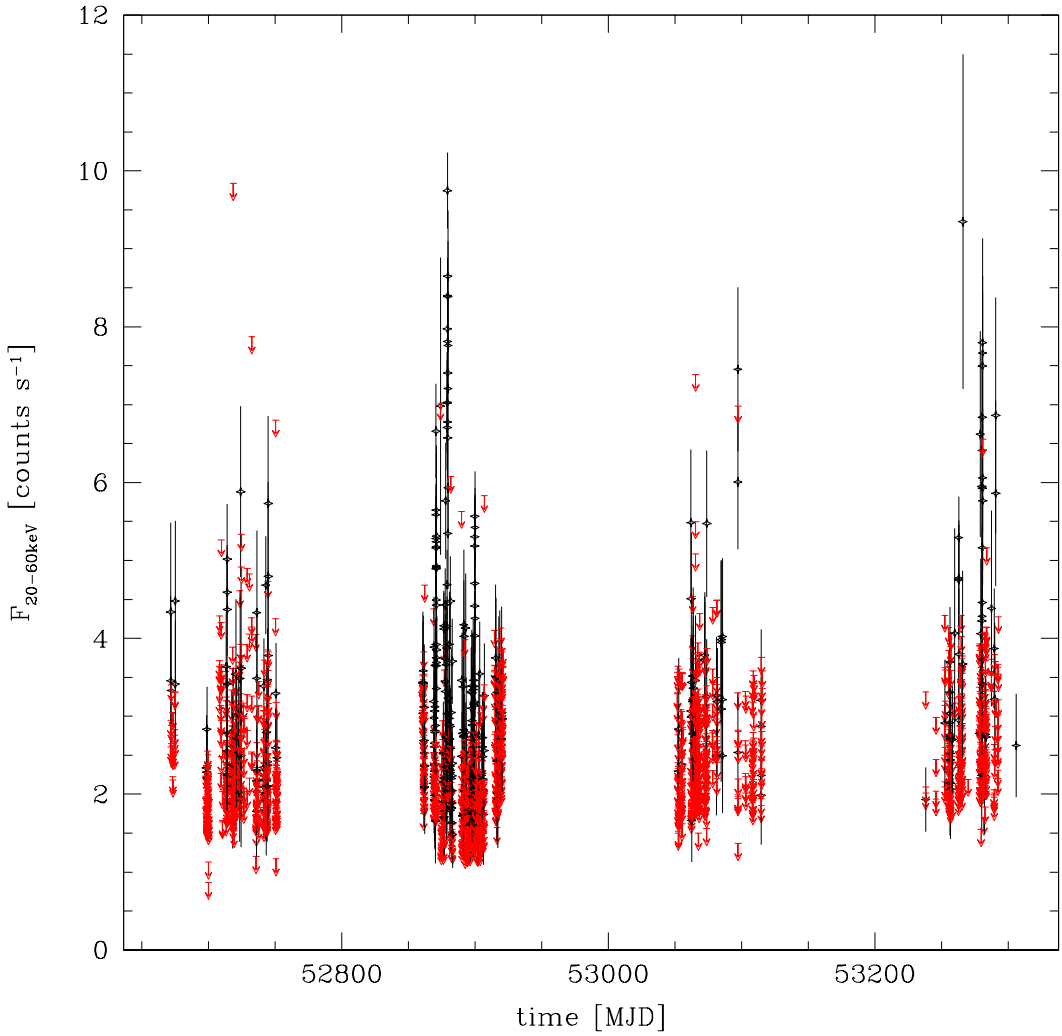


**Figure** *6.8: 20–60 keV count rate per pointing of IGR J17252−3616. Only pointings for which the source was within a circle of 12° are selected. The points out of this limit add only noise with significant upper limits since the source is situated near the detector border. The black points represent the observed source flux and the red arrows are the 3σ flux upper limit when the source is not detected in the ScW (The same points definition is used in further light curve plots).*

**Table** 6.5: Summary of the flares of IGR J17252−3616.

| Flare | Start Time MJD | Elapsed time MJD | 20–60 keV count rate counts $s^{-1}$ |
|---|---|---|---|
| #1 | 52870.7 | 0.5 | 4–6 |
| #2 | 52879.0 | 0.9 | 6–10 |
| #3 | 52899.7 | 0.3 | 4–6 |
| #4 | 53280.4 | 0.6 | 4–8 |

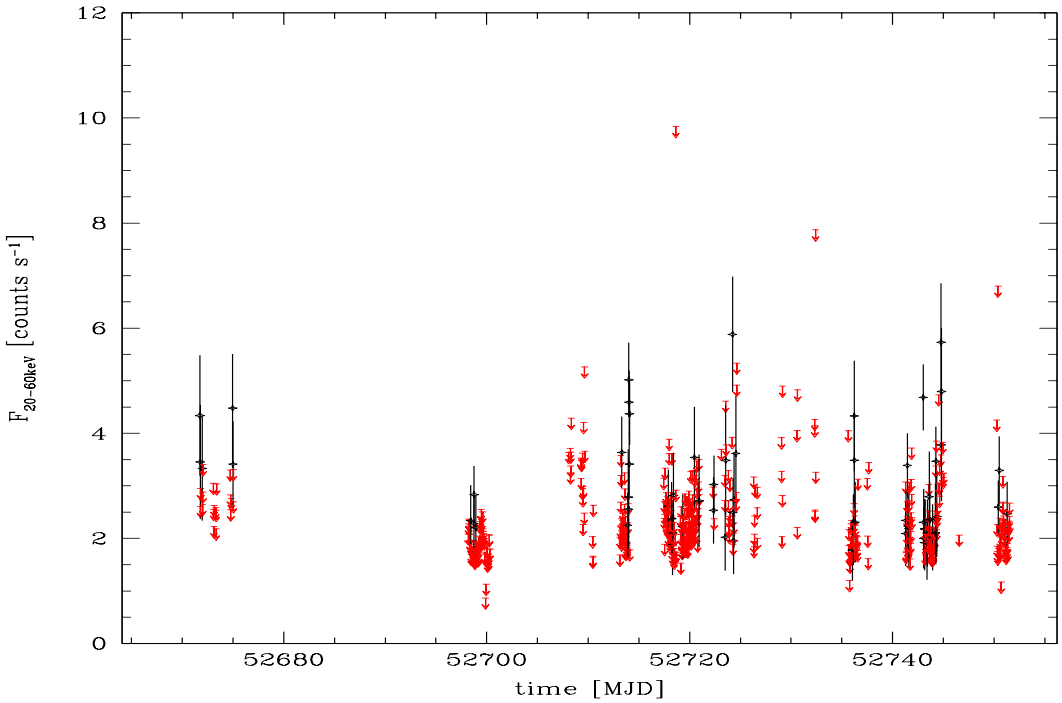


(a) GCDE#1

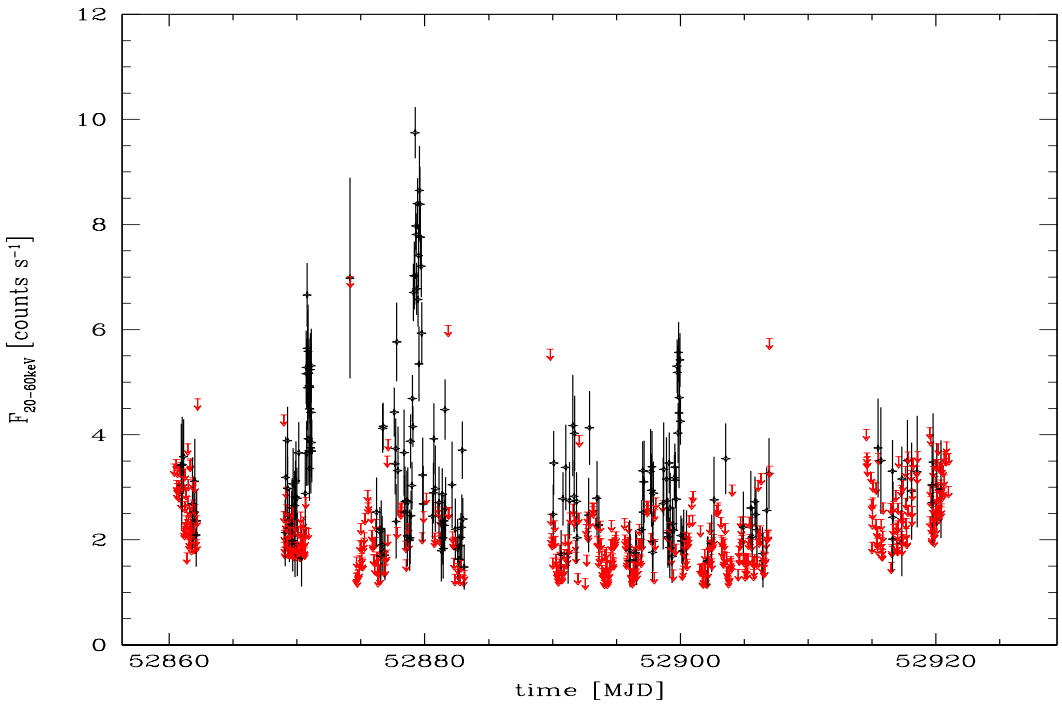


(b) GCDE#2

**Figure** *6.9: 20–60 keV count rate per pointing of IGR J17252−3616. Only pointings for which the source was within a circle of 12° are selected. The points out of this limit add only noise with significant upper limits since the source is situated near the detector border. We zoom on each GCDE period.*

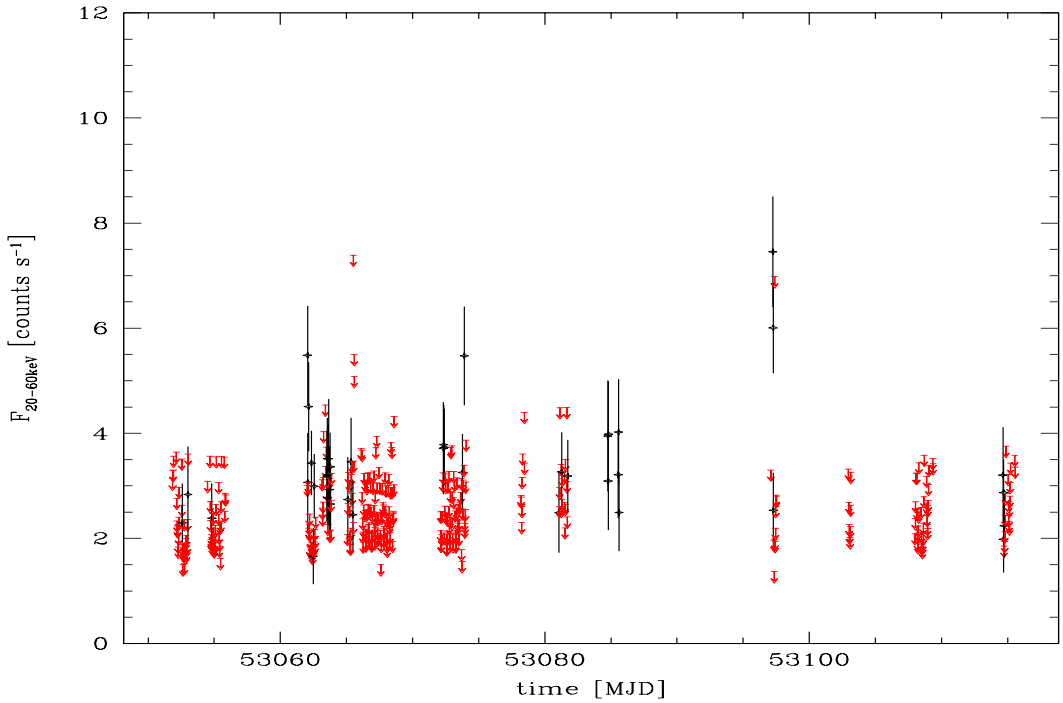


(a) GCDE#3

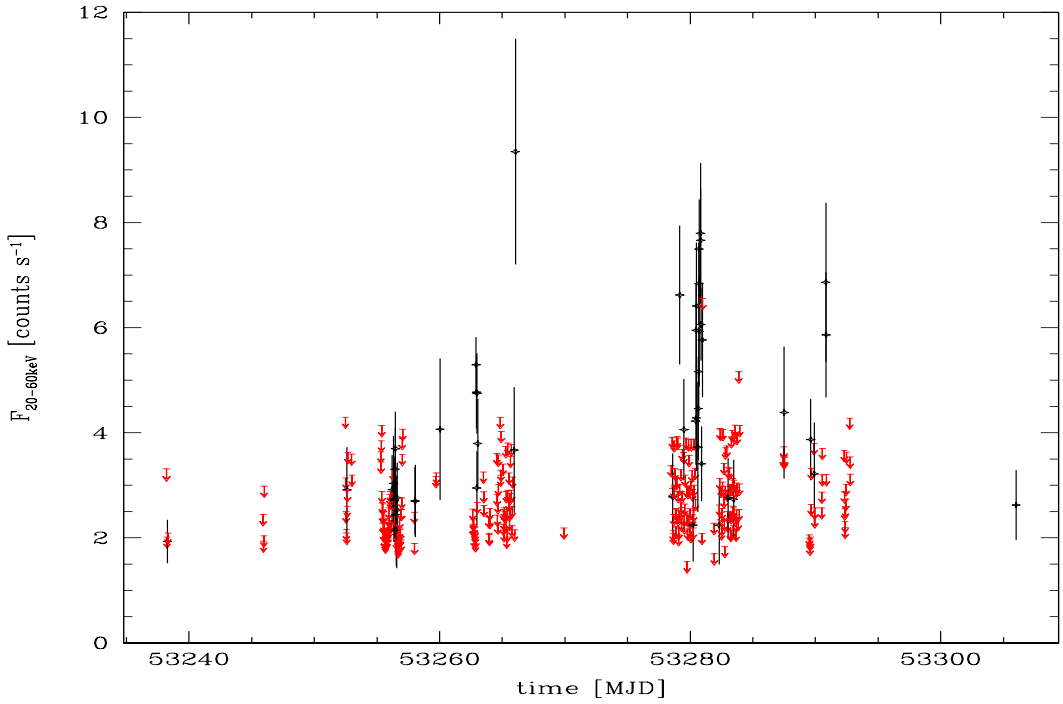


(b) GCDE#4

**Figure** *6.10: 20–60 keV count rate per pointing of IGR J17252−3616. Only pointings for which the source was within a circle of 12° are selected. The points out of this limit add only noise with significant upper limits since the source is situated near the detector border. We zoom on each GCDE period.*

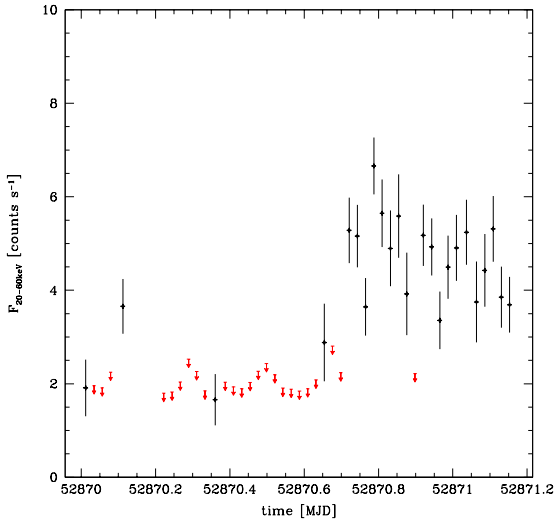


(a) Flare#1, revolution 0103

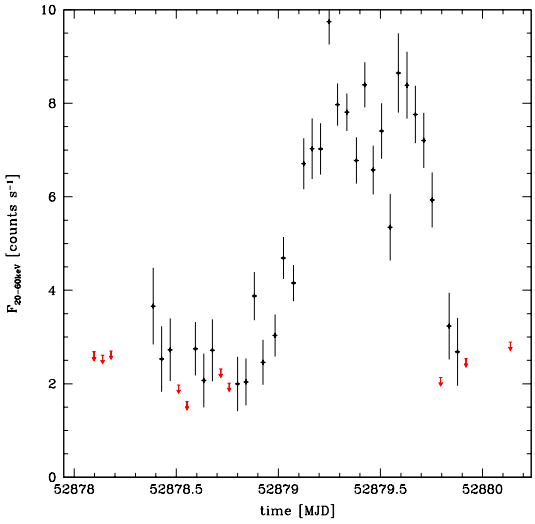


(b) Flare#2, revolution 0106

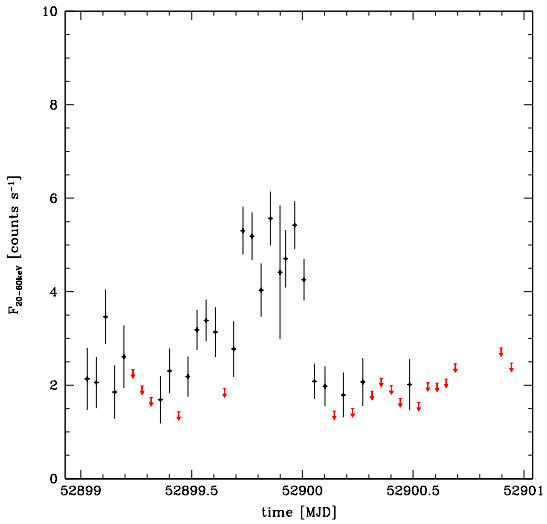


(c) Flare#3, revolution 0113

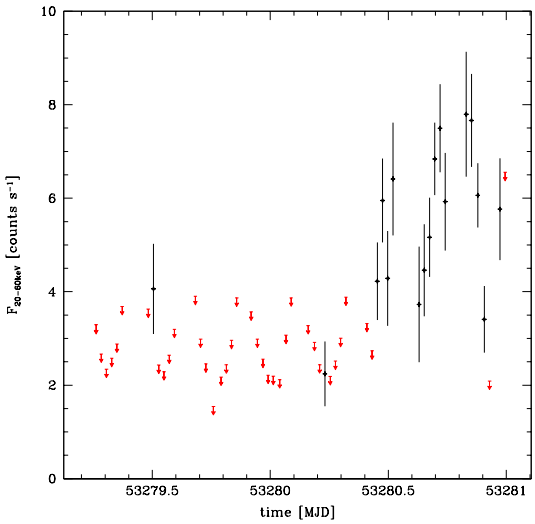


(d) Flare#4, revolution 0240

**Figure** *6.11: 20–60 keV count rate per pointing of IGR J17252−3616. Only pointings for which the source was within a circle of 12° are selected. We zoom on the flares visible in Fig. 6.9 and 6.10.*

Indeed, three flares occur during the second GCDE and one in the fourth one. They might be a bias due to shorter exposure for the 3rd and 4th GCDE/GPS since only CP data are available for these periods. Nevertheless, the effective exposure is still significant for each GCDE : 400 ks for GCDE#1, 740 ks for GCDE#2, 250 ks for GCDE#3, and 225 ks for GCDE#4.

If we consider the two intensity extremes measured, 0.19 and 10.0 counts $s^{-1}$, IGR J17252−3616 shows variations as strong as a factor of 50.

These long flares are more typical of HMXB systems than LMXB : random, rather long, and variable.

**Coherent modulation: spin?**

Once the general behaviour in the long-term was known (persistent, variable, a few random flares), the source could be studied on shorter time scales.

We built the EPIC/pn light curve. From the pn image, the list of events was extracted from a circle with a radius of 50″ centered on the source. Only the single and double events (`PATTERN<=4`) with an energy lying between 0.4–10 keV (`ENERGY in [400:10000]`), and good events (`FLAG==0`) are collected. A similar region of the same size, in the same CCD, at the same distance from the read-out node (situated in the centre of pn between the CCD), near the source (but far enough not to be contaminated), was chosen to extract the background light curve. We used the `FTOOLS lcmath` to subtract the background from the source+background light curve. The resulting light curve was rebinned to 10 s and is shown in Fig. 6 of Zurita Heras et al. (2005) (see Sect. 6.6).

A clear modulation is visible in the light curve. The periodic oscillation lasts ∼400 s (see Fig. 6 of Zurita Heras et al. (2005)). A Fourier analysis was undertaken and power spectra were generated. We computed Lomb-Scargle periodograms using the Press & Rybicki (1989) fast method[9]. A significant peak appears at $2.4\,10^{-3}$ Hz (see Fig. 6.12).

The period can be refined using an epoch-folding search (see Sect.4.3) and computing the $\chi^2$-distribution when folding the light curve over a range of trial periods using the `FTOOLS efsearch`. The curve was fitted with a gaussian distribution in order to obtain the best period (see Fig. 7 *top* of Zurita Heras et al. (2005) in Sect. 6.6). The estimated best period is 414.8±0.5 s. The EPIC/pn folded light curve is shown in Fig. 7 *bottom* of Zurita Heras et al. (2005) and the ephemeris is:

$$\mathrm{MJD}\,T = \mathrm{MJD}\,53085.55144 + n \times \frac{414.8\,\mathrm{s}}{86400} \tag{6.1}$$

where $n$ is the cycle number.

Once this period was discovered in the EPIC data, we searched for it in the ISGRI data. The ISGRI light curves generated with short time scales (100 s, 10 s, 1 s) are totally dominated by background[10]. An example is presented in Fig. 6.13 and corresponds to the light curve of IGR J17252−3616 during revolution 106. When rebinning the 100 s light curve, we clearly see the source signal (see Fig. 6.13). However, the source signal is very weak on this time scale.

[9] A description of the timing analysis method can be found in Sect. 4.2

[10] un mot sur ii_light

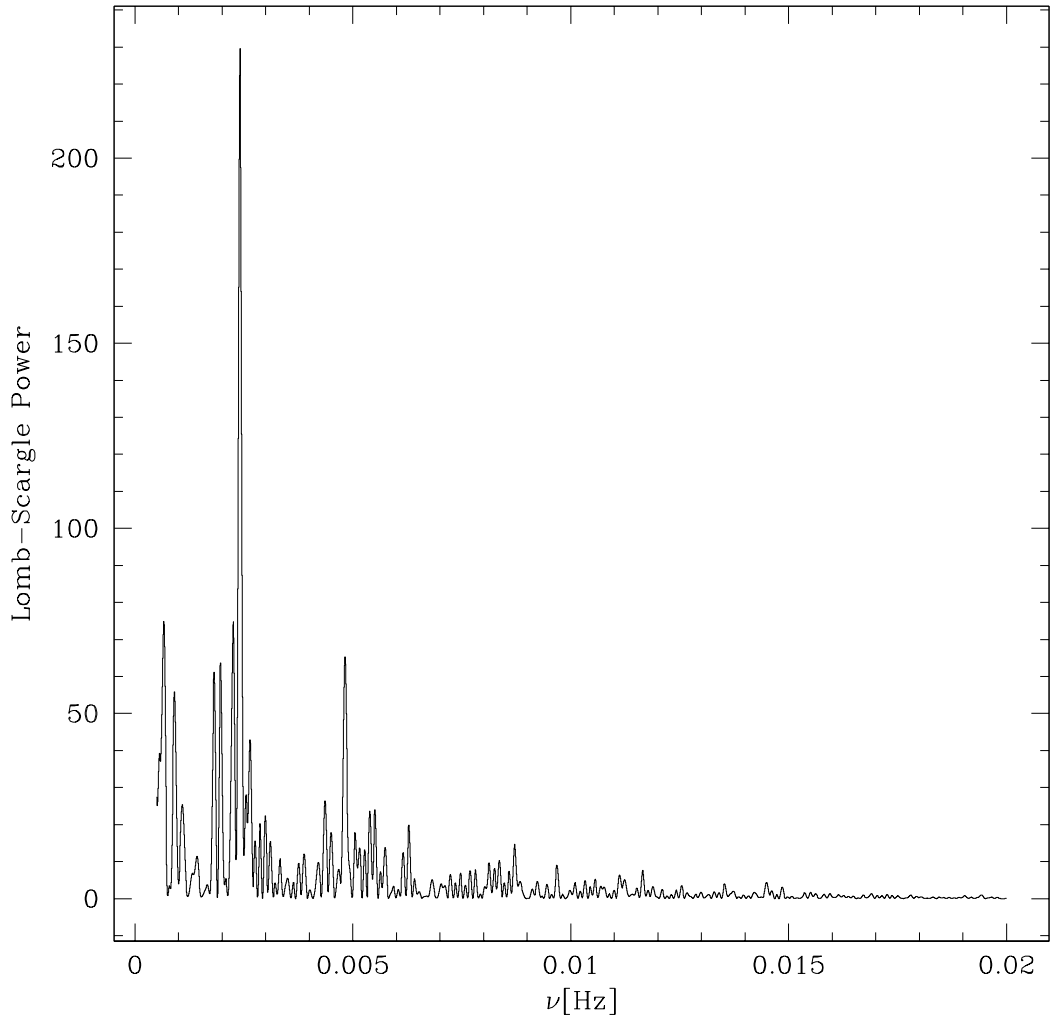


**Figure** *6.12: EPIC/pn Lomb-Scargle periodogram of IGR J17252−3616. There is one peak that corresponds to a period of 414.9±0.5 s.*

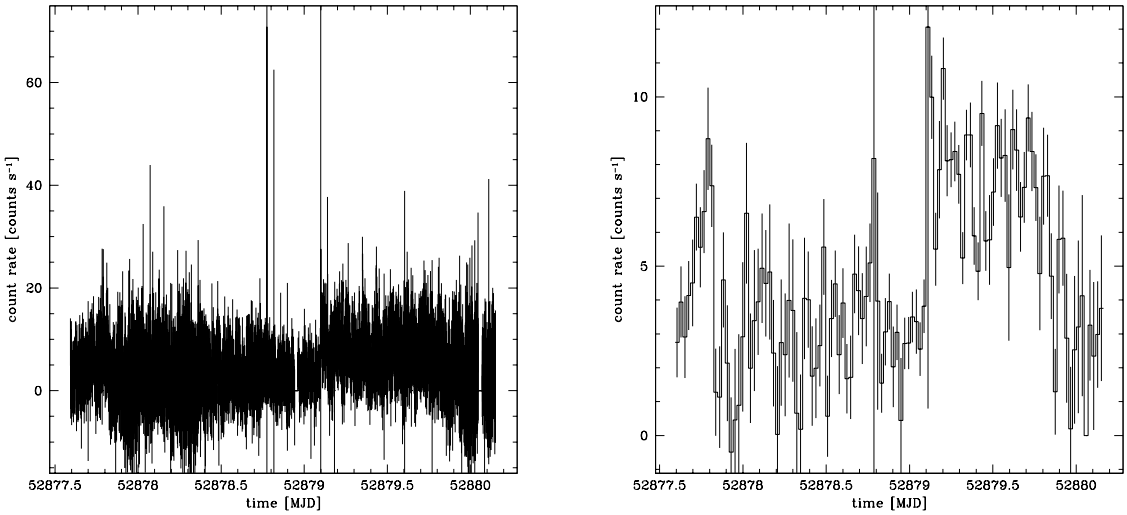


(a) 100 s binning

(b) 2 ks binning

**Figure** *6.13: 15–30 keV binned light curve of IGR J17252−3616 during revolution 106. The 100 s binned light curve is totally dominated by the background. However, once largely rebinned at 2 ks, the source signal is clearly visible.*

**Table** 6.6: Summary of the found period per revolution of IGR J17252−3616 with ISGRI.

| Revolution | Period | Error |
|---|---|---|
| | s | s |
| 0051 | 413.7 | 0.7 |
| 0103 | 413.9 | 0.3 |
| 0105 | 414.4 | 0.3 |
| 0106 | 413.7 | 0.3 |
| 0107 | 414.1 | 0.3 |
| 0113 | 413.9 | 0.3 |

The same timing analysis (*i.e.* Lomb-Scargle periodogram, epoch-folding $\chi^2$-distribution search, folded light curves) was applied to the ISGRI data. We first tried with revolution 106 where IGR J17252−3616 showed its brightest flare. The best period is 413.7±0.3 s. The results and folded light curve are presented in section 4.2.2 of Zurita Heras et al. (2005).

The period was also searched in other revolutions in the GCDE#1 and #2. The source intensity was too faint to find anything consistent with the epoch-folding $\chi^2$-distribution method. However, the Lomb-Scargle periodograms proved to be a powerful tool to search for periodicities. Indeed, this method is less sensitive to gaps in the light curve such as those often present in ISGRI data. The coverage is long and, due to the observational strategy (see Sect. 5.1 for details), it might happen that the source appears and disappears in consecutive pointings. The period was searched in every revolution with sufficient exposure time. It is detected only in 5 other revolutions : 0051, 0103, 0105, 0107 and 0113. No evolution of the period is detected in the ISGRI data (see Table 6.6).

### Coherent modulation: orbit?

In fact, this section should come at the very end of this chapter since it was the last feature we discovered analysing the ISGRI data. Nevertheless, it suits well at this stage of the explanation (see also Sect. 6.5.1).

The 20–60 keV light curve based on the flux extracted in each deconvolved image of each pointing was carefully studied to find any significant repetitive structure (see Fig. 6.8). Computing the Lomb-Scargle periodogram on the interval 4 to 28 days, a peak located at 9.71±0.09 days appears in the power spectrum density with a power of 50 (see Fig. 6.14). The power spectrum is quite noisy and secondary peaks are present. Nevertheless, the folded light curve is reasonable (see Fig. 6.15). The two main features are the strong flare at phase $\phi \sim 0.5$ where the intensity increased by a factor of three compared to the *plateau* and the eclipse-like feature at phase $\phi \sim 0.0$ where the intensity is consistent with zero. The origin of this flare is ambiguous. When flare periods were removed from the light curve, the flare at phase $\phi \sim 0.5$ disappeared from the folded light curve (see Fig. 9 in Zurita Heras et al. (2005)).

### Interpretation

The timing analysis of IGR J17252−3616 reveals important features. The source is persistent and variable, and shows strong flares during which the source intensity can increase by a factor of tens in a few hours.

Two coherent modulations were discovered in the various light curves built on different time scales. If the nature of IGR J17252−3616 is interpreted as a binary system, the two periods can be interpreted as the orbital period for the longest one and as the spin period for the shorter one.

The 414 s periodic X-ray emission enhancement is due to the misalignment between the spin axis and the magnetic axis. When the magnetic axis is directed towards the detector, the X-ray emission increases. The pulse period can be seen as the time needed by the compact object to turn once around itself, so the spin period. The presence of a magnetic field confirms that the compact object is a neutron star. The presence of a black hole is discarded.

The observed ten days orbital period is more characteristic of a high-mass X-ray binary system than a low-mass X-ray binary system. Indeed, the LMXB systems show orbital periods on timescales of hours, even if some known LMXB have been discovered with orbital periods lasting a few days. Generally in HMXB systems, there is a dichotomy around 15 days to separate the transient HMXB (>15 d) from the OB super-giant systems (<15 d). Moreover, almost all the known accreting pulsars are HMXB. When plotting the observed orbital and pulse period in a diagram (the so-called *Corbet diagram*), some trends specific to each category are observed (Corbet 1984, 1986) (see Fig. 6.16). IGR J17252−3616 locates itself in the underfilled Roche-Lobe super-giant system zone.

From the timing analysis, the image of IGR J17252−3616 is that of a binary system with a compact object being a neutron star that captures matter from the strong stellar wind expelled by a companion supergiant star.

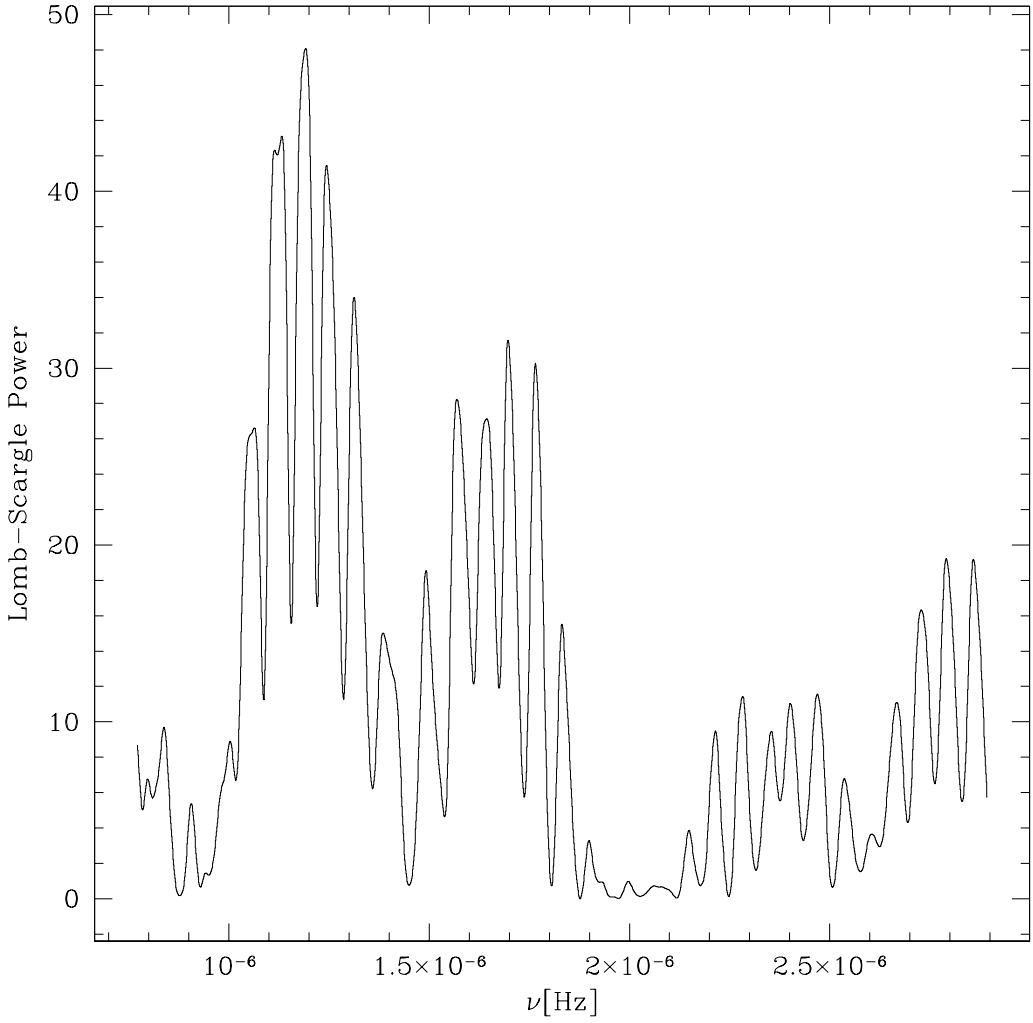


**Figure** *6.14: Lomb-Scargle periodogram of IGR J17252−3616 between 4 d and 15 d. The highest peak corresponds to a period of 9.71±0.09 d.*

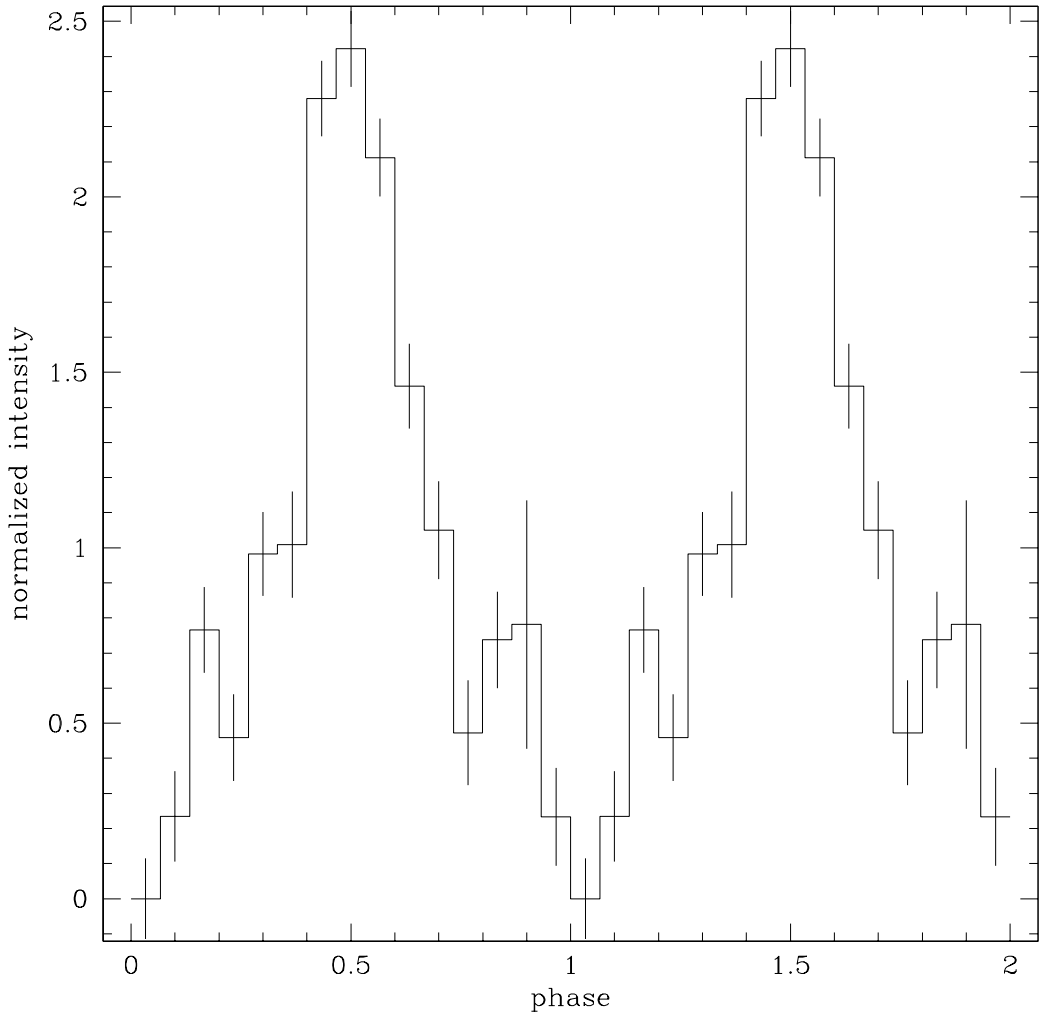


**Figure** *6.15: Orbital folded light curve of IGR J17252−3616. The period is 9.71 d and the time zero is MJD 52700. The object shows an eclipse-like feature at phase 0 and a strong flare at phase 0.5.*

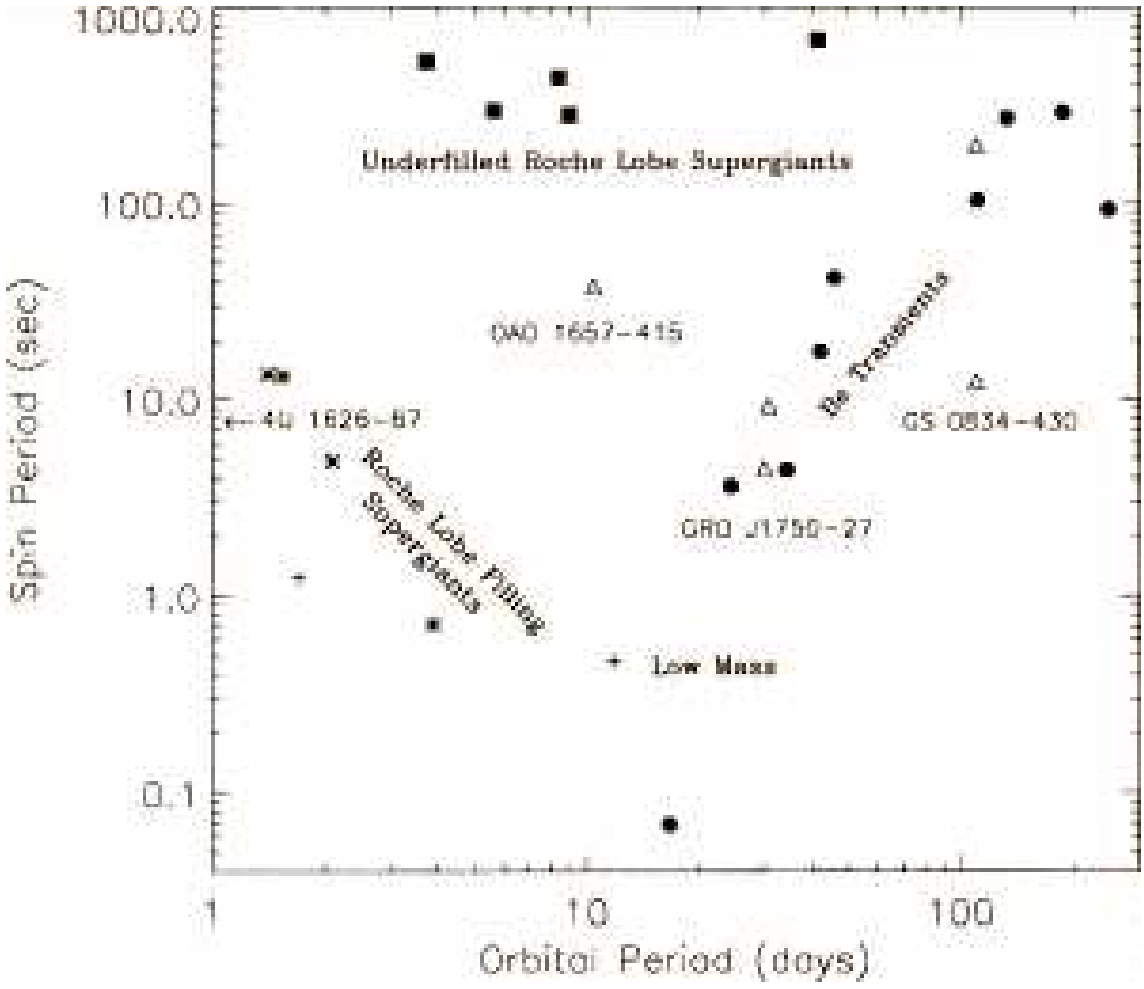


**Figure** *6.16: Spin period vs orbital period of accreting pulsars. Credits : Bildsten et al. (1997).*

### 6.4.3 Spectral analysis

No emission at energies higher than 60 keV was detected from IGR J17252−3616 in the imaging analysis (see Fig. 6.2) but the energy limit where the source fades away is still unknown. The source is widely covered in time in the hard X-ray range (E>20 keV). However, the X-ray observation (0.2–12 keV) is very short in comparison. Simultaneous studies are impossible except for the few kiloseconds of the *XMM-Newton* observation. Indeed, there is no information coming from JEM-X.

Besides, extracting spectra with ISGRI data remains complicated when considering a faint source as IGR J17252−3616. Its average intensity is 6 mCrab. The standard spectral extraction method works on a ScW level, *i.e.* one spectrum is built per pointing, and the source is not detected in many ScW as seen in Fig. 6.8. Therefore, many spectra need to be accumulated together in order to obtain a good signal-to-noise average spectrum.

The spectrum of IGR J17252−3616 is also studied on different time scales: (average over two years, average over a revolution, the three simultaneous pointings) and phase-resolved spectroscopy is also performed on the X-ray part.

#### The average spectrum

The first step is to build the average spectrum over all the data. We start with the ISGRI data as it was discovered with this detector.

Two methods to extract spectra with ISGRI can be used. The standard method (`method=1`) works on individual ScW. Spectra for all the selected sources and the background are extracted. It works with a Pixel Illuminated Function (PIF) methods. The PIF selects all the pixels illuminated by a source once its position in the FOV and the mask is considered. The PIF of IGR J17252−3616 during the pointing `010600350010` is shown in Fig. 6.17. The analysis has to be done at the spectral level (`startLevel=BIN_S` and `endLevel=SPE`).

```
ibis_science_analysis \
  ogDOL="./og_ibis.fits[1]" \
  method=1 \
  startLevel="BIN_S" endLevel="SPE" \
  SWITCH_disablePICsIT=yes \
  IBIS_SI_ChanNum="-1" \
  IBIS_SI_inEnergyValues="rebin_response_matrix.fits[3]" \
  SCW2_cat_for_extract="file_with_sources.fits[1]" \
  SCW2_racolumn=RA_OBJ SCW2_deccolumn=DEC_OBJ
```

The alternative technique consists in creating mosaic images in fine energy bins and to build the spectrum extracting the fluxes at the source position in the images. Both methods have been used throughout this study. There are no significant differences in the spectra. For historical reasons[11], we have extracted spectra from images and from standard method depending on the quality of each new release and the results of the different testings.

[11] Indeed, we have seen OSA *grow up*, and extracting spectra has been (and still is) the most controversial point. The accuracy of the resulting spectra were under debate, so alternative methods were explored.

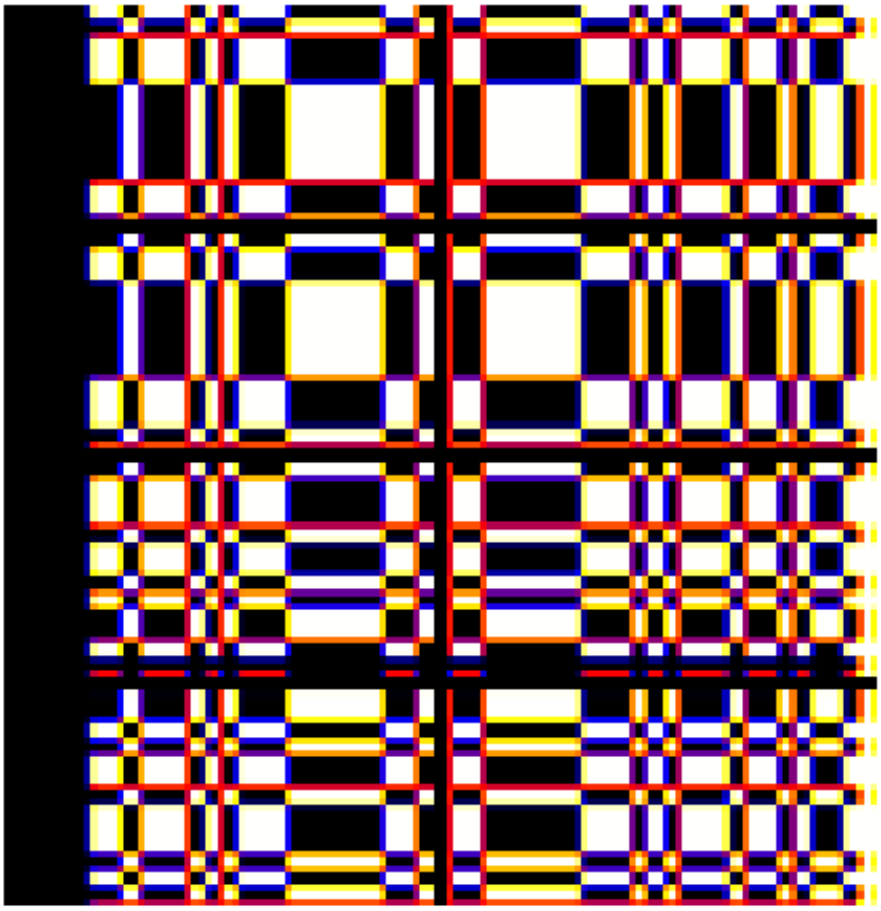

**Figure** *6.17: Example of a PIF for IGR J17252−3616 in ScW* 010600350010.

Extracting spectra in mosaic images needs some specifications when performing the analysis. The flux should not be spread in the reconstructed mosaic images (`OBS1_PixSpread=0`). Afterwards, the flux can be extracted from the images with the help of the `mosaic_spec` tool. It was released with OSA 5.0. This tool gives the possibility to find the best source position in the first energy band (`posmode=1`) or to keep it fixed (`posmode=-1`) if the source position is known with a better accuracy than *INTEGRAL*, for example, from IR/optical follow-ups. On the given position, the flux is extracted in a region of 12′ as the ISGRI PSF (`widthmode=-1 psf=6`). If the background remains important, an estimate of it can be made and subtracted (`size=10 back=yes`).

The ISGRI average spectrum was extracted from the mosaic image of revolution 106 for which the source has the highest signal-to-noise (significance=46, see Table 6.3), hence the possibility to extract a good spectrum. This is the revolution where the source shows its brightest flare (see Fig. 6.11). However, the spectral shape does not experience changes outside and inside the flare. The average hard X-ray spectrum is shown in Fig. 10 of Zurita Heras et al. (2005).

Revolution 106 corresponds to MJD 52877.42–52880.41. This is 6 months earlier than the *XMM-Newton* observation. However, we decided to combine the spectra of both instruments as it better constrains the possible models we could use to fit the observational data.

The spectrum of IGR J17252−3616 was extracted for the EPIC/pn instrument as it is the best instrument for extracting spectra. A selection in the pn event lists has to be done in order to extract the spectrum. The source is located at a precise place in the images. Only a subset of photons corresponds to the source. Two regions have to be specified: one for the source+background and one for the background. An example of regions to select events for EPIC/pn is shown in Fig. 6.18. Only single and double events were kept for the spectral analysis (`PATTERN<=4`). Bad pixels were discarded (`FLAG==0`).

```
evselect \
  table=pnCleanEventList.fits \
  withspectrumset=yes spectrumset=pnSpecSrc.fits \
  energycolumn=PI spectralbinsize=5 \
  withspecranges=yes specchannelmin=0 specchannelmax=20479 \
  expression='(FLAG==0) && (PATTERN<=4) && ((X,Y) IN circle(XXXX,XXXXX,XX))' \
  xcolumn=X ycolumn=Y \
  ximagebinsize=20 yimagebinsize=20 imageset=pnImgSpecSrc.fits \
  filteredset=pnFltClean.fits destruct=Y keepfilteroutput=T
```

As the source is bright in the image, possible pile-up contamination was checked (see Fig. 6.19). The pile-up effects consist of photons reaching a pixel before it is read-out, so the recorded event has a higher energy and the resulting spectrum is much harder. As correcting pile-up effects remains a complex task, the calibration document advice is to ignore it if the effect is not important[12].

[12]One technique would be to ignore the events at the very centre of the source selecting events in a double-circle. It was advised to avoid this technique in the last calibration documentation except if pile-up is too obvious.

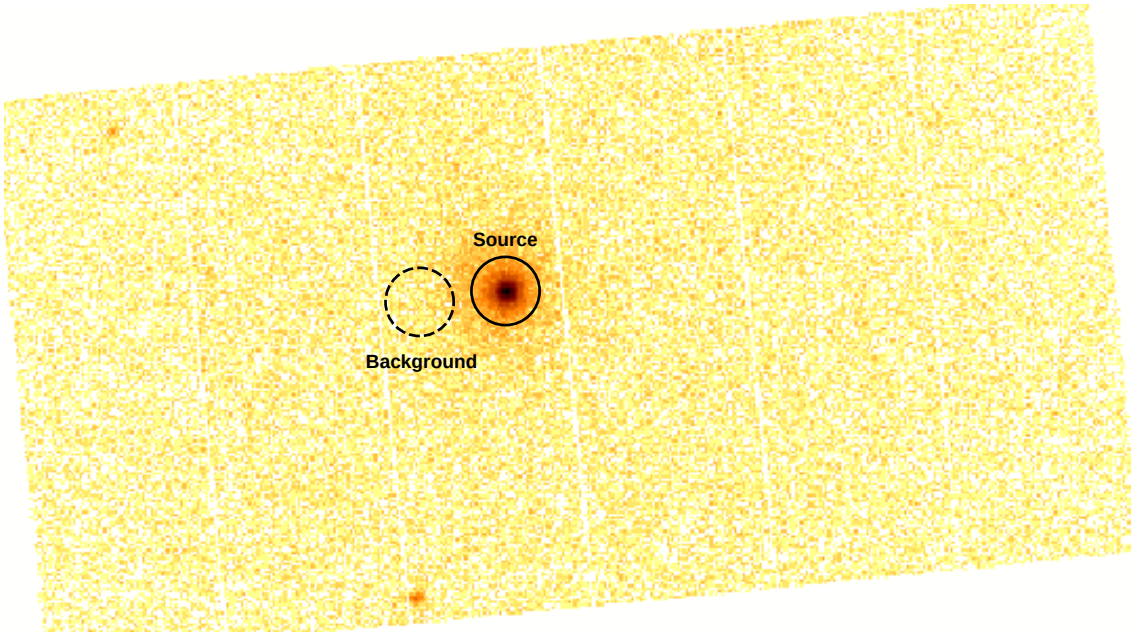


**Figure** *6.18: EPIC/pn image extracted between 0.8 and 10 keV*

The area of source and background regions used to make the spectral files are also calculated.

```
backscale spectrumset=pnSpecSrc.fits  badpixlocation=pnCleanEventList.fits
```

Once the spectral files are ready, the response matrix function and the ancillary file have to be prepared.

```
rmfgen spectrumset=pnSpecSrc.fits rmfset=pnSpec.rmf
```

```
arfgen spectrumset=pnSpecSrc.fits arfset=pnSpec.arf \
  withrmfset=yes rmfset=pnSpec.rmf \
  badpixlocation=pnCleanEventList.fits detmaptype=psf
```

The combined ISGRI+pn analysis is fully explained in Sect. 4.3 and 5.3 of Zurita Heras et al. (2005).

### The RGS spectrometer

The data of the grating spectrometer RGS were also checked in order to extract a fine spectrum at soft X-rays (6–35 Å, *i.e.* 0.35–2.5keV). However, the source is highly absorbed at soft X-rays and nothing is detected (see Fig. 6.20).

### The simultaneous spectrum

3 pointings of *INTEGRAL* are simultaneous to the *XMM-Newton* observation. The source is sometimes bright enough to be detected in a single ScW (see Fig. 6.10). The field was

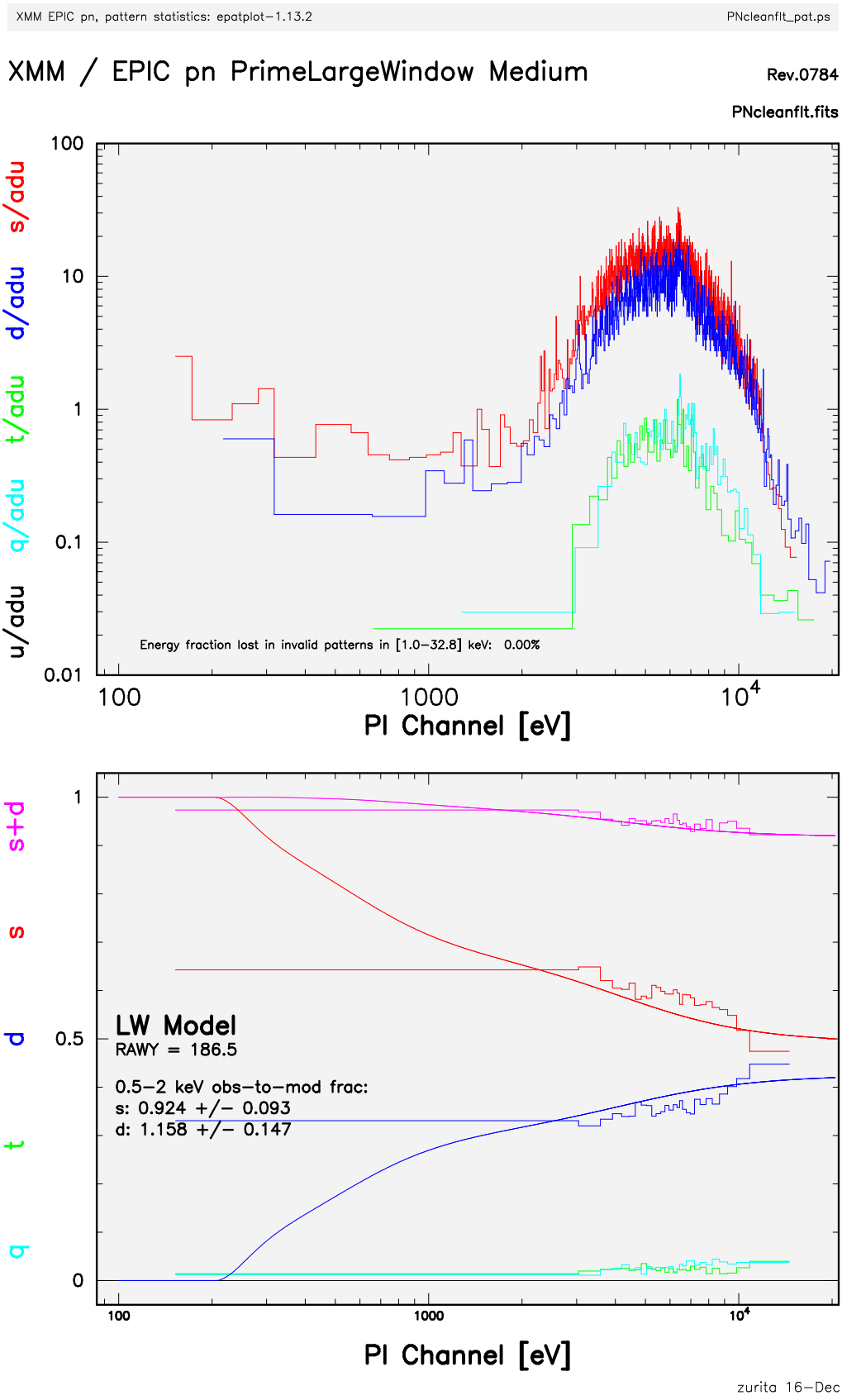


**Figure** *6.19: Effect of pile-up in the EPIC/pn camera : negligible. The upper panel shows the spectral distribution of single, double, etc. events. The lower panel shows the fraction relative to the sum of each event type. They are compared to the model curves. If the observation suffers from pile-up, the measured distribution would diverge from the model distribution. A maximum count rates per instrument is defined and listed in the* XMM-Newton *User's Handbook.*

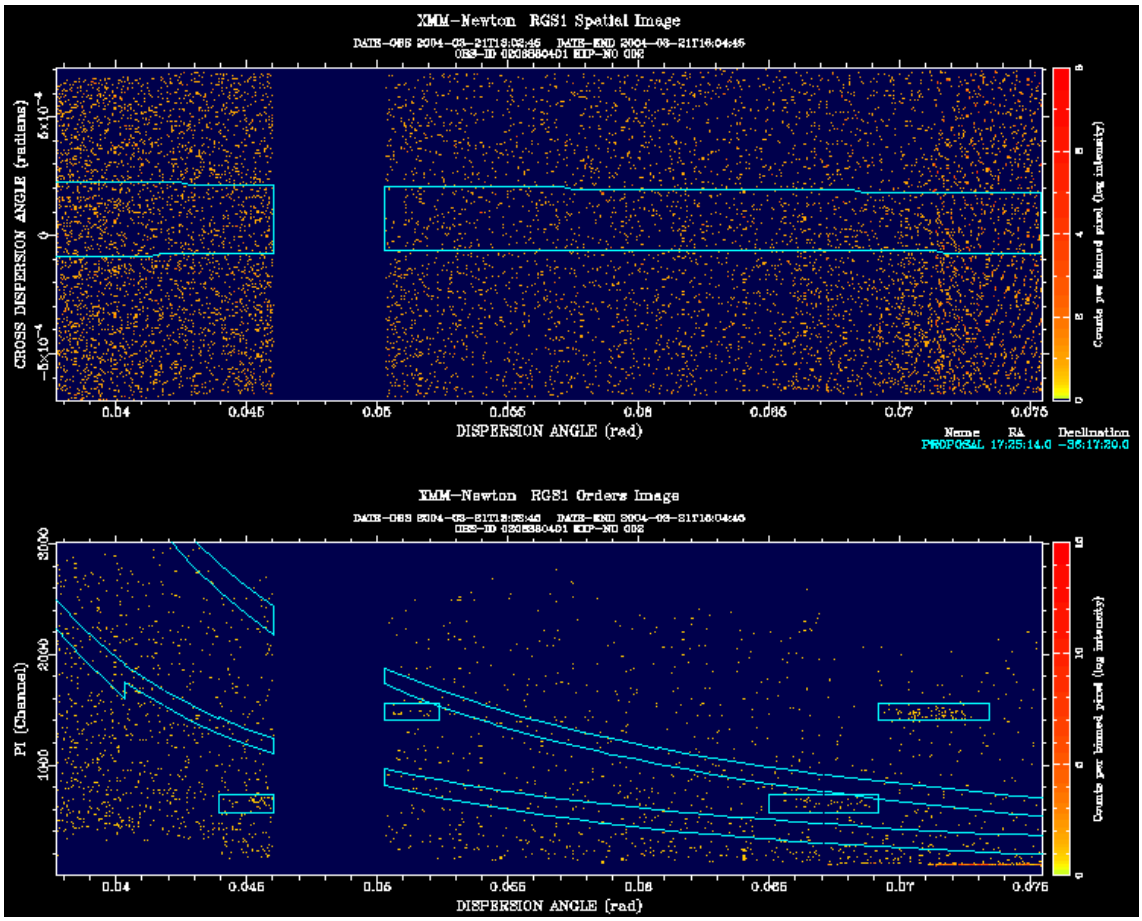


**Figure** *6.20: RGS1 with dead CCD#7. The light blue boxes corresponds to where the source signal should be present if the source was detected by the detector.*

carefully studied for these 3 ScW. In Fig. 6.21, we clearly note that IGR J17252−3616 is not detected in the individual ScW images and the mosaic images of the 3 ScW together.

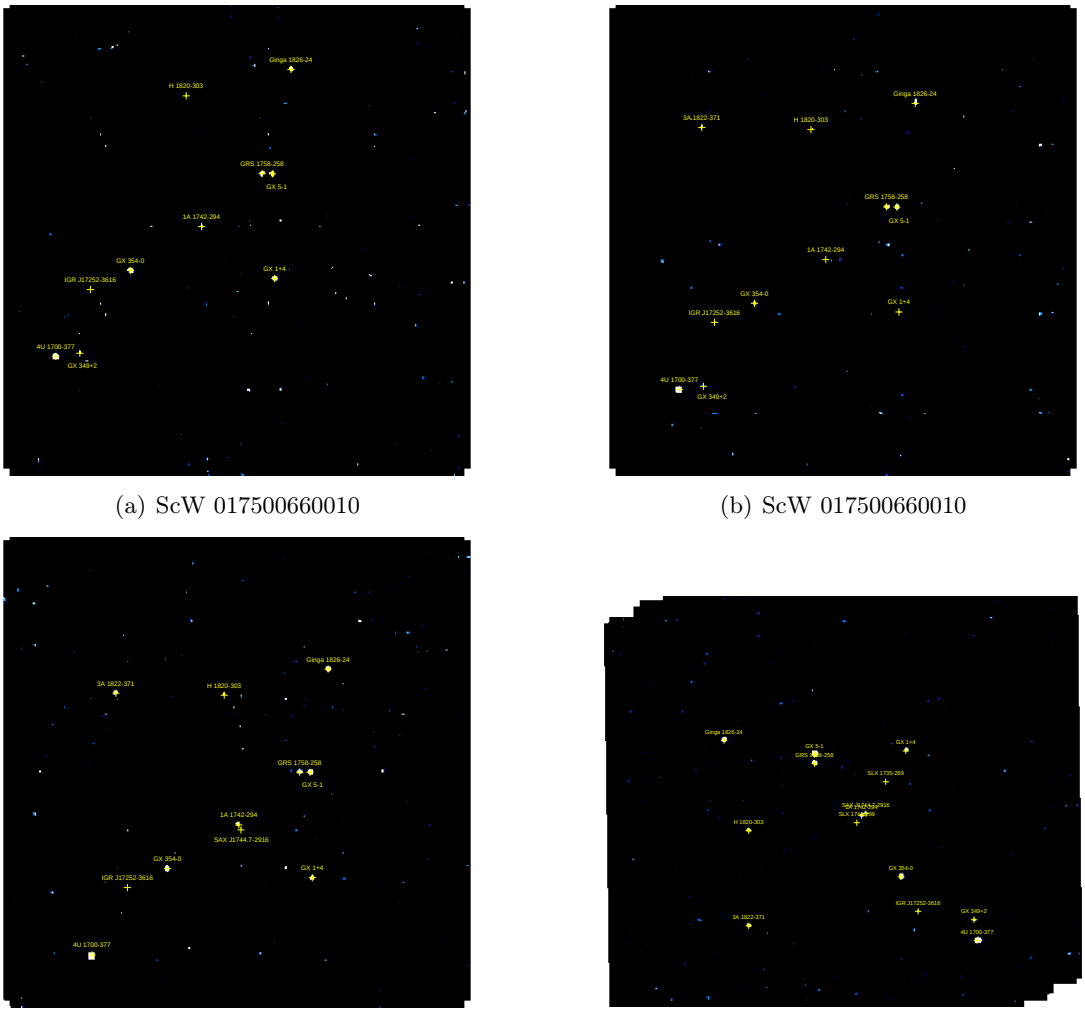


(a) ScW 017500660010

(b) ScW 017500660010

(c) ScW 017500660010

(d) Mosaic 3 ScW

**Figure** *6.21: ISGRI images of the field of IGR J17252−3616 simultaneous to the* XMM-Newton *observation.*

Indeed, when plotting both count rates of pn and ISGRI, we note that the source ISGRI intensity is too low to be detected in only a few ScW (see Fig. 6.22).

When extracting a spectrum at the source position with the ISGRI data, we obtain only background noise (see Fig. 6.23).

### Phase-resolved spectroscopy

Phase-resolved spectroscopy was performed with the pn data. The folded light curve was cut as shown in Fig. 6.24. The selection of the events was done using the `Xselect` software.

The detailed analysis is explained in Sect. 4.3 and 5.3 of Zurita Heras et al. (2005). The main result is that the spectrum does evolve with the pulse period except for its intensity

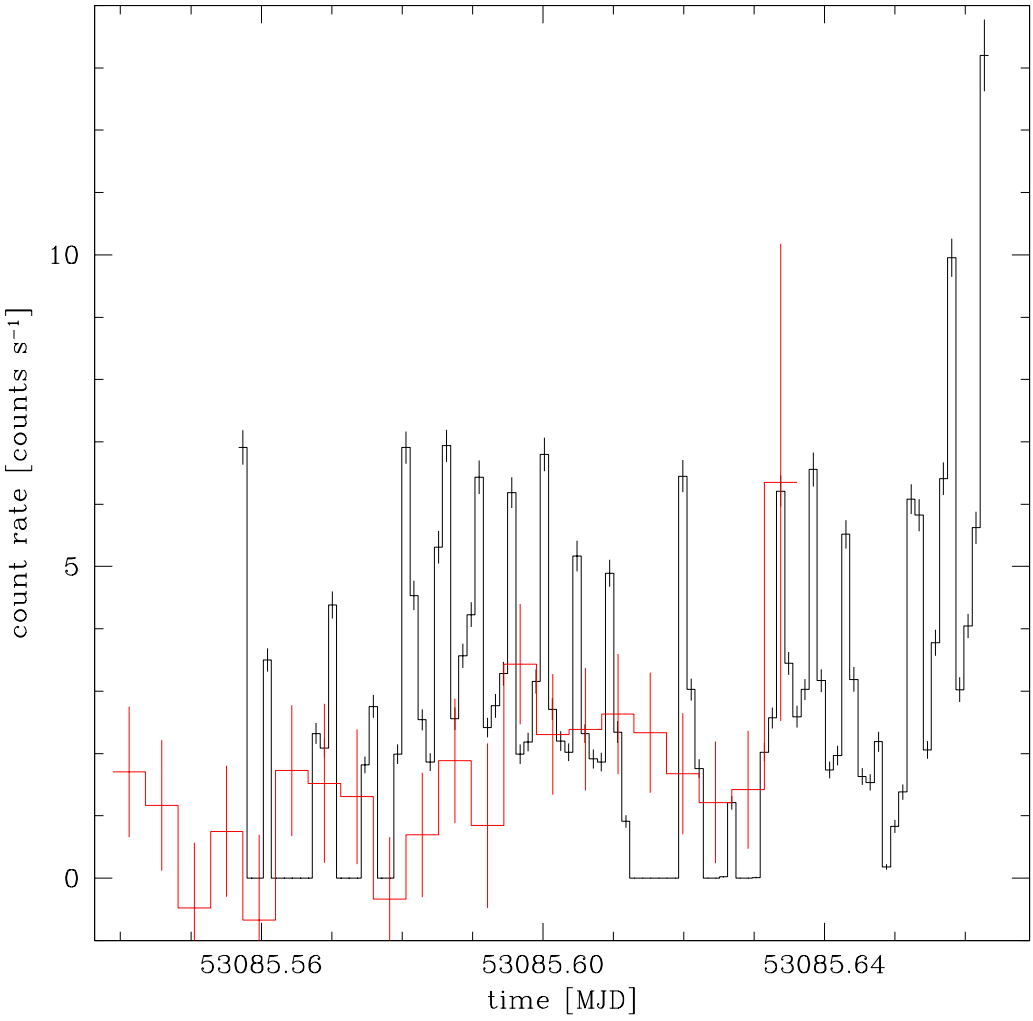


**Figure** *6.22: Simultaneous observation of IGR J17252−3616 with ISGRI (red) and pn (black). Both count rates are rebinned.*

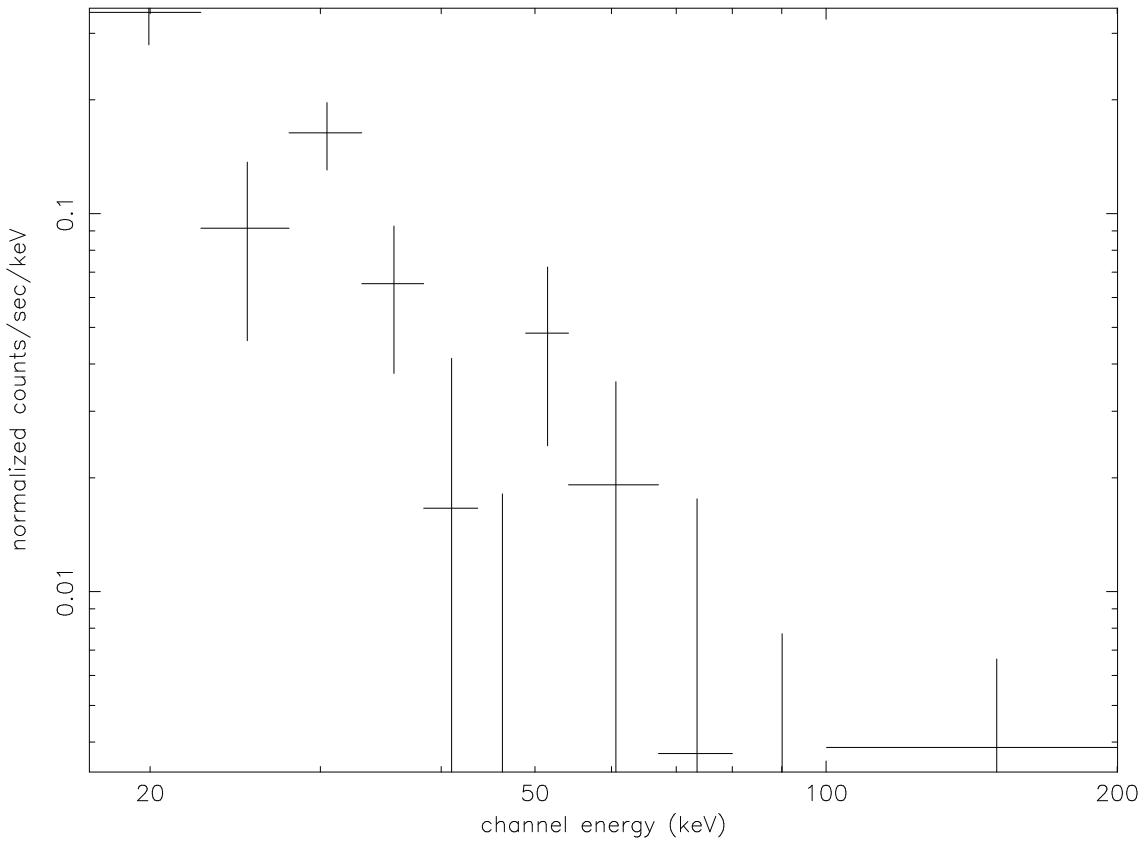


**Figure** *6.23: ISGRI spectrum extracted at the IGR J17252−3616 position during the 3 pointings simultaneous to the* XMM-Newton *observation. No significant emission of the source is detected as confirmed by the images.*

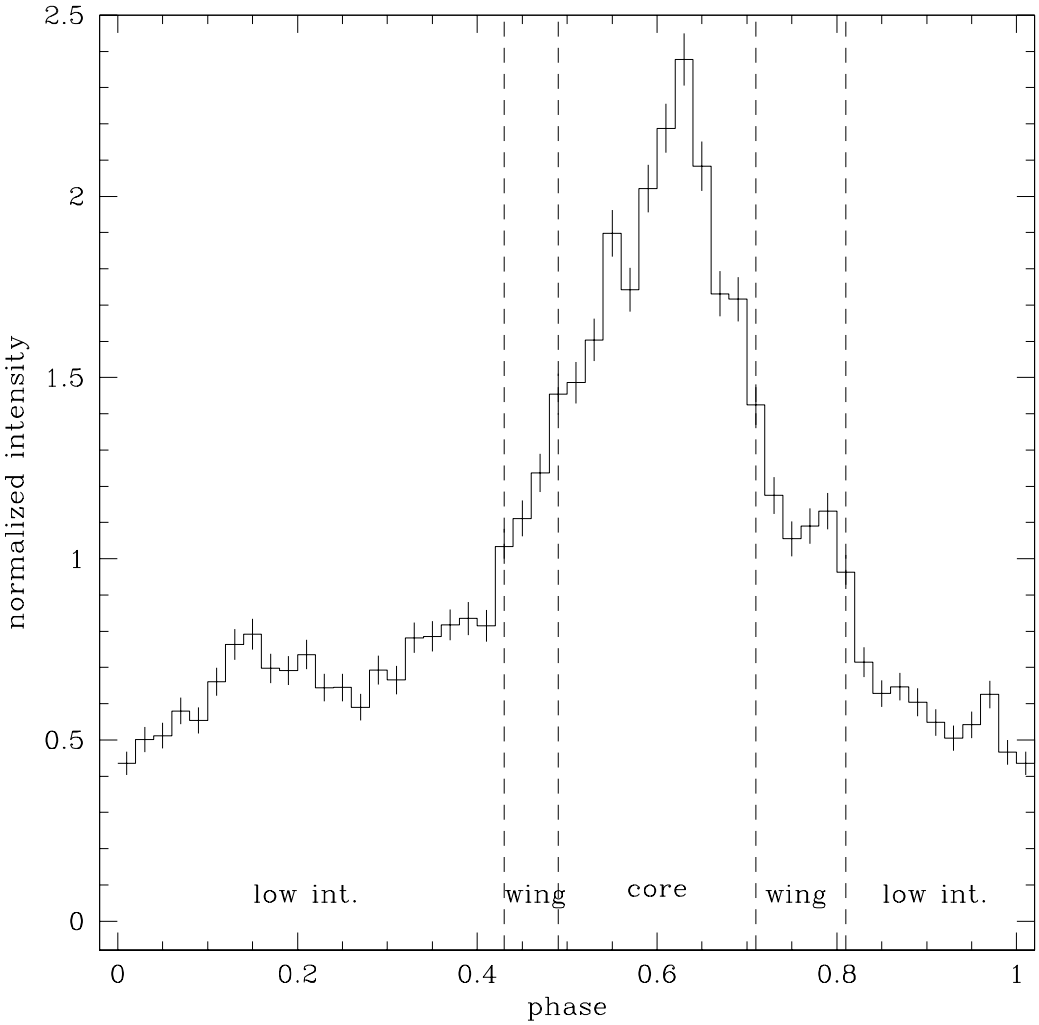


**Figure** *6.24: The 0.4–10 keV folded light curve is cut in 3 parts in order to perform phase-resolved spectroscopy.*

**Table** 6.7: Summary of the position of IGR J17252−3616/EXO 1722−363 reported in the literature.

| Reference | R.A. (2000) [h m s] | Dec. [° ′ ″] | Angular distance[a] ′ |
|---|---|---|---|
| Warwick et al. (1988) | 17 25 24.0 | -36 24 40.8(9) | 9 |
| Tawara et al. (1989) | 17 25 21.6 | -35 56 38.2 | 19 |
| Lutovinov et al. (2003a) | 17 25 24.0 | -36 18 00.0(2) | 3 |
| Lutovinov et al. (2004) | 17 25 08.6 | -36 16 48.0(2) | 1 |
| Walter et al. (2004) | 17 25 12.0 | -36 16 00.0(2) | |
| Zurita Heras et al. (2005) | 17 25 11.4 | -36 16 58.6(4″) | 1 |

[a]in comparison with the position of Walter et al. (2004) when IGR J17252−3616 was discovered.

that changes according to the pulse profile.

## 6.5 Counterparts and summary of known features

The source was tagged as a new source by the *INTEGRAL* survey team (Walter et al. 2004; Bird et al. 2004) as no other known X-ray source corresponded to its position, even with the most accurate one. The nearest source was EXO 1722−363 whose position (with uncertainty) is not compatible either with the ISGRI or the EPIC one. Only with the spatial information, it was reasonable to claim the detection of a new source.

### 6.5.1 Other X-ray counterparts

However, once the source fully analysed with *INTEGRAL* and *XMM-Newton*, the timing and spectral analysis clearly showed similarities between IGR J17252−3616 and EXO 1722−363. The observed orbital and pulse periods, and the spectrum were compatible for both sources between our study and precedent studies on EXO 1722−363 by Tawara et al. (1989) and Takeuchi et al. (1990). In Table 6.7, all the positions reported in literature are listed with angular distance between the published position and the one reported by Walter et al. (2004) claiming the discovery of the new source. The EXO 1722−363 position is just marginally compatible with IGR J17252−3616, hence the reason why the source was claimed as new. Meanwhile, Lutovinov et al. (2003a) and Lutovinov et al. (2004) reported the detection of EXO 1722−363 with *INTEGRAL*, but they never associated it with IGR J17252−3616.

With the improved position given by Lutovinov et al. (2004), Corbet et al. (2005b) could resolve the system timing parameters with *RXTE* data. They are summarised in Table 6.8. The orbital period found with *RXTE* is compatible with the orbital period found with ISGRI (Lutovinov et al. 2004; Zurita Heras et al. 2005).

### 6.5.2 The infra-red counterpart

The OM image given with the pipeline products shows no source at IGR J17252−3616 position. However, one IR counterpart is found in the 2MASS catalogue : 2MASS J17251139-3616575. The IR counterpart candidate is shown in Fig. 3 of Zurita Heras et al. (2005).

**Table** 6.8: Summary of all the system timing parameters of IGR J17252−3616/EXO 1722−363 from Corbet et al. (2005b).

| Parameter | Value |
|---|---|
| $P_{\rm orb}$ | 9.741 d |
| $T_{\rm mid}$ | 51 219.35 MJD |
| $P_{\rm pulse}$ | 413.86 s |
| $a \sin i$ | 111.1 lt s |
| f(M) | 15.4 $M_\odot$ |

Its position is 1.1″ from the X-ray position.

### 6.5.3 Galactic Bulge region

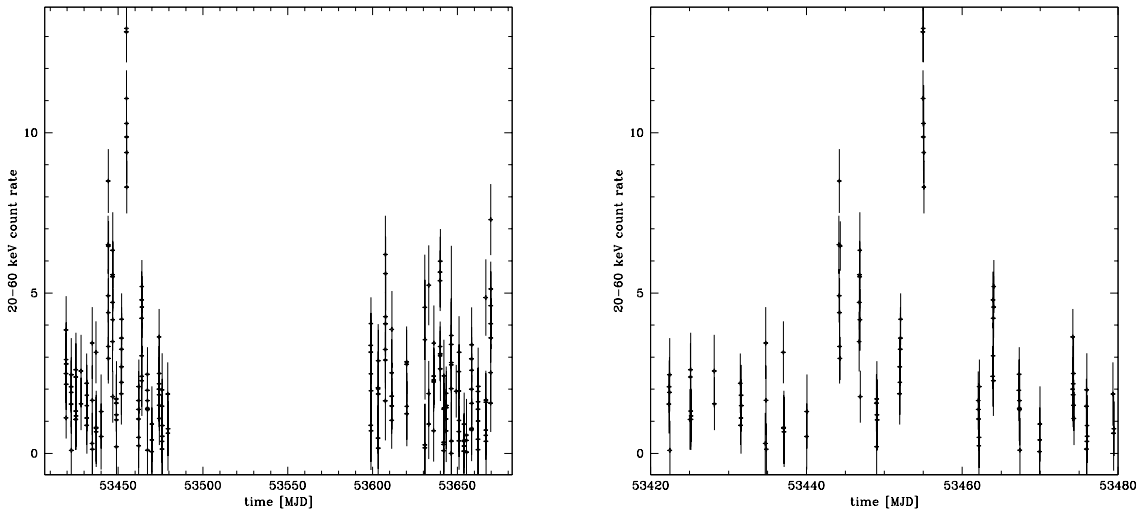


(a) Complete Galactic Bulge observation

(b) Zoom MJD 53420–53480

**Figure** *6.25: 20–60 keV count rate of IGR J17252−3616. Three flares are visible in the light curve : MJD 53444.2, MJD 53446.8 and MJD 53454.9.*

The bulge region has been regularly monitored during the AO3 period as part of a proposal by Kuulkers et al. (in preparation). This galactic central region is rich in X/$\gamma$-ray sources and IGR J17252−3616 is included in this field. They observe the central region with a hexagonal dither pattern every revolution (7 pointings of 1.8 ks). ISGRI light curves of sources present in this field are made publicly available at

`http://isdc.unige.ch/Science/BULGE/`.

The 20–60 keV light curve of IGR J17252−3616 between MJD 53419.31 and 53669.81 (revolutions 0287–370) is shown in Fig. 6.25. The source shows three new flares at MJD 53444.2 (rev. 0295), MJD 53446.8 (rev. 0296) and MJD 53454.9 (rev. 0299). In the last one, the source reaches its highest flux level for one pointing : 13 counts $s^{-1}$ in two ScW.

These results comes from Kuulkers et al. (2006) using the OSA software[13], distributed by the ISDC (Courvoisier et al. 2003a).

## 6.6 Scientific paper published in AA

The investigation on IGR J17252−3616 lead to a paper that has been accepted for publication in the *A*stronomy & Astrophysics journal.

[13]The data were processed with OSA 5.0.

*Astronomy & Astrophysics* manuscript no. aa3876-05
November 8, 2005


Article published by EDP Sciences and available at http://www.edpsciences.org/aa
To be cited as: A&A preprint doi http://dx.doi.org/10.1051/20053876

# IGR J17252−3616: an accreting pulsar observed by *INTEGRAL* and *XMM-Newton*

J.A. Zurita Heras[1,2], G. De Cesare[3,4,5], R. Walter[1,2], A. Bodaghee[1,2], G. Bélanger[8], T.J.-L. Courvoisier[1,2], S.E. Shaw[6,1], and J.B. Stephen[7]

[1] INTEGRAL Science Data Centre, ch. d'Ecogia 16, 1290 Versoix, Switzerland
[2] Observatoire de Genève, ch. des Maillettes 51, 1290 Sauverny, Switzerland
[3] IASF-INAF, Via Fosso del Cavaliere 100, 00133 Roma, Italy
[4] Dipartimento di Astronomia, Universita degli Studi di Bologna, Via Ranzani 1, I40127 Bologna, Italy
[5] Centre d'Etude Spatiale des Rayonnements, CNRS/UPS, B.P. 4346, 31028 Toulouse Cedex 4, France
[6] School of Physics and Astronomy, University of Southampton, Highfield, SO17 1BJ, UK
[7] IASF/CNR, Via Piero Gobetti 101, 40129 Bologna, Italy
[8] Service d'Astrophysique, DAPNIA/DSM/CEA, 91191 Gif-sur-Yvette, France

Received / Accepted

**ABSTRACT**

The discovery of the X-ray source IGR J17252−3616 by *INTEGRAL* was reported on 9 February 2004. Regular monitoring by *INTEGRAL* shows that IGR J17252−3616 is a persistent hard X-ray source with an average count rate of 0.96 counts $s^{-1}$ (∼6.4 mCrab) in the 20–60 keV energy band. A follow-up observation with *XMM-Newton* which was performed on 21 March 21 2004, showed that the source is located at R.A. (2000.0) = $17^h25^m11.4^s$ and Dec. = $-36°16'58.6''$ with an uncertainty of 4″. The only infra-red counterpart to be found within the *XMM-Newton* error circle was 2MASS J17251139−3616575, which has a Ks-band magnitude of 10.7 and is located 1″ away from the *XMM-Newton* position.
The analysis of the combined *INTEGRAL* and *XMM-Newton* observations shows that the source is a binary X-ray pulsar with a spin period of 413.7 s and an orbital period of 9.72 days. The spectrum can be fitted with a flat power law plus an energy cut off ($\Gamma \sim 0.02, E_c \sim 8.2$ keV) or a Comptonized model ($kT_e \sim 5.5$ keV, $\tau \sim 7.8$). The spectrum also indicates a large hydrogen column density of $N_H \sim 15\,10^{22}$ atoms $cm^{-2}$ suggesting an intrinsic absorption. The Fe K$\alpha$ line at 6.4 keV is clearly detected. Phase-resolved spectroscopy does not show any variation in the continuum except the total emitted flux. The absorption is constant along the pulse phase. This source can be associated with EXO 1722−363 as both systems show common timing and spectral features. The observations suggest that the source is a wind-fed accreting pulsar accompanied by a supergiant star.

**Key words.** Gamma rays: observations, X-rays: binaries, pulsars: individual: IGR J17252−3616=EXO 1722−363

## 1. Introduction

X-ray binaries consist of a compact object, either a black hole or a neutron star, accreting matter from a companion star; they are usually classified according to the mass of the companion as a high mass (HMXB, $M_C \gtrsim 10\,M_\odot$), intermediate-mass (IMXB, $M_C = 1$–$10\,M_\odot$) or low mass X-ray binary (LMXB, $M_C \lesssim 1\,M_\odot$). The LMXB and IMXB accrete matter through Roche-Lobe overflow from the companion star and through an accretion disk around the compact object (Tauris & van den Heuvel 2005).

The HMXB can be divided into two categories as the companion star can be either an OB supergiant or a Be star. OB supergiant stars feed the compact object through strong stellar winds and/or in some cases Roche-Lobe overflow. Be stars expell matter around their equator that fuels the compact object. The orbits of Be binary systems are eccentric and generally have a longer period than OB supergiant systems ($\gtrsim 15$ days). The X-ray emission of HMXB presents a wide variety of patterns: from transient to persistent, outbursts on different times scales (seconds, days and/or years), periodic modulations, eclipses and others. Strongly magnetized neutron stars accompanied by massive stars show periodic pulsations; the accreted matter is funneled towards the poles by the magnetic field leading to an increase of the observed X-ray emission when these regions cross the line of sight. These HMXB usually show a hard X-ray spectrum between 2–10 keV with an energy cutoff around 10 keV.

Several new hard X-ray sources have been discovered by *INTEGRAL* (Winkler et al. 2003) in surveys of the galac-

*Send offprint requests to*: J.A. Zurita Heras
e-mail: Juan.Zurita@obs.unige.ch

tic plane. Most of them have been detected by IBIS/ISGRI (Ubertini et al. 2003; Lebrun et al. 2003), the most sensitive instrument on board *INTEGRAL* between 20 and 300 keV. The brightest sources detected during the first year of the *INTEGRAL* mission are listed in Bird et al. (2004). A few tens of them have never been detected before *INTEGRAL*'s observation. Most of these new objects show common features in their spectra, such as a high intrinsic low-energy absorption, and they are believed to be HMXB (Walter et al. 2003; Rodriguez et al. 2003; Patel et al. 2004).

IGR J17252−3616's discovery was reported on February 9, 2004, with 13 other hard X-ray sources (Walter et al. 2004) detected with ISGRI in all-sky mosaic images built from core programme data. However, there is evidence that IGR J17252−3616 has already been observed with previous missions. A galactic plane scan performed by *EXOSAT* in June 1984 revealed a point like X-ray source emission, GPS 1722-363 (Warwick et al. 1988), at a position not compatible with IGR J17252−3616 but with a low accuracy. *Ginga* observations in 1987 and 1988 confirmed the presence of a powerful X-ray accretor neutron star, X1722-36, with a pulsation of 413.9 s and important variations of the intensity in X-rays (Tawara et al. 1989). The source also showed a hard spectrum with important low-energy absorption and an emission line at 6.2 keV. Further investigations with Ginga in 1988 confirmed the spectral analysis, and lower limits for the orbital period of 9 days and the mass of the primary star of 15 $M_{\odot}$were deduced from pulse timing analysis (Takeuchi et al. 1990). Both investigations conclude that the system is a HMXB. Recently, those results were confirmed by Corbet et al. (2005) using *RXTE* data. They also found an orbital period of 9.741±0.004 d.

IGR J17252−3616 is regularly monitored by *INTEGRAL*. A follow-up observation lasting three hours was performed with the X-ray Multi-Mirror Mission (*XMM-Newton*) on 21 March 2004. The new data available on this source is presented in this paper. *INTEGRAL* and *XMM-Newton* observations and data analysis techniques are described in Sects. 2 and 3, respectively. The results are presented in Sect. 4 and discussed in Sect. 5. The conclusions are presented in Sect. 6.

## 2. Observations

### 2.1. INTEGRAL

*INTEGRAL* is a hard X-ray and $\gamma$-ray observatory of the European Space Agency (ESA) launched on 17 October 2002. The payload consists of four instruments: the imager IBIS with two detector layers, ISGRI (20 keV–1 MeV) and PICsIT (200 keV–10 MeV, Labanti et al. (2003)); the spectrometer SPI (20 keV–8 MeV, Vedrenne et al. (2003)); the X-ray monitor JEM-X (3–30 keV, Lund et al. (2003)) and the optical camera OMC (V filter, Mas-Hesse et al. (2003)). Most of the *INTEGRAL* observing time is spent in the Galactic Plane.

IGR J17252−3616 is located close to the Galactic Centre, which has been observed regularly. The observing strategy consists of pointings each lasting ∼ 30 minutes distributed in various grids around the Galactic Plane. The focus of the effort for this paper is on IBIS/ISGRI, since IBIS/PICsIT and SPI are less sensitive at energies lower than 300 keV where the source is detected. We did not use data from the JEM-X instrument because its smaller field of view and the dithering observation approach of *INTEGRAL* mean that the effective exposure on IGR J17252−3616 is ten times smaller than obtained with ISGRI.

The data set consists of core programme data obtained until MJD 53341.1 and of public data obtained until MJD 52928.3, giving a total exposure of 6.5 Ms. Table 1 lists the source visibility periods, and for each of them the fraction of the time when the source was effectively observed in the partially-coded field of view (PCFOV).

### 2.2. XMM-Newton

IGR J17252−3616 was observed by *XMM-Newton* (Jansen et al. 2001) on 21 March 2004, from 13:02:45 to 16:04:45 UTC (MJD 53085.544–53085.671) for a total exposure of 11 ks. *XMM-Newton* operates with three instruments that cover the optical/UV and X-ray spectral bands. The main instrument for the purpose of this work is the European Photon Imaging Camera (EPIC) instrument, which consists of two MOS (Turner et al. 2001) and one pn (Strüder et al. 2001) CCD cameras. EPIC has a 30′ field of view, and coverage of the 0.15–12 keV energy range with imaging, timing and spectral capabilities. The EPIC/MOS[12] and pn were all operating in imaging science mode with a large window and a medium filter.

The *XMM-Newton* observation was simultaneous with three *INTEGRAL* pointings in revolution 175 between MJD 53085.542 and 53085.667. However, the signal to noise (S/N) of ISGRI data during those simultaneous observations was too low to perform cross analysis.

## 3. Data Analysis

### 3.1. INTEGRAL

The data were reduced with the Offline Scientific Analysis version 4.2 software (OSA 4.2) that is publicly released by the *INTEGRAL* Science Data Centre (ISDC) (Courvoisier et al. 2003). All the pointings for which the source was either within the ISGRI fully coded (FCFOV, 9° × 9°) or partially coded (PCFOV, 29° × 29°) fields of view were analysed. Around 3000 pointings, distributed between revolutions 37 and 244, were selected. Sky images were extracted for each pointing and combined into mosaic images with longer exposures. As the source is weak, light curves were extracted from the imaging results (pointings and mosaics). During flares, light curves were extracted on shorter time scales using `ii_light` v7.3. Extracting high-energy spectra with OSA 4.2 remains a difficult task for faint sources. Spectra were extracted using `ii_spectra_extract` v2.3.1 and from the mosaic images, and compared. In the energy range in which the source is detected, both methods give consistent results. The redistribution matrix and ancillary response files (RMF and ARF) used were `isgr_rmf_grp_0012.fits` and `isgr_arf_rsp_0006.fits`, respectively. The RMF was rebinned in to 17 channels. Average

**Table 1.** The *INTEGRAL* Data set. We selected all public and core programme revolutions when IGR J17252−3616 was within the ISGRI PCFOV of 29° × 29°. The observing time fraction was calculated as the ratio between the net exposure time on the source and the elapsed time during the visibility periods.

| Visibility Periods | Start [MJD] | End [MJD] | Revolutions | Observing time fraction |
|---|---|---|---|---|
| 1 | 52671 | 52752 | 37- 63 | 0.23 |
| 2 | 52859 | 52925 | 100-121 | 0.51 |
| 3 | 53050 | 53116 | 164-185 | 0.20 |
| 4 | 53236 | 53294 | 226-244 | 0.16 |

fluxes and the source position were obtained from the mosaic images with `mosaic_spec` v1.0[1].

### 3.2. XMM-Newton

The Science Analysis System (SAS) version 6.1.0 was used to produce new event lists for the EPIC instrument running `epchain` for pn and `emchain` for MOS[12]. The event lists were corrected for enhanced background features at energies higher than 10 keV, disregarding time lapses when count rates above 10 keV exceeded 4 counts $s^{-1}$ for pn, 1 count $s^{-1}$ for MOS1 and 1 count $s^{-1}$ for MOS2. Finally, only 5.9 ks of 9.2 ks, 6.2 ks of 10.7 ks and 7.0 ks of 10.7 ks for each instrument, respectively, were kept as good time intervals.

Images were built from the cleaned event lists for the MOS[12] and pn cameras with 2″ and 4″ resolution, respectively. Bad pixels were disregarded and good events were selected until the quadruple level. The lower threshold was fixed at 0.8 keV as recommended in the calibration status documentation (see calibration document XMM-SOC-CAL-TN-0018[2] , p25).

To find the source location, the SAS task `edetect_chain` was used on each individual EPIC camera. Four images, with energy ranges of 0.5–2, 2–4.5, 4.5–7.5 and 7.5–12 keV, were created. The source position was calculated as the mean of the best position from each MOS and pn camera.

The source was clearly visible in the pn images in CCD 1, near the read-out node. An event list of source+background counts was selected from a circle of 50″ around the bright object. The background was estimated from a region adjacent to the source region, with a similar size and at the same distance from the read-out node in the same CCD. To build light curves, only single and double events with an energy between 0.4 and 10 keV were collected, as advocated in the user guide. The background light curve was subtracted using the `FTOOLS lcmath`.

Source+background and background spectra were extracted from all EPIC cameras, MOS[12] and pn, disregarding bad pixels and selecting single and double events. Specific redistribution matrix and ancillary response files were generated for each EPIC instrument with the standard tasks `rmfgen` and `arfgen`, respectively. An average spectrum of the source from the complete observation was first obtained and the `Xspec` version 11.3.1 package was used to fit and plot the resulting spectra corrected for the background.

For the phase-resolved spectra, the `Xselect` version 2.2 software was used to select events corresponding to a specific phase bin given the start epoch and the periodicity of the object. Source and background spectra for each selected phase bin were calculated from the same regions as defined previously.

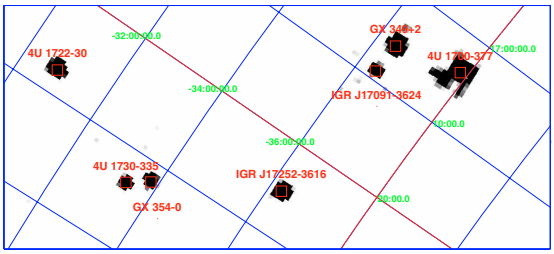


**Fig. 1.** Mosaic image of IGR J17252−3616 with ISGRI during revolution 106 (MJD 52877.4–52880.4).

## 4. Results

### 4.1. Source position

The source's brightest epoch occurred during revolution 106 between MJD 52877.4 and 52880.4 with an average flux of 4.08±0.09 counts $s^{-1}$ and a significance of 47$\sigma$. The ISGRI 20–60 keV mosaic of that epoch was used to extract the hard X-ray source position at R.A. (2000.0) = $17^h25^m10^s$ and Dec. = −36°17′18″, with an uncertainty of 23″ that includes a 10″ systematic error due to the instrument misalignment (see Fig. 1). This statistical error is of the same order as the systematic error that comes from the image reconstruction, which is proportional to the source significance: ∼ 36″ for a S/N of 47 (Gros et al. 2003). This position is compatible with the position obtained by Walter et al. (2004).

Fig. 2 shows the *XMM-Newton* EPIC/MOS1 image with the ISGRI error circle. A single X-ray source corresponds to the *INTEGRAL* position. Its position is R.A. (2000.0) = $17^h25^m11.4^s$ and Dec. = −36°16′58.6″ with an uncertainty of 4″.

With the accurate source position obtained with EPIC, the Two Microns All-Sky Survey (2MASS) catalog (Cutri et al. 2003) was searched for an infra-red counterpart. Only one

[1] `ii_light` and `ii_spectra_extract` are OSA 4.2 standard tools. `mosaic_spec` is released with OSA 5.0.

[2] `http://xmm.vilspa.esa.es/external/xmm_sw_cal/calib/documentation/index.shtml#EPIC`

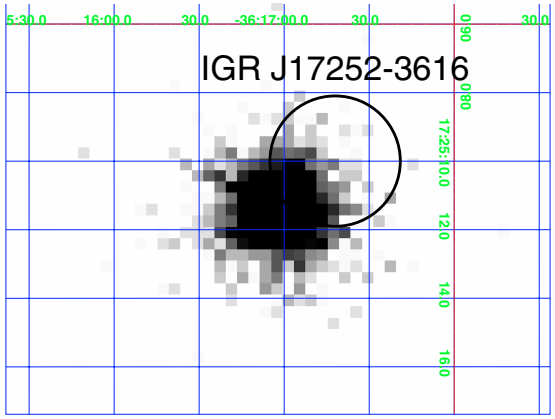


**Fig. 2.** IGR J17252−3616 EPIC/MOS1 image with the 23″ *INTEGRAL*/ISGRI error circle

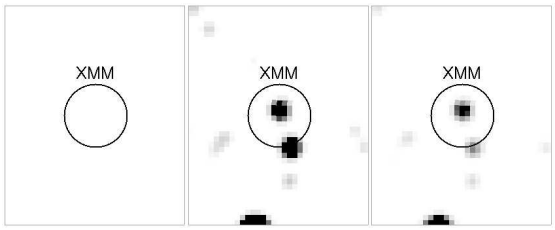


**Fig. 3.** Infrared counterpart of IGR J17252−3616. Images taken from the 2MASS survey: J-band (left), H-band (middle) and K-band (right). The EPIC error circle of 4″ is displayed. 2MASS J17251139-3616575 is only present in the H and K images.

2MASS source appears fully within the 4″ EPIC error circle, 2MASS J17251139-3616575, located 1″ away from the EPIC position. The source is not detected in the J-band with an upper limit of 14.2 magn at 95% confidence level, but appears in the H-band with 11.8 magn and the $K_s$-band with 10.7 magn (see Fig. 3). The colours obtained when dereddening those infrared magnitudes can either be interpreted as a close cool star or a distant hot star (Walter et al. 2005).

### *4.2. Timing analysis*

#### 4.2.1. Long-term variability

The long term variability of IGR J17252−3616 was studied using ISGRI data in two energy ranges: 20–60 keV and 60–150 keV. Mosaic images were built for each three days revolution and light curves extracted for both energy bands. When the source was not detected, 3$\sigma$ flux upper limits were calculated. Net exposures higher than 5 ks at the source location were considered. Typical net exposures for one revolution vary from a few ks to several tens of ks. The source was never detected above 60 keV. The 3$\sigma$ 60–150 keV average count rate upper limit is ∼0.3 counts s$^{-1}$ (∼7 mCrab) with the highest and lowest values being ∼0.6 counts s$^{-1}$ (∼14 mCrab) and ∼0.6 counts s$^{-1}$

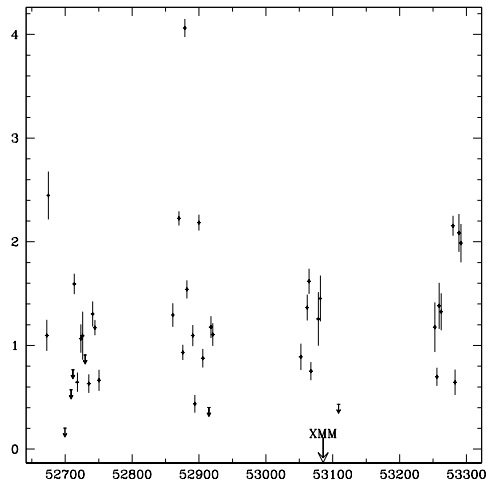


**Fig. 4.** IGR J17252−3616 20–60 keV light curve with average count rate per revolution (∼3 days). 3$\sigma$ upper limits are indicated when the source was not detected. The *XMM-Newton* observation time is shown.

(∼3.5 mCrab). The 20–60 keV light curve on the time scale of a spacecraft revolution is shown in Fig. 4.

The source is detected in almost every single revolution. Its average 20–60 keV flux is 0.96±0.01 counts s$^{-1}$ (∼6.4 mCrab), derived from a 20–60 keV mosaic image generated with data of the first three visibility periods for a total net exposure of 1.7 Ms. The average flux of the object selecting only revolutions when the source is detected is 1.39±0.02 counts s$^{-1}$ (∼9.3 mCrab) as calculated from Fig. 4. When selecting revolutions for which only upper limits are available (rev. 46, 49, 50, 56, 118 and 183) and building a mosaic image with a net exposure of 165 ks, the source is detected with a significance of 5$\sigma$, and the mean 20–60 keV flux reaches 0.19±0.04 counts s$^{-1}$ (∼1.3 mCrab); this is five times less than the average mean flux over all the revolutions and seven times less than the average flux over revolutions when the source was detected. Nevertheless, the source is persistent as, once cumulating enough exposure time, it remains detectable.

On revolution time scales, the source flared up to 4 counts s$^{-1}$ (∼27 mCrab), or a factor of 10 stronger than the lowest detection of 0.4 counts s$^{-1}$ (∼2.7 mCrab), on one occasion (see Fig. 4). IGR J17252−3616 varies by a factor ∼4 outside of this flare.

Variability on time scales shorter than a single revolution was also investigated. Light curves based on flux per pointing were built considering the full *INTEGRAL* data set in the 20–60 keV energy range. The source is often not detected in single pointings. The average count rate per pointing when the source is detected with a significance higher than 4$\sigma$ varies between 2 and 4 counts s$^{-1}$ (∼13–27 mCrab) outside the flares. Four flares are detected in total, three in the 2nd visibility period and one

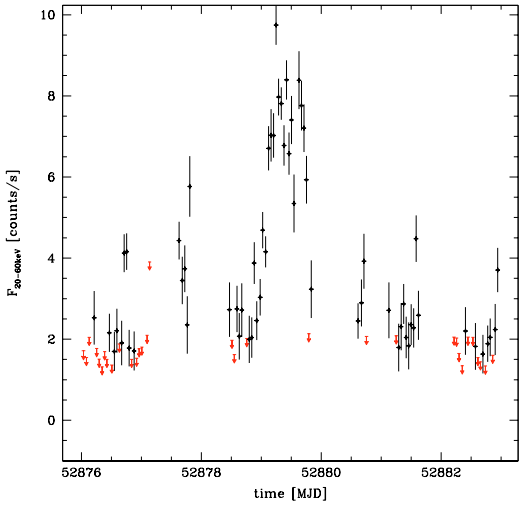


**Fig. 5.** IGR J17252−3616 20–60 keV light curve with average count rates per pointing (~30 min). Around MJD 52879, we observe the brightest flare during the four visibility periods. $3\sigma$ upper limits are indicated when the source was not detected.

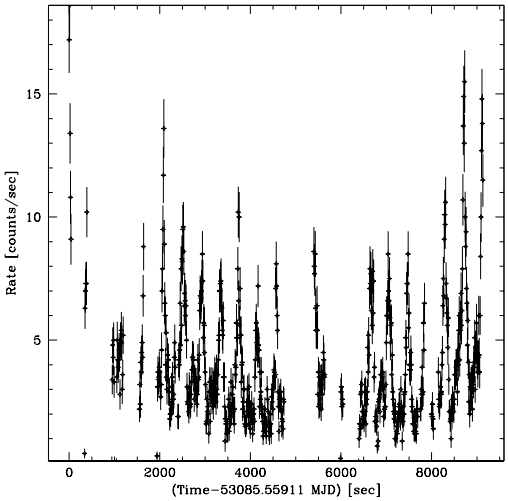


**Fig. 6.** IGR J17252−3616 EPIC/pn 10 s binned light curve. The gaps correspond to the periods with enhanced background activity that were discarded before starting the analysis.

in the 4th visibility period. The brightest flare occured at MJD 52879 when the flux increased from ~2 counts $s^{-1}$ to a peak of 10 counts $s^{-1}$ (~67 mCrab) and decreased again in ~1 day (see Fig. 5). The other flares reached a flux level of ~6–8 counts $s^{-1}$ (~40–53 mCrab) and lasted less than one day. Considering the observed count rates limit values of 0.2 and 10 counts $s^{-1}$, the source varies by a factor of more than 50 between different epochs.

#### 4.2.2. Pulse period

Fig. 6 shows the *XMM-Newton* light curve. A periodic oscillation of ~ 400 s is clearly visible. A power spectral density distribution was created from the entire light curve in order to search for periodicity. A main peak was found around ~400 s with a harmonic at 200 s.

Starting from the estimated period, the best period was searched for in the $\chi^2$ distribution when folding the light curve over a range of different periods. A significant peak was obtained, giving the best period of 414.8±0.5 s when fitted with a Gaussian (see Fig. 7 *top*). The uncertainty on the period was estimated using Eq. 14 of Horne & Baliunas (1986) and Eq. 2 of Hill et al. (2005). Lomb-Scargle periodograms were generated using Press & Rybicki (1989) fast method. The light curve was folded with the best period to obtain the pulse profile between 0.4–10 keV (see Fig.7 *bottom*). The *XMM-Newton* folded light curve is defined so that the minimum flux is set at phase 0 corresponding to MJD 53085.55144. A first local maximum is observed at phase ~ 0.15 followed by a broad maximum at phase ~0.6. The pulse fraction, defined as $P_f = (I_{max} - I_{min})/(I_{max} + I_{min})$ with $I_{max}$ and $I_{min}$ being the maximum and minimum intensities of the folded light curve, respectively, reaches 68 ± 3%.

An ISGRI 50 s binned light curve was made during the bright flare observed at MJD 52879 in two energy bands 20–40 keV and 40–60 keV. Epoch folding the *INTEGRAL* data, starting with the period found in the EPIC/pn light curve, returned a period of 413.7±0.3 s in the 20–40 keV band (see Fig.8 *top*). The signal to noise of the 40–60 keV light curve is not significant enough to detect the modulation. The pulse profile shape shows a broad peak without complex structures (see Fig. 8 *bottom*). The pulse fraction reaches 56±12% and is consistent with the value observed between 0.4–10 keV.

The shape of the X- and $\gamma$-ray pulse profiles show some differences. Due to the less significant detection in the ISGRI data, the number of phase bins is different in the pn and ISGRI folded light curves. The main peak in ISGRI seems broader than in pn. There is also a hint of a secondary peak in the pn data that is absent in the ISGRI data. The folded light curves cannot be compared in phase, because the phase 0 of both pulse profiles do not correspond in time as the observations are separated by 7 months. Notice that the 20–60 keV source intensity was three times brighter during the flare (MJD 52879) than during the *XMM-Newton* observation (~MJD 53085.6) (see Fig. 4).

#### 4.2.3. Orbital period

Indications of an orbital period in the 20–60 keV light curve were searched for, based on flux per pointing. A Lomb-Scargle periodogram was generated between 4 and 28 days. The periods with flaring activity were removed in the light curve before searching for any coherent modulation. A significant peak at 9.72±0.09 days is visible and the folded light curve is shown in

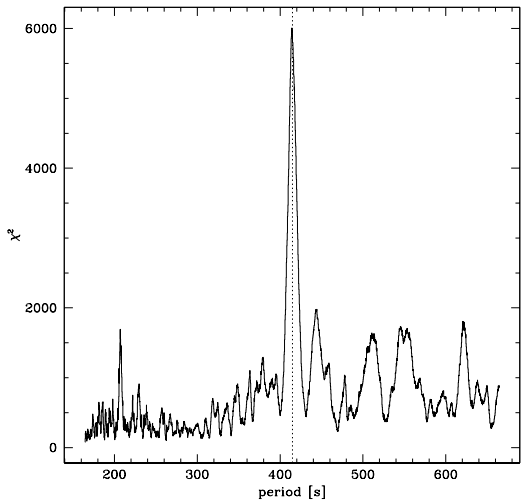


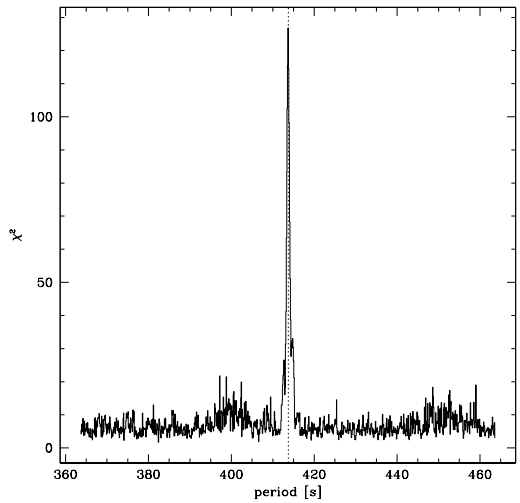


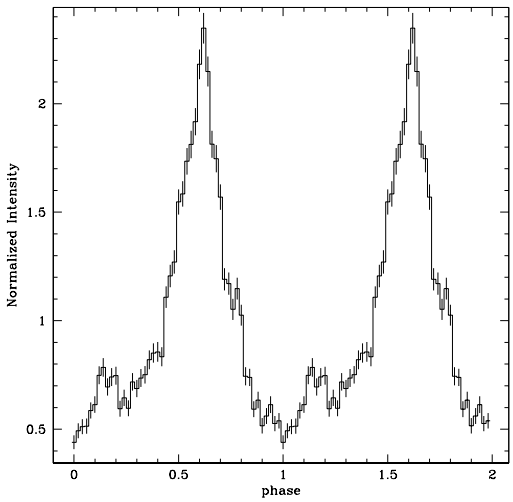


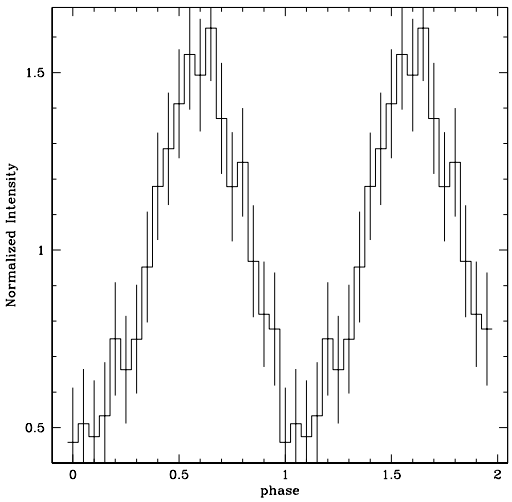


**Fig. 7.** *top:* $\chi^2$ distribution of trials periods for epoch folding search on EPIC/pn data. The best value was fitted with a Gaussian. The best period of 414.8±0.5 s is indicated with a dashed-line. *bottom:* IGR J17252−3616 pulse phase folded light curve in the 0.4–10 keV energy band obtained with the best spin period. The zero epoch is MJD 53085.55144.

**Fig. 8.** *top:* IGR J17252−3616 IBIS/ISGRI epoch folding search $\chi^2$ distribution. The best period was fitted with a Gaussian and resulted in 413.7±0.3 s (see dashed-line). *bottom:* ISGRI folded light curve built with data from revolution 106 (MJD 52877.4–52880.4). IGR J17252−3616 pulse phase folded light curve in the 20–40 keV energy band was obtained with the best spin period. The zero epoch is MJD 52877.50072.

Fig. 9. A minimum flux consistent with an eclipse is visible at phase 0. It lasts between phases 0.97–1.1 that corresponds to a lapse of time of ∼1.26 days. The normalized intensity smoothly increases from phase 0.1 to 0.3 to reach a plateau that lasts ∼3.9 days. Afterwards, the intensity gradually decreases from phase 0.7 to the start of the eclipse at phase 0.97. The *XMM-Newton* observation corresponds to phase ∼0.7.

### *4.3. Spectral analysis*

The X-ray spectral bins were grouped to have at least 100 counts per channel (see Fig. 10). This allows the use of the $\chi^2$ statistic. The spectrum is strongly absorbed at energies lower than 4 keV. An emission line at 6.4 keV and an edge at 7 keV are clearly detected. The spectra were first fitted with a simple absorbed power law and a blackbody model. In terms of

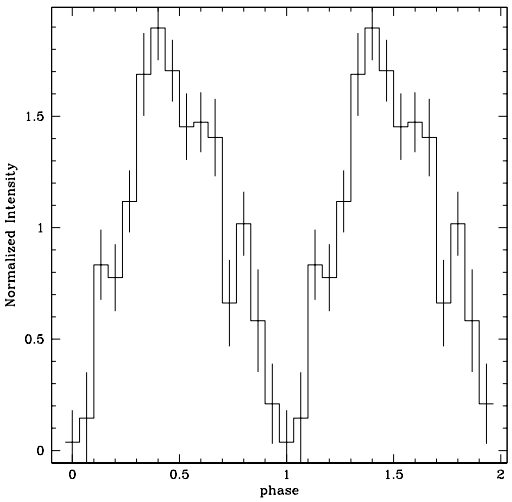


**Fig. 9.** IGR J17252−3616 orbital folded light curve in the 20–60 keV energy band was obtained with the best period of 9.72 d. The zero epoch is MJD 52671. The *XMM-Newton* observation correspond to phase ∼0.7.

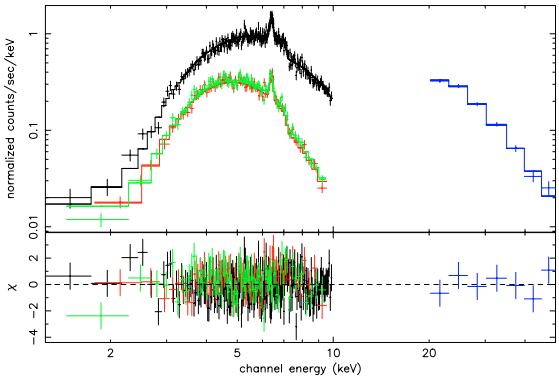


**Fig. 10.** Combined IGR J17252−3616 EPIC+ISGRI averaged spectrum. All three EPIC spectra are displayed in the X-ray band: pn (top) and MOS[12] (bottom). The ISGRI spectra is in the hard X-ray band. The source is detected up to 50 keV. CTT model is used.

reduced $\chi^2$, these simple models fitted the *XMM-Newton* data well. In order to distinguish between the two models, the EPIC and ISGRI spectra are used together.

The ISGRI spectrum was extracted from revolution 106 data when the source intensity was the strongest (see Fig. 5) and also from an average mosaic image of all visibility periods. The two spectra do not show any significant difference beside their normalisations. In the following spectral analysis, the revolution 106 source spectrum was used since it has the highest S/N.

When fitting EPIC and ISGRI spectra together, an inter calibration factor, $C_{\rm ISGRI}$, was applied to take into account the different source flux levels during the non simultaneous observations. The simple absorbed power law and blackbody models failed to fit the data between 1–50 keV. The blackbody is too narrow and the power law requires a high-energy cutoff.

A cutoff power law (CPL) was therefore chosen as a phenomenological model to fit the data. Moreover, a more physical model based on Comptonization (CTT) (Titarchuk 1994) was also adopted as suggested by other observations (Torrejón et al. 2004; Bodaghee et al. 2005; Masetti et al. 2005; Walter et al. 2005). In `Xspec`, the CPL model is defined as `cst*wabs(bbody+vphabs(cutoffpl+ga))` and CTT as `cst*wabs(bbody+vphabs(compTT+ga))`. The 6.4 keV line was fitted with a Gaussian. An absorption model was used, where the iron abundance was left as a free parameter. The soft excess at low energies was modelled with a black body. The galactic absorption is also taken into account. All the spectral parameters errors were calculated at the 90% confidence level. Parameters resulting from the spectral fitting are listed in Table 2.

The CPL model gives typical values of an accreting pulsar with a flat powerlaw, $\Gamma = 0.0 \pm 0.1$, and an energy cutoff, $E_{\rm c} = 8.2 \pm 0.4$ keV. The CTT model also fits the data well with characteristic values for the electron temperature of $kT_{\rm e} = 5.5 \pm 0.2$ keV and an optical depth of $\tau = 7.8 \pm 0.6$. In both cases, the unabsorbed flux between 2–12 keV and 13–100 keV is 2 and 5 $10^{-10}$ ergs cm$^{-2}$ s$^{-1}$, respectively.

The line centroid at 6.40 ± 0.01 keV is compatible with what is expected from cold iron. The line width is consistent with zero and was fixed for the spectral fits. The equivalent width of that line is 84 eV and was calculated considering the unabsorbed continuum.

A soft excess is required below 3 keV and was represented by a blackbody absorbed by the galactic column density (without soft excess, $\chi^2$/d.o.f.=415/376 and 420/376 for CPL and CTT models, respectively). In this case, the 1-2 keV soft X-ray flux is 1.6 or 2.0 $10^{-14}$ ergs cm$^{-2}$ s$^{-1}$ (CPL or CTT). An alternative model was also used to explain the origin of the soft X-ray excess based on the idea that the absorbing matter could only partially cover the X-ray emitting source (model `pcfabs` in Xspec). A covering factor of 0.995±0.002 could also explain the soft excess with a good fit of $\chi^2$/d.o.f. = 406/378 for CTT model (411/378 for CPL).

For phase-resolved spectroscopy with EPIC/pn, the pulse profile was cut into three phase intervals: 0.00–0.43 + 0.81–1.00 for the low intensity par;, 0.43–0.49 + 0.71–0.81 for the wings of the broad pulse; 0.49–0.71 for the pulse core. The effective exposures for each phase resolved bin are 3383 s, 894 s and 1229 s, respectively. The phase-resolved spectra were extracted and the channel bins were grouped to have at least 50 counts per channel for the low intensity part and the pulse core, and 20 counts per channel for the pulse wings. All the resulting spectra were fitted inside `Xspec` using the CTT model again combined with the ISGRI spectrum to better constrain the spectral fit. No significant variation of the spectral shape with the phase was found, excepting the change in the normalisation (see Table 3).

**Table 2.** Spectral analysis. The EPIC and ISGRI spectra were fitted together. Two models in `Xspec` were selected to fit the data. Model CPL is `constant*wabs(bbody+vphabs(cutoffpl+gaussian))` and model CTT is `constant*wabs(bbody+vphabs(compTT+gaussian))`. The galactic absorption $N_{\rm H}^{\rm gal}$ was fixed. The errors are calculated at the 90% confidence level.

| Models | Parameters | Values | Unit |
|---|---|---|---|
| model CPL | $C_{\rm ISGRI}$ | 2.6 | |
| | $N_{\rm H}^{\rm gal}$ | 1.5 | $10^{22}$ cm$^{-2}$ |
| | $kT_{\rm soft}$ | 0.5 | keV (fixed) |
| | $F_{1-2{\rm keV}}$ | 1.6 | $10^{-14}$ ergs cm$^{-2}$ s$^{-1}$ |
| | $N_{\rm H}$ | $12.8^{+0.7}_{-1.3}$ | $10^{22}$ cm$^{-2}$ |
| | $Z_{\rm Fe}$ | $1.5^{+0.2}_{-0.2}$ | $Z_\odot$ |
| | $\Gamma$ | $0.02^{+0.17}_{-0.10}$ | |
| | $E_{\rm c}$ | $8.2^{+0.4}_{-0.3}$ | keV |
| | $E_{\rm line}$ | $6.400^{+0.001}_{-0.013}$ | keV |
| | $F_{\rm line}$ | $1.9^{+0.2}_{-0.2}$ | $10^{-4}$ ph cm$^{-2}$ s$^{-1}$ |
| | unabs $F_{2-12{\rm keV}}$ | 1.5 | $10^{-10}$ ergs cm$^{-2}$ s$^{-1}$ |
| | unabs $F_{13-100{\rm keV}}$ | 5.1 | $10^{-10}$ ergs cm$^{-2}$ s$^{-1}$ |
| | $\chi^2$/d.o.f. | 401/376 | |
| model CTT | $C_{\rm ISGRI}$ | 1.7 | |
| | $N_{\rm H}^{\rm gal}$ | 1.5 | $10^{22}$ cm$^{-2}$ |
| | $kT_{\rm soft}$ | 0.5 | keV (fixed) |
| | $F_{1-2{\rm keV}}$ | 2.0 | $10^{-14}$ ergs cm$^{-2}$ s$^{-1}$ |
| | $N_{\rm H}$ | $15.3^{+1.1}_{-1.0}$ | $10^{22}$ cm$^{-2}$ |
| | $Z_{\rm Fe}$ | $1.4^{+0.3}_{-0.3}$ | $Z_\odot$ |
| | $kT_0$ | 0.1 | keV (fixed) |
| | $kT_{\rm e}$ | $5.5^{+0.2}_{-0.2}$ | keV |
| | $\tau$ | $7.8^{+0.6}_{-0.5}$ | |
| | $E_{\rm line}$ | $6.401^{+0.005}_{-0.009}$ | keV |
| | $F_{\rm line}$ | $2.1^{+0.2}_{-0.3}$ | $10^{-4}$ ph cm$^{-2}$ s$^{-1}$ |
| | unabs $F_{2-12{\rm keV}}$ | 1.7 | $10^{-10}$ ergs cm$^{-2}$ s$^{-1}$ |
| | unabs $F_{13-100{\rm keV}}$ | 4.8 | $10^{-10}$ ergs cm$^{-2}$ s$^{-1}$ |
| | $\chi^2$/d.o.f. | 401/376 | |

**Table 3.** Phase-resolved spectral analysis. We used the CTT model. All continuum and normalisation parameters were left free. A few parameters were fixed as for the average spectrum (see Table 2): $N_{\rm H}^{\rm gal} = 1.5\,10^{22}$ cm$^{-2}$, $kT_{\rm soft} = 0.5$ keV, $kT_0 = 0.1$ keV. Only pn data were used for the phase-resolved spectral analysis.

| Parameters | low intensity | pulse wings | pulse core | Unit |
|---|---|---|---|---|
| $C_{\rm ISGRI}$ | 2.6 | 1.4 | 0.9 | |
| $F_{1-2{\rm keV}}$ | 1.4 | 4.2 | 2.8 | $10^{-14}$ ergs cm$^{-2}$ s$^{-1}$ |
| $N_{\rm H}$ | $15.2^{+2.0}_{-2.2}$ | $13.7^{+2.9}_{-2.6}$ | $15.1^{+1.8}_{-1.8}$ | $10^{22}$ cm$^{-2}$ |
| $Z_{\rm Fe}$ | $1.2^{+0.6}_{-0.5}$ | $2.0^{+1.2}_{-0.8}$ | $1.6^{+0.5}_{-0.4}$ | $Z_\odot$ |
| $kT_{\rm e}$ | $5.5^{+0.2}_{-0.2}$ | $5.4^{+0.2}_{-0.2}$ | $5.5^{+0.2}_{-0.2}$ | keV |
| $\tau$ | $8.0^{+1.0}_{-0.8}$ | $8.7^{+1.5}_{-1.2}$ | $7.8^{+0.8}_{-0.7}$ | |
| $E_{\rm line}$ | $6.40^{+0.01}_{-0.02}$ | $6.42^{+0.04}_{-0.03}$ | $6.40^{+0.04}_{-0.05}$ | keV |
| $F_{\rm line}$ | $2.2^{+0.3}_{-0.3}$ | $1.6^{+0.6}_{-0.6}$ | $1.4^{+0.7}_{-0.6}$ | $10^{-4}$ ph cm$^{-2}$ s$^{-1}$ |
| unabs $F_{2-12{\rm keV}}$ | 1.2 | 2.0 | 3.4 | $10^{-10}$ ergs cm$^{-2}$ s$^{-1}$ |
| $\chi^2$/d.o.f. | 145/160 | 208/217 | 180/197 | |

Therefore, the three phase-resolved spectra were fitted with the Comptonization model and all the continuum parameters were fixed, except its normalisation, the column density, and the soft excess and the line normalisations. The results are summarized in Table 4. No significant variation of the line flux nor of the absorbing column density was observed. The unabsorbed 2–10 keV flux changes according to the pulse phase. The variations of the 1–2 keV flux are not significant once the errors are considered.

## 5. Discussion

### 5.1. X-ray counterpart

When IGR J17252−3616 was discovered in the $\gamma$-rays, it was first labelled as a new source since no other known sources lay within the ISGRI error circle of 2′. The nearest source was EXO 1722−363 at a distance of 12′. The EXOSAT source was considered to be too far to be the X-ray counterpart of IGR J17252−3616. With the improved ISGRI and EPIC po-

**Table 4.** Phase-resolved spectroscopy with all the spectral modeling parameters of model CTT except normalisations equal to the values of the average spectrum (see Table 2). Only pn data were used for the phase-resolved spectral analysis.

| phase | $N_{\rm H}$ | $F_{\rm line}$ | $F_{1-2\ \rm keV}$ | unabsorbed $F_{2-10\ \rm keV}$ | $\chi^2$/d.o.f |
|---|---|---|---|---|---|
| | $10^{22}$ cm$^{-2}$ | $10^{-4}$ ph cm$^{-2}$ s$^{-1}$ | $10^{-14}$ ergs cm$^{-2}$ s$^{-1}$ | $10^{-10}$ ergs cm$^{-2}$ s$^{-1}$ | |
| low intensity | $15.3^{+0.7}_{-0.7}$ | $2.1^{+0.4}_{-0.3}$ | $1.5^{+1.5}_{-1.2}$ | 0.9 | 147/164 |
| pulse wings | $15.8^{+1.3}_{-0.7}$ | $1.5^{+0.7}_{-0.6}$ | $6.8^{+0.4}_{-4.9}$ | 1.4 | 214/221 |
| pulse core | $15.5^{+0.5}_{-0.5}$ | $1.6^{+0.5}_{-0.7}$ | $2.8^{+2.2}_{-2.2}$ | 2.4 | 181/201 |

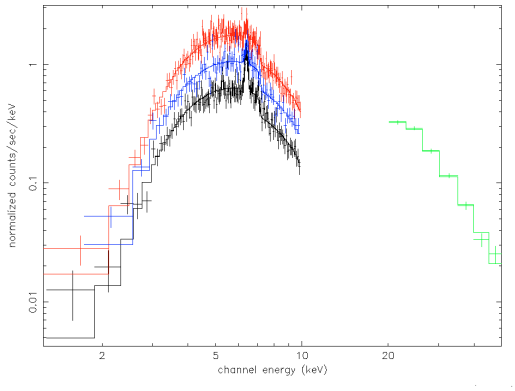


**Fig. 11.** EPIC/pn phase-resolved spectra. Only the pn spectra of the three phase intervals are displayed in the X-ray band: low intensity (bottom), pulse wings (middle) and pulse core (top). The ISGRI spectrum in the hard X-ray band is not phase resolved.

sition, the source still lies 12′ away from the given EXOSAT position with an accuracy of 9′ (Warwick et al. 1988).

Tawara et al. (1989) also gave a new position within a box of 2° × 4° that is 20′ away from the EPIC position. They discovered a pulsation of 413.9 s. The pulse profile shows a single peak that is independent of the energy and a high pulse fraction of 80%. The spectrum is heavily absorbed at low energy and shows a very hard shape plus an emission line at 6.2±0.5 keV. Even if the position given by all these studies is quite far from the accurate IGR J17252−3616 position, the informations given by Tawara et al. (1989) strongly confirm that the same source is seen since the same features are seen in this study.

From archival data of RXTE/PCA taken between 1999 and 2003, Markwardt & Swank (2003) reported an orbital period of 9.737±0.004 days, consistent with the lower limit given by Takeuchi et al. (1990). This result with *RXTE* was confirmed by Corbet et al. (2005). Their best orbital period is 9.741±0.004 d. They also find a pulse period of 413.88553±0.00001 s, equivalent to the previous studies and with the measurement presented here.

### 5.2. Temporal modulations

In this paper, periodic or episodic time variations were searched for on time scales of seconds to days. First, the two years long ISGRI 20–60 keV light curve indicates that the source is persistent. However, variations in the $\gamma$-ray count rates larger than 50 were observed for this system. Four flares were detected on a time scale of hours.

An orbital period of 9.72±0.09 days was derived that is consistent with the one derived by Corbet et al. (2005). The eclipse duration is a bit lower in the ISGRI data than in the *RXTE* data (∼1.3 days and ∼1.7 days respectively). Both orbital profile at 2–10 keV and 20–60 keV are consistent. The progressive decrease of the intensity before entering the eclipse between phase 0.7 and 0.97 can be explained by the changing hydrogenic column density that increases from $\sim 10^{23}$ cm$^{-2}$ to $\sim 10^{24}$ cm$^{-2}$. This larger amount of matter along the line of sight implies that a larger part of the flux is scattered.

Similar pulsations were found in EPIC/pn and ISGRI data: 414.8±0.5 s and 413.7±0.3 s, respectively. The EPIC and ISGRI pulsations are consistent with the one detected by Tawara et al. (1989) and Corbet et al. (2005). Therefore, the spin period did not change significantly in the last 17 years. Takeuchi et al. (1990) also searched for pulse period changes and did not find any significant spin variation in Ginga data. The neutron star seems to not accrete kinetic momentum, which suggests accretion from a stellar wind.

With such spin pulsation and orbital period, the source is situated in the underfilled Roche-Lobe supergiant region in the $P_{\rm spin}$ vs $P_{\rm orb}$ Corbet diagram (Corbet 1986). Together with the fact that the source is persistent and shows non-periodic flares with different intensities, this strongly suggests that IGR J17252−3616 is a high mass system fed by stellar wind with the primary star being a supergiant.

### 5.3. Spectra

The EPIC and ISGRI spectra that could be well fitted with a flat power law ($\Gamma \sim 0$) and an energy cutoff at $E_{\rm c} = 8.2$ keV are typical of X-ray pulsars (White et al. 1995). Three spectral features can give more clues about the physics of this object: the apparent soft excess, the huge hydrogen column density and the cold Fe K$\alpha$ line.

A soft excess is detected below 2 keV. Such soft X-ray excess has been observed in other HMXB (Hickox et al. 2004). It could originate in X-ray scattering or partial ionization in the stellar wind (White et al. 1995). The spectrum at soft X-rays could also be explained by a partial covering of the X-ray source by the absorbing matter. In the latter case, pulsations at soft X-rays would be expected. The 0.4–2 keV light curve was extracted and folded using the same ephemeris and period used to fold the 0.4–10 keV light curve. Then, it was compared to a constant model with $\chi^2$/d.o.f. ∼ 57/50 and the 0.4–10 keV pulse profile with $\chi^2$/d.o.f. ∼ 54/50. Both models are compati-

ble with the 0.4–2 keV folded light curve. However, the number of events gathered below 2 keV is too poor to decide if the soft excess is pulsating or not.

The absorbing column density was estimated at 13–15 $10^{22}$ atoms cm$^{-2}$ (model CPL-CTT) that is ten times larger than expected on the line of sight $N_{\rm H}$ = 1.5 $10^{22}$ atoms cm$^{-2}$. This high absorption could be explained by the stellar wind expelled by the primary star that surrounds the neutron star. During the *XMM-Newton* observation, the column density did not vary with the pulse. The fact that the amount of matter did not change noticeably during the 10 ks *XMM-Newton* observation could indicate that the surrounding matter is stable on this time scale. However, other values of the column density were reported at different epochs by Tawara et al. (1989), Takeuchi et al. (1990) and Corbet et al. (2005). The column density has been observed to increase up to $10^{24}$ atoms cm$^{-2}$ in the past. This could be related to the neutron star moving along the orbit (Tawara et al. 1989; Corbet et al. 2005). Therefore, the matter does not homogeneously surround the binary system. Instabilities in the stellar wind of the companion star could also be responsible for this evolving absorption. However, in Corbet et al. (2005), the column density seems to be linked to the orbital phase where the highest values correspond to the exit of the eclipse and the lowest ones when the source is in front of the companion star. The absorption is therefore intrinsic to the binary system.

The 6.4 keV Fe K$\alpha$ line is detected. The Fe K$\alpha$ line flux does not vary with the pulse phase (see Table 4). Therefore, either the matter responsible for the fluorescence is homogeneously distributed around the source or the thickness of the shell emitting the fluorescence is larger than 1.2 $10^8$ km around the accreting system. The Fe K$\alpha$ line energy is $6.401^{+0.005}_{-0.009}$ keV (CTT model) and corresponds to iron that is at most 12 times ionized (House 1969). An upper limit of the ionization parameter can be estimated as $log(L/nR^2) < 1$, where $L$ is the luminosity, $n$ the gas density, and $R$ is the distance from the ionizing continuum source to the inner shell surface (Kallman et al. 2004). Since $nR \sim N_{\rm H}$, the distance of the fluorescence source from the X-ray source is larger than $10^7$ km. The values derived for the hydrogen column density, the equivalent width, and the estimated over abundance of iron are compatible with a spherical distribution of matter around the source (Matt 2002).

Considering a typical luminosity of an active accretion-powered pulsars of 1.2 $10^{36}$ ergs s$^{-1}$ (Bildsten et al. 1997), the distance of IGR J17252−3616 can be estimated as 7 kpc, close to the galactic centre.

## 6. Conclusions

IGR J17252−3616 is the hard X-ray counterpart of EXO 1722−363, and the most accurate source position to date has been provided here. IGR J17252−3616 has been monitored by *INTEGRAL* during two years for a total exposure of 6.5 Ms and *XMM-Newton* performed a follow-up observation of 3 hours. The source is persistent with an average 20–60 keV flux of 6.4 mCrab. Four flares lasting less than one day were detected by *INTEGRAL*. The source's count rate varies by a factor larger than 50 on such timescales. A pulsation has been detected in both EPIC and IBIS/ISGRI data of 414.8±0.5 s and 413.7±0.3 s, respectively. There is no evidence of spin period variation. An orbital period of 9.72±0.09 d is also found in IBIS/ISGRI data. The spectral shape is typical for an accreting pulsar except that a huge intrinsic absorption and a cold iron fluorescence line are detected. The absorbing column density and cold iron line do not vary with the pulse period. The absorbing fluorescent material is distributed around the neutron star in a shell comparable in size with the orbital radius. With the accurate X-ray position, we provide a likely infra-red counterpart within the X-ray error box: 2MASS J17251139−3616575. The observed features of the source suggest that it is a wind-fed accreting pulsar. This object is a new member of the growing family of heavily-obscured HMXB systems that have been recently discovered with *INTEGRAL*. The source is located ∼7 kpc away, near the Galactic Centre.

*Acknowledgements.* Based on observations obtained with the ESA science missions *INTEGRAL* and *XMM-Newton*. The *INTEGRAL* and *XMM-Newton* instruments and data centres were directly funded by ESA member states and the USA (NASA). JAZH thanks J.Rodriguez for his useful comments and N.Produit for his help with `ii_light`.

## References

Bildsten, L., Chakrabarty, D., Chiu, J., et al. 1997, ApJS, 113, 367
Bird, A. J., Barlow, E. J., Bassani, L., et al. 2004, ApJ, 607, L33
Bodaghee, A., Walter, R., Zurita Heras, J. A., et al. 2005, accepted for publication in A&A
Corbet, R. H. D. 1986, MNRAS, 220, 1047
Corbet, R. H. D., Markwardt, C. B., & Swank, J. H. 2005, ApJ, in press
Courvoisier, T. J.-L., Walter, R., Beckmann, V., et al. 2003, A&A, 411, L53
Cutri, R. M., Skrutskie, M. F., van Dyk, S., et al. 2003, VizieR Online Data Catalog, 2246, 0
Gros, A., Goldwurm, A., Cadolle-Bel, M., et al. 2003, A&A, 411, L179
Hickox, R. C., Narayan, R., & Kallman, T. R. 2004, ApJ, 614, 881
Hill, A. B., Walter, R., Knigge, C., et al. 2005, A&A, 439, 255
Horne, J. H. & Baliunas, S. L. 1986, ApJ, 302, 757
House, L. L. 1969, ApJS, 18, 21
Jansen, F., Lumb, D., Altieri, B., et al. 2001, A&A, 365, L1
Kallman, T. R., Palmeri, P., Bautista, M. A., Mendoza, C., & Krolik, J. H. 2004, ApJS, 155, 675
Labanti, C., Di Cocco, G., Ferro, G., et al. 2003, A&A, 411, L149
Lebrun, F., Leray, J. P., Lavocat, P., et al. 2003, A&A, 411, L141
Lund, N., Budtz-Jørgensen, C., Westergaard, N. J., et al. 2003, A&A, 411, L231
Markwardt, C. B. & Swank, J. H. 2003, The Astronomer's Telegram, 179, 1
Mas-Hesse, J. M., Giménez, A., Culhane, J. L., et al. 2003, A&A, 411, L261
Masetti, N., Orlandini, M., Dal Fiume, D., et al. 2005, astro-ph/0508451, accepted for publication in å
Matt, G. 2002, MNRAS, 337, 147
Patel, S. K., Kouveliotou, C., Tennant, A., et al. 2004, ApJ, 602, L45
Press, W. H. & Rybicki, G. B. 1989, ApJ, 338, 277
Rodriguez, J., Tomsick, J. A., Foschini, L., et al. 2003, A&A, 407, L41

Strüder, L., Briel, U., Dennerl, K., et al. 2001, A&A, 365, L18
Takeuchi, Y., Koyama, K., & Warwick, R. S. 1990, PASJ, 42, 287
Tauris, T. M. & van den Heuvel, E. P. J. 2005, Formation and Evolution of Compact Stellar X-ray Sources (Compact Stellar X-Ray Sources, eds. W.H.G. Lewin and M. van der Klis, Cambridge University Press), in press
Tawara, Y., Yamauchi, S., Awaki, H., et al. 1989, PASJ, 41, 473
Titarchuk, L. 1994, ApJ, 434, 570
Torrejón, J. M., Kreykenbohm, I., Orr, A., Titarchuk, L., & Negueruela, I. 2004, A&A, 423, 301
Turner, M. J. L., Abbey, A., Arnaud, M., et al. 2001, A&A, 365, L27
Ubertini, P., Lebrun, F., Di Cocco, G., et al. 2003, A&A, 411, L131
Vedrenne, G., Roques, J.-P., Schönfelder, V., et al. 2003, A&A, 411, L63
Walter, R., Bodaghee, A., Barlow, E. J., et al. 2004, The Astronomer's Telegram, 229, 1
Walter, R., Rodriguez, J., Foschini, L., et al. 2003, A&A, 411, L427
Walter, R., Zurita Heras, J. A., Bassani, L., et al. 2005, submitted to A&A
Warwick, R. S., Norton, A. J., Turner, M. J. L., Watson, M. G., & Willingale, R. 1988, MNRAS, 232, 551
White, N. E., Nagase, F., & Parmar, A. N. 1995, X-ray binaries (Cambridge Astrophysics Series, Cambridge, MA: Cambridge University Press, —c1995, edited by Lewin, Walter H.G.; Van Paradijs, Jan; Van den Heuvel, Edward P.J.), 1–57
Winkler, C., Courvoisier, T. J.-L., Di Cocco, G., et al. 2003, A&A, 411, L1

## 6.7 Future perspectives and open questions

The GCDE+GPS *INTEGRAL* monitoring will continue in the future, so the source will still be observed several times. Moreover, as seen in Sect. 9.4, there are also other observations that catch the source in their FOV.

The object is an eclipsing system with known orbital parameters (Corbet et al. 2005b; Zurita Heras et al. 2005). This rare characteristic represents an opportunity to observe spectral variability before/during/after the eclipse. This would allow to study the environment of the compact object. Possible variations of the intrinsic absorption and the fluorescence iron lines along the orbit can help to better determine the distribution of matter around the neutron star : a homogeneous distribution of the matter against a clumpiness scenario. Therefore, we submitted a proposal for the next *XMM-Newton* AO round of observations.

This source still has some mysteries to reveal.

# Chapter 7
# IGR J16358−4726 OBSERVATIONS WITH *INTEGRAL* AND *Chandra*

In this chapter, we describe in detail the *INTEGRAL* analysis of IGR J16358−4726. This source is located near the galactic plane in the Norma Arm region, a field which was extensively observed with the *INTEGRAL* satellite during part of the CP.

We first describe the discovery of IGR J16358−4726 and present the few other detections reported in the literature. Then, we describe the *INTEGRAL* data analysis. The source was also studied jointly with two other X-ray missions, *Chandra* and *XMM-Newton* and the results are presented here.

## 7.1 Discovery and detection: a review of IGR J16358−4726

IGR J16358−4726 was first detected with the IBIS imager on March 19, 2003, during an outburst of the source. It was located at the position R.A. (2000.0)=16h35m.8 and Dec.=$-47^{\rm o}\,26'$ with an uncertainty of $1.5'$. It is a variable source on timescales of hours with an average flux of 50 mCrab in the 15–40 keV energy band and 20 mCrab in the 40–100 keV energy band (Revnivtsev et al. 2003b).

Looking into archival data of previous high energy missions, Revnivtsev et al. (2003a) reported that a faint X-ray source was located at a position consistent with that of *INTEGRAL* in an *ASCA* observation on February 26, 1999, and in a *BeppoSAX* observation on August 8, 1999, while other observations of the same field in 1998 and 2000 did not result in any detection at an upper limit of $\sim 10^{-13}$ ergs cm$^{-2}$ s$^{-1}$. In both detections, photo-electric absorption was important, with a hydrogen column density of $\sim 10^{23}$ cm$^{-2}$ and a 2–10 keV unabsorbed flux around a few $10^{-12}$ ergs cm$^{-2}$ s$^{-1}$ (Revnivtsev et al. 2003a; Patel et al. 2004).

After its discovery with *INTEGRAL*, this transient source was serendipitously observed by *Chandra* on March 24, 2003, during an observation of SGR 1627-41 (Kouveliotou et al. 2003). The accuracy of the source location was improved : the new position is R.A. (2000.0)=16h35m53s.8 and Dec.=$-47^{\rm o}\,25'\,41''.1$, with an uncertainty of $0''.6$. Kouveliotou et al. (2003) reported a bright IR source listed in the 2MASS catalogue located $1''.7$ away : 2MASS J16355369-4725398. IGR J16358−4726 showed a hard ($\Gamma = 0.5$) and highly absorbed ($N_{\rm H} = 3.3\,10^{23}$ cm$^{-2}$) power law spectrum. An emission line feature at ∼6.4 keV was also visible. The 2–10 keV unabsorbed flux was $1.7\,10^{-10}$ ergs cm$^{-2}$ s$^{-1}$. Strong pulsa-

tions with a period of (5880±50) s were also detected in the X-ray light curve (Kouveliotou et al. 2003; Patel et al. 2004).

A Target of Opportunity (ToO) was also triggered on March 25, 2003, with the *RXTE* satellite. The results confirmed those of *Chandra* concerning the high photo-electric absorption ($N_{\rm H} = (4 \pm 1)\, 10^{23}$ cm$^{-2}$) and the hardness of this source ($\Gamma = 0.1$). Due to the galactic ridge emission, the line feature was impossible to detect (Revnivtsev 2003).

IGR J16358−4726 was observed again with *Chandra* on April 21, 2003. Both *Chandra* observations were presented in Patel et al. (2004). The source is weaker by a factor of 15 during this second observation. The 1.6 h pulsation was detected in both cases with no apparent variation. The pulse fraction remained constant : (37±8)% and (39±2)%, respectively. The spectra were well described by an absorbed hard power law. During this second observation, the absorption was lower than during the first observation, and the Fe K$\alpha$ line at 6.4 keV was not detected anymore. Two interpretations for this system were proposed. It could be either a transient HMXB with a "long" spin period of 1.6 h, and a characteristic hard spectrum and strong absorption due to the companion star wind; but how could the lack of spin up be explained? Or, it could be a LMXB with a "short" orbital period of 1.6 h, but what would the origin of the dense material provoking this huge absorption and iron fluorescence line be?

This source was also listed in the first ISGRI survey catalog of Bird et al. (2004) at the position R.A. (2000.0)=16h35m57.60 and Dec.=$-47^{\rm o}\, 24'\, 25''2$, with an uncertainty of $0'.72$. The average 20–40 and 40–100 keV fluxes were 4.7 and 3.0 mCrab, respectively.

A programme of radio observations of the IGR sources was undertaken by Pandey et al. (2005a,b) with the Giant Meterwave Radio Telescope (GMRT). IGR J16358−4726 was observed on July 31, 2004, at 0.61 GHz. No radio emission was detected with an upper limit of $S_\nu \sim$7.50 mJy.

Recent observations (September 22, 2004) of SGR 1627-41 with *XMM-Newton* revealed IGR J16358−4726 with the faintest 2–10 keV flux ever estimated of $5.4\, 10^{-13}$ ergs cm$^{-2}$ s$^{-1}$. The flux is a factor 5 lower than the one from the previous *ASCA* and *BeppoSAX* detections.

## 7.2 *INTEGRAL* analysis of IGR J16358−4726

In this section, we describe the full *INTEGRAL* data analysis performed on IGR J16358−4726 : the available observations, image creation, timing analysis and, finally, spectral analysis. OSA 4.2 and 5.0 were used throughout the analysis.

### 7.2.1 Monitoring of IGR J16358−4726

As described earlier, IGR J16358−4726 is a transient source that was detected in revolution 52 and faded away a few days later. No other detections were reported with *INTEGRAL* after its decay one week later. The source is located in the Norma Arm region, near the galactic plane, which is a field covered regularly thanks to the GCDE and GPS programmes.

**Table** 7.1: Summary of IGR J16358−4726 positions

| Mission | Observation Date UTC | R.A. [h m s] | Dec. [° ′ ″] | Uncertainty ″ |
|---|---|---|---|---|
| *ASCA* | 26 February 1999 | 16 35 53.0 | −47 25 18.0 | 48 |
| *BeppoSAX* | 8 August 1999 | 16 35 55.0 | −47 26 00.0 | 48 |
| *INTEGRAL* | 19 March 2003 | 16 35 48.0 | −47 26 00.0 | 90 |
| *INTEGRAL* | 19 March 2003 | 16 35 52.5 | −47 25 16.0 | 36 |
| *Chandra* | 24 March 2003 | 16 35 53.8 | −47 25 41.1 | 0.6 |
| *INTEGRAL* | 28 Feb.–10 Oct. 2003 | 16 35 57.6 | −47 24 25.2 | 43 |

As for IGR J17252−3616, there is thus a huge amount of ISGRI data available[14].

The *INTEGRAL* data set was similar to that of IGR J17252−3616[15], and contained public data obtained until MJD 52928.3 and core programme data obtained until MJD 53341.1. A total exposure of 4.3 Ms was accumulated at the source position. Table 1 of our paper (presented in Sect. 7.3) lists the source visibility periods, and also lists for each of them the fraction of time when the source was effectively observed in the partially-coded field of view (PCFOV). Revolutions that had net exposure times below 1 ks were discarded for the data analysis. This corresponds to revolutions in which the source crossed the FOV far from the centre during only a few pointings. These revolutions were: 56, 61, 63, 164, 169, 179, 183, 241, 243 and 244.

### 7.2.2 Image creation and source position

The data were reduced with OSA 4.2 in the same way as for IGR J17252−3616 (see Chapter 6). We produced images for each ScW, and then mosaic images for each revolution in two energy bands : 20–60 and 60–150 keV. The source was detected only in four almost consecutive revolutions belonging to the 1st GCDE : 52, 54, 55 and 57 in the 20–60 keV energy range (see Fig. 7.1). Looking at the other GCDE mosaic images (by grouping revolution mosaic images) (see Fig. **??**), the source was not detected. There was no detection at energies higher than 60 keV.

The source brightest epoch occurred during revolution 52 with an average count rate of (5.4±0.1) counts $s^{-1}$ and a significance of 47. We used that mosaic to extract the best source position at R.A. (2000.0) = $16h35m52.5s$ and Dec. = $-47^{o}25'16''$, with an uncertainty of $20''$ (including a $10''$ systematic error due to the instrument misalignment (see Fig. 7.1). However, the systematic errors coming from the image reconstruction and proportional to the source significance is higher than the statistical one : $\sim 0.6'$ for a S/N of 47 (Gros et al. 2003). This position is consistent with the ones previously known (see Table 7.1 for a summary).

[14]Both sources are separated by 12°, which is less than the ISGRI FOV size. Therefore, we ran the analysis for both sources at once, selecting all the pointings for which at least one of the two sources was located within the ISGRI PCFOV.

[15]IGR J17252−3616 and IGR J16358−4726 are separated by 10° that is less wide than the IBIS FOV. Therefore, many pointings contain both sources within their limits.

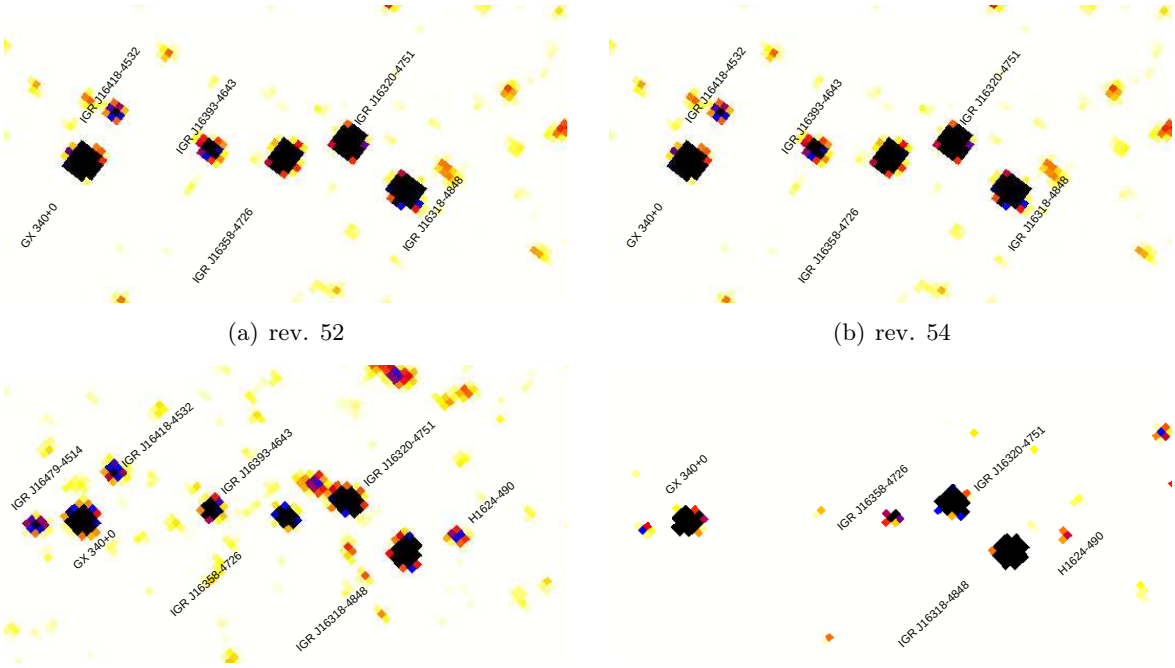


(a) rev. 52 (b) rev. 54

(c) rev. 55 (d) rev. 57

**Figure** *7.1: Revolution mosaic image in the 20–60 keV energy range. The source is very bright in revolution 0052 and slowly fades away. It is marginally detected in rev. 0057.*

### 7.2.3 Timing analysis

As for IGR J17252−3616, the mosaic images at the revolution level with no detection of IGR J16358−4726 were grouped together when close in time, in order to increase the net exposure and to decrease the background level. Based on the individual GCDE mosaic images, we already suspected that only flux upper limits would be available. The 20–60 keV light curve was completed with $3\sigma$ upper flux limits (see Equ. 10.8) when no detection was available (see Fig. 7.2).

The source shows a clear transient behaviour as the field was regularly covered over two years. It was detected only with *INTEGRAL* during that outburst. IGR J16358−4726 was bright for 2.5 weeks (see Table 2 of our paper [PZSal06]), and faded away beyond the ISGRI sensitivity.

Zooming on the visible period, the 20–60 keV light curve was studied in more details (see Fig. 7.3) which gives one point per pointing. The source flared up to 10 counts $s^{-1}$ in a few individual pointings. It represents a flux higher by a factor of 100 when compared to the lowest flux upper limit estimated from the mosaic of the revolutions before revolution 52 (see Fig. 7.2) in a lapse of time of ∼5 days. In revolution 52, the source seemed to show two mean flux states : a medium around 4–5 counts $s^{-1}$, and a bright one around 9–10 counts $s^{-1}$.

A 50 s binned light curve was extracted for the first part of revolution 52, for which there are no gaps and the source was at the brightest level. In Fig. 7.4, the 20-60 keV rebinned (500 s) light curve clearly shows the 1.6 h modulation discovered by *Chandra*.

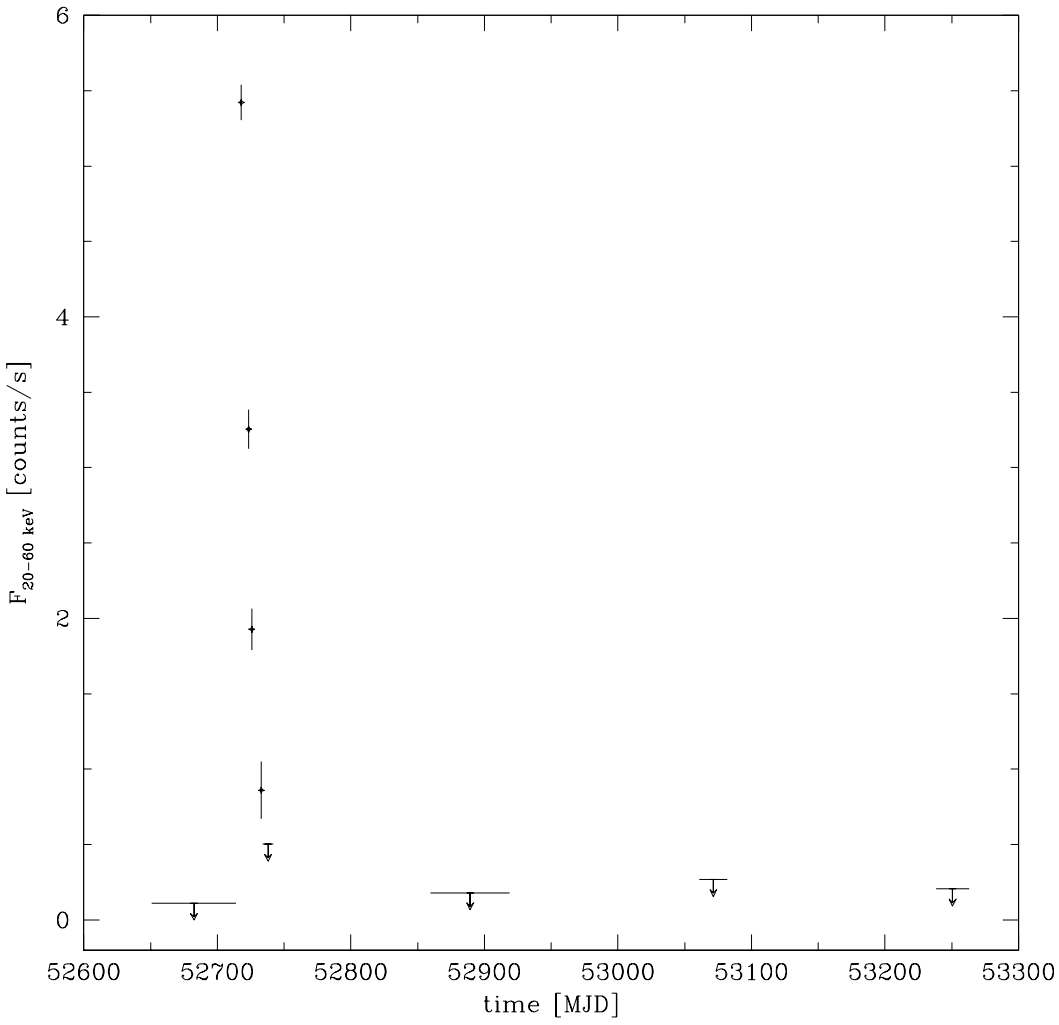


**Figure** *7.2: Long-term 20–60 keV light curve of IGR J16358−4726. Each detection point corresponds to one revolution. The upper limits are at the 3σ level. Consecutive revolutions were grouped together when there was no detection.*

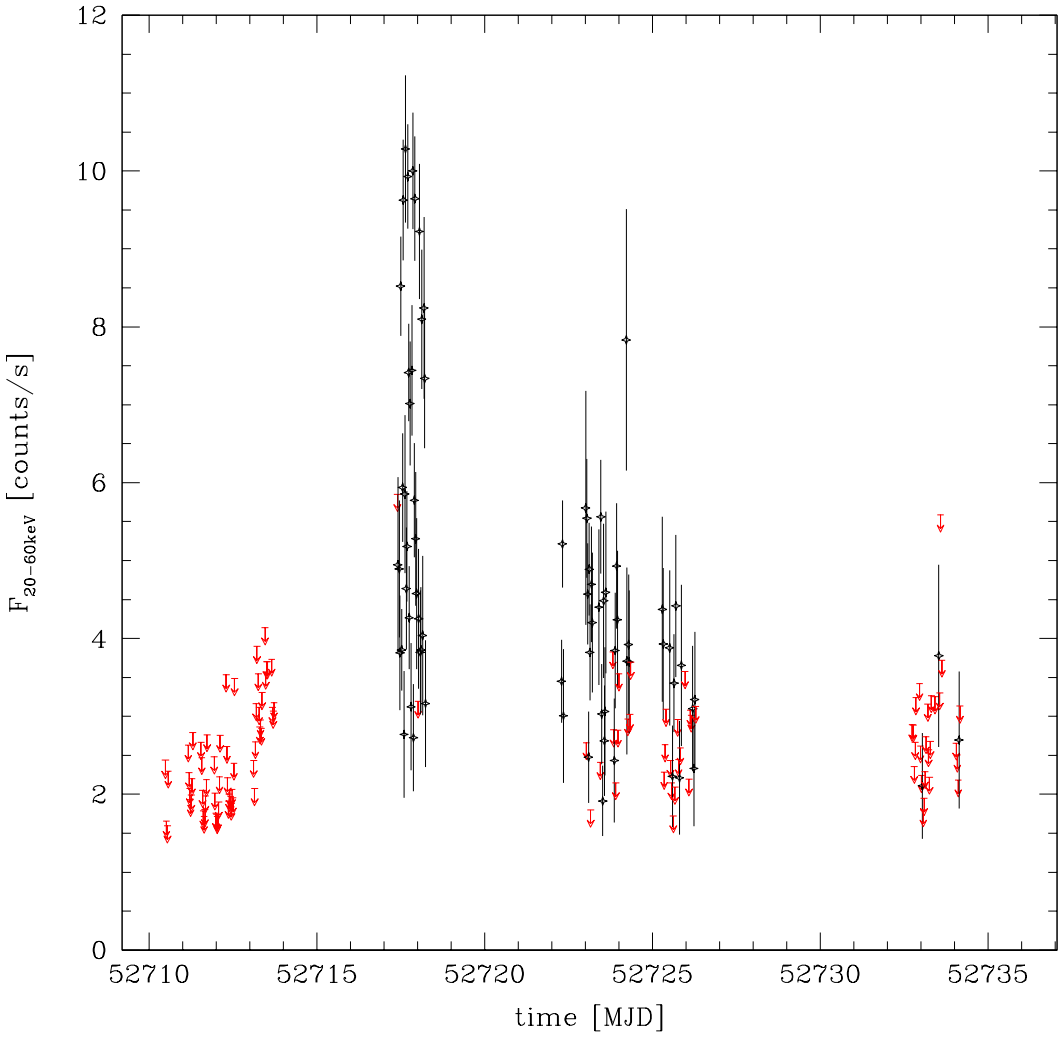


**Figure** *7.3: 20–60 keV light curve of IGR J16358−4726 from revolution 51 until revolution 57. The upper limits are at the 3σ level. The bright outburst corresponds to revolution 52.*

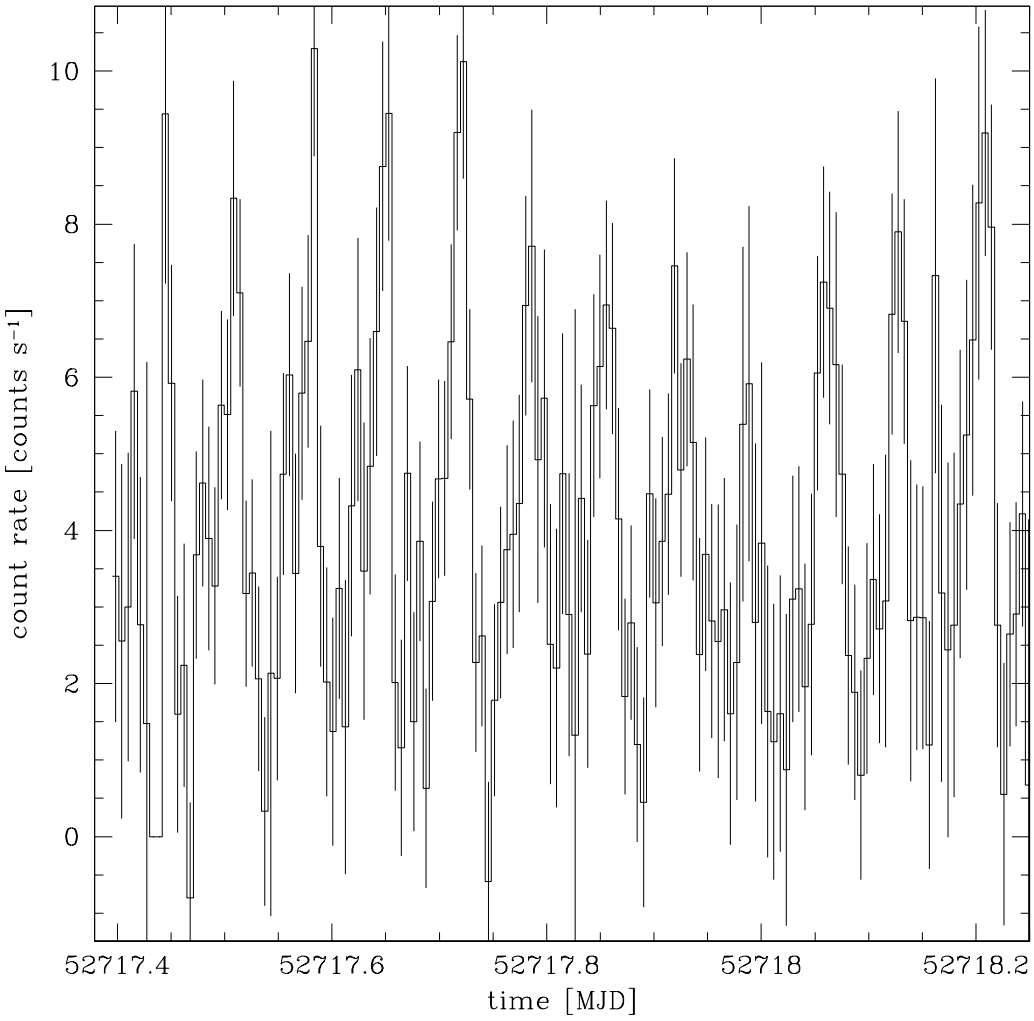


**Figure** *7.4: 20-60 keV rebinned (500 s) light curve of IGR J16358−4726 for revolution 52 only.*

**Table** 7.2: Summary of the found periods. The pulsation is not detected in rev. 0057.

| Revolution | Period s | Error s |
|---|---|---|
| 0052 | 5981 | 156 |
| 0054 | 5914 | 110 |
| 0055 | 5907 | 142 |
| 0057 | 54348 | 32603 |

We built Lomb-Scargle periodograms for each individual revolution (see Fig. 7.5). The 6000 s modulation peak is clearly visible for revolution 0052, but slowly disappears in the next revolutions until it completely disappears in revolution 0057. The periods found in each revolution are listed in Table 7.2. No variation of the period is noted with the Lomb-Scargle periodogram. The period is 5981±156 s in revolution 0052, and it is a bit lower in next revolutions : 5914±110 s (rev. 54) and 5907±142 s (rev. 55).

The period of revolution 0052 being the best detection, the value was refined with the epoch-folding search method computing the $\chi^2$distribution of trial periods using the `Xronos` tool `efsearch` (see Fig. 7.6). The best period was found fitting a Gaussian on the $\chi^2$distribution : P=5974 s. For revolution 52, the ephemeris is :

$$\mathrm{MJD}\, T = \mathrm{MJD}\, 52717.40046 + n \times \frac{5974\,\mathrm{s}}{86400} \tag{7.1}$$

where $n$ is the cycle number.

Light curves were extracted in three energy bands : 20–30, 30–45, and 45–60 keV. They were folded over the 5974 s period (see Fig. 7.7). The pulse profile is clearly not energy dependent. It has a broad maximum between phases 0.45 and 0.75, but remains constant otherwise. No evident structure is observed except this step in intensity. The pulse fraction $P_\mathrm{f}$ defined as

$$P_\mathrm{f} = \frac{I_{max} - I_{min}}{I_{max} + I_{min}} \tag{7.2}$$

reaches (62±13) % in the 20–30 keV energy band. It can also be noted that in the 30–45 keV energy range, the drop after the high intensity step is less sharp than in the 20–30 keV energy range. Over 45 keV, the signal-to-noise ratio was not high enough to detect the pulsation.

### 7.2.4 Spectral analysis

Average spectra were extracted for each revolution where the source was detected (see Fig. 7.8). The source is just marginally detected in revolution 57.

The hard X-ray spectrum of rev. 52 is fitted with simple phenomenological models (power law, black body, power law with a cutoff). A fixed absorption was also added as the source has been observed with *Chandra* and significant absorption at low energies was found of $N_\mathrm{H} = 33\,10^{22}$ cm$^{-2}$ (Patel et al. 2004). The fitting led to poor results. The $\chi^2_\nu$is higher than 2 in all cases apart from the absorbed power law with energy cutoff : $\Gamma = 0.8^{+0.8}_{-1.1}$, $E_\mathrm{cut} = 14^{+4}_{-3}$ and $\chi^2_\nu$=0.71 (4 dof). The unabsorbed 20–50 keV flux is $4\,10^{-10}$ ergs cm$^{-2}$ s$^{-1}$. The tentative fitting on the other two revolutions spectra led to poor statistical results.

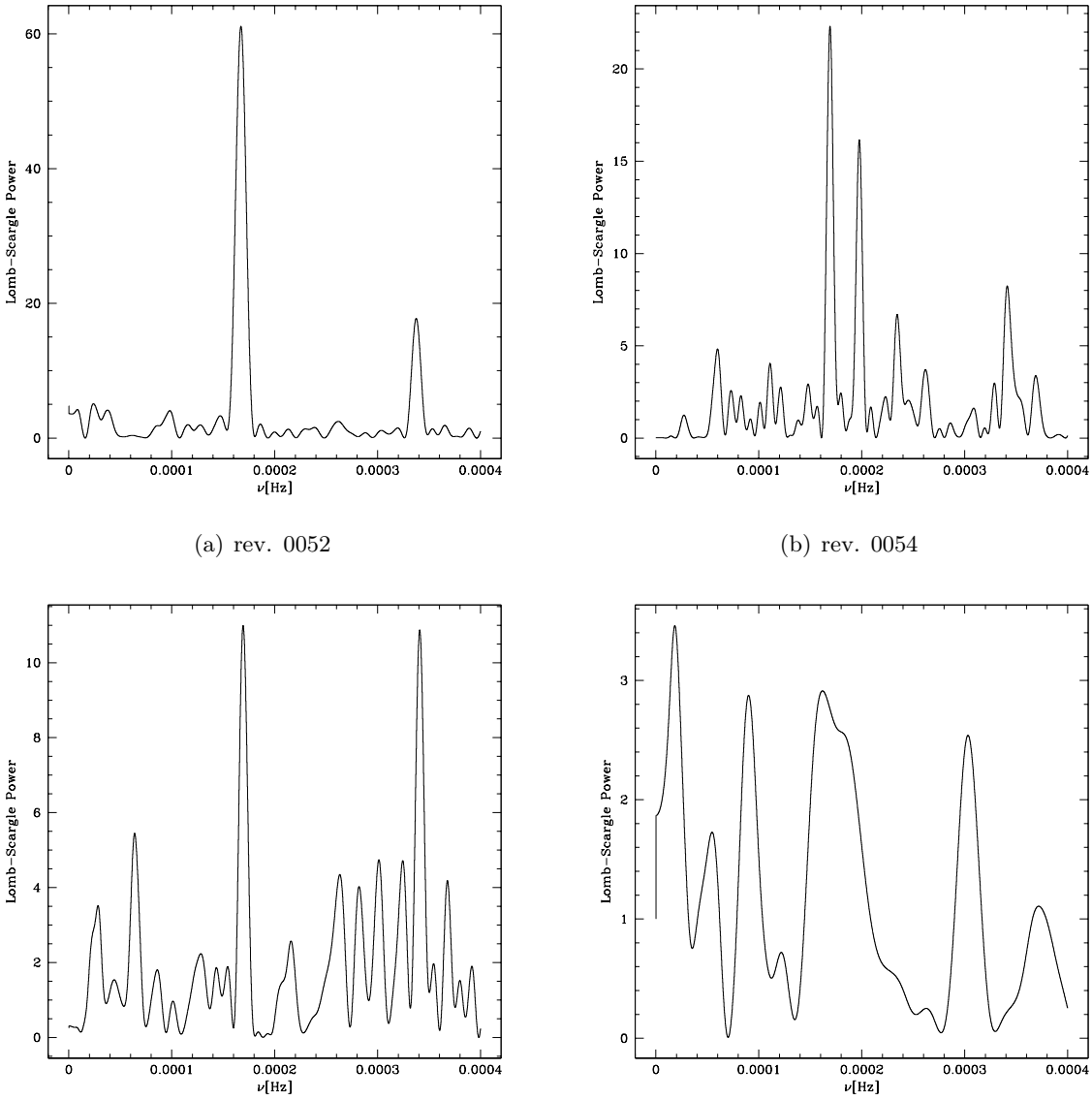


(a) rev. 0052

(b) rev. 0054

(c) rev. 0055

(d) rev. 0057

**Figure** *7.5: Lomb-Scargle periodogram for the 4 revolutions in which IGR J16358−4726 has been detected. 5981±156 s (rev. 52), 5914±110 s (rev. 54), 5907±142 s (rev. 55) and none for rev.0057.*

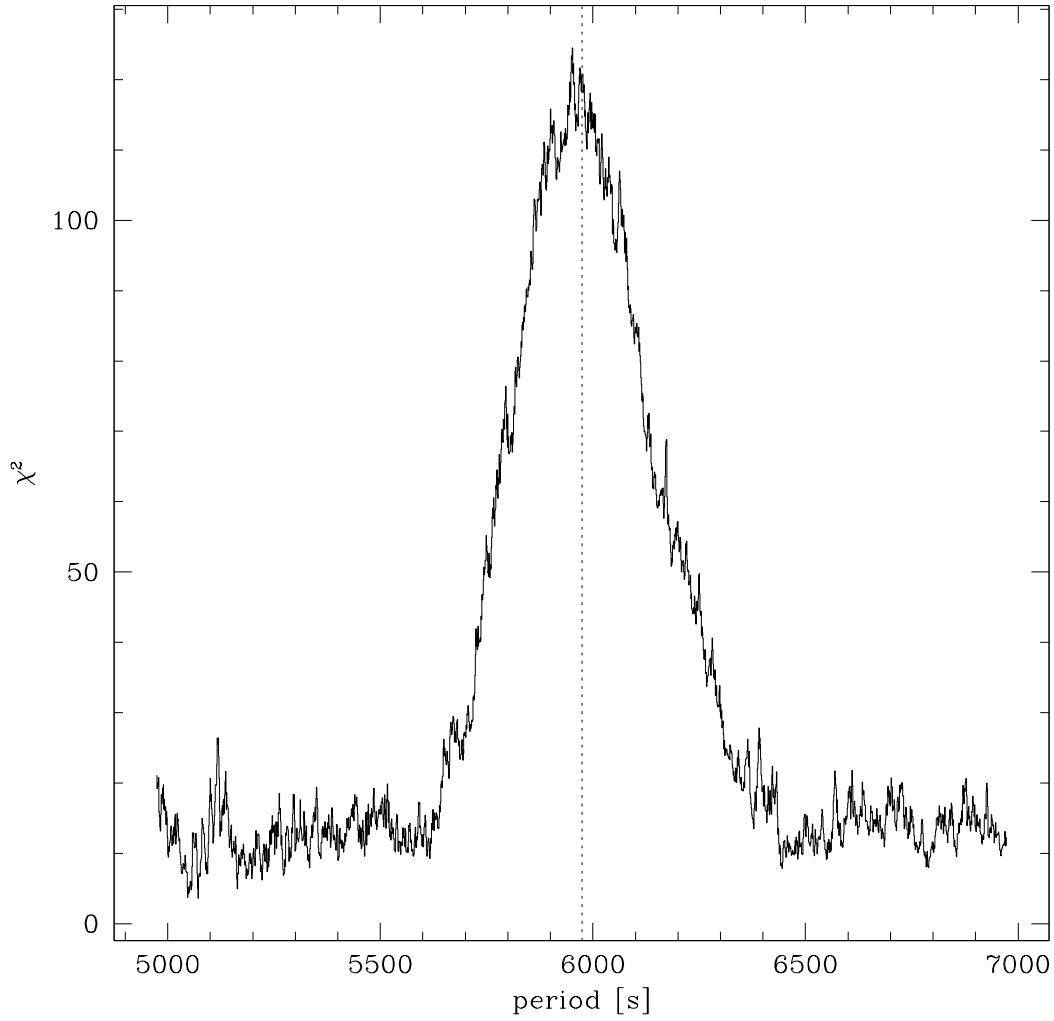


**Figure** *7.6: $\chi^2$ distribution of trial periods using the epoch-folding search method for IGR J16358−4726. The best value (fitting a Gaussian) is 5974 s.*

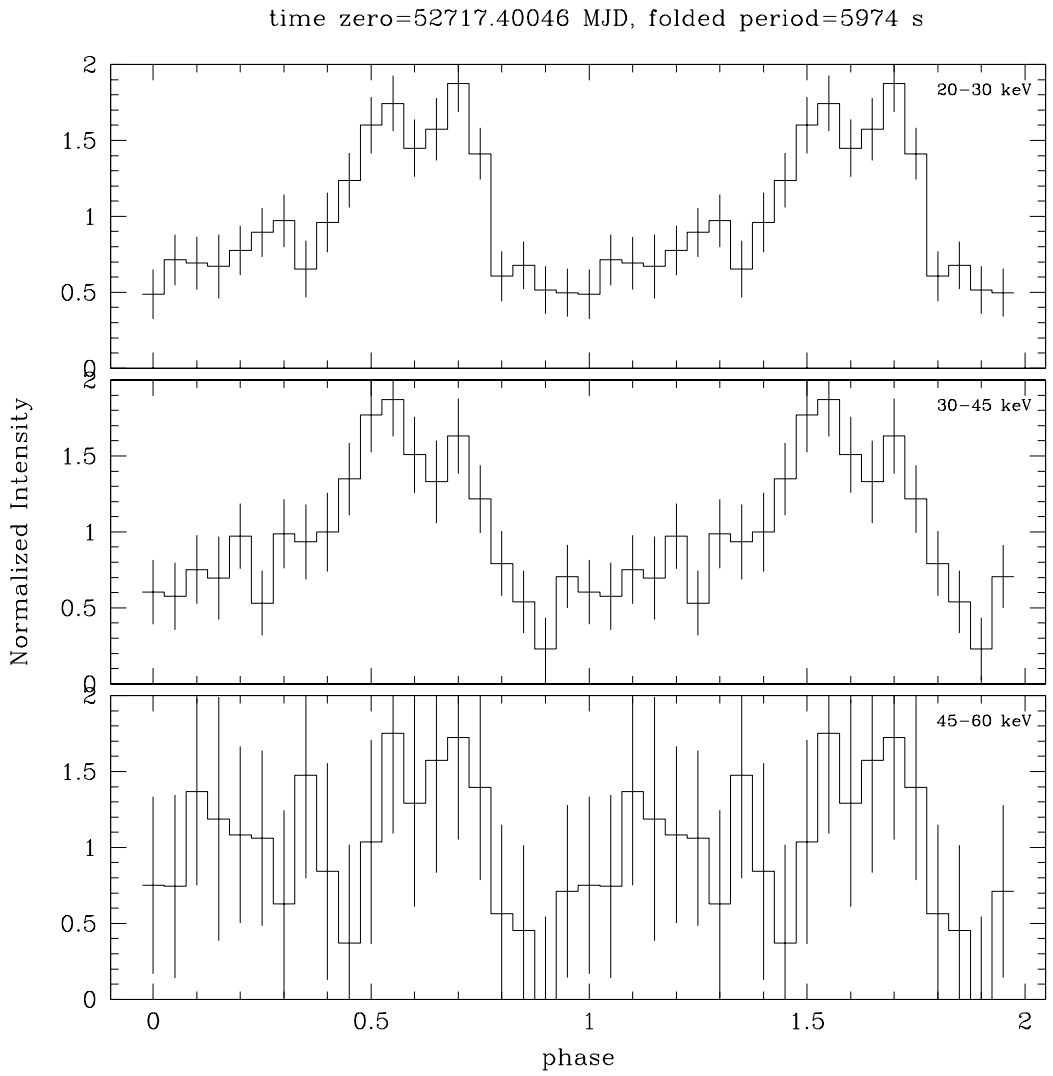


**Figure** *7.7: Folded light curve of IGR J16358−4726 for revolution 52 only.*

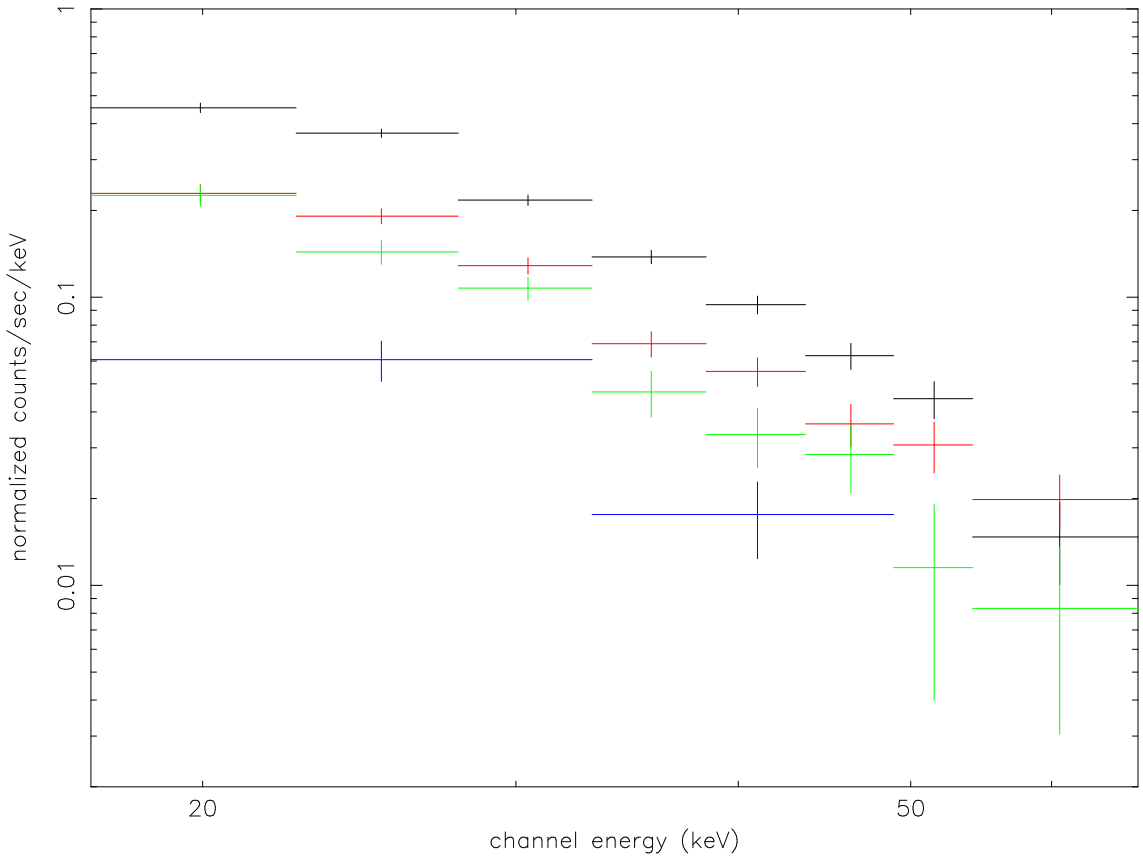


**Figure** *7.8: Average spectrum of IGR J16358−4726 for each revolution (black=rev. 52, red=rev. 54, green=rev. 52, blue=rev. 57).*

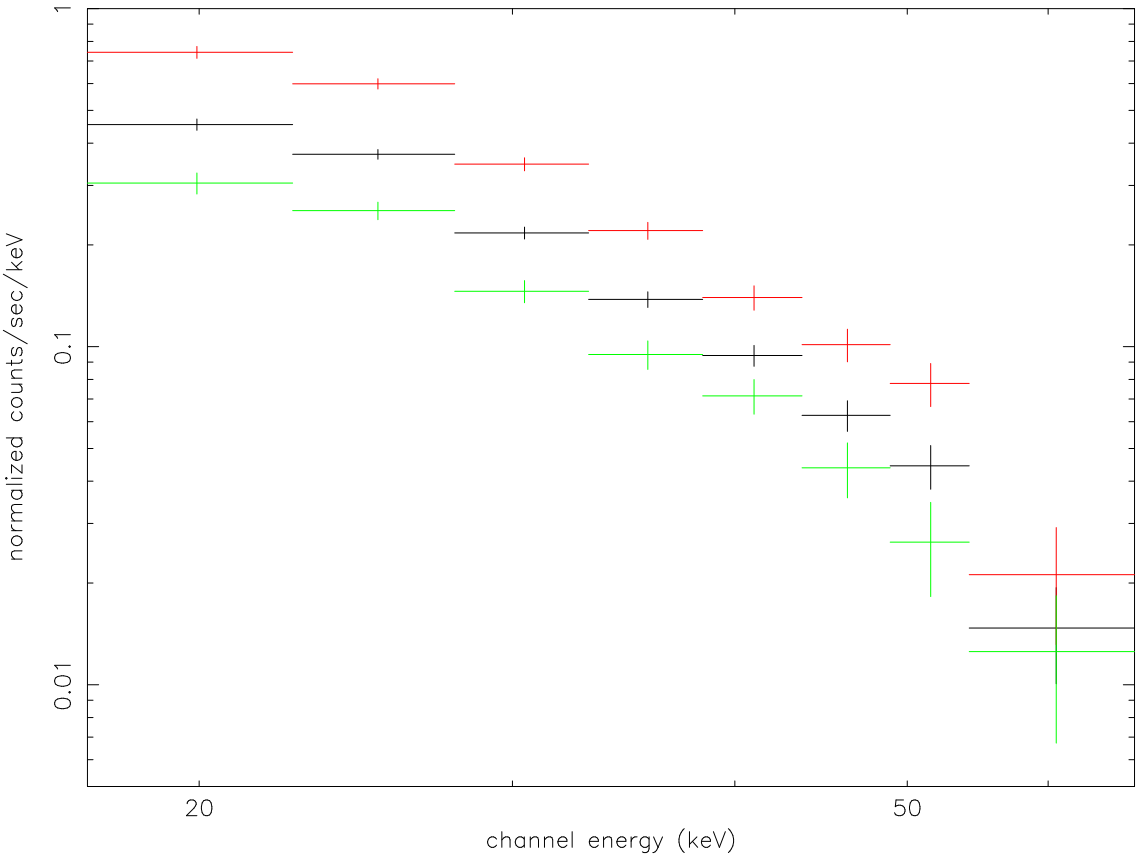


**Figure** *7.9: Phase-resolved spectroscopy of IGR J16358−4726 for revolution 52 (red=high intensity pulse spectrum, green=low intensity pulse spectrum, black=average spectrum.*

Besides, phase-resolved spectroscopy could be performed on the revolution 52 data as the pulse profile could clearly be cut in two parts (see Fig. 7.7) : the high intensity part corresponds to phase $\phi$=0.62–0.98 with the ephemeris being time zero MJD 52717.455772 and period 5974 s. The fitting of the 2 phase-resolved spectra with the absorbed power law with an energy cutoff does not reveal variability of the continuum parameters except for the intensity : $6.5\,10^{-10}$ ergs cm$^{-2}$ s$^{-1}$ in the peak part and $2.8\,10^{-10}$ ergs cm$^{-2}$ s$^{-1}$ in the flat part. This is compatible with the folded light curve (see Fig. 7.7).

However, studying only the hard X-ray spectrum cannot give many clues about the nature of the source. As we have seen with the study of IGR J17252−3616 combining spectra from soft to hard X-rays can help a lot to constrain the models. The combined *Chandra+INTEGRAL* spectral analysis can be found in Sect. 3.3 of Patel et al. (2006).

## 7.3 Scientific paper in preparation

The investigation of IGR J16358−4726 with *INTEGRAL* was combined with *Chandra* and *XMM-Newton* data. The following paper is in preparation and it will be submitted to the Astrophysical Journal.

to appear in ApJ

## Exploring the Nature of IGR J16358-4726

S. Patel[1,2], J. Zurita[3], M. del Santo[4], M. Finger[2], C. Kouveliotou[1], P. Ubertini[4], R. Walter [3], P. Woods[2], C. A. Wilson[4], S. Wachter[5], D. Eichler[6], A. Bazzano[4]

### ABSTRACT

We present spectral and timing analysis of the hard x-ray transient IGR J16358-4726. Joint spectral fits using simultaneous *Chandra*/ACIS and *INTEGRAL*/ISGRI data reveal a spectrum well described by broken power law model. The modulations initially reported using Chandra/ACIS observation are also detected in the ISGRI light curve and in subsequent XMM observations. This transient was observed with XMM-Newton twice in 2004. The initial observation resulted in an non-detection with an upper limit on the 1-10 keV unabsorbed flux of $5.4 \times 10^{-14}$ ergs cm$^{-2}$ s$^{-1}$ while the second pointing detected the source at the $4.9 \times 10^{-13}$ ergs s$^{-1}$ cm$^{-2}$ flux level. We present comparisons with other highly absorbed systems recently discovered by *INTEGRAL* and discuss the likely source classification.

*Subject headings:* pulsars: x-ray : individual (IGR J16358-4726)

### 1. Introduction

Since shortly after it's launch on October 17, 2002, ESA's INTErnational Gamma-Ray Astronomy Laboratory (*INTEGRAL*), a hard X-ray and $\gamma$-ray observatory (Winkler et al. 2003) discovered several transient hard x-ray sources during regular scans of the Galactic plane. Based on their spectral properties and presence of high intrinsic photo-absorption and, in some cases, detections of

[1]NASA/Marshall Space Flight Center, National Space Science and Technology Center, SD-50, 320 Sparkman Drive, Huntsville, AL 35805

[2]Universities Space Research Association, National Space Science and Technology Center, XD-12, 320 Sparkman Drive, Huntsville, AL 35805

[3]*INTEGRAL* Science Data Centre, 16 Ch. d'cogia, 1290 Versoix, Switzerland; Observatoire de Genve, Chemin des Maillettes 51, 1290 Sauverny, Switzerland

[4]Istituto di Astrofisica Spaziale e Fisica cosmica - CNR, via del Fosso del Cavaliere 100, 00133 Roma, Italy

[5]Spitzer Science Center, California Institute of Technology, MS 220-6, Pasadena, CA 91125

[6]Physics Department, Ben-Gurion University, Beer-Sheva 84105, Israel

pulse or orbital modulations, they are typically categorized as high mass x-ray binaries (HMXB) (see review by Kuulkers 2005, and references therein). X-ray and $\gamma$-ray observation of some of these sources have revealed clear evidence for pulsations in their high energy light curves including IGR J16465-4507 ($228 \pm 6$ s, Lutovinov et al. 2005), IGR J18027-2015 ($P_{spin} = 139.47 \pm 0.04s$, $P_{orb} = 4.570 \pm 0.003$ d, Hill et al. 2005; Augello et al. 2003), IGR J18410-0535 (= AX J18410-0536)(4.74± s Bamba et al. 2001), IGR J16320-4751 (1309±40 s Lutovinov et al. 2005), IGR 17252-3616 ($P_{spin} = 413.7 \pm 0.3s$, $P_{orb} = 9.72 \pm 0.09$ d, Zurita et al., 2005)and IGR J16358-4726 (5880±80 s Patel et al. 2004) which is indicative of an accreting neutron star with a strong magnetic field. Recently orbital periods of $8.9 \pm 0.1$ d and $9.72 \pm 0.09$ d have been reported for IGR J16320-4751 and IGR J17252-3616, respectivelyCorbet et al. (2005); Zurita et al., (2005). Based on their location on the pulse/orbital period diagram (a.k.a. Corbet Diagram) it has been suggested these are high mass wind fed systems.

Understanding the nature of IGR J16358-4726 is essential, as it has revealed one of the hardest x-ray spectra and the longest period of all the new *INTEGRAL* transients (thus far); this source then provides an excellent avenue toward understanding the nature of similar objects by investigating an extreme case. *Chandra* and *XMM-Newton* x-ray observations showed a hard power-law spectrum that was highly absorbed during the source outburst as well as in quiescence. Coherent frequency modulations at a period near 1.6 hr were clearly seen in outburst with *Chandra* and *INTEGRAL* and were also measured in quiescence, suggesting that the source is either a transient accreting pulsar with an unusually long spin period, or a transient Low Mass X-ray Binary with a short orbit. We have investigated phase and time resolved spectra with *Chandra* and we find no highly significant evidence for spectral evolution. However, in the X-ray pulse profile we observe a sharp drop that is suggestive of an eclipse; we also detect a significant decrease in the absorption along the line of sight in the weeks following the outburst after the source had faded. Finally, we present here our joint analysis of the *INTEGRAL* and *Chandra* spectra.

IGR J16358-4726 was discovered in outburst by IBIS/ISGRI on 19 March 2003 during Galactic Plane Scans. An image of this field is presented in Figure 1. Subsequent *INTEGRAL* observations of this part of the sky detected the source for $\sim 9$ days until the source was not longer in the useful field of view. We serendipitously observed the location of this new transient with *Chandra* while in outburst during a scheduled observation of SGR 1627-41 Kouveliotou et al. (2003). An ISGRI light curve encompassing the time when the source was detected in the useful FOV is presented in Figure 2 with the time of the *Chandra* observation noted. The source was previously detected with other X-ray observatories albeit at a much lower flux level. A long term X-ray light curve including all available archival data for this source is shown in Figure 3. The details of the *XMM-Newton* observations in 2004 are presented in this paper.

In Section 2 we present the details of the observation used in this report and the data reduction methods. In Section 3 we present the observation results and joint soft and hard x-ray spectral analysis. In Section 4 we discuss the observation properties of this source with respect to similar sources discovered by *INTEGRAL* and other well studies binaries.

## 2. Observations and Data Reduction

### 2.1. *INTEGRAL*

A significant portion of the observing time alloted for the *INTEGRAL* Core Program is dedicated to the study of hard X- and $\gamma$-ray emissions in the Galaxy. This is part of the Core Program and is mainly divided in Galactic Plane Scans (GPS) and Galactic Center Deep Exposures (GCDE). The observing strategy consists in pointing lasting 2.2 or 1.8 ks for GPS and GCDE, respectively, that are spread in various grid patters to ensure the best use of the coded-mask instruments. As IGR J16358-4726 is located in the Norma Arm region near the galactic plane and has been regularly monitored by *INTEGRAL*Lutovinov et al. (2005). The *INTEGRAL* observation data are referenced by *revolution* number (1 rev$\sim$ 3 day) and by furthermore by individual *science window* number (1 scw$\sim 2ks$). During such a monitoring observation, IGR J16358-4726 was discovered as a transient source revolution 52 and faded beyond detection a few days later. To date, no other detection of this source has been reported using *INTEGRAL* after this subsequent decay.

To search for times when IGR J16358-4726 was active, we investigate all the public *INTEGRAL* data obtained from the start of the mission until MJD 52928.3 and core program data obtained until MJD 53341.1. The total data set corresponds to the four epochs when the Galactic center was deeply observed resulting in a total exposure time of 4.3 Ms. Table 1 details the source visibility periods, and for each of them the fraction of the time when the source was effectively observed in the partially-coded field of view (PCFOV) of $29^\circ \times 29^\circ$. Revolutions with net source exposure $< 1$ ks were discarded since these times typically correspond to pointings in which the source crossed the FOV far from the center. These omitted revolutions include: 56, 61, 63, 164, 169, 179, 183, 241, 243 and 244.

The coded-mask instrument IBIS/ISGRI (20 keV-1 MeV, Ubertini et al. 2003; Lebrun et al. 2003) is the only instrument on board *INTEGRAL* used in this investigation. The average off-axis angle is larger than 10 degrees. Therefore, it is impossible to gather information from JEM-X as its FOV has a diameter of 13.2 degrees. Moreover, it is highly difficult to analyze sources lying more than 3 degrees away from the center of the JEM-X FOV. Only one pointing got the source at 2.5 degrees from the center in revolution 54. The source is non detected in one individual pointing with a $3\sigma$ upper limit of 0.005 count $s^{-1}$. The SPI data are not analyzed since its angular resolution of 2 degrees is too large for the crowded region where the source is located (i.e., 4U 1630-47 is located only $19'$ away from IGR J16358-4726).

The IBIS data were reduced with the Offline Scientific Analysis (OSA) software[1] (v4.2 and v5.0) provided by the *INTEGRAL* Science Data Center (Courvoisier et al. 2003). All the pointings with the source within the ISGRI fully-coded (FCFOV, $9^\circ \times 9^\circ$) or partially-coded (PCFOV, $29^\circ \times 29^\circ$) fields of view were selected. This resulted in $\sim 2000$ science windows distributed between revolutions

[1] http://isdc.unige.ch/

30 and 234 from which we extracted sky images for each pointing and built mosaic images with longer exposures. As the source is a transient, we extracted and inspected light curves from the individual pointing and mosaicked images. During the times the source was detected, we extracted light curves on shorter time scales ($\sim$ 0.1 s). We also generated individual spectra for each pointing and summed them in order to obtain one average spectra per revolution. The same technique is used to generate phase-resolved spectra based on our derived pulse period. All the pointings were initially analyzed with OSA 4.2 and subsequently the revolutions in which the source was detected were re-analyzed with OSA 5.0 (see details in Table 2).

### 2.2. *XMM-Newton*

We observed the location of IGR J16358-4726 with *XMM-Newton* starting on 2004 February 15.6 UT and again on 2004 September 4.8 for $\sim$ 32 ks for each pointing. The observation data files were processed using the *XMM-Newton* Standard Analysis System (SAS v6.5.0) tools *emchain* and *epchain* and HEASOFT/FTOOLS (v6.0.2). To identify times of high background in the PN and both MOS detectors, we first removed times of extremely high background rates ($>$ 15 counts s$^{-1}$ across the entire detector) and then repeatedly applied a 3 $\sigma$ clipping criterion to the 0.5-10.0 keV count rates until all the remaining events were within $\pm$3 $\sigma$ of the mean rate. The useful exposure times after removing times with high background were 16.7 ks (PN) and 20.0/17.7 ks (MOS1/MOS2) for the earlier observation and 22.7 ks (PN) and 24.9/25.8 ks (MOS1/MOS2) for the subsequent pointing.

When the source was detectable, we extract source spectra from each detector using an extraction radius of $r = 18''$ and build instruments response files using standard SAS tools *arfgen* and *rmfgen*. Background spectra are collected using the same observation from an offset regions close to the source location with a total area 15 times the source region. To justify use of the $\chi^2$ statistic, we grouped spectral bins to obtain at least 15 counts per bin before background subtraction in each spectrum.

The Chandra data presented here were initially presented in Patel et al. (2004).

## 3. Results

### 3.1. Source position

The source's brightest epoch occurred during revolution 52 with an average count rate of 5.4$\pm$0.1 count s$^{-1}$ and a detection significance of 47. We used a mosaic of that epoch (20-60 keV) to extract the best source position at RA = $16^h35^m52.5^s$ and Dec. = $-47°25'16''$ (J2000) with an uncertainty of $20''$ that includes a $10''$ systematic error due to the instrument misalignment. An additional systematic error (proportional to the source significance) from the image reconstruction

of 44″ is also present (Gros et al. 2003). This position is consistent with the location initially reported by Kouveliotou et al. (2003b).

We are able to determine a more accurate location using the second *XMM-Newton* observation and the initial *Chandra* observations are presented in a companion paper by Wachter et al. (2006) where we derive the most accurate x-ray source location and discuss our search for infrared counterparts.

### 3.2. Timing analysis

As IGR J16358-4726 is a transient source, we first searched for all detections in the two-year long ISGRI database in two energy ranges: 20-60 keV and 60-150 keV. We built mosaic images for each $\sim 3$ day revolution and extracted the light curves for both energy bands. To achieve a reliable detection, we only considered net exposures (at the source location) higher than 5 ks. At no time was the source detected above 60 keV. When the source was not detected in the 20-60 keV range in one revolution (these gave $3\sigma$ flux upper limits of $\sim 0.3$count s$^{-1}$ typically), we grouped adjacent revolutions to increase sensitivity. Typical net exposures for one revolution varied from a few to several tens of ks. The log of the four resulting detection revolution numbers, MJDs, and exposure times are giving in Table 2.

We have generated an Lomb-Scargle periodogram from the ISGRI light curve using the higher count rate detection from Rev 52,54, and 55 (Figure 2, left) and have detected significant modulations (Figure 2, right) at 1.65 h (as well as the first harmonic). We further examine the initial portion of the ISGRI light curve (until $\sim 7 \times 10^4$ s after the first detection) and clearly detect pulsations in the light curve with a period of $5970 \pm 15$ s (Figures 4). We have dissected the light curve into to 2 sections in search of any gross changes in modulation frequency which would be indicative of neutron star spin. The sections are delineated by the black dashed line at $2 \times 10^5$ s shown in Figure 2. The latter portion of the ISGRI light curve shows moderate evidence for pulsations consistent with the previously measured frequency (Figure 4, bottom). Also there is power in the harmonics ($\sim 3000$ s). Due to the poor statistics during this time, we are not able to conclusively determine pulse period changes exclusively with this ISGRI data.

We have folded the first $\sim 10^5$ s of the ISGRI light curve on the best determined *INTEGRAL* period and the resulting pulse profile is shown in Figure 5. For comparison we have also folded the *Chandra* X-ray light curve, acquired on 24 March 2004, with the same ephemeris. There appears to be evidence of a phase shift between these two profiles suggesting evolution of the pulse profile or period over a few days.

We also determine a pulse period using the *XMM-Newton* observation from 2004 September. We correct the photon times of arrival in the events list to the solar system barycenter and extract all events between 0.5-10.0 keV from a slightly smaller extraction region (12″) as was used in the spectral analysis. We performed a $Z_2^2$ test on periods ranging from 4000-7000 sec and clearly detect

the pulsation in the EPIC-PN light curve with a period $P = 5858 \pm 74$ s. This period is consistent with those measured using *Chandra* and *INTEGRAL* in 2003. We present the folded EPIC-PN light curve in Figure 6

### 3.3. Spectral analysis

#### *3.3.1. INTEGRAL/ISGRI + Chandra/ACIS-S Spectral Analysis*

The phase averaged spectral fit results from the *Chandra* data alone have already been presented in **?**. A power law fit to the *INTEGRAL*/ISGRI 20-200 keV spectrum resulted in an unacceptable fit ($\chi^2/\nu = 79/9$). A fit to a thermal blackbody model resulted in a more acceptable fit ($\chi^2/\nu = 13.7/9$) with $kT_{BB} = 6.2 \pm 0.1$ keV, however the model normalizations results in a source radius of only 0.15 km (assuming a source distance of 7 kpc).

To better characterize the spectrum of IGR J16358-4726 during its observed active state in 2003 we we jointly fit the phase averaged spectra measured by ISGRI and the initial *Chandra* observation. Since these data were collected at slightly different times, we allow the model normalizations between data sets to be free. We fix all other spectral parameters. The data were well fit by a comptonization model with the best fit parameters given in Table 3

We are fortunate to also have simultaneous *INTEGRAL* and *Chandra* observation on 24 March. These observations provide us with the only simultaneous broadband high energy spectral coverage for IGR J16358-4726 to date. The *INTEGRAL* data available during the time of the *Chandra* observations consists of 4 science windows from which we are able to extract $\sim 4600$ s of useful exposure time. The light curve from these observations are shown in Figure 7. Here we see that over all shape of the ISGRI light curve is consistent with the shape of the *Chandra* light curve during the same time interval suggesting an evolution in the hard x-ray ephemeris.

We have performed joint phase averaged spectroscopy using these simultaneous observations covering approximately one entire pulse. The data are represented by a broken-power law model with a Gaussian line feature at 6.4 keV. The best fit parameters are given in Table 4 and resulting spectrum in Figure 8.

#### *3.3.2. XMM-Newton/EPIC-PN Spectral Analysis*

We extracted events (1.0-10.0 keV) from a $15''$ region centered on the source location from the initial *XMM-Newton* observation and do not detect the source. Using WebPimms and assuming the spectral model last measured with *Chandra* ($\Gamma = 0.8$, $\log N_{\rm H} = 23.3$) (Patel et al. 2004) we derive a $3\sigma$ upper limit on the 1-10 keV unabsorbed flux of $5.4 \times 10^{-14}$ ergs cm$^{-2}$ s$^{-1}$. The limits derived from the MOS detectors are consistent with but not more constraining than the PN measurement.

– 7 –

During the second XMM observation we clearly detect a source at the location of IGR J16358-4726 with an average total 1-10 keV PN count rate of $(1.78 \pm 0.09) \times 10^{-2}$ count s$^{-1}$ within an 18″extraction radius. We estimate a PN background rate of $(0.31 \pm 0.01) \times 10^{-2}$ count s$^{-1}$ in the same region. For the MOS1 and MOS2 detectors using the same extraction region we find total rates of $(5.5 \pm 0.5) \times 10^{-3}$ count s$^{-1}$ and $(6.0 \pm 0.5) \times 10^{-3}$count s$^{-1}$ and calculate background rates of $(1.06 \pm 0.03) \times 10^{-3}$ count s$^{-1}$ and $(1.53 \pm 0.04) \times 10^{-3}$ count s$^{-1}$ respectively.

To test if $\chi^2$ fitting was valid, we fit the unbinned data using the C-statistic Cash (1979) and again using the grouped data and $\chi^2$ fitting with the weighting method described by Churazov et al. (1996) as implemented in XSPEC and find consistent results. We therefor employ standard $\chi^2$ methods in obtaining the best fit to the spectral data. We analyzed the spectra using the XSPEC (v11.3.2l) spectral-fitting package (Arnaud 1996). When fitting the MOS and PN spectra simultaneously we link the model parameters. However, since the instruments relative flux calibration is somewhat uncertain, we allowed the individual normalizations to be free to obtain their best fit value. We fit the MOS and PN (0.5-10.0 keV) spectra jointly to a power-law and again to a thermal blackbody model. We account for absorption due to intervening gas and dust from the Galaxy using the Tuebingen-Boulder ISM absorption model (XSPEC model *tbabs*) with the relative abundances and cross-sections from Wilms et al. (2000) and with He cross section from Yan et al. (1998). An acceptable fit ($\chi^2/\nu = 30.3/38$) resulted when modeled with the power law with a best fit spectral index $\Gamma = 1.1^{+0.4}_{-0.3}$ and column density $N_{\rm H} = 18^{+4}_{-3} \times 10^{22}$ cm$^{-2}$. The unabsorbed 1-10 keV flux measured from this model is $7.1 \times 10^{-13}$ ergs s$^{-1}$ cm$^{-2}$. A fit using a blackbody model resulted in a nearly identical quality fit ($\chi^2/\nu = 30.4/38$) with $kT_{BB} = 2.3^{+0.6}_{-0.2}$ and $N_{\rm H} = (14 \pm 3) \times 10^{22}$ cm$^{-2}$. The unabsorbed 1-10 keV flux measured for this model is $4.9 \times 10^{-13}$ ergs s$^{-1}$ cm$^{-2}$.

### *3.3.3. Phase Resolved Spectroscopy*

We have extracted 10 individual phase resolved spectra from the *Chandra* ACIS observation of 24 March. We have fit each spectra with an absorbed power law + Gaussian model and to an absorbed black body + Gaussian model. Acceptable fits for both models were obtained for all phase bins except bin 6 ($\chi^2/\nu = 104/59$) which is located on the rise of the main pulse. Bin 5 showed evidence of an additional line feature at 7.0 keV ($\Delta\chi^2 = 14.5$ for 3 additional parameters). The 2 lines present are found to be at $6.29 \pm 0.04$ and $7.00 \pm 0.05$ keV During this 26 ks observation there does not appear to be any significant change in the absorbing column density, $N_{\rm H}$, or the emission line energy centroid. Moderate changes in the spectral index suggests a hardening of the spectrum during the rise of the pulse profile.

Due to limited statistics we are only able to extract 2 useful phase bins from the ISGRI data. We

SKP acknowledges support from NASA grants NNG04GH33G and DD3-4023X.

**REFERENCES**

Augello, G., Iaria, R., Robba, N. R., Di Salvo, T., Burderi, L., Lavagetto, G., & Stella, L. 2003, ApJ, 596, L63

Arnaud, K. A. 1996, ASP Conf. Ser. 101: Astronomical Data Analysis Software and Systems V, 101, 17

Bamba, A., Yokogawa, J., Ueno, M., Koyama, K., & Yamauchi, S. 2001, PASJ, 53, 1179

Cash, W. 1979, ApJ, 228, 939

Churazov, E., Gilfanov, M., Forman, W., & Jones, C. 1996, ApJ, 471, 673

Corbet, R., et al. 2005, The Astronomer's Telegram, 649, 1

Courvoisier, T. J.-L., et al. 2003, A&A, 411, L53

Gros, A., Goldwurm, A., Cadolle-Bel, M., Goldoni, P., Rodriguez, J., Foschini, L., Del Santo, M., & Blay, P. 2003, A&A, 411, L179

Hill, A. B., et al. 2005, A&A, 439, 255

Kouveliotou, C., et al. 2003, ApJ, 596, L79

Kouveliotou, C., Patel, S., Tennant, A., Woods, P., Finger, M., & Wachter, S. 2003, IAU Circ., 8109, 2

Kuulkers, E. 2005, Proc. of the Interacting Binaries Meeting of Cefalu, Italy, Eds. L.A. Antonelli, et al., AIP, in press

Lebrun, F., et al. 2003, A&A, 411, L141

Lutovinov, A., Revnivtsev, M., Gilfanov, M., Shtykovskiy, P., Molkov, S., & Sunyaev, R. 2005, A&A, in press, arXiv:astro-ph/0411550

Lutovinov, A., Rodriguez, J., Revnivtsev, M., & Shtykovskiy, P. 2005, A&A, 433, L41

Patel, S. K., et al. 2004, ApJ, 602, L45

Titarchuk, L. 1994, ApJ, 434, 570

Ubertini, P., et al. 2003, A&A, 411, L131

Wachter, S., et al. 2006, ApJ, in preparation

Wilms, J., Allen, A., & McCray, R. 2000, ApJ, 542, 914

Winkler, C., et al. 2003, A&A, 411, L1

Yan, M., Sadeghpour, H. R., & Dalgarno, A. 1998, ApJ, 496, 1044

Zurita Heras, J. A., et al. 2005, å, in press

– 10 –

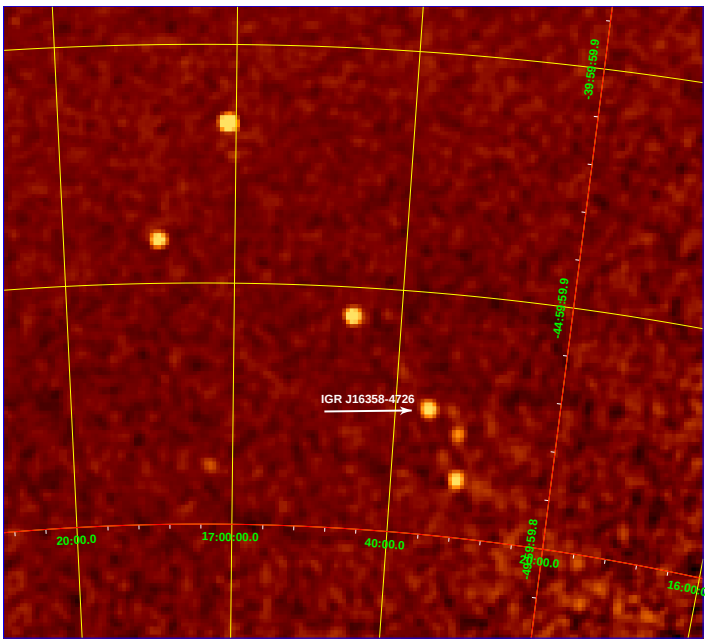


Fig. 1.— *INTEGRAL* IBIS/ISGRI 20−30 keV image of field containing IGR J16358-4726 taken on 19 March 2003 (Rev 52). The source was detected with confidence of 41 $\sigma$ in 67 ks of useful exposure time.

Table 1. Observation Catalog for IGR J16358-4726

| Observatory | Start (MJD) | End (MJD) | Revolutions | OTF[a] |
|---|---|---|---|---|
| INTEGRAL | 52650 | 52743 | 30- 60 | 0.05 |
| INTEGRAL | 52859 | 52919 | 100-119 | 0.02 |
| INTEGRAL | 53060 | 53084 | 167-174 | 0.02 |
| INTEGRAL | 53236 | 53263 | 226-234 | 0.04 |
| Chandra | 52750.1484 | 52750.7093 | - | 1 |
| Chandra | 52722.1691 | 52722.4939 | - | 1 |
| XMM-Newton | 53051.6064 | 53051.9865 | - | 1 |
| XMM-Newton | 53252.7663 | 53253.1255 | - | 1 |

Note. — All public and core programme revolutions when IGR J16358-4726 was within the ISGRI PCFOV are included

[a]The observing time fraction (OTF) was calculated as the ratio between the net exposure time on the source and the elapsed time during the visibility periods.

Table 2. Log of *INTEGRAL*/ISGRI Observations with Detections of IGR J16358-4726

| Revolution | Start (MJD) | End (MJD) | Exposure sec | Average off-axis angle[a] deg |
|---|---|---|---|---|
| 052 | 52717.3972 | 52718.7003 | 89207 | 11.2 (6-17) |
| 054 | 52722.2812 | 52724.6796 | 98194 | 10.2 (2.5-18) |
| 055 | 52725.0607 | 52726.4123 | 98700 | 11.3 (5.7-14.3) |
| 057 | 52732.5051 | 52733.6327 | 84164 | 11.3 (5.7-11.3) |

[a]Numbers in parenthesis indicate the range of off-axis angle.Rev 52 and 56 were not considered since the source fell outside the PCFOV.

Table 3. *INTEGRAL* & *Chandra* Joint Spectral Fit Results

| Parameter | Value[a] |
|---|---|
| $N_{\rm H}$ ($\times 10^{22}$ cm$^{-}$2) | $27.9 \pm 0.9$ |
| $E_{line}$ (keV) | $6.39 \pm 0.01$ |
| $\sigma$ (keV) | $0.07 \pm 0.02$ |
| $kT_{injection}$ (keV) | $2.1 \pm 0.1$ |
| $kT_{plasma}$ (keV) | $7.9 \pm 0.6$ |
| $\tau$ | $3.8 \pm 0.6$ |

[a]Value in parenthesis represents the 1 $\sigma$ uncertainty in the final digit.

Table 4. *INTEGRAL* & *Chandra* Joint Spectral Fit Results

| Parameter | Value[a] |
|---|---|
| $N_{\rm H}$ ($\times 10^{22}$ cm$^{-}$2) | 35(2) |
| $\Gamma_1$ | 0.5(1) |
| $\Gamma_2$ | 3.0(5) |
| $E_{break}$ (keV) | 27(3) |
| $E_{line}$ (keV) | 6.38(2) |
| $\sigma$ (keV) | 0.06(3) |
| $F_x$ (2−50 keV,erg s$^{-1}$ cm$^{-2}$) | $1.3 \times 10^{-9}$ |

[a]Value in parenthesis represents the 1 $\sigma$ uncertainty in the final digit.

Table 5. XMM-PN/MOS Spectral Fit Results IGR J16358-4726

| Parameter | Value[a] |
|---|---|
| $N_{\rm H}$ (cm$^{-2}$) | $18^{+4}_{-3} \times 10^{22}$ |
| $\Gamma$ | $1.1^{+0.4}_{-0.3}$ |
| $f_x$ (ergs s$^{-1}$ cm$^{-2}$)[b] | $7^{+1}_{-2} \times 10^{-13}$ |
| $\chi^2/\nu$ | 30.3/38 |

[a]errors reflect the $\pm 1\sigma$ uncertainty

[b]1−10 keV unabsorbed flux measured by the PN

– 13 –

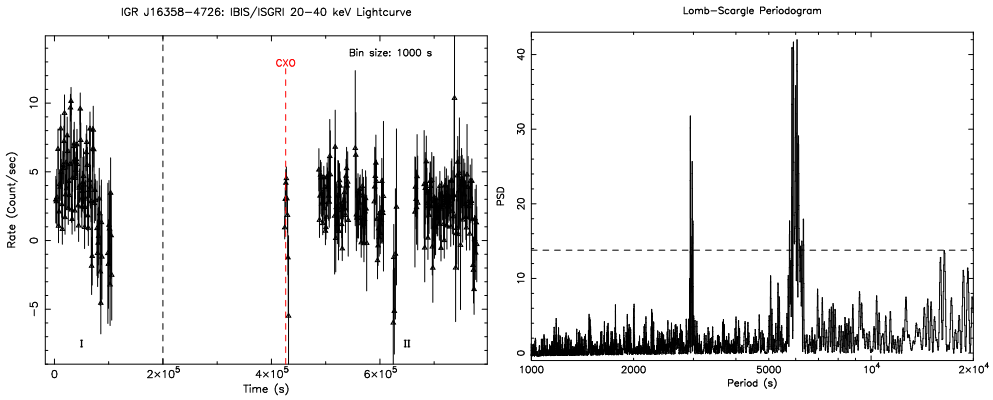


Fig. 2.— *INTEGRAL* 20-40 keV lightcurve of IGR J16358-4726. The source was initially dectected by integral on March 19, 2006 and is clearly detected is *INTEGRAL* Revolutions 52, 54, and 55 spanning $\sim$ 9days. The red dashed line indicates the time of the initial *Chandra* observation.

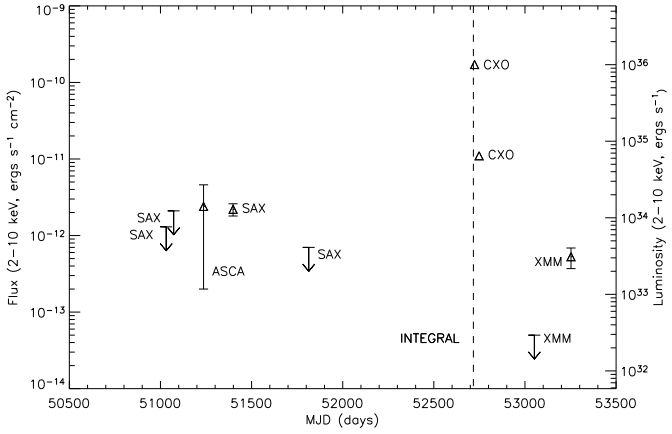


Fig. 3.— X-ray flux history of IGR J16358-4726. 90% upper-limits are indicated for 3 *BeppoSAX* measurements and 1 *XMM-Newton* measurement. The dashed line indicates the initial detection of the 2003 outburst by *INTEGRAL* on 19 March.

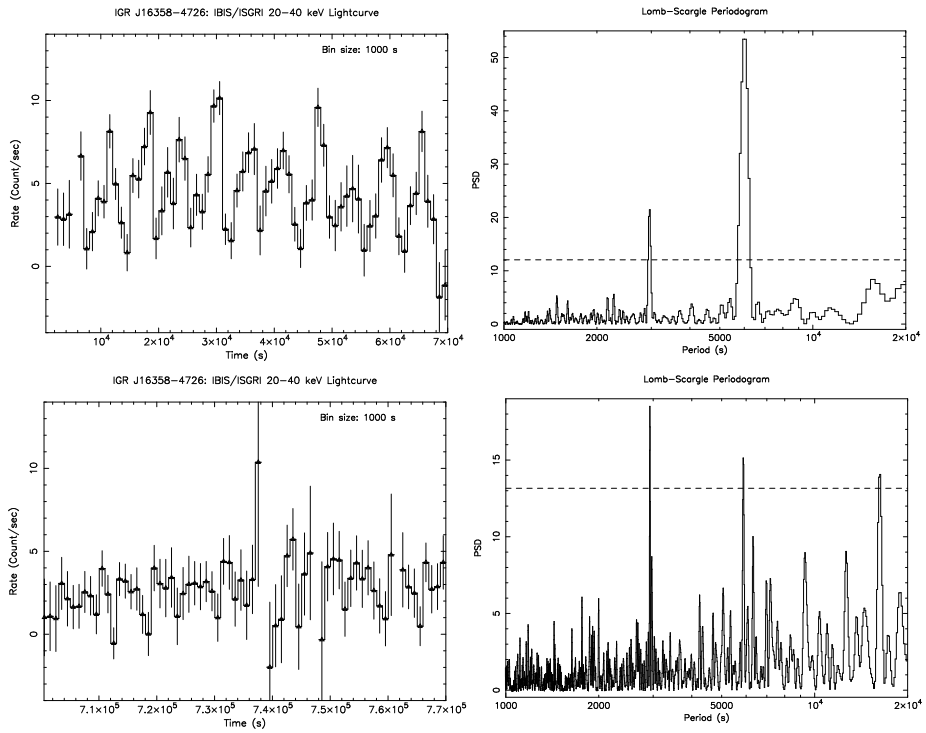


Fig. 4.— *Top Panels: INTEGRAL* 20-40 keV lightcurve of IGR J16358-4726 on 19 March 2004 (Rev 52) and the Lomb-Scargle Periodogram derived from this light curve. *Bottom Panels: INTEGRAL* 20-40 keV lightcurve of IGR J16358-4726 (Rev 54 and 55) and Lomb-Scargle Periodogram derived from light curve.

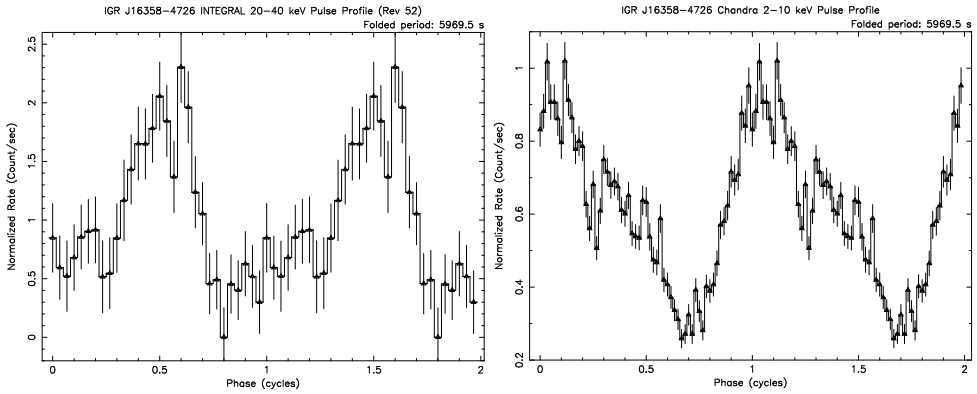


Fig. 5.— *Left:* Folded 20-40 keV Integral IBIS pulse profile with period $P = 5970(15)$ s. *Right:* 2-10 keV *Chandra* ACIS pulse profile folded on the same period. Both profiles are referenced to the same date (MJD=52721). The *Chandra* data was acquired $\sim 5$ days after the ISGRI detection.

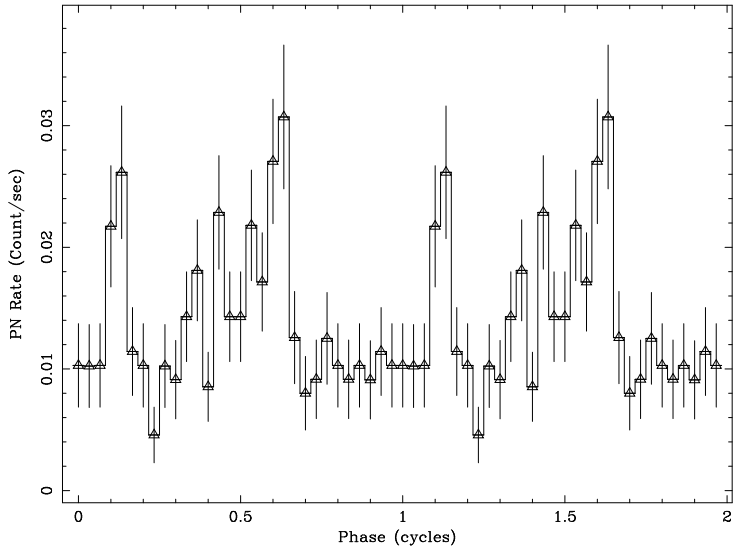


Fig. 6.— *Left:* Folded 0.5-10.0 *XMM-Newton* EPIC/PN pulse profile with period $P = 5858 \pm 74$ s.

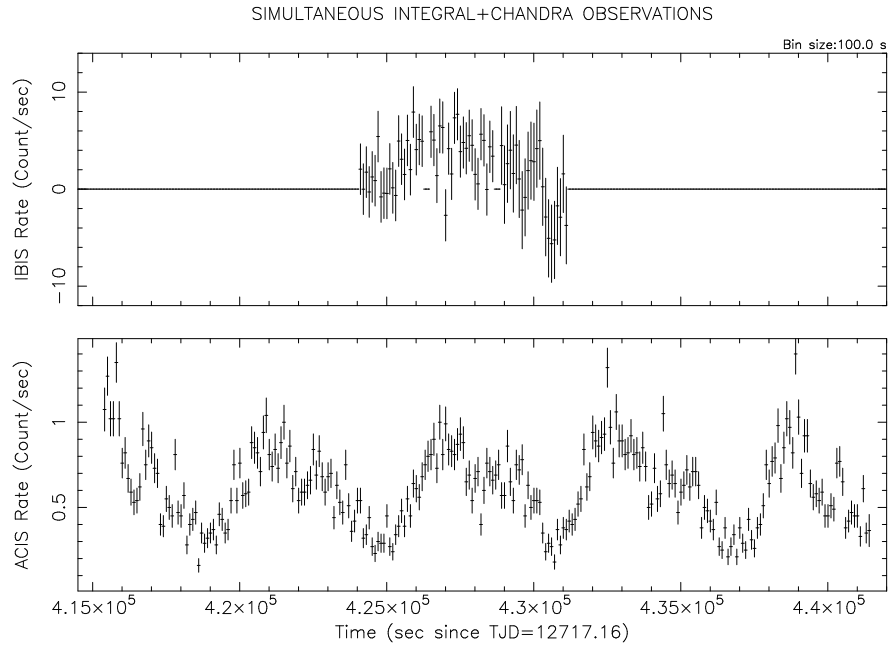


Fig. 7.— Simultaneous *Chandra* ACIS-S2 (2-10 keV) and *INTEGRAL* ISGRI (20-40 keV) lightcurve of IGR J16358-4726.

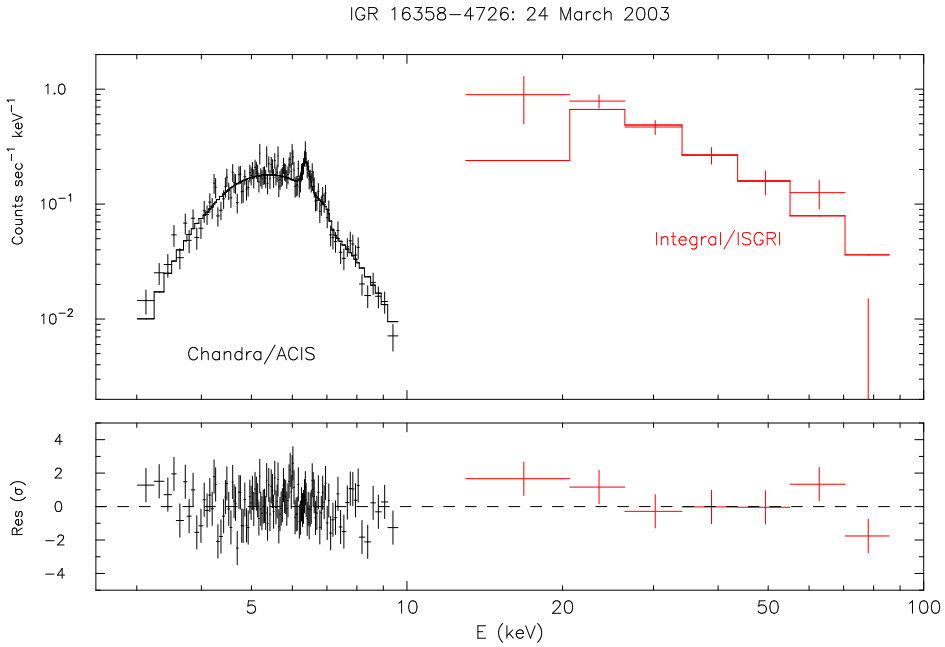


Fig. 8.— *Chandra* ACIS-S3 and *INTEGRAL* ISGRI spectrum of IGR J16358-4726 in an active state on 24 March 2003. We find that a highly absorbed broken power law model gives the best fit to the data. A Fe $K_\alpha$ line feature clearly seen at 6.4 keV during the 24 March observation had faded below the detection capability of *Chandra* during the second observation on 21 April.

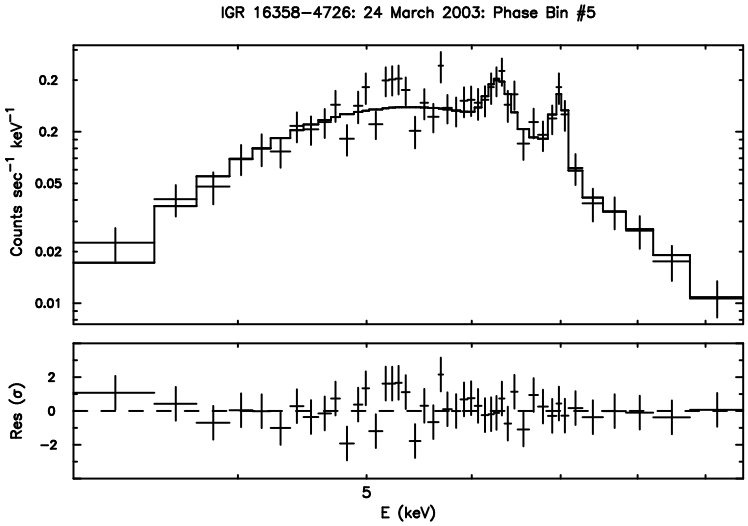


Fig. 9.— *Chandra* ACIS Spectral of single phase bin #5 (see Figure 10). A model consisting of an absorved powerlaw (or blackbody) component plus 2 gaussian lines best describe this spectrum $\chi^2/\nu = 34.9/36$.

– 19 –

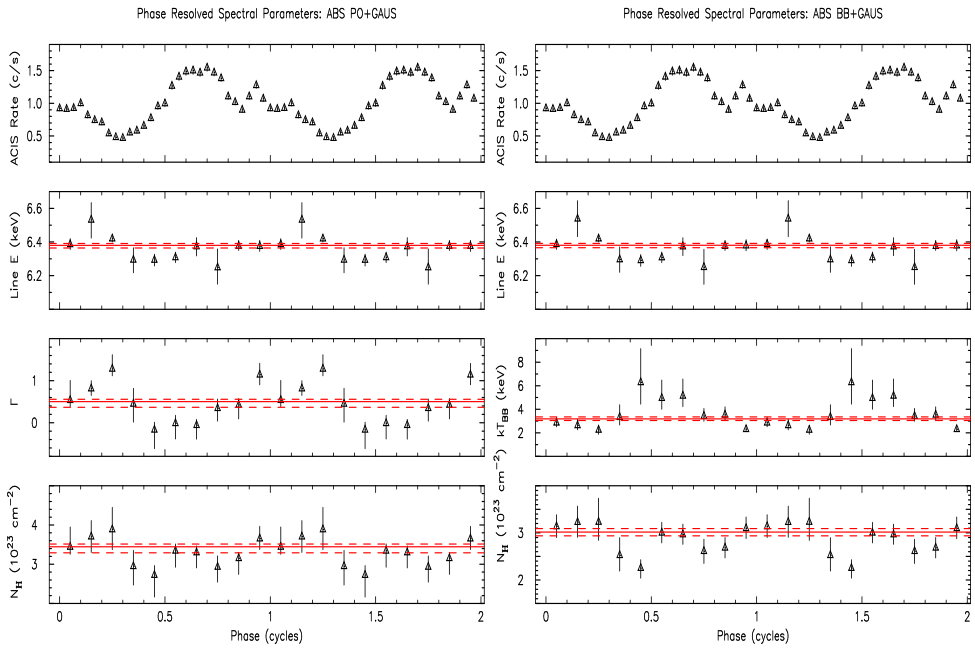


Fig. 10.— *Top panel*:Phase resolves spectral fit results derived from *Chandra* ACIS-S2 (2.0 – 10.0 keV) observed of IGR J16358-4726 in an active state on 2003 March 24. Solid line indicated phase averaged values and dashed lines and errors reflect the 1 $\sigma$ uncertainty. There is marginal evidence for evolution in the the spectral index with the hardest spectra occuring during pulse rise.

# Chapter 8
# IGR J16393−4643 OBSERVED BY *INTEGRAL* AND *XMM-Newton*

In this chapter we describe in full detail the analysis of IGR J16393−4643. This source was extensively observed by the *INTEGRAL* satellite during the core programme dedicated to the study of the galactic centre and of the galactic plane. This object was also observed by *XMM-Newton* for three hours.

This is another source belonging to the same *XMM-Newton* programme follow-up as IGR J17252−3616. We first introduce the re-discovery of this source. We continue with the timing and spectral analysis that are similar to those of IGR J17252−3616. We conclude with the interpretation of nature of this source.

## 8.1 Discovery of IGR J16393−4643

The detection of IGR J16393−4643 was reported on January 30, 2004, at the position R.A. (2000.0)=16h39m18s and Dec.=$-46^{\rm o}\,43'\,00''$ with an uncertainty of $2'$, a significance of $20\sigma$, and a 20–100 keV flux of $5\,10^{-11}$ ergs cm$^{-2}$ s$^{-1}$ (Malizia et al. 2004). It was detected by ISGRI in a 700 ks exposure of the Norma Arm region and it showed some variability. There are two possible counterparts : a variable *ASCA* source, AX J1639.0-4642, and an EGRET source, 3EG 1639-4702.

After a multi-wavelength study, Combi et al. (2004) proposed that IGR J16393−4643 could be a HMXB surrounded by a huge quantity of matter, and there is also some radio emission consistent with the source location that would support a micro-quasar scenario.

## 8.2 Observation of IGR J16393−4643

IGR J16393−4643 is located approximately $1^{\rm o}$ away from IGR J16358−4726. Therefore, the *INTEGRAL* monitoring at the source position is the same as described in Sect. 7.2.1. The *INTEGRAL* data set contains the public data obtained until MJD 52928.3 and the core programme data obtained until MJD 53341.1. The total exposure at the source position is 4.4 Ms. The observations per revolution are summarised in Tables 8.1 and 8.2. Only the revolutions with 5 or more ScW are listed. IGR J16393−4643 has been observed by *XMM-Newton* on March 21, 2004, for three hours. It is also part of the guest observer progamme 020638 (PI : Walter R., see Sect. 9.2). The instrument science modes are :

**Table** 8.1: Journal of IGR J16393−4643 observations with *INTEGRAL*. The data set is composed of public data.

| Revolution | ScW | Start time MJD | Exposure ks | Off-axis angle $^{o}$ | JEM-X |
|---|---|---|---|---|---|
| 0030 | 21 | 52650.86 | 48.5 | 14.7 | 0 |
| 0032 | 8 | 52657.93 | 19.4 | 14.8 | 0 |
| 0037 | 94 | 52671.23 | 208.5 | 3.8 | 0[a] |
| 0038 | 42 | 52674.12 | 92.5 | 3.6 | 0[a] |
| 0046 | 37 | 52698.57 | 76.7 | 13.6 | 0 |
| 0047 | 90 | 52701.03 | 160.9 | 7.0 | 31 (5) |
| 0049 | 49 | 52707.78 | 87.6 | 6.2 | 26 (5) |
| 0050 | 60 | 52710.00 | 111.3 | 9.7 | 15 (3) |
| 0051 | 44 | 52712.99 | 79.5 | 11.3 | 0 |
| 0052 | 53 | 52717.40 | 96.0 | 10.1 | 9 (0) |
| 0053 | 18 | 52718.97 | 32.1 | 16.8 | 0 |
| 0054 | 59 | 52722.25 | 108.2 | 10.0 | 13 (4) |
| 0055 | 44 | 52724.95 | 98.7 | 11.9 | 0 |
| 0057 | 34 | 52732.51 | 77.2 | 11.7 | 0 |
| 0058 | 16 | 52734.03 | 36.3 | 15.0 | 0 |
| 0060 | 50 | 52739.91 | 105.8 | 12.6 | 0 |
| 0061 | 12 | 52742.90 | 24.8 | 15.8 | 0 |
| 0063 | 7 | 52750.26 | 13.0 | 16.5 | 0 |
| 0100 | 113 | 52859.62 | 209.8 | 6.9 | 45 (7) |
| 0101 | 15 | 52862.50 | 27.9 | 9.1 | 4 (2) |
| 0103 | 61 | 52868.96 | 109.7 | 13.6 | 0 |
| 0105 | 12 | 52874.57 | 41.2 | 18.1 | 0 |
| 0106 | 8 | 52878.96 | 29.9 | 18.2 | 0 |
| 0107 | 8 | 52882.72 | 28.5 | 18.2 | 0 |
| 0108 | 5 | 52885.20 | 18.0 | 18.3 | 0 |
| 0116 | 64 | 52907.95 | 129.1 | 7.0 | 29 (5) |
| 0118 | 83 | 52913.45 | 153.4 | 10.1 | 17 (3) |
| 0119 | 16 | 52916.46 | 30.1 | 15.0 | 0 |

[a]Science mode=43, bad

**Table** 8.2: Journal of IGR J16393−4643 observations with *INTEGRAL*. The data set is composed of CP data.

| Revolution | ScW | Start time MJD | Exposure ks | Off-axis angle ° | JEM-X |
|---|---|---|---|---|---|
| 0164 | 13 | 53052.23 | 24.7 | 14.2 | 0 |
| 0165 | 14 | 53054.43 | 26.0 | 13.2 | 1 (0) |
| 0167 | 58 | 53061.24 | 108.5 | 9.5 | 20 (4) |
| 0168 | 18 | 53063.10 | 32.7 | 10.8 | 1 (0) |
| 0169 | 8 | 53066.48 | 14.4 | 18.2 | 0 |
| 0171 | 7 | 53072.18 | 13.2 | 18.2 | 0 |
| 0173 | 15 | 53078.14 | 27.0 | 9.3 | 2 (0) |
| 0174 | 30 | 53081.06 | 54.2 | 9.3 | 4 (0) |
| 0179 | 6 | 53097.31 | 10.7 | 15.2 | 0 |
| 0183 | 10 | 53107.98 | 18.0 | 15.6 | 0 |
| 0185 | 10 | 53114.69 | 18.0 | 15.6 | 0 |
| 0226 | 7 | 53236.57 | 17.6 | 10.6 | 3 (1) |
| 0229 | 5 | 53245.82 | 11.0 | 7.3 | 3 (1) |
| 0232 | 79 | 53254.49 | 143.3 | 9.3 | 24 (6) |
| 0233 | 39 | 53257.99 | 77.0 | 9.2 | 15 (6) |
| 0234 | 26 | 53260.35 | 49.5 | 13.1 | 0 |
| 0235 | 28 | 53263.35 | 54.2 | 10.3 | 2 (0) |
| 0243 | 6 | 53289.53 | 10.8 | 16.2 | 0 |
| 0244 | 7 | 53290.47 | 12.7 | 17.1 | 0 |

**EPIC** medium filter and large window science mode;

**RGS** no filter and HCR science mode; and

**OMC** imaging mode.

## 8.3 The combined *INTEGRAL*+*XMM-Newton* analysis

As for IGR J17252−3616 and IGR J16358−4726, we start with the images and the source location determination. We continue with the timing analysis and we finish with the spectral analysis.

### 8.3.1 Images and position improvement

We first start with ISGRI and we finish with the EPIC cameras.

#### ISGRI

As the data set is almost equivalent to that of IGR J16358−4726, all the analysis performed for that source could be used for IGR J16393−4643. This is one of the advantages of working with *INTEGRAL* : several sources can be studied simultaneously due to the wide FOV. This is a good thing as it takes a long time to analyse huge *INTEGRAL* data set as in our case. Therefore, we have images per ScW and per revolution in two energy bands : 20–60 keV and 60–150 keV. Looking at the GCDE images (see Fig. 6.3 and 6.4), we note there is a significant bright spot coincident with the IGR J16393−4643 position in each image. However when looking in each individual revolution, there are some where the source is not detected. The summary of detections (or non-detections) is summarised in Table 8.3. We chose a conservative value to discriminate between detection and non-detection : the 20–60 keV significance should be higher than 4. The $1\sigma$ upper limit is given when the significance is lower than 4.

The detection of IGR J16393−4643 with the greatest significance happened during revolution 100 (see Fig. 8.1). The average count rate was (0.93±0.06) counts $s^{-1}$ with a significance of 15. The position extracted in this mosaic is R.A. (2000.0)=16h39m05s and Dec.=$-46^{o}\,42'\,13''$ with an uncertainty of $0.5'$. However, with a significance of 15, the systematic errors are $0.9'$.

#### EPIC

Before creating images, the event lists were screened for periods of background flares (see Fig. 8.2). The lapses of time that are removed correspond to when the count rates at energies higher than 10 keV are greater than : 0.17 counts $s^{-1}$for MOS1 and for MOS2, and 1 counts $s^{-1}$ for pn.

Once the cleaned event lists are ready, images with $2''$ (MOS[12]) and $4''$ (pn) resolution are created. Events until the quadrupole level are kept. The images are in the 0.8–10 keV energy band (see Fig. 8.3).

Only one bright source is visible in the EPIC images. The best source position (derived as for IGR J17252−3616, see Sect. **??**) is : R.A. (2000.0)=16h39m05.4s and Dec.=$-46^{o}\,42'\,11''.9$

**Table** 8.3: Journal of IGR J16393−4643 detections with *INTEGRAL*. When IGR J16393−4643 is not detected within one revolution, the $1\sigma$ upper limit is reported.

| Revolution | 20–60 keV Flux counts $s^{-1}$ | Flux error counts $s^{-1}$ | Significance | Exposure s |
|---|---|---|---|---|
| 0030 | <0.5 | | 1.8 | 2909 |
| 0032 | <0.5 | | 2.6 | 1347 |
| 0037 | 0.63 | 0.06 | 11.2 | 95287 |
| 0038 | 0.92 | 0.09 | 10.4 | 46148 |
| 0046 | <0.3 | | 0.0 | 7322 |
| 0047 | 0.73 | 0.07 | 10.0 | 61432 |
| 0049 | 0.98 | 0.09 | 10.9 | 40893 |
| 0050 | 0.97 | 0.10 | 9.7 | 33362 |
| 0051 | 1.04 | 0.16 | 6.5 | 15588 |
| 0052 | 0.73 | 0.10 | 7.2 | 34153 |
| 0054 | 1.09 | 0.11 | 9.5 | 27016 |
| 0055 | 1.55 | 0.15 | 10.6 | 20636 |
| 0057 | <0.2 | | 3.0 | 10814 |
| 0058 | <0.4 | | 3.0 | 3447 |
| 0060 | <0.2 | | 2.7 | 7532 |
| 0100 | 0.93 | 0.06 | 14.8 | 84586 |
| 0101 | <0.3 | | 1.8 | 4753 |
| 0103 | <0.2 | | 3.5 | 12132 |
| 0116 | 0.35 | 0.08 | 4.3 | 56689 |
| 0118 | 0.89 | 0.09 | 9.4 | 42308 |
| 0119 | <0.5 | | 1.3 | 2467 |
| 0164 | <0.5 | | 0.0 | 1862 |
| 0167 | <0.1 | | 3.6 | 31120 |
| 0168 | <0.3 | | 2.2 | 5257 |
| 0173 | 1.01 | 0.23 | 4.5 | 6726 |
| 0174 | <0.2 | | 3.5 | 13299 |
| 0183 | <0.7 | | 0.4 | 1488 |
| 0226 | <0.4 | | 1.7 | 3491 |
| 0229 | <0.3 | | 1.3 | 3077 |
| 0232 | <0.1 | | 1.4 | 44866 |
| 0233 | 0.83 | 0.11 | 7.7 | 31333 |
| 0234 | <0.3 | | 3.3 | 6167 |

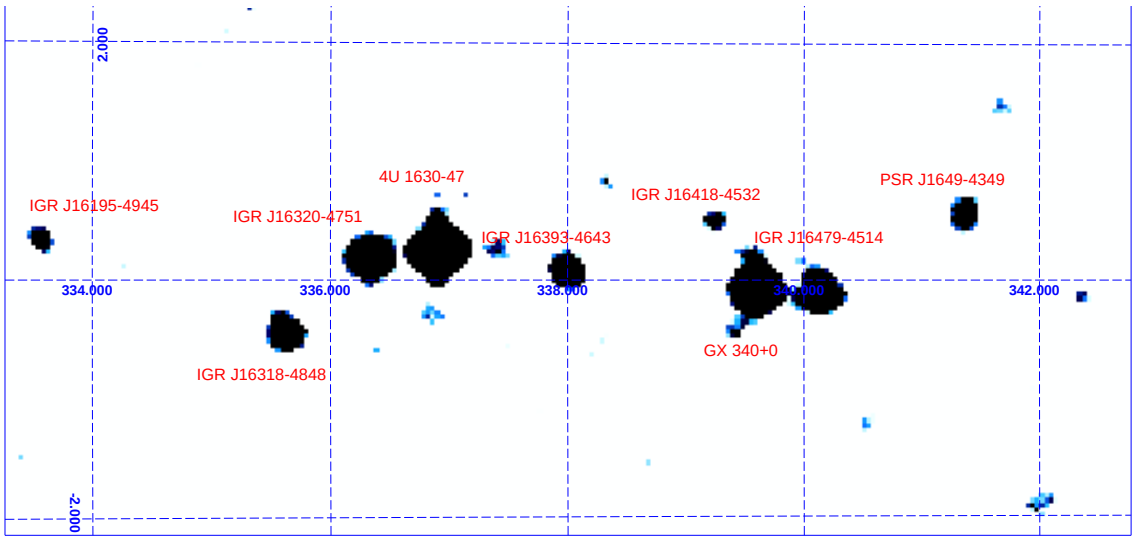


**Figure** *8.1: 20–60 keV significance map of IGR J16393−4643 during revolution 100 (MJD 52859.5–52862.5) : $\sigma = 15$.*

with an uncertainty of $4''$. The position is consistent with IGR J16393−4643.

#### Conclusion

There is only one source emitting in X-rays and hard X-rays (0.8–60 keV) at the position R.A. (2000.0)=16h39m05.4s and Dec.=$-46^{\circ}\,42'\,11''.9$. No detection at energies higher than 60 keV happened over two years.

### 8.3.2 Timing analysis

As for IGR J17252−3616, there are long observations at hard X-rays and one short observation for the 0.5–10 keV energy range. The two energy bands are studied separately. The *XMM-Newton* observation was coincident with an *INTEGRAL* observation of the Norma Arm field. The ScW are : 017500590010, 017500600010, 017500610010, 017500620010, and 017500630010. However, the data were private at the time of this study.

#### The two-years light curve

As for IGR J17252−3616 (see Sect. 6.4.2), we extract the average flux per revolution when the source is detected and a $3\sigma$ upper limit when the source is too faint to be detected by ISGRI. Consecutive revolutions are grouped together when the source is not detected in a single revolution. The source is detected in every GCDE observation period, in most of the revolutions, so it is persistent (see Fig. 8.5). IGR J16393−4643 shows significant variability with a lowest flux (detected) of $(0.35\pm0.08)$ counts $s^{-1}$ and a highest flux of $(1.6\pm0.1)$ counts $s^{-1}$. The average flux is low, just a bit higher than the detector sensitivity. There are some revolutions where the source is not detected. The lowest $3\sigma$ upper limit is 0.28 counts $s^{-1}$.

The light curve per pointing is not relevant. All the pointings with the source placed more

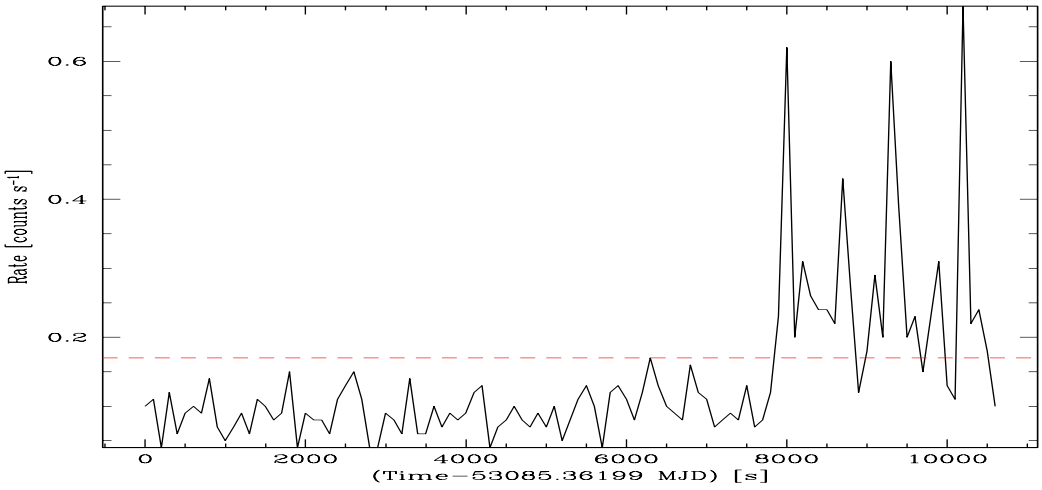


(a) MOS1

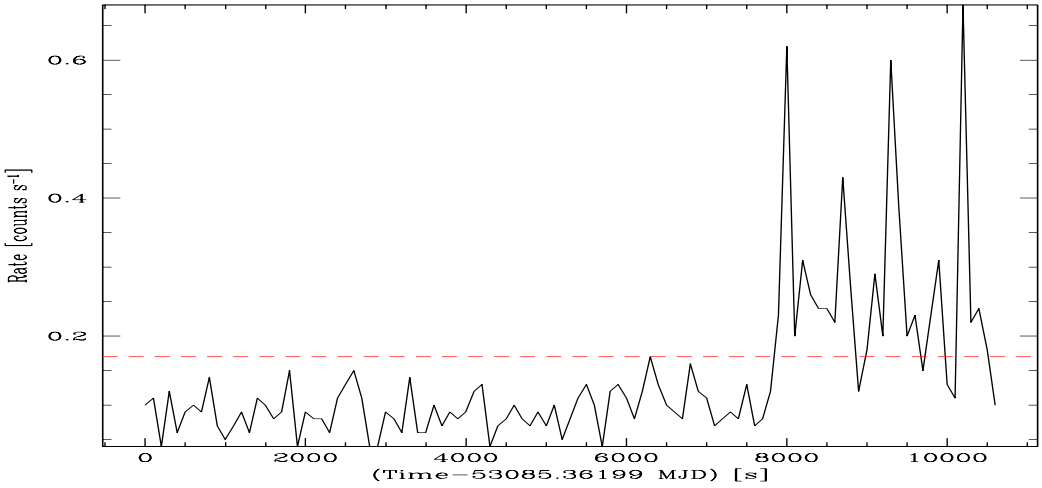


(b) MOS2

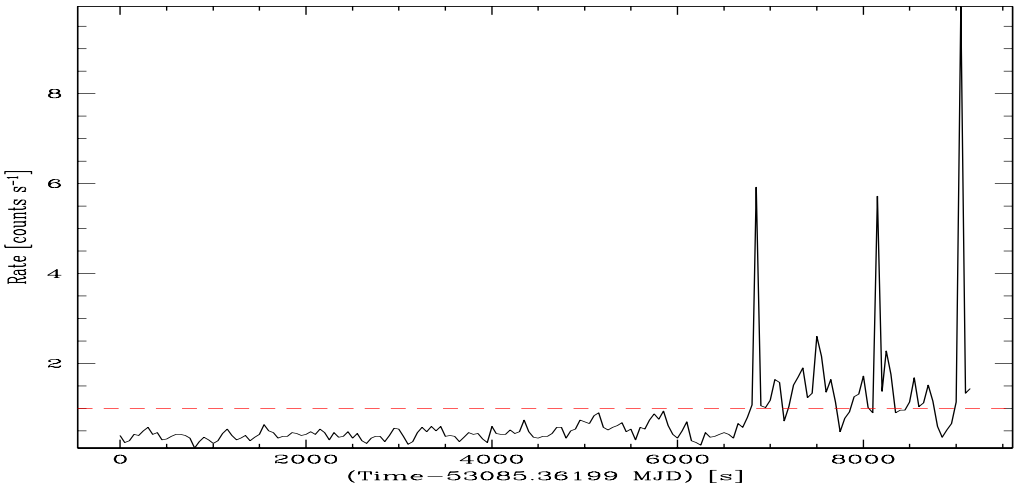


(c) pn

**Figure** *8.2: EPIC count rates at energies higher than 10 keV. The red dotted lines represent the cut for each detector: 0.17 counts*$\mathrm{s}^{-1}$ *for MOS1 and MOS2, and 1 counts*$\mathrm{s}^{-1}$ *for pn.*

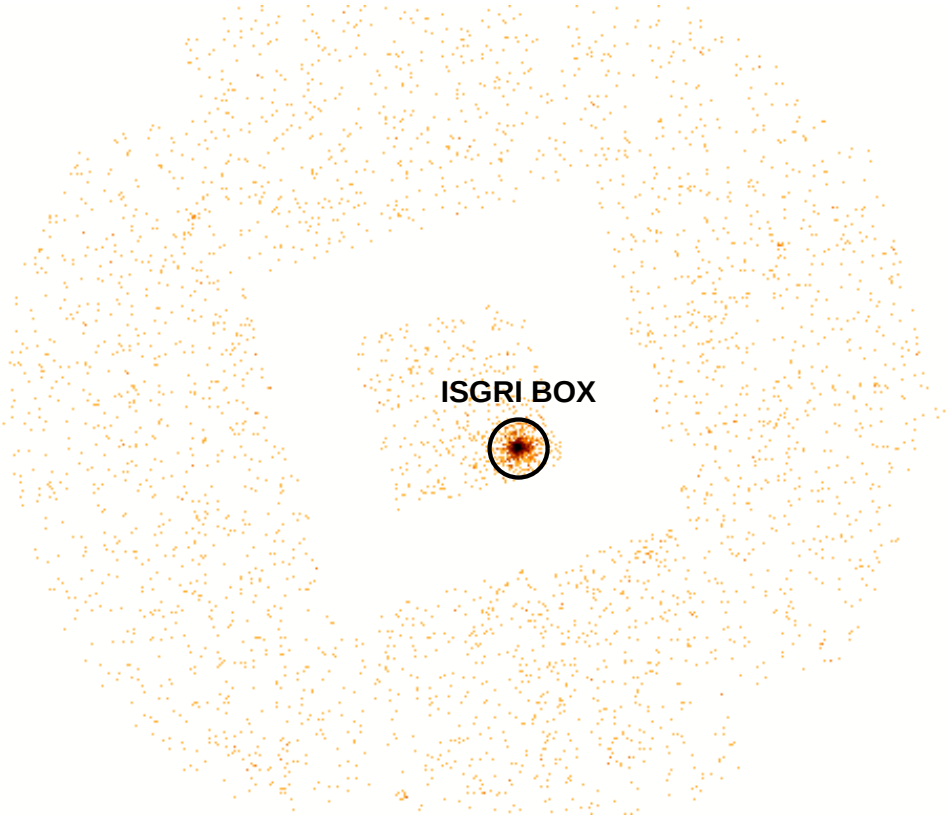


(a) MOS1

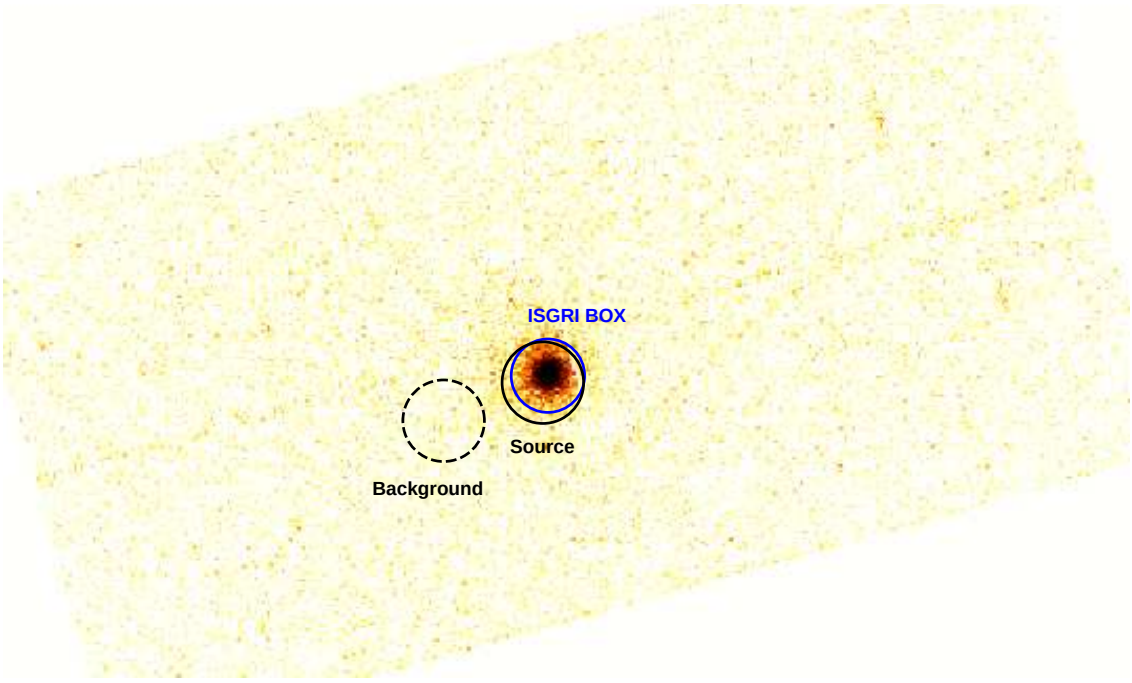


(b) pn

**Figure** *8.3: EPIC 0.8–10 keV image of IGR J16393−4643. The ISGRI error box of 0.9′ is shown in blue. The regions to extract spectra of the source and the background are also shown in black in the pn image.*

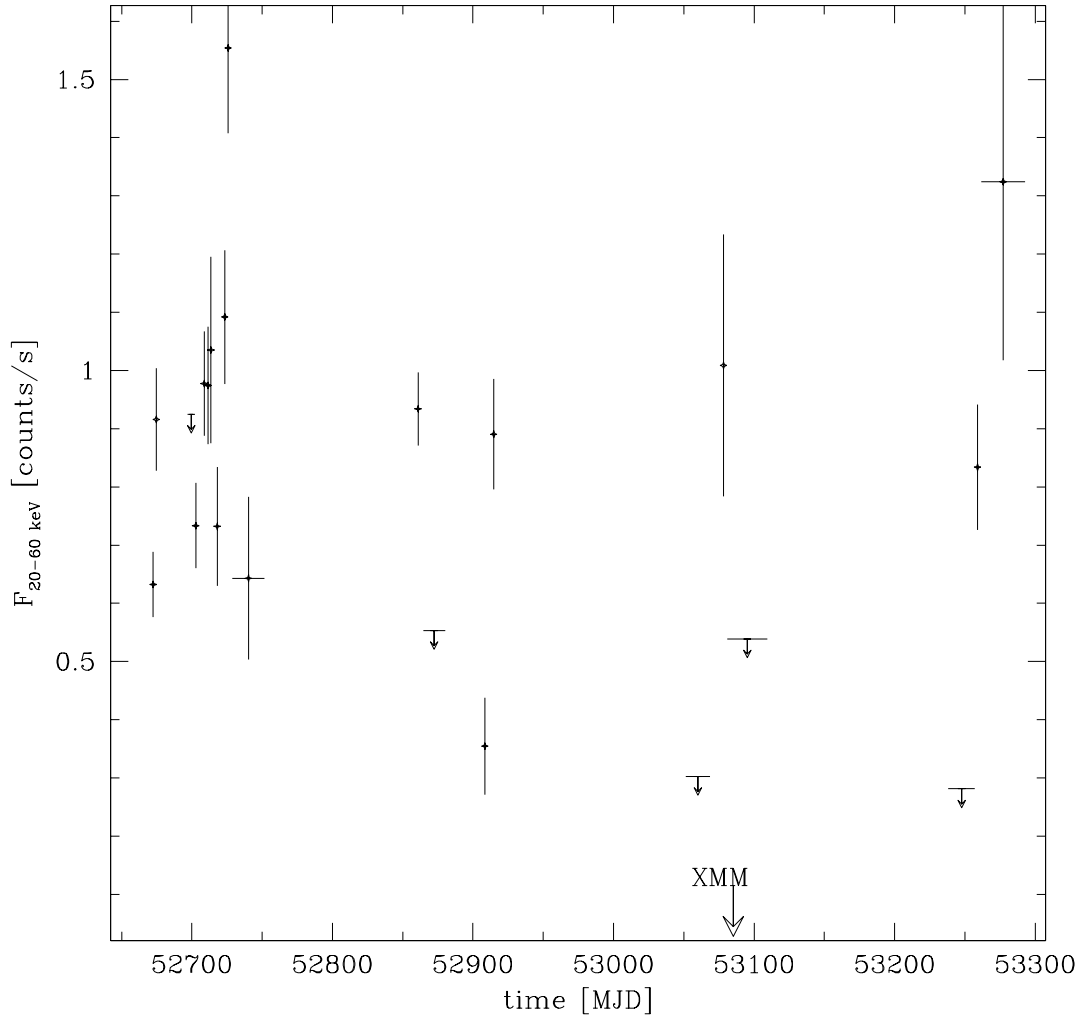


**Figure** *8.4: 20–60 keV count rate of IGR J16393−4643 from revolution 30 to revolution 244 (MJD 52650.15–53293.23). The upper limits are at the 3σ level.*

than 10° from the FOV centre were discarded. The background activity is too important far from the FOV centre and the sensitivity is not sufficient enough, so the source is never detected and it just adds noise in the light curve. Most of the time, the source is too faint to be observed in a single ScW (see Fig. 8.5). The 20–60 keV average flux varies between 1.5 and 3.0 counts $s^{-1}$ with a few pointings where the source flux reaches $\geq$4 counts $s^{-1}$.

### The spin period

Once the long-term behaviour of IGR J16393−4643 is known, we can study the light curve on short time scales. A 0.4–10 keV light curve is extracted from the EPIC/pn data. All the single+double events within a radius of 60″ centred on the source (see Fig. 8.3.1) and with an energy comprised in the 4000–10000 eV range were collected, except for the events tagged as bad. A similar region was extracted for the background in the same CCD, at a similar distance from the read out node, but far enough not to be affected by the source emission. The chosen binning is 3 s. The background was subtracted with the help of the `FTOOLS lcmath`. The resulting 0.4–10 keV light curve is shown in Fig. 8.6.

A periodic modulation is clearly visible in the light curve. It lasts around 900 s. There is also substructure within one cycle. Two peaks are visible in one cycle. Due to the shortness of the observation and the lapse time removed at the end of the observation due to background activity (see Fig. 8.2), IGR J16393−4643 has been observed only during 5 cycles.

We generated a Lomb-Scargle periodogram with this light curve (see Fig. 8.7). Four peaks are detected : (1481±10) s, (912±4) s, (581±2) s, and (457±1) s. However, only the 912 s modulation corresponds to that observed in the light curve. The 0.4–10 keV light curve is folded on this period (see Fig. 8.8). The corresponding ephemeris is :

$$\mathrm{MJD}\, T = \mathrm{MJD}\, 53085.36528 + n \times (912\,\mathrm{s}/86400) \tag{8.1}$$

where n is the number cycle. Two peaks are visible. The shape is similar to the light curve (see Fig. 8.6). The emission between both peaks is important. The pulse fraction is of 35±3% (see Eq. 7.2). The shape is similar to that of the Crab pulsar with two peaks and a significant emission in between (the *bridge* emission) (Kuiper et al. 2001). The peak at 457 s would be the harmonic of the 912 s period. The other 2 periods might be due to the fact that the light curve shows strong substructure in one cycle and that the observation is so short we get very few cycles. We also searched for this period in the ISGRI data. However, a Lomb-Scargle periodogram on the time set covering the revolutions 37, 38, 47, 49, 50, 51, 52, 54, 55, 100, and 118 does not show any modulation (see Fig. 8.9). The source is too faint.

This modulation can be interpreted as the spin period of IGR J16393−4643. In the polar cap scenario where the presence of a magnetic field would force the accretion at the pole of the source, we see the X-ray emission increase when one of the poles is directed towards the detectors. The presence of the two peaks would mean that we are seeing both poles at periodic times where the accretion is more important. The emission does not drop to zero in between both peaks.

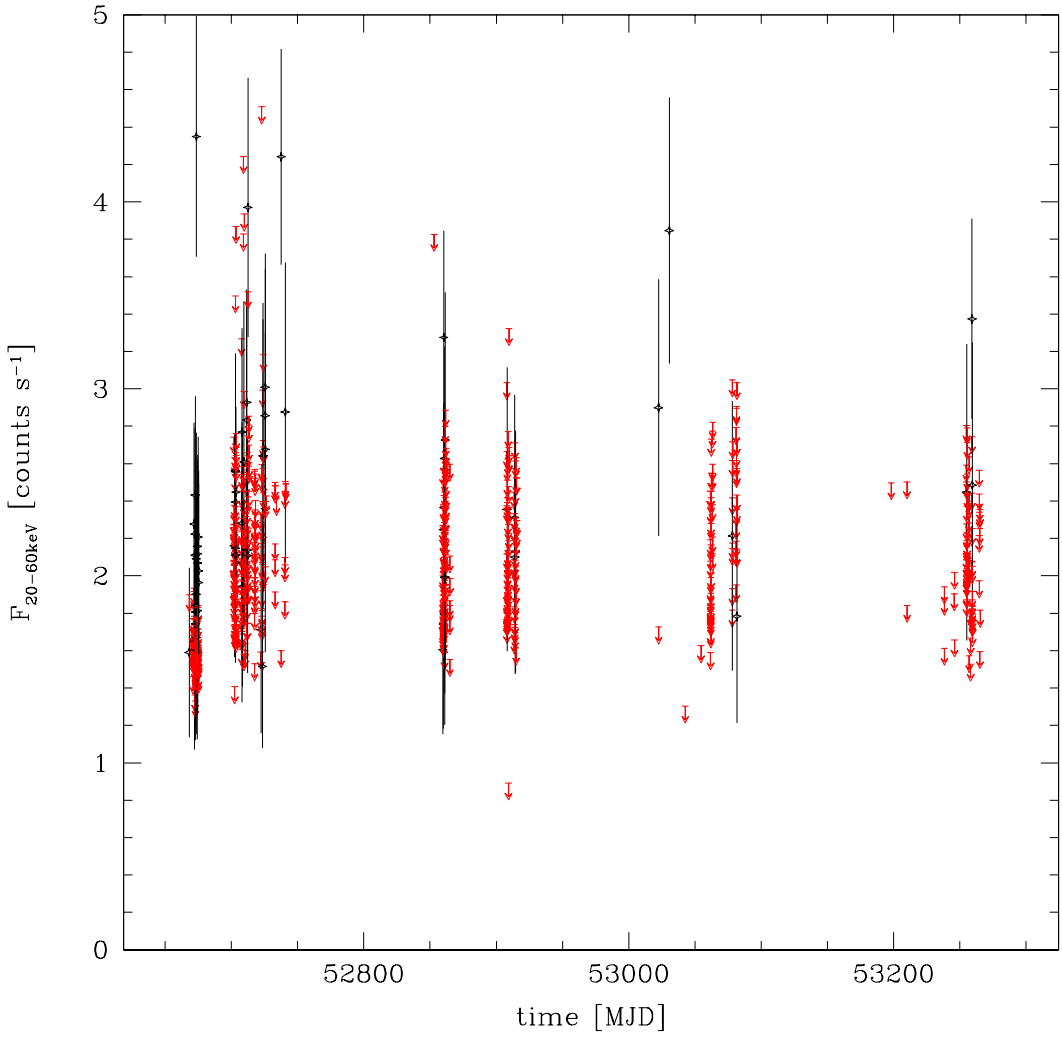


**Figure** *8.5: 20–60 keV count rate per pointing (exposure ∼2 ks) of IGR J16393−4643 from revolution 30 to revolution 244 (MJD 52650.15–53293.23). The upper limits are at the 3σ level. Only pointings with the off-axis angle of IGR J16393−4643 lower than 10º are considered.*

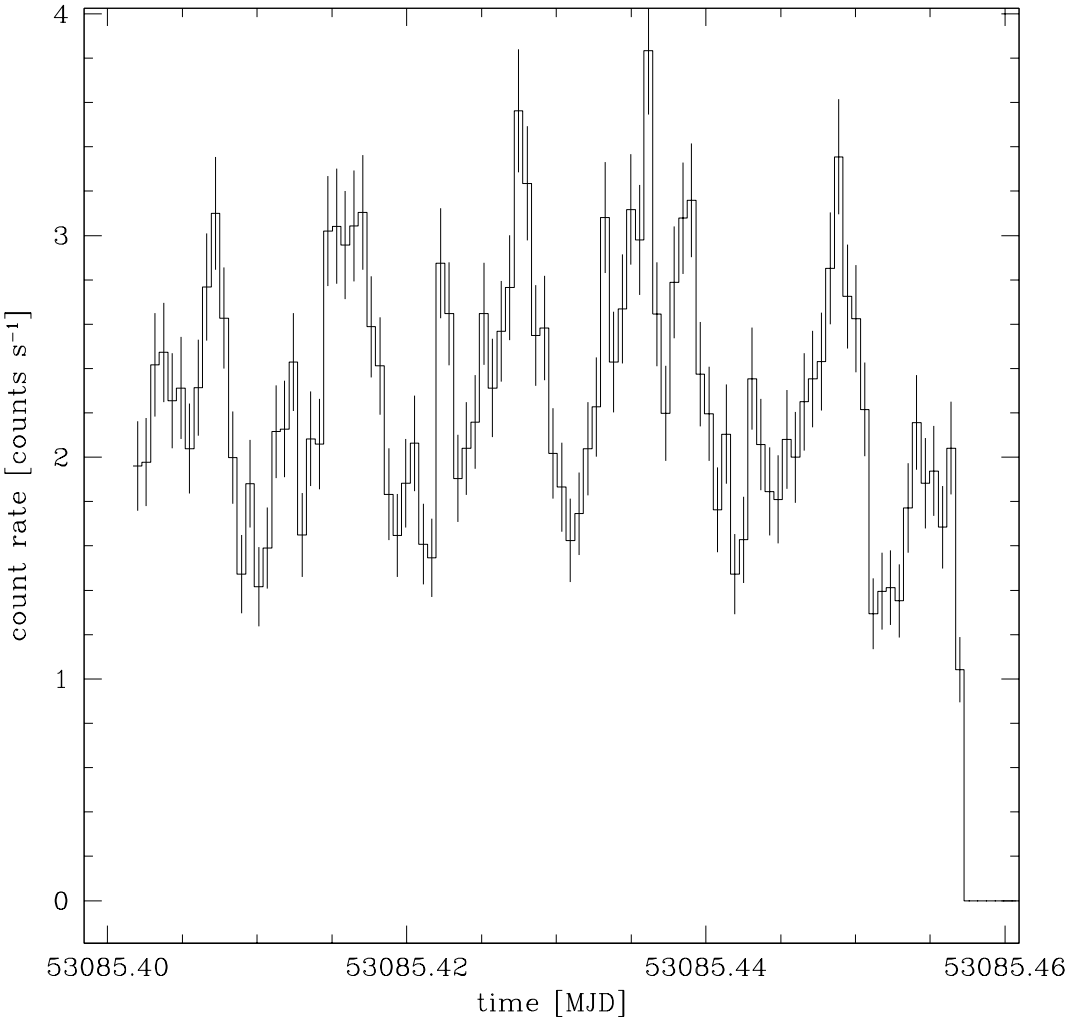


**Figure** *8.6: 0.4–10 keV light curve of IGR J16393−4643. The light curve drops to zero because the events at the end of the observation are discarded due to high background activity.*

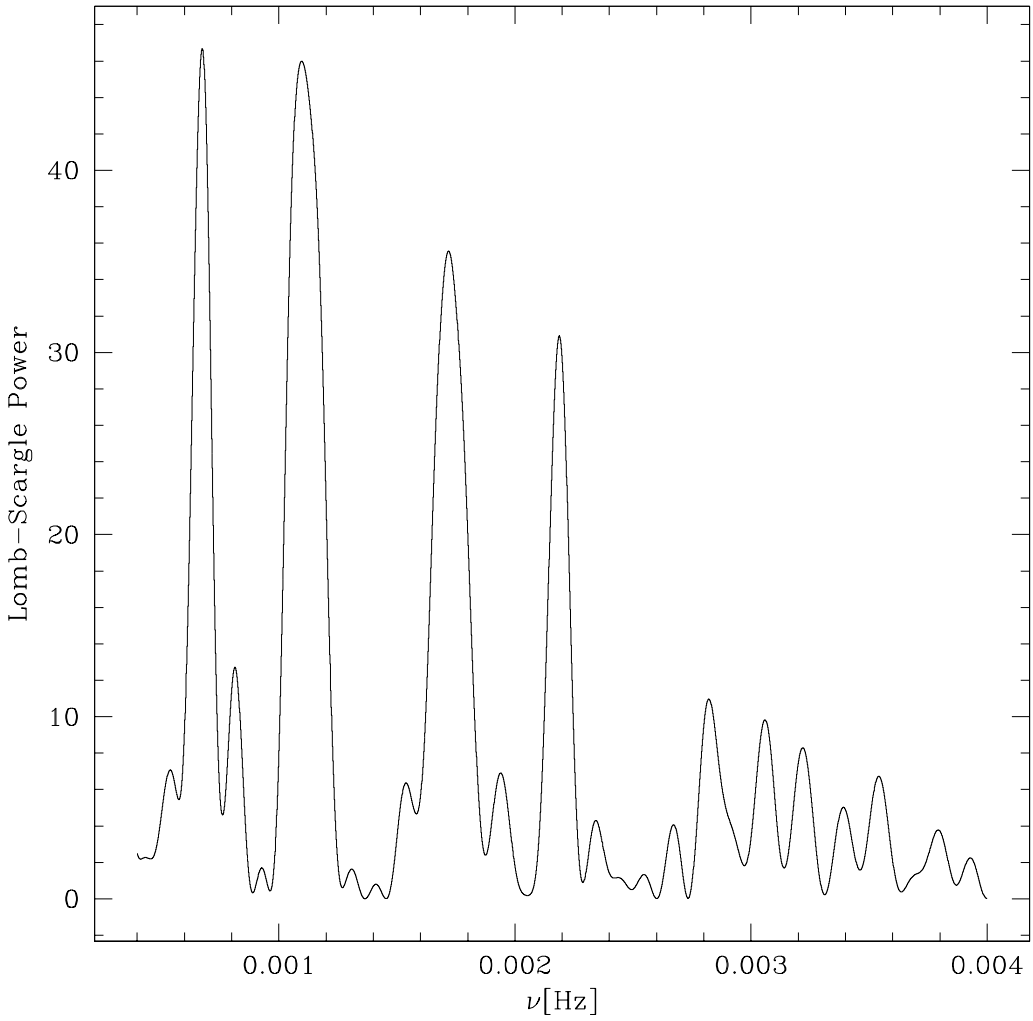


**Figure** *8.7: Lomb-Scargle periodogram of IGR J16393−4643. 4 peaks are visible : (1481±10) s, (912±4) s, (581±2) s, and (457±1) s. The peak corresponding to the modulation seen in the light curve is the second one.*

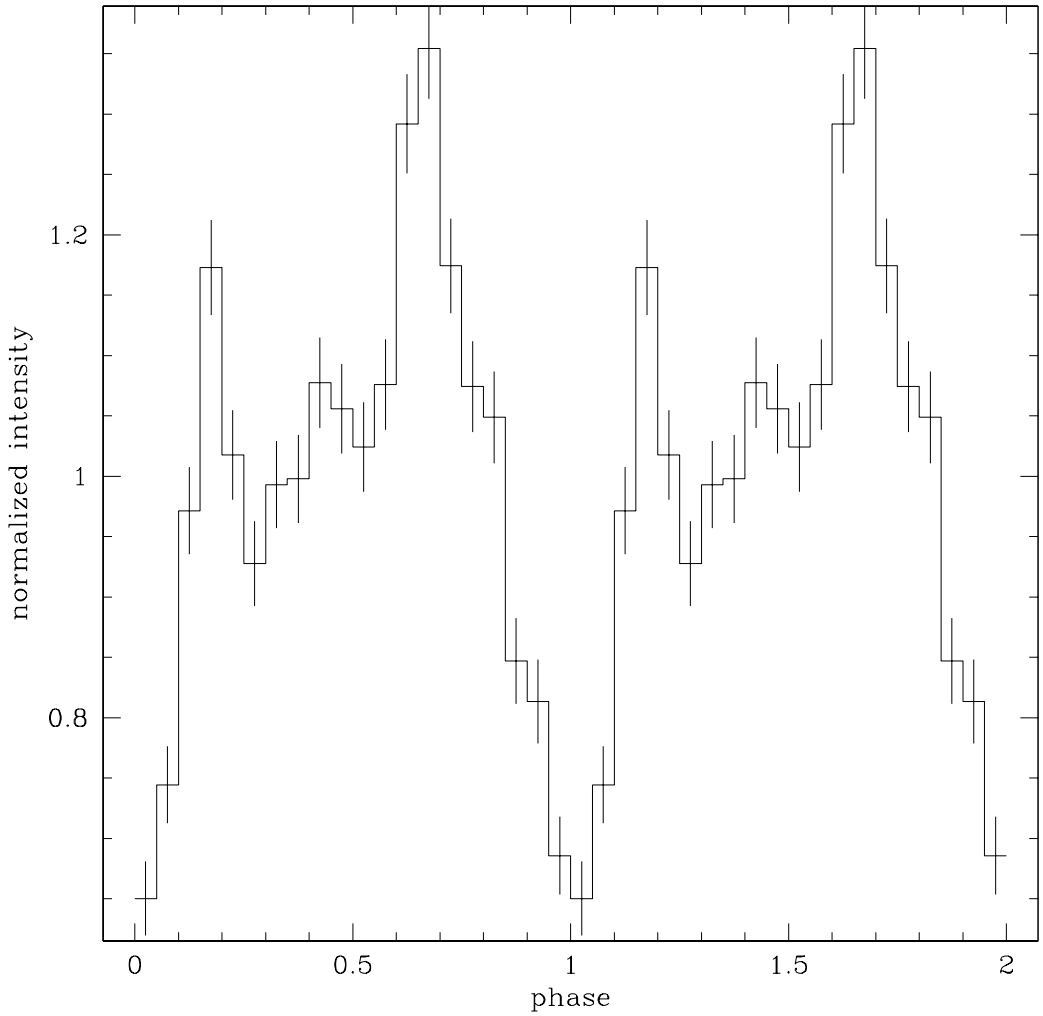


**Figure** *8.8: 0.4–10 keV folded light curve of IGR J16393−4643. The period is 912 s and the time zero is MJD 53085.36528.*

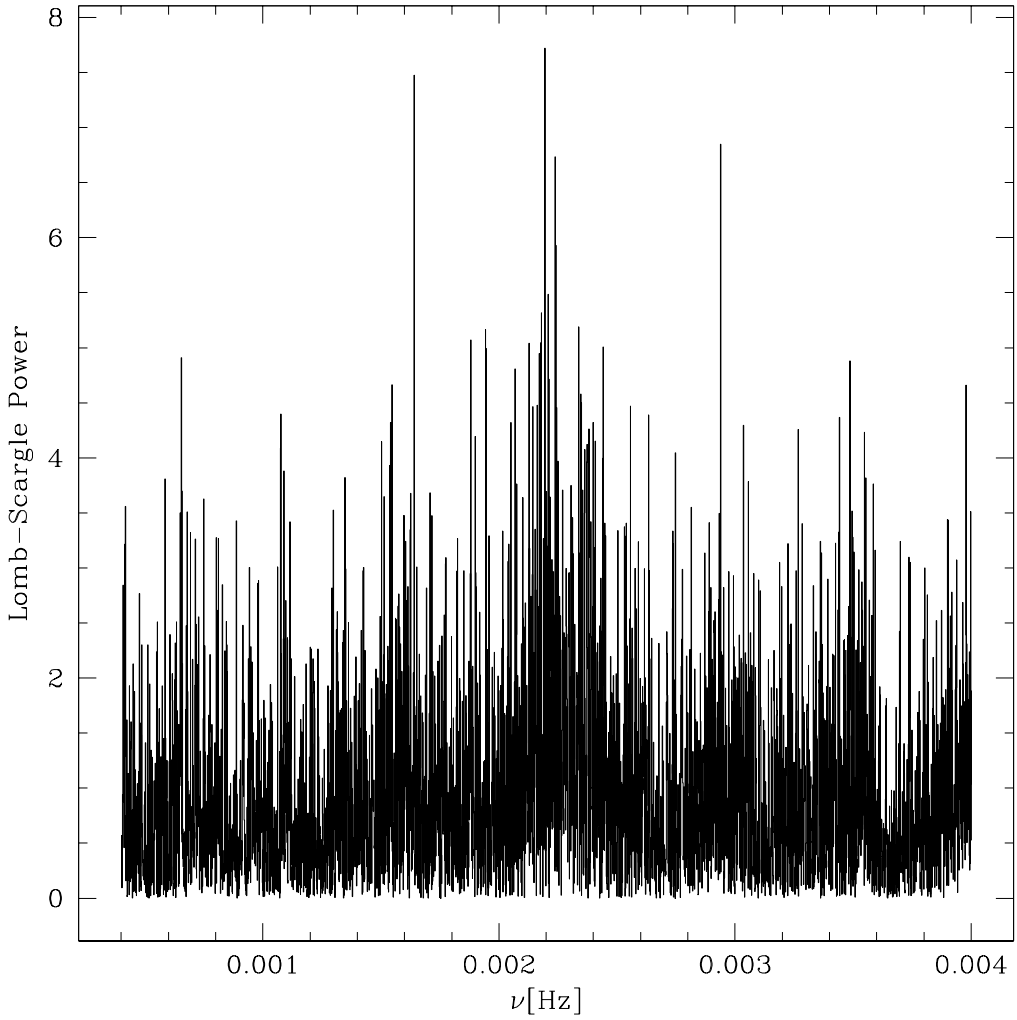


**Figure** *8.9: Lomb-Scargle periodogram of IGR J16393−4643 generated from the 15–30 keV light curve grouping the revolutions 37, 38, 47, 49, 50, 51, 52, 54, 55, 100, and 118.*

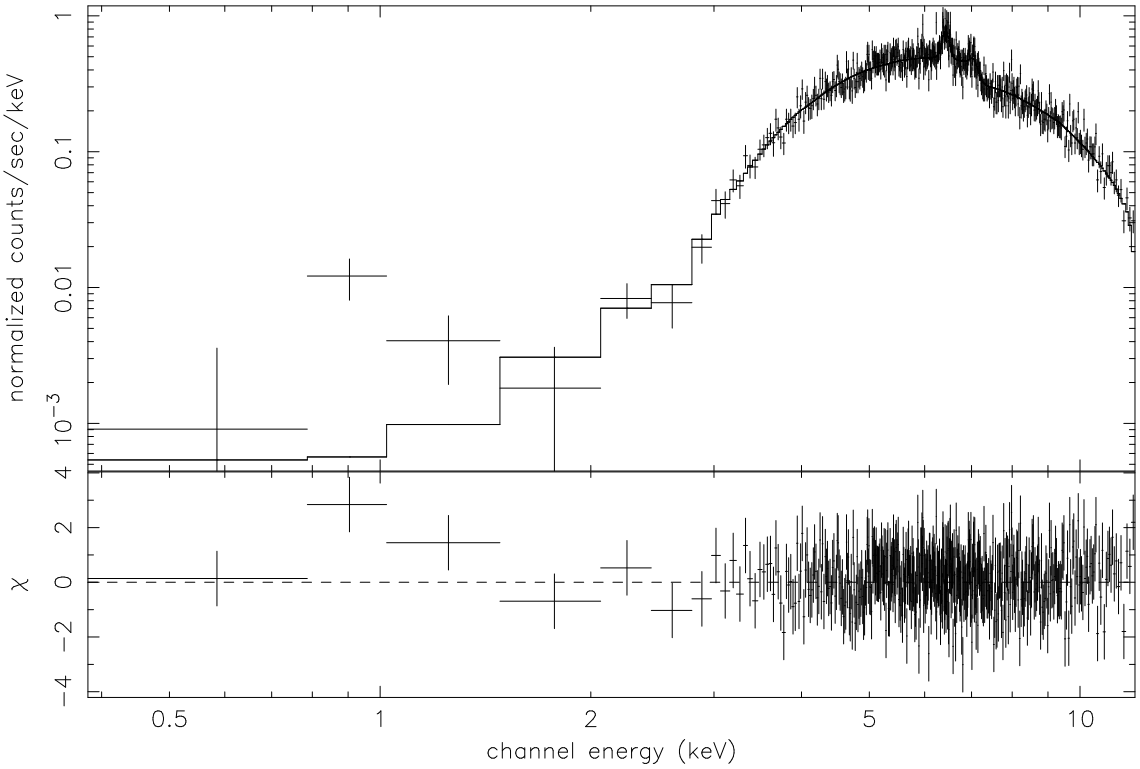


**Figure** *8.10: 0.2–12 keV average spectrum of IGR J16393−4643. The spectrum has been modelled with an absorbed power law, plus 2 emission lines that correspond to cold iron. A black body is added at low energies to take into account the apparent excess. The best fit gives :* $N_{\rm H} = (27.6 \pm 0.8)$ *cm*$^{-2}$, $\Gamma = 0.81 \pm 0.09$, *and lines at E=(6.42±0.02) keV and (7.08±0.08) keV. The unabsorbed 2–10 keV flux is* $2\,10^{-10}$ *ergs cm*$^{-2}$ *s*$^{-1}$.

### 8.3.3 Spectral analysis

EPIC/pn average spectra of the source and the background are extracted in the same regions as seen previously for the light curve extraction (see Fig. 8.3.1). As for IGR J17252−3616 (see Sect. 6.4.3), only single+double events are kept. Even if the source is bright in the pn image (see Fig. 8.3.1), pile-up contamination is acceptable. The response matrix file and the ancillary file are created after calculating the area where the 2 spectra are extracted. The resulting spectra are rebinned to have a minimum of 30 counts per channel in order to avoid too many channels and be able to use the $\chi^2$ statistic.

The 0.2–12 keV average spectrum is shown in Fig. 8.10. The visible characteristics at first sight are the strong absorption at low energies and the presence of an emission line at 6.4 keV. The spectral analysis was performed with `Xspec` package version 11.3.1.

The spectrum is first fitted with the simplest phenomenological model, a single absorbed power law. This fitting leads to a reduced $\chi^2$ ($\chi^2_\nu$) of 1.12 (450 degrees of freedom (dof)). The spectrum is hard with $\Gamma = 0.91 \pm 0.09$ and the absorption is high with $N_{\rm H} = (29 \pm 1)\,10^{22}$ cm$^{-2}$. However, in the residual, there is clearly a deviation at 6.4 keV between the data and the model.

Therefore, we add a new component to the model : a Gaussian to fit the emission line.

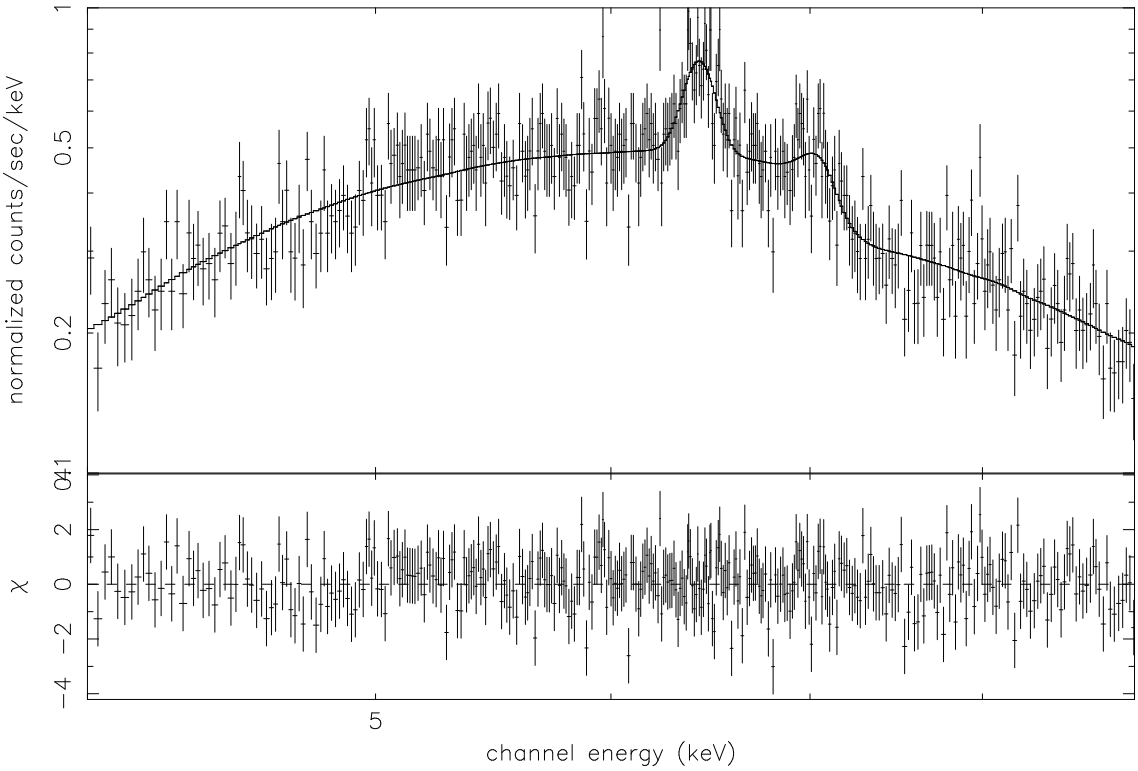


**Figure** *8.11: Zoom of the average spectrum of IGR J16393−4643. The two emission lines due to the cold iron fluorescence are clearly visible. The fluxes are :* $K\alpha = (1.3 \pm 0.3)\,10^{-4}$ *ph cm*$^{-2}$ *s*$^{-1}$ *and* $K\beta = (0.4 \pm 0.3)\,10^{-4}$ *ph cm*$^{-2}$ *s*$^{-1}$.

This improves the fitting. The $\chi^2_\nu$ is 0.94 (447 dof) and we obtain : $\Gamma = 0.91 \pm 0.09$, $N_{\rm H} = (29 \pm 1)\,10^{22}$ cm$^{-2}$ and $E_{\rm l} = (6.42 \pm 0.02)$ keV. Going further and when rebinning the spectrum more, there is some hint of a second line at 7.1 keV.

A second Gaussian emission line is added to the model. This results in a $\chi^2_\nu$ of 0.92 (444 dof) that is comparable to the one without a second line. In Fig. 8.11, we zoom on the part of the spectrum containing the two lines. The 2nd line is visible in the spectrum even if the statistic does not change. The 2nd line is situated at $E_{\rm l} = (7.08 \pm 0.09)$ keV.

Finally, we add a phenomenological black-body model at low energies to take into account the apparent excess at 1 keV. This new component does not change the fitting accuracy : $\chi^2_\nu$=0.92 (442 dof). The unabsorbed 2–10 keV flux is $2\,10^{-10}$ ergs cm$^{-2}$ s$^{-1}$. The best fit model is reported in Fig. 8.10.

All the fitting steps are summarised in Table 8.4. The absorption is too large to be accounted for by interstellar absorption alone. Indeed, the galactic absorption is $2.1\,10^{22}$ cm$^{-2}$ in the source direction (Dickey & Lockman 1990). The local absorption is ten times higher. The matter density must be high locally around the system. The 2 emission lines correspond to the fluorescence emission line of cold iron.

The combined pn+ISGRI spectral analysis is done in the papers Bodaghee et al. (2005) (see next section) and Walter et al. (2005) (see Sect. 9.4).

**Table** 8.4: Summary of the models fitted on the pn spectrum of IGR J16393−4643. The spectral analysis was performed with `Xspec`. The model abbreviations stand for : pl=power law, ga=Gaussian, bb=black-body, w=absorption model `wabs`. EW stands for line equivalent width. The errors are noted at the 90% confidence level.

| model | `w*pl` | `w*(pl+ga)` | `w*(pl+ga+ga)` | `w*(bb+pl+ga+ga)` | unit |
|---|---|---|---|---|---|
| $N_{\rm H}$ | 29±1 | 28±1 | 28±1 | 27.6±0.8 | $10^{22}$ cm$^{-2}$ |
| kT | | | | $0.09^{+0.02}_{-0.09}$ | keV |
| $\Gamma$ | 0.91±0.09 | 0.82±0.09 | $0.81^{+0.09}_{-0.10}$ | 0.81±0.09 | |
| $E_{\rm l1}$ | | 6.42±0.02 | 6.42±0.02 | 6.42±0.02 | keV |
| EW1 | | 106 | 111 | 111 | eV |
| Flux line 1 | | $1.2^{+0.3}_{-0.2}$ | $1.3^{+0.3}_{-0.2}$ | $1.3^{+0.3}_{-0.2}$ | $10^{-4}$ ph cm$^{-2}$ s$^{-1}$ |
| $E_{\rm l2}$ | | | 7.08±0.09 | 7.08±0.08 | keV |
| EW2 | | | 40 | 38 | eV |
| Flux line 2 | | | $4^{+3}_{-2}$ | 4±3 | $10^{-5}$ ph cm$^{-2}$ s$^{-1}$ |

## 8.4 Scientific paper on IGR J16393−4643 published in AA

This investigation resulted in a scientific article that has been accepted for publication in *A*stronomy & Astrophysics :

*IGR J16393-4643: a new heavily-obscured X-ray pulsar*, Bodaghee A., Walter R., Zurita Heras J. A., Bird A.J., Courvoisier T.J.-L., Malizia A., Terrier R., and Ubertini P., 2005, astroph/0510112,

for which we give a quick summary.

With the improved X-ray position, one infrared counterpart has been identified, 2MASSS J16390535−4642137. The microquasar scenario proposed by Combi et al. (2004) is discarded since the radio source error box is not compatible with EPIC error box.

The average pn+ISGRI spectrum of IGR J16393−4643 can be well fitted with an absorbed power law with an energy cutoff or a Compton emission (CE) model. As seen in Sect. 8.3.3, the spectrum is hard ($\Gamma = 0.8$) with the an energy cutoff at 10 keV. The absorption is large with $N_{\rm H} = 25\,10^{22}$ cm$^{-2}$, ten times higher than the galactic one ($N_{\rm H} = 2.1\,10^{22}$ cm$^{-2}$) (Dickey & Lockman 1990). Pulse phase-resolved spectroscopy does not show any spectral variability except its continuum normalisation. The spectral parameters are typical of pulsar systems (White et al. 1995). The huge absorption and the strength of the cold iron K$\alpha$ line are compatible with a spherical distribution of matter around the compact object (Matt 2002).

IGR J16393−4643 is a HMXB wind-fed accreting pulsar system. Considering its unabsorbed flux and the typical HMXB luminosity of $1.2\,10^{36}$ ergs s$^{-1}$, IGR J16393−4643 would be located ∼10 kpc away.

# Chapter 9
# A SAMPLE OF *IGR SOURCES* OBSERVED BY ***INTEGRAL*** AND ***XMM-Newton***

In this chapter, we describe in full detail the *INTEGRAL* and *XMM-Newton* analysis of a sample of (re-)discovered *INTEGRAL* sources. These sources were extensively observed with the satellite *INTEGRAL* during the core programme dedicated to the galactic centre and galactic plane.

A follow-up campaign with *XMM-Newton* was performed on a sub-sample of 6 IGR sources as already seen for IGR J17252−3616 (see Chapter 6) and IGR J16393−4643 (see Chapter 8). The rest of the list of sources belonging to this programme is : IGR J16418−4532, IGR J16479−4514, IGR J17597−2201, and IGR J18027−2016.

The other sources selected for our paper have already been observed by other space missions : IGR J16318−4848, IGR J16320−4751, IGR J16465−4507, and IGR J17544−2619.

## 9.1 Discovery and history

### IGR J16318−4848

IGR J16318−4848 was the first hard X-ray source discovered by *INTEGRAL* on January 29, 2003 (Courvoisier et al. 2003a). This new point source was localised at the position R.A. (2000.0)=16h31m52s and Dec.=$-48^{o}\,48'\,30''$ with an uncertainty of $2'$. The 15–40 keV flux varied between 50–100 mCrab on a time scale as short as 1 ks. The source is located in the Norma Arm region.

After its discovery, the source was observed by *XMM-Newton* (Walter et al. 2003; Matt & Guainazzi 2003). The improved position was R.A. (2000.0)=16h31m48s.6 and Dec.=$-48^{o}\,49'\,00''$ with an uncertainty of $4''$. The X-ray averaged spectrum showed strong emission lines of iron (Fe K$\alpha$ at 6.4 keV and Fe K$\beta$ at 7.1 keV) and nickel (Ni K$\alpha$ at 7.5 keV). The spectrum was highly absorbed at energies softer than 5 keV with an estimated intrinsic photo-electric absorption as large as $\sim 2\,10^{24}$ cm$^{-2}$.

The source was observed in optical and IR wavelengths on February 23–25, 2003, using the NTT telescope at La Silla (Filliatre & Chaty 2004). They confirmed the binary nature of IGR J16318−4848. The companion star would be an early-type supergiant star (classified

as a sgB[e] star) surrounded by a dense circumstellar material. Several emission lines were detected. IGR J16318−4848 is therefore a HMXB.

### IGR J16320−4751

IGR J16320−4751 was discovered a few days later than IGR J16318−4848 in the same field (Norma Arm) on February 1, 2003 (Tomsick et al. 2003). Its position is R.A. (2000.0)=16h32m00s and Dec.=$-47^{\rm o}\,51'\,00''$ with an uncertainty of $2'$. The 15–40 keV flux varied between <10–50 mCrab on a time scale as short as 1 ks. The source was also detected on some occasions at energies higher than 60 keV. The position was consistent with the *ASCA* source AX J1631.9-4752.

IGR J16320−4751 was observed on two occasions by *XMM-Newton* (Mar. 4-5, 2003, and Aug. 19-20 2004) (Rodriguez et al. 2003b, 2005). The best X-ray position is R.A. (2000.0)=16h32m01s.9 and Dec.=$-47^{\rm o}\,52'\,27''$ with an uncertainty of $3''$. The 2–12 keV and 20–60 keV light curves showed significant variability with flaring activity. A pulsation at ∼1300 s was also detected in the EPIC and ISGRI data (Lutovinov et al. 2005b). The spectral properties of IGR J16320−4751 were a hard continuum ($\Gamma < 1$), strong absorption ($N_{\rm H} \sim 10^{23}$ cm$^{-2}$), the detection of the Fe K$\alpha$ fluorescence line, and a soft excess. The features shown in the spectrum are consistent with a HMXB system.

Recently, Corbet et al. (2005a) have discovered the orbital period with *Swift*/BAT data : 8.96±0.01 d and the epoch of maximum flux MJD 53507.1±0.1.

### IGR J16418−4532

IGR J16418−4532 was discovered during the observation of the black hole 4U 1630-47 on the February 1–5, 2003 (Tomsick et al. 2004). The source is located at R.A. (2000.0)=16h41m48s and Dec.=$-45^{\rm o}\,32'\,00''$ with an uncertainty of $2'$. The 20–40 keV flux is $3\,10^{-11}$ ergs cm$^{-2}$ s$^{-1}$.

### IGR J16465−4507

IGR J16465−4507 is a transient source discovered on September 6–7, 2004 (Lutovinov et al. 2004). The position was R.A. (2000.0)=16h45m30s and Dec.=$-45^{\rm o}\,07'\,30''$ with an uncertainty of $2'.5$. The average 18–60 keV flux was 9 mCrab. The source flared up to 28 mCrab on September 7 at 12:00 UTC and decayed to previous flux level afterwards.

An *XMM-Newton* ToO observation on September 14, 2004, allowed us to improve the X-ray position as a single counterpart lying within the ISGRI error box: R.A. (2000.0)=16h46m35s.5 and Dec.=$-45^{\rm o}\,07'\,04''$ with an uncertainty of $4''$ (Zurita Heras & Walter 2004). The 4–10 keV flux was $3\,10^{-12}$ ergs cm$^{-2}$ s$^{-1}$ (∼ 0.3 mCrab), 100 times fainter than during the flare detected by *INTEGRAL*. A bright infrared counterpart (2MASS J16463526-4507045, J=10.54) is found in the 2MASS catalogue.

Negueruela et al. (2005b) confirm that it is a HMXB. Optical observations of the companion star indicates the presence of an early-type supergiant star.

### IGR J16479−4514

IGR J16479−4514 was discovered at the position R.A. (2000.0)=16h47m54s and Dec.=−45° 14′ 00″ with an uncertainty of 3′ during a GCDE observation on August 8–9, 2003 (Molkov et al. 2003). The 18–25 and 25–50 keV fluxes were 12 and 8 mCrab, respectively. On August 10, the flux increased by a factor 2.

Another detection with the *Swift* Burst Alert System (BAT) was reported on August 30, 2005 (Kennea et al. 2005). The improved position is R.A. (2000.0)=16h48m07s and Dec.=−45° 12′ 05″.8 with an uncertainty of 6″. The source was highly variable and displayed two flares lasting several hundreds of seconds (400 s and 1000 s). The spectrum is well fitted with an absorbed power law with $N_{\rm H} = 6.4\,10^{22}$ cm$^{-2}$ and $\Gamma \sim 1.1$.

Sguera et al. (2005) also report *INTEGRAL* observations of IGR J16479−4514. They propose that the source could be a LMXB system such as a Fast X-ray Transient (FXT). They found 4 short bright outbursts (20–30 keV flux greater than 30 mCrab) lasting less than 3 hours that are interpreted as type I X-ray bursts. On the other hand, Negueruela et al. (2005a) introduce a new sub-class of Supergiant Fast X-ray Transients (SFXT) composed of HMXB systems that show strong short outbursts and that would have a quiescent flux lower than the typical $\sim 10^{36}$ ergs s$^{-1}$. Therefore, they propose that IGR J16479−4514 is a HMXB belonging to that class.

### IGR J17544−2619

IGR J17544−2619 was discovered on September 17, 2003, at the position R.A. (2000.0)=17h54m.4 and Dec.=−26° 19′ with an uncertainty of 2′ during a Galactic Centre field observation with IBIS/ISGRI (Sunyaev et al. 2003). The source was bright for 2 hours and then faded away. The 18–25, 25–50 and 50–100 keV fluxes were of 160, 60 and <15 mCrab, respectively.

Wijnands (2003) proposed that IGR J17544−2619 is the hard X-ray counterpart of 1RXS J175428.3-262035 that is located at the edge of the ISGRI error box.

A new outburst happened a few hours after its discovery that lasted 8 hours with a 18–25 keV flux of 45 mCrab (Grebenev et al. 2003). The profile was complex with two peaks reaching 60 and 80 mCrab, respectively.

Besides, Gonzalez-Riestra et al. (2003) report the detection of IGR J17544−2619 on September 11.92 UTC, *i.e.* 5 days earlier than the discovery, during a 10 ks *XMM-Newton* observation of V4643 Sgr. The X-ray position is R.A. (2000.0)=17h54m25s.7 and Dec.=−26° 19′ 58″ with an uncertainty of 10″. The 2–10 keV flux was $4.5\,10^{-12}$ ergs cm$^{-2}$ s$^{-1}$. Thanks to the improved position, Rodriguez et al. (2003a) report a possible IR/optical counterpart, 2MASS J17542527-2619526 (also present in the USNO B1.0 optical catalogue). The field where IGR J17544−2619 is located was observed three times by *XMM-Newton* in 2003 : March 11 and September 11 and 17 (González-Riestra et al. 2004). The source is transient : no detection in March, 0.5–10 keV flux of $1.1\,10^{35}$ ergs s$^{-1}$ on Sept. 11, and $5.7\,10^{35}$ ergs s$^{-1}$ on Sept. 17 (for an assumed distance of 8 kpc). They provide the most accurate X-ray position that is R.A. (2000.0)=17h54m25s.37 and Dec.=−26° 19′ 52″.9 with an uncertainty of 4″. This new position excludes the ROSAT counterpart. The spectra extracted during the outbursts show no intrinsic absorption and a hardening with increasing intensity. The source intensity is indicative of a binary system-type with a compact object (either neutron star or black hole). Combining the OM image and IR counterpart

proposed by Rodriguez et al. (2003a), the companion star would be an early O-type star.

A new outburst was detected by *INTEGRAL* on March 8, 2004 (Grebenev et al. 2003). At the peak, the 17–45 keV flux reached ∼160 mCrab. It lasted approximately 10 h. This would suggest that the source is a recurrent transient system.

in't Zand & et al. (2004) reported observations of IGR J17544−2619 with *BeppoSAX* and *RXTE*. *BeppoSAX* detected 5 outbursts with fluxes compatible with those detected by *INTEGRAL*. *RXTE* only caught a few times the source emitting upper the instruments detection threshold, but when it happened, the source showed some flares that could reach 0.4 Crab (2–12 keV). The source is very variable and the duration of outbursts span from a few minutes to a few hours.

IGR J17544−2619 has been also observed with *Chandra*, both in quiescence and in outburst state (in't Zand 2005). The most accurate position is R.A. (2000.0)=17h54m25s.284 and Dec.=$-26^{\rm o}\,19'\,52''.62$ with an uncertainty of $0''.6$. The companion star is a blue supergiant of spectral type O9Ib at 3–4 kpc. The quiescent spectrum is very soft and is more indicative of a neutron star than a black hole as compact object.

### IGR J17597−2201

IGR J17597−2201 was discovered by *INTEGRAL* during an observation of the galactic central region on March 31–April 1, 2003 (Lutovinov et al. 2003b). The 15–40 keV flux was 5 mCrab and increased up to 10–15 mCrab during April 15–24. At that time, the 40–100 keV flux was 10 mCrab.

Markwardt & Swank (2003) associate IGR J17597−2201 with the transient XTE J1759-220. This source was first detected by *RXTE*/PCA at February 7, 2001, during a galactic bulge scan. It has been active since its discovery. The source shows erratic variability with a 2–10 keV flux varying between 2 to 17 mCrab. They also suggest that the source shows dipping features and a period of 1–3 h. The spectrum is soft ($\Gamma$ ∼1.8–2.9). An emission line, probably Fe K, with a centroid at 6.5–6.7 keV and an equivalent width of 130–250 keV is also detected. They also add that the source might be a neutron star in a short-period binary system.

IGR J17597−2201 was extensively observed in 2003 (exposure 1.5 Ms) and 2004 (179 ks) during a deep observation of the Galactic Centre region (Lutovinov et al. 2005a). The 18–60 keV X-ray flux drastically changed between both years : 6.9 and 2.8 mCrab, respectively. This was accompanied by a spectral state change from low/hard to high/soft. Their spectral analysis confirms the Markwardt & Swank (2003) suggestion that IGR J17597−2201 is a neutron star within a LMXB system.

### IGR J18027−2016

IGR J18027−2016 is reported in both hard X-ray catalogues of Bird et al. (2004) and Revnivtsev et al. (2004).

This helped the serendipitous discovery of the X-ray pulsar SAX J18027.7-2017 (Augello et al. 2003). The source was found near GX 9+1 in archival *BeppoSAX* data. The source was observed in September 16–20, 2001. The average 0.1–10 keV flux was $3.6\,10^{-11}$ ergs cm$^{-2}$ s$^{-1}$. A timing analysis reveals a pulse period of 139.6 s, an orbital period of 4.6 d, a projected semi-major axis $a_x \sin i \sim 70$ lt-s, and a mass function $f(M) \sim 17 M_\odot$. The object

**Table** 9.1: Journal of the *XMM-Newton* observations of IGR sources

| Source | Date | | exposure |
|---|---|---|---|
| | start UTC | MJD | ks |
| IGR J16393−4643 | 2004-03-21T08:38:45.0 | 53085.36 | 10.9 |
| IGR J16418−4532 | 2004-08-19T06:00:25.0 | 53236.25 | 23.2 |
| IGR J16465−4507 | 2004-09-14T02:16:23.0 | 53262.10 | 8.9 |
| IGR J16479−4514 | 2004-03-21T16:55:33.0 | 53085.71 | 14.4 |
| IGR J17252−3616 | 2004-03-21T13:02:45.0 | 53085.54 | 10.9 |
| IGR J17597−2201 | 2004-03-21T21:57:22.0 | 53085.92 | 24.7 |
| IGR J18027−2016 | 2004-04-06T06:34:16.0 | 53101.27 | 11.9 |

shows periods typical of a HMXB accreting through stellar wind. Its position is R.A. (2000.0)=18h02m39s.9 and Dec.=$-20^{\rm o}\,17'\,13''.50$ with an uncertainty of $2'$.

Lutovinov et al. (2005a) confirms the HMXB scenario using *INTEGRAL* data and performing spectral analysis. The 18–60 keV flux is ∼5 mCrab.

Hill et al. (2005) performed a combined analysis using the *BeppoSAX*, *INTEGRAL* and *XMM-Newton* data. The source is persistent in the 20–40 keV energy range with an average flux of 6 mCrab. The source shows intrinsic absorption, $N_{\rm H} = 6.8\,10^{22}$ cm$^{-2}$. They confirmed the timing parameters and the nature of the object. The *XMM-Newton* data are also presented in Walter et al. (2005) (and in this thesis).

## 9.2 The observations

As all these sources are concentratred in the same portion of sky (*i.e.* Norma Arm or in its vicinity), the same database built for the data analysis of IGR J17252−3616 and IGR J16358−4726 could be used for all the sources of the selected sample. This is due to the wide FOV of ISGRI.

Therefore, the data set is composed of many pointings whose selection has already been described in Sect. 6.3 and 7.2.1.

A sub-sample of the IGR sources was observed by *XMM-Newton* during allocated guest observer time (programme 020638, PI Walter R.). The sub-sample was composed of: IGR J16393−4643 (already described in Chap. 8), IGR J16418−4532, IGR J16479−4514, IGR J17252−3616 (already described in Chap. 6), IGR J17597−2201, and IGR J18027−2016. IGR J16465−4507 was also observed through a public ToO. The journal of the observations is presented in Table 9.1.

## 9.3 The *INTEGRAL* and *XMM-Newton* combined analysis

The combined *INTEGRAL* and *XMM-Newton* analysis and interpretation of the results are presented in Walter et al. (2005) (see next Sect. 9.4). However, we will just add some comments about the analysis of these sources.

### *XMM-Newton* analysis

The EPIC analysis of the sample is similar to what is described in Chapters 6 and 8.

The analysis of two sources belonging to our sample have already been presented in this thesis (See Chapters 6 and 8). The observation of IGR J16418−4532, IGR J16479−4514 and IGR J17597−2201 were strongly affected by background activity (see Fig. 9.1), but the IGR J18027−2016 observation was good. There is a big long flare in the middle of the IGR J16418−4532 observation. For IGR J16479−4514, the background activity was important with a high count rate whose level is between 10–20 counts $s^{-1}$ during the whole observation. It is similar for IGR J17597−2201 except a decrease for a short time in the middle of the observation where the count rate went down $\leq$10 counts $s^{-1}$. There is only one short flare for IGR J18027−2016. The end of the observation was also discarded because of an increase of the background rate.

Therefore, only IGR J18027−2016 light curve shows a long uninterrupted observation. IGR J16418−4532 shows strong outbursts (3) that are very short in time (<100 s) where the flux increased by a factor higher than 10 compared to the average flux. The other two light curves are affected by the background that provokes a saturation of the data acquistion, so there are interruptions that makes the flux drop to zero.

No significant modulation is found in Lomb-Scargle periodograms of IGR J16418−4532 and IGR J16479−4514. In IGR J17597−2201, the periodic stop of data acquisition is clearly seen in the periodogram. The period is 153.8±0.1 s. As found by Augello et al. (2003) and Hill et al. (2005), IGR J18027−2016 periodogram has a clear peak that corresponds to a period of 139.5±0.1 s. The harmonic is also detected. The folded light curve is shown in Fig. 9.3 with an ephemeris of

$$\mathrm{MJD}\, T = \mathrm{MJD}\, 53101.27 + n \times \frac{139.5\,\mathrm{s}}{86400} \tag{9.1}$$

where $n$ is the cycle number.

### Orbital period of IGR J16320−4751

The orbital period of IGR J16320−4751 has been discovered with the help of *Swift*/BAT data (Corbet et al. 2005a). This instrument covers an energy range similar to ISGRI. However, the analysis of the ISGRI data of IGR J16320−4751 processed with OSA 4.2 are not good enough to find any orbital period of several days. No significant peak is visible in the Lomb-Scargle periodogram.

However, once the period of IGR J16320−4751 has been known, a new ISGRI light curve per pointing has been extracted with OSA 5.0. The study of the 22–60 keV light curve shows a period of 8.99±0.04 d in a Lomb-Scargle periodogram (see Fig. 9.3). This period is compatible with the one found by Corbet et al. (2005a). The folded light curve shows complex structures with a maximum flux at phase 0.6 (see Fig. 9.3). The ephemeris is :

$$\mathrm{MJD}\, T = \mathrm{MJD}\, 53512.04732 + n \times 8.99 \tag{9.2}$$

where $n$ is the number of cycles.

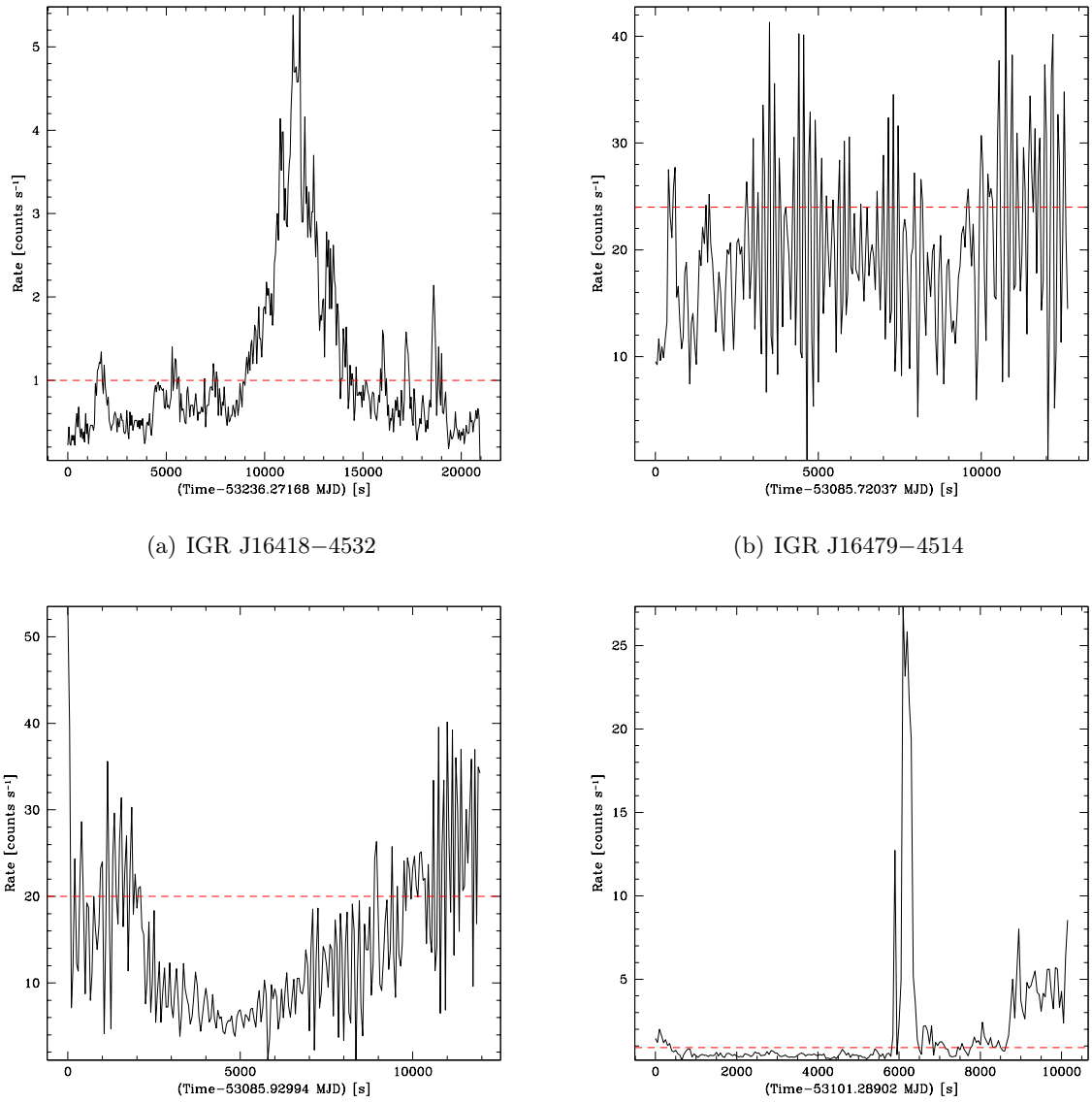


(a) IGR J16418−4532

(b) IGR J16479−4514

(c) IGR J17597−2201

(d) IGR J18027−2016

**Figure** *9.1: EPIC/pn count rates at energies higher than 10 keV. The red dotted lines represent the cut to clean the event lists.*

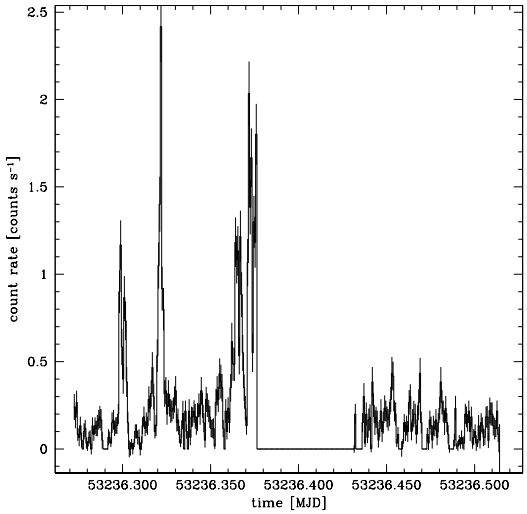


(a) IGR J16418−4532, 60 s bin

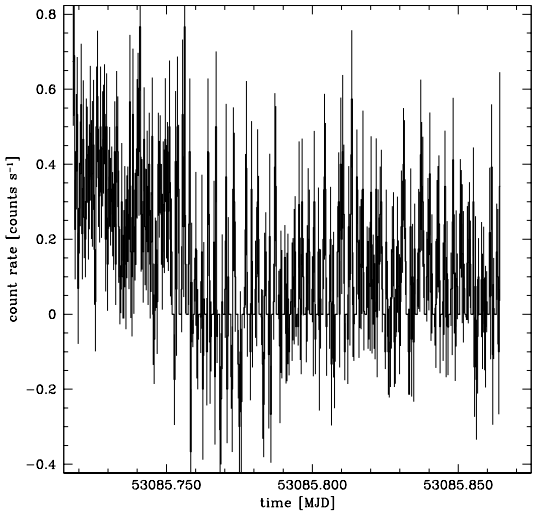


(b) IGR J16479−4514, 30 s bin

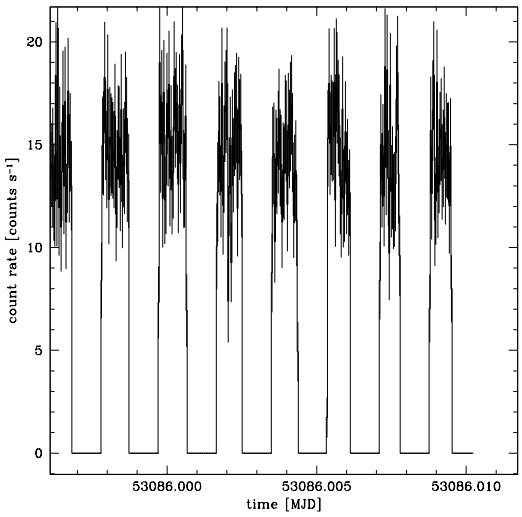


(c) IGR J17597−2201, 3 s bin

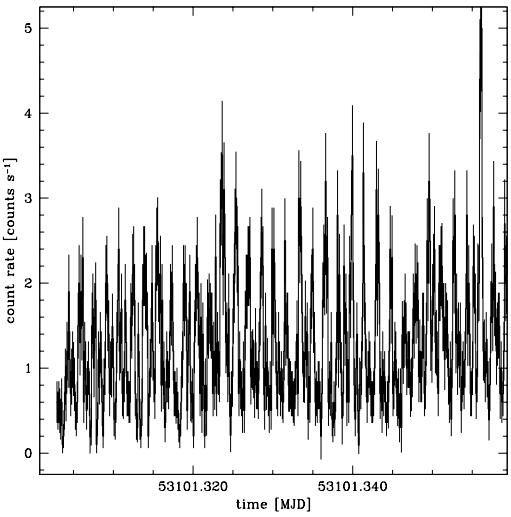


(d) IGR J18027−2016, 20 s bin

**Figure** *9.2: 0.4–10 keV pn light curve. For IGR J16479−4514 and IGR J17597−2201, due to the combination of the intensity of the source and the background produce a stop of data acquisition on-board the S/C, so the count rate goes down to zero. We show a zoom of IGR J17597−2201 light curve. A periodic modulation is observed in IGR J18027−2016 that lasts ∼100 s.*

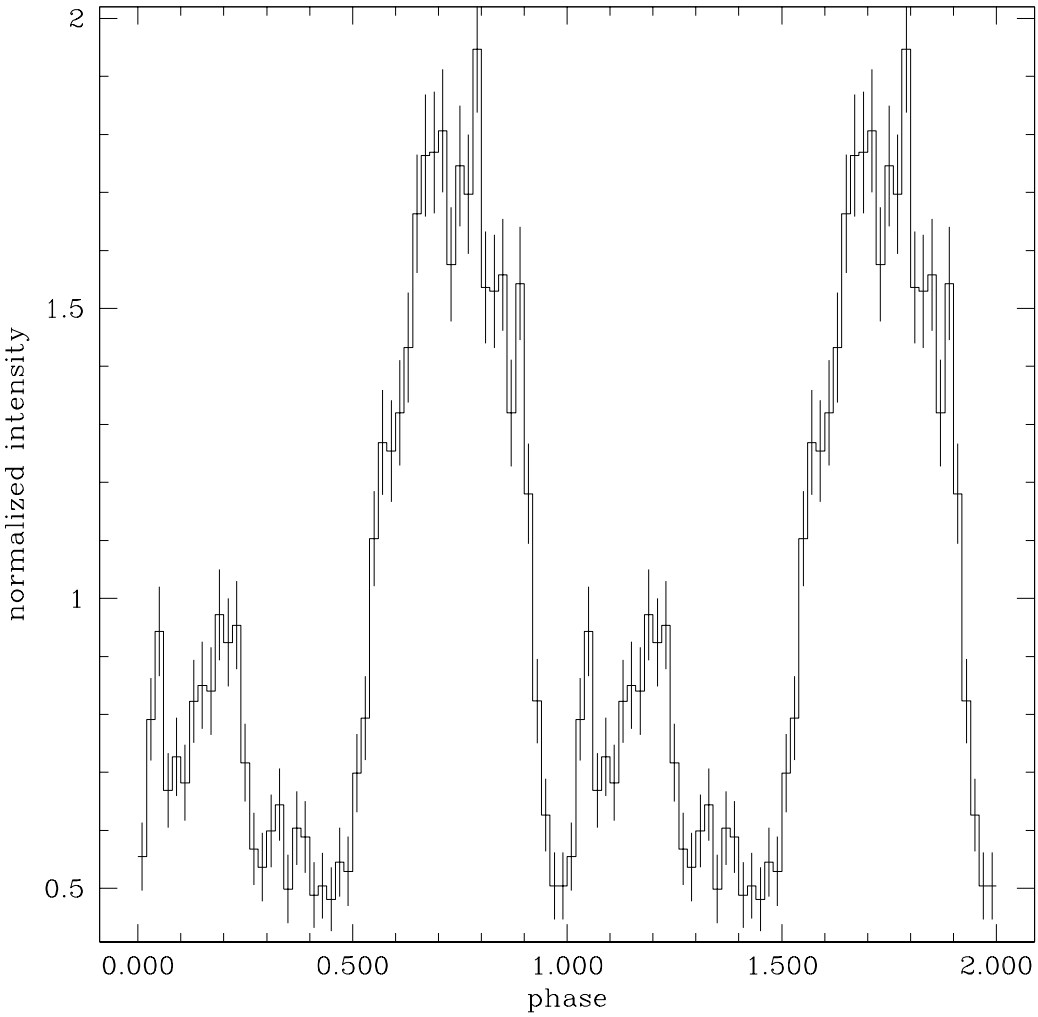


**Figure** *9.3: Folded light curve of IGR J18027−2016 with P=139.5 s and $T_0$=53101.27 MJD.*

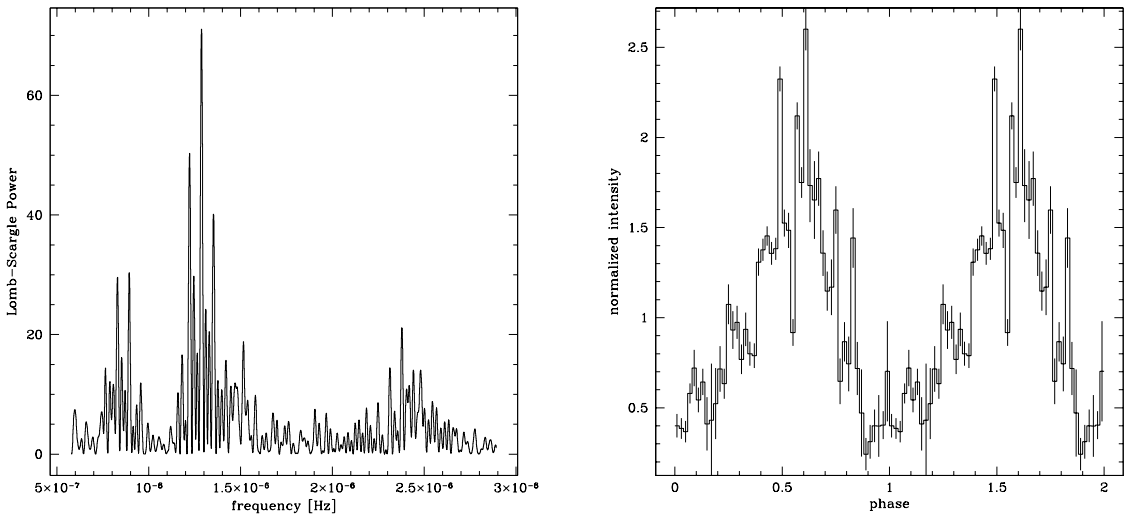


(a) Lomb-Scargle periodogram

(b) 22–60 keV folded light curve

**Figure** *9.4: Orbital timing analysis of IGR J16320−4751 with ISGRI data. A period of 8.99±0.04 d is detected. The 22–60 keV folded light curve shows complex structures.*

## 9.4 Scientific paper on a sample of *IGR sources* published in AA

The 10 IGR sources were jointly studied in order to find common features. The paper has been submitted to the *Astronomy & Astrophysics* journal. It will be accepted after minor revision.

*Astronomy & Astrophysics* manuscript no. abssrc February 2, 2006
(DOI: will be inserted by hand later)

# XMM-Newton and INTEGRAL observations of new absorbed supergiant high-mass X-ray binaries

R. Walter[1,2], J. Zurita Heras[1,2], L. Bassani[3], A. Bazzano[3], A. Bodaghee[1,2], A. Dean[4], P. Dubath[1,2], A. N. Parmar[6], M. Renaud[7], and P. Ubertini[3]

[1] INTEGRAL Science Data Centre, Chemin d'Ecogia 16, CH-1290 Versoix, Switzerland
[2] Observatoire de Genève, Chemin des Maillettes 51, CH-1290 Sauverny, Switzerland
[3] IASF/INAF, Via Godetti 101, I-40129 Bologna, Italy
[4] IASF/INAF, Via Fosso del Cavaliere 100, I-00133 Rome, Italy
[5] School of Physics and Astronomy, University of Southampton, Highfield, Southampton, SO 17 1BJ, United Kingdom
[6] Astrophysics Missions Division, Research and Scientific Support Department of ESA, ESTEC, Postbus 299, NL-2200 AG Noordwijk, The Netherlands
[7] CEA Saclay, DSM/DAPNIA/SAp, 91191 Gif-sur-Yvette Cedex, France

Received ; Accepted:

**Abstract.** During the first year in operation, INTEGRAL, the European Space Agency's $\gamma$-ray observatory, has detected more than 28 new bright sources which emit the bulk of their emission above 10 keV. Follow-up observations of a subset of these sources in the X-ray band with XMM-Newton indicate that 70% of them are strongly absorbed ($N_H \geq 10^{23}$ atom cm$^{-2}$). More than half of these absorbed sources show pulsations with periods ranging from 139 to 1300 s, i.e., they are slow X-ray pulsars. The candidate infrared counterparts are not as strongly absorbed demonstrating that part of the absorbing matter is local to the sources. Many of these new sources are supergiant high-mass X-ray binaries (HMXB) in which the stellar wind of the companion star is accreted onto the compact object. The large local absorption in these new sources can be understood if the compact objects are buried deep in their stellar winds. These new objects represent half of the population of supergiant HMXB.

**Key words.** Gamma-Rays:observations, X-rays: binaries, Pulsars: individuals, Stars: early type

## 1. Introduction

High-mass X-ray binaries (HMXBs) consist of a compact object orbiting a massive star. The X-ray emission is due to the accretion of matter from the early-type mass-losing star onto the compact companion, which is generally a neutron star. HMXBs can be divided into two groups (van Paradijs 1983) depending on the nature of the massive star.

Most of the 130 HMXBs cataloged by Liu et al. (2000) belong to the first group and contain a Be primary star in a relatively wide orbit of moderate eccentricity. The compact companions spend most of the time far away from the disk surrounding the Be star (van Paradijs 1995; Apparao 1994). X-ray outbursts occur primarily during the perigee passage of the compact object which accretes from a low-velocity and high-density wind from the Be star. These systems exhibit hard X-ray spectra and tend to be transient X-ray emitters.

*Send offprint requests to*: Roland.Walter@obs.unige.ch

In the second group, the compact object orbits inside the wind of an OB supergiant star. The X-ray emission is either powered by direct accretion of the stellar wind or by Roche-lobe overflow via an accretion disk. The X-ray emission from these systems is generally persistent. They can provide insights into the masses of neutron stars, the structure of stellar winds and binary evolution. These systems may ultimately evolve into highly interesting neutron star - black hole binaries. However, supergiant X-ray binaries are rare, with only 10 such systems known in the Galaxy prior to INTEGRAL (e.g., Liu et al. 2000) and so the discovery of new examples is of great interest.

The INTEGRAL survey of the galactic plane and central regions have so far revealed the presence of $\sim$120 sources in the energy range 20–100 keV. Sources are located with an accuracy better than $2'$, depending on count rate, position in the field of view (FOV) and exposure. This excellent source location accuracy has allowed the majority of the detected sources to be identified with already known X-ray sources. However, 28 of the objects in the first INTEGRAL soft $\gamma$-ray galactic plane survey

catalog (Bird et al. 2004) had no known counterparts and so their nature was unclear. The majority of those sources were detected in the galactic bulge and Norma arm tangent region (Walter et al. 2004).

XMM-Newton follow-up observations of the first of the newly-detected INTEGRAL source, IGR J16318−4848, revealed a spectrum with intense Fe K$\alpha$ and K$\beta$ and Ni K$\alpha$ emission features as well as strong ($\gtrsim 10^{24}$ atom cm$^{-2}$) low-energy absorption which makes the source extremely difficult to observe at energies $\lesssim$4 keV (Matt & Guainazzi 2003; Walter et al. 2003b; Revnivtsev et al. 2003). The strong absorption and unusual spectral properties led to the suggestion that IGR 16318−4848 is the first representative of a group of highly absorbed galactic binaries.

Following the discovery of IGR J16318−4848, there have been a number of sensitive X-ray observations of some of the other newly-discovered INTEGRAL sources. These observations have revealed that several of the sources share similar spectral properties (Rodriguez et al. 2003; Patel et al. 2004).

Here, we present the results of INTEGRAL and XMM-Newton observations of 10 newly-discovered sources. These were selected among the new sources detected by INTEGRAL in the galactic plane during the first year of the mission. We also collected infrared photometry for the candidate counterparts from existing catalogues. We demonstrate that 8 out of the 10 sources are intrinsically absorbed and that 8 of them are persistent X-ray emitters. Many systems appear to have supergiant companions. Since the X-ray properties of the other unknown systems are similar, we propose that significant numbers of the unknown sources are likely to be OB supergiant systems - doubling the number of such systems known in the Galaxy.

## 2. Observations and data analysis

### 2.1. INTEGRAL

The INTEGRAL payload (Winkler et al. 2003) consists of two $\gamma$-ray instruments, one of which is optimized for 15 keV to 10 MeV high-resolution imaging (IBIS; Ubertini et al. 2003) and the other for 20 keV to 8 MeV high-resolution spectroscopy (SPI; Vedrenne et al. 2003). IBIS provides an angular resolution of 12′ full-width at half-maximum ($FWHM$) and an energy resolution, $E/\Delta E$, of $\sim$12 $FWHM$ at 100 keV. SPI provides an angular resolution of 2.°7 $FWHM$ and an $E/\Delta E$ of $\sim$500 $FWHM$ at 1.3 MeV. The extremely broad energy range of IBIS is covered by two separate detector arrays, ISGRI (15–500 keV, Lebrun et al. 2003) and PICsIT (0.2–10 MeV, Labanti et al. 2003). The payload is completed by X-ray (JEM-X; 3–35 keV, Lund et al. 2003) and optical monitors (OMC; V-band, Mas-Hesse et al. 2003). The instruments are co-aligned and are operated simultaneously.

The 3 high-energy instruments use coded masks to provide imaging information. This means that photons from a source within the FOV are distributed over the detector area in a pattern determined by the position of the source in the FOV. Source positions and intensities are determined by matching the observed distribution of counts with those produced by the mask modulation.

Most of the new sources discovered by INTEGRAL could be detected with ISGRI in mosaics of sky images obtained in hundreds of short (2000 s) pointings scheduled during each of the source visibility periods (a source is visible during about 2 months every 6 months).

Table 1 lists the net ISGRI effective exposure time and the average source count rate obtained during the first

**Table 1.** INTEGRAL ISGRI vignetting-corrected effective exposure time and average source count rate during the first year of the mission. 3$\sigma$ upper limits are provided when the source was not detected during that period.

| Source | Eff Exp [ksec] | 20–60 keV count rate [ct/s] |
|---|---|---|
| **PERSISTENT SOURCES** | | |
| IGR J16318−4848 | 554 | $3.52 \pm 0.02$ |
| IGR J16320−4751 | 510 | $2.24 \pm 0.02$ |
| IGR J16393−4641 | 387 | $1.16 \pm 0.02$ |
| IGR J16418−4532 | 489 | $0.95 \pm 0.02$ |
| IGR J16479−4514 | 532 | $0.75 \pm 0.03$ |
| IGR J17252−3616 | 1248 | $1.48 \pm 0.02$ |
| IGR J17597−2201 | 288 | $1.40 \pm 0.03$ |
| IGR J18027−2016 | 276 | $0.85 \pm 0.07$ |
| **TRANSIENT SOURCES** | | |
| IGR J16465−4507 | 504 | <0.08 |
| IGR J17544−2619 | 208 | <0.12 |

**Table 2.** XMM-Newton EPIC pn observation log. All EPIC observations used the medium filter (except IGR J16465−4507 and IGR J16320-4751 for which the thick and thin, filters were used respectively) and have been performed in large window mode. The third column gives the net time accumulated in the source spectrum. The last column ($B_{cut}$) gives the threshold in detector count rate above 10 keV used to remove periods with high background.

| Source | Start Time | Net Exp [ksec] | $B_{cut}$ [ct/s] |
|---|---|---|---|
| **PERSISTENT SOURCES** | | | |
| IGR J16318−4848 | 2003-02-10 16:21 | 21.1 | 60 |
| IGR J16320−4751 | 2004-08-19 17:07 | 33.1 | |
| IGR J16393−4641 | 2004-03-21 08:59 | 6.9 | 1 |
| IGR J16418−4532 | 2004-08-19 06:30 | 10.5 | 2 |
| IGR J16479−4514 | 2004-03-21 22:18 | 5.8 | 60 |
| IGR J17252−3616 | 2004-03-21 13:23 | 5.5 | 4 |
| IGR J17597−2201 | 2004-03-21 22:18 | 2.4 | 30 |
| IGR J18027−2016 | 2004-04-06 06:55 | 7.6 | 6 |
| **TRANSIENT SOURCES** | | | |
| IGR J16465−4507 | 2004-09-14 02:46 | 2.9 | 1 |
| IGR J17544−2619 | 2003-09-11 19:25 | 4.9 | 1 |

**Table 3.** Consolidated position of the INTEGRAL sources with X-ray and candidate infrared counterparts. The K magnitude and the angular separation, $\Delta r$, between the infrared counterpart and the X-ray source are also indicated.

| Source | ISGRI position (uncertainty ["]) | X-ray position (uncertainty ["]) | 2MASS | K | $\Delta r$["] |
|---|---|---|---|---|---|
| **PERSISTENT SOURCES** | | | | | |
| IGR J16318−4848 | 16 31 48 −48 49.0 (13) | 16 31 48.6 −48 49 00 (4)[1] | 16314831-4849005 | 7.2 | 2.9 |
| IGR J16320−4751 | 16 32 02 −47 52.2 (16) | 16 32 01.9 −47 52 27 (3)[2] | 16320175-4752289 | 10.9 | 1.9 |
| IGR J16393−4641 | 16 39 06 −46 42.1 (26) | 16 39 05.4 −46 42 12 (4)[3] | 16390535-4642137 | 12.8 | 1.8 |
| IGR J16418−4532 | 16 41 46 −45 31.8 (36) | 16 41 51.0 −45 32 25 (4) | 16415078-4532253 | 11.5 | 2.4 |
| IGR J16479−4514 | 16 48 03 −45 12.8 (34) | 16 48 06.6 −45 12 08 (4) | 16480656-4512068 | 9.8 | 1.3 |
| IGR J17252−3616 | 17 25 10 −36 17.3 (22) | 17 25 11.3 −36 16 58 (4)[4] | 17251139-3616575 | 10.7 | 1.2 |
| IGR J17597−2201 | 17 59 46 −22 01.8 (30) | 17 59 45.7 −22 01 39 (4) | 17594556-2201435 | 12.9 | 4.9 |
| IGR J18027−2016 | 18 02 39 −20 17.6 (35) | 18 02 42.0 −20 17 18 (4) | 18024194-2017172 | 11.4 | 1.1 |
| | | | 180242.0-201720.2 | | 3.0 |
| **TRANSIENT SOURCES** | | | | | |
| IGR J16465−4507 | 16 46 30 −45 07.5 (120) | 16 46 35.5 −45 07 04 (4) | 16463526-4507045 | 9.8 | 2.6 |
| IGR J17544−2619 | 17 54 24 −26 19.0 (120) | 17 54 25.4 −26 19 53 (4)[5] | 17542527-2619526 | 8.0 | 1.7 |

References: [1]Schartel et al. (2003); [2]Rodriguez et al (in prep.); [3]Bodaghee et al. (2005); [4]Zurita Heras et al. (2005); [5] González-Riestra et al. (2004)

year of the mission for the new sources for which high-resolution X-ray follow-up observations were performed.

The INTEGRAL data were processed using the Off-line Scientific Analysis (OSA) version 4.2 software provided by the INTEGRAL Science Data Centre (Courvoisier et al. 2003).

Extracting source spectra with OSA 4.2 in each pointing and averaging the results is a method affected by systematic errors that are large for sources of low significance. We therefore extracted source average spectra from mosaic images, which is a more reliable approach. Although source count rates extracted from mosaic images are 5% less than obtained using other spectral extraction methods (Lubinski et al. 2004), the source relative variability and spectral shape are not affected.

The ISGRI source positions and average spectra were derived with the `mosaic_spec` (version 1) software from a set of mosaic images generated in narrow energy bands from the data of the first two visibility periods (the first year of the mission). For IGR J16465-4507 and IGR J17544-2619, which are transient sources, the ISGRI spectra were derived from revolutions 232/233 (MJD 53254.34-53257.34) and 113 (MJD 52898.35-52901.35) respectively.

To study the long term variability of the sources, we included Core Programme data from the second year of the mission. The lightcurves, with a binning of one spacecraft revolution (3 days), were extracted from mosaic images built for each revolution.

### 2.2. XMM-Newton

The XMM-Newton Observatory (Jansen et al. 2001) includes three 1500 cm$^2$ X-ray telescopes each with a European Photon Imaging Camera (EPIC) at the focus. Two of the EPIC imaging spectrometers use MOS CCDs (Turner et al. 2001) and one uses pn CCDs (Strüder et al. 2001).

All sources listed in Table 2 were observed by the EPIC camera of XMM-Newton with the medium (thick in the case of IGR J16465-4507, thin in the case of IGR J16320-4751) optical blocking filter. The EPIC pn cameras were operated in large-window mode. Pile-up is negligeable for all sources.

For this paper, only the EPIC data were considered. Source positions were derived using the SAS task `edetect_chain` from the EPIC MOS and pn data. Source spectra and lightcurves were derived from EPIC pn data (MOS data are consistent but of lower significance).

All data products were obtained using the Science Analysis Software (SAS) version 6.1.0. Only single and double pixel events were selected. Known hot, or flickering, pixels and electronic noise were rejected. Source events were selected in a circle centered on the source. Background events were obtained from source-free regions of identical size located in the same CCD and at the same distance from the read-out node.

Periods with enhanced background (EPIC pn count rate above 10 keV larger than the threshold listed in Table 2) were disregarded in the analysis.

## 3. Results

### 3.1. Positions and counterparts

The statistical accuracy on the determination of the position of point sources with ISGRI depends on the source significance in the mosaic image and varies from 2 arcmin to 10 arcsec in our sample. ISGRI source positions with 90% uncertainty radius (including a 10 arcsec systematic uncertainty on the instrument misalignment – Walter et al. 2003a) are listed in Table 3. ISGRI positions derived by the current software are affected by additional

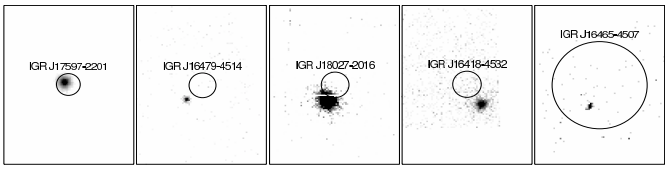


**Fig. 1.** EPIC counterpart images for 5 INTEGRAL sources for which that information is not presented elsewhere. North is left. The size of each image is 2.8 x 3.7 arcmin. The ISGRI 90% uncertainty regions (not including systematics of the reconstruction) are shown.

systematic errors related with the image reconstruction. These errors are proportional to the source significance and amount to a good fraction of the statistical uncertainties (Gros et al. 2003).

EPIC pn images with superimposed ISGRI error circles are presented in Fig. 1 if not already presented elsewhere (Bodaghee et al. 2005; Zurita Heras et al. 2005; Walter et al. 2003b; Rodriguez et al. 2003; González-Riestra et al. 2004). XMM-Newton detected an X-ray counterpart for all the INTEGRAL sources observed. The counterpart detected by EPIC are often on the border of the ISGRI error circles because of the systematic errors. The X-ray positions derived from follow-up observations of our sample of sources are listed in Table 3.

We searched in several catalogues for candidate counterparts. None of the sources are detected in the radio. The only known optical/infrared candidate counterparts found within the X-ray error circles are listed in Table 3. The coordinates come from the 2MASS catalogue excepting for the second candidate counterpart of IGR J18027−2016 which was found in the Second Guide Star Catalogue. In most cases a single candidate counterpart was found. The closest 2MASS source to IGR J17597−2201 lies outside of the X-ray error circle and may not be the real stellar counterpart.

### 3.2. Long term variability

To study the long term variability of the sources we have constructed ISGRI 20-60 keV lightcurves with one time bin every one (or several when the source was not detected) 3 day spacecraft revolution. The count rate in each time bin were extracted from a mosaic of all pointings performed during the revolution(s). When the source was not detected in a time bin, a $3\sigma$ upper limit was derived from the variance map. Only revolutions with an effective exposure time on source longer than 5000 sec have been considered.

Figure 2 displays the long term lightcurve of all selected sources except IGR J16393-4641, IGR J17252-3616, IGR J18027-2016 for which similar information can be found in Bodaghee et al. (2005); Zurita Heras et al. (2005) and Hill et al. (2005).

The first 8 sources listed in Table 1 are significantly detected during each of the periods of visibility. These

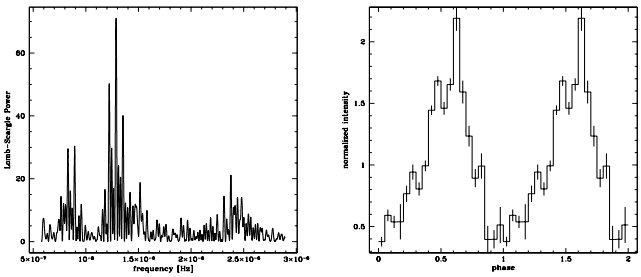


**Fig. 3.** ISGRI (>20 keV) periodogram of IGR J16320-4751 (left) and folded lightcurve (right) with a period of 8.99 day (phase 0 = MJD 53512.05).

sources were persistent, at least on a time scale of 2 years, but vary by factor 5 to 20 at least. Weak detection of all these sources, excepting IGR J16418-4532, by previous mission (Murakami et al. 2003; Rodriguez et al. 2003; Sugizaki et al. 2001; Warwick et al. 1988; Augello et al. 2003; Lutovinov et al. 2005a) also support their persistent nature.

IGR J16479-4514 has been detected with a low flux by XMM-Newton (see Sect. 3.3) and is not detected by INTEGRAL in many revolutions indicating that it is highly variable, and usually faint.

The two transient sources were observed by XMM-Newton in TOO mode close to the flaring periods detected by INTEGRAL:

IGR J16465-4507 was detected during a week of the fourth visibility period. During that time, its average count rate was about 10 times higher than the average upper limit over the first two visibility periods, suggesting that the source is transient.

IGR J17544-2619 was detected for less than 3 days during each of the first 3 visibility periods. These detections are separated by $56 \pm 1$ and $54 \pm 1$ spacecraft revolutions indicating that it is probably a transient system with a period of $165 \pm 3$ days.

Orbital periods are known in IGR J17252-3616 (9.72 d – Zurita Heras et al. 2005) and in IGR J18027-1455 (4.57 d – Hill et al. 2005). We searched the ISGRI lightcurves for long period signals and found additional signature in a single source: IGR J16320-4751. Figure 3 displays the Lomb-Scargle periodogram of IGR J16320-4751 that features a period of $8.99 \pm 0.05$ d and the folded lightcurve that indicates an orbital modulation with a pulse fraction of $70 \pm 4\%$ without any evidence for an eclipse. Those results are in agreement with the recent SWIFT/BAT results (Corbet et al. 2005).

### 3.3. High-Energy Spectra

Simultaneous fits were performed with the average XMM-Newton EPIC pn and INTEGRAL IBIS ISGRI spectra extracted as described in Sect. 2. The EPIC spectra were rebinned to oversample the $FWHM$ of the energy resolution and to have a minimum of 20 counts per bin to

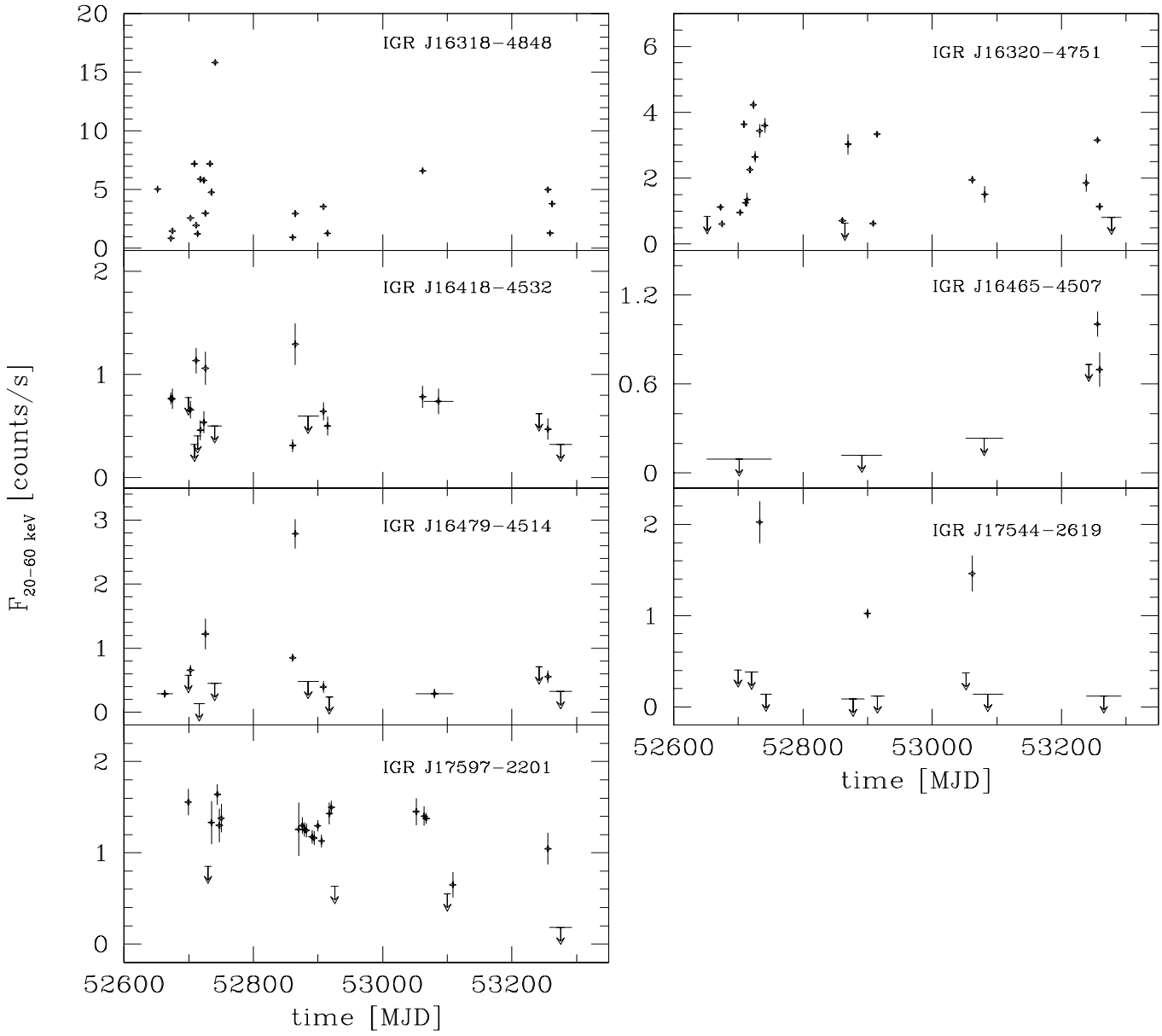


**Fig. 2.** INTEGRAL ISGRI long term source lightcurves (20–60 keV).

allow use of the $\chi^2$ statistic. The photo-electric absorption cross sections of Morrison & McCammon (1983) are used throughout. All spectral uncertainties are given at 90% confidence.

The X- and $\gamma$-ray spectra derived from the XMM-Newton and INTEGRAL observations are very similar among the studied sources (Fig. 4). The continuum emission is steep and requires a spectral break above 20 keV when the statistic is good enough. The continuum is absorbed below 10 keV with photoelectric absorbing column densities between $1.8\times10^{22}$ and $2\times10^{24}$ atom cm$^{-2}$, much larger than the typical interstellar column density in the plane of the Galaxy excepting for one transient source (listed in Table 6). When the absorbing column density is large enough, (and enough data were collected) strong fluorescence Fe lines are evident in the XMM-Newton EPIC spectra.

### 3.3.1. Continuum modeling

The low energy curvature and the very steep spectra observed at high energy cannot be represented by Compton reflection. The geometry of the sources is therefore characterized by transmission rather than reflection, as already established for IGR J16318-4848 (Matt & Guainazzi 2003).

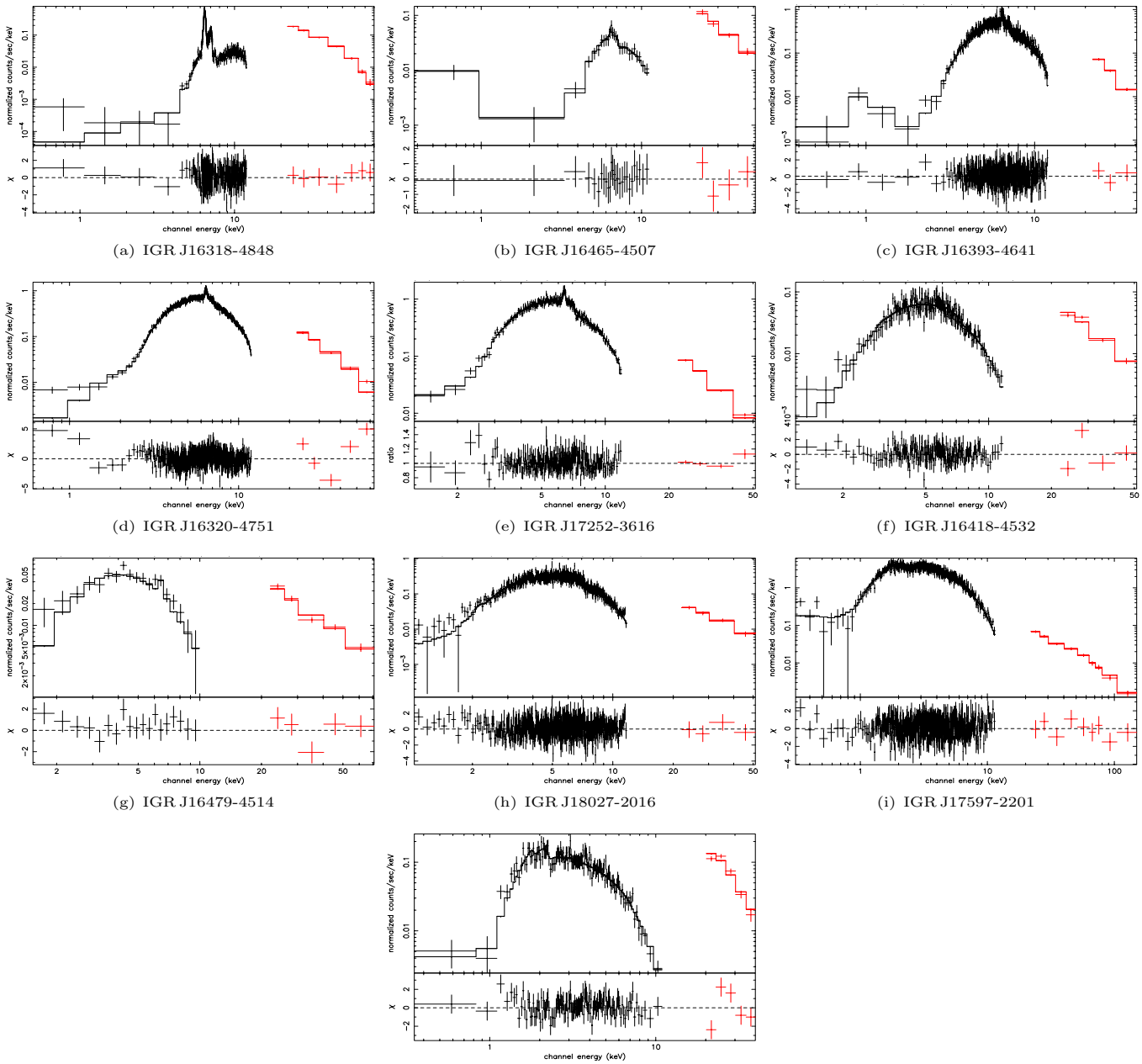


(a) IGR J16318-4848 (b) IGR J16465-4507 (c) IGR J16393-4641

(d) IGR J16320-4751 (e) IGR J17252-3616 (f) IGR J16418-4532

(g) IGR J16479-4514 (h) IGR J18027-2016 (i) IGR J17597-2201

(j) IGR J17544-2619

**Fig. 4.** ISGRI (>20 keV) and EPIC (<15 keV) source count spectra with best fit model predictions and residuals. The spectral model, identical in all sources, is described in the text. The sources are ordered from highest to lowest intrinsic absorption.

The spectral break could be modeled with a cut-off power-law or a broken power-law continuum model. However, in those cases very hard power-law slope (even positive photon index) are often obtained that are highly correlated to the absorbing column density. To minimize such effects and allow a comparison of the source parameters that is less model dependent, we decided to use an thermal inverse Comptonization continuum model.

The continuum was modified by an intrinsic photo-electric absorption (with Fe abundances left free when needed). We also added an Fe K$\alpha$ fluorescence line (F K$\beta$ and Ni K$\alpha$ were added in a few cases) modeled as a Gaussian, and, when required by the data, a soft X-ray excess absorbed by the galactic column density in the direction of the source derived from the measurements by Dickey & Lockman (1990). Table 4 lists the main spectral parameters obtained for each source.

**Table 4.** Parameters resulting from the spectral modeling of the EPIC pn and ISGRI spectra of the sources. The `xspec` spectral model is `constant*wabs*(bbody+gaussian+vphabs*compTT)`. The galactic absorption is fixed. $\chi^2_\nu$ is the goodness of fit; $C_I$ is the ISGRI normalization factor; $N_{\rm H}$ is the intrinsic absorbing column density; $Z_{Fe}$ is the relative Fe abundance, if needed to fit the Iron edge; $kT_e$ and $\tau$ are the electronic temperature and optical depth of the Comptonizing medium; $EW^{UA}_{K\alpha}$ is the equivalent width of the Fe K$\alpha$ line measured with reference to the unabsorbed intrinsic continuum. Integrated fluxes are listed for the ISGRI spectrum normalisation for both the continuum as observed ($F_{2-100}$) and corrected ($F^{UA}_{2-100}$) for the intrinsic photoelectric absorption. The observed flux of the soft excess component ($F^{SE}_{0.5-2}$) is listed separately.

| Source | $\chi^2_\nu$ | $C_I$ | $N_{\rm H}$ [$10^{22}$ cm$^{-2}$] | $Z_{Fe}$ [$Z_\odot$] | $kT_e$ [keV] | $\tau$ | $EW^{UA}_{K\alpha}$ [eV] | $F_{2-100}$ | $F^{UA}_{2-100}$ | $F^{SE}_{0.5-2}$ [$10^{-10}$ erg/cm$^2$s] [erg/cm$^2$s] |
|---|---|---|---|---|---|---|---|---|---|---|
| **PERSISTENT SOURCES** | | | | | | | | | | |
| IGR J16318−4848 | 0.94 | 1.2 | $193 \pm 11$ | 0.88 | $8.5 \pm 0.4$ | $3.8^{+0.7}_{-0.2}$ | $82 \pm 3$ | 3.5 | 8.0 | $< 4\ 10^{-16}$ |
| IGR J16320−4751 | 1.35 | 0.55 | $18.3 \pm 0.7$ | 0.74 | $5.6 \pm 0.2$ | $7.9 \pm 0.5$ | $85 \pm 5$ | 2.5 | 2.8 | $85\ 10^{-15}$ |
| IGR J16393−4641 | 0.92 | 0.76 | $23.7 \pm 0.7$ | | $4.4 \pm 0.4$ | $10.1 \pm 0.4$ | $60 \pm 10$ | 1.7 | 2.1 | $8\ 10^{-15}$ |
| IGR J16418−4532 | 0.98 | 4.7 | $10.0 \pm 1.2$ | | $6.0 \pm 0.5$ | $5.5 \pm 0.7$ | $< 34$ | 1.1 | 1.3 | $< 7\ 10^{-15}$ |
| IGR J16479−4514 | 1.22 | 19.3 | $7.7 \pm 1.7$ | | $> 13$ | $< 1.8$ | $< 280$ | 1.4 | 1.8 | $< 35\ 10^{-15}$ |
| IGR J17252−3616 | 1.04 | 0.44 | $14.9 \pm 1.2$ | 1.5 | $5.6 \pm 0.2$ | $7.9 \pm 0.5$ | $84 \pm 11$ | 1.8 | 2.2 | $26\ 10^{-15}$ |
| IGR J17597−2201 | 1.00 | 0.49 | $4.5 \pm 0.7$ | | $> 20$ | $< 2.0$ | $< 10$ | 3.0 | 3.4 | $6\ 10^{-12}$ |
| IGR J18027−2016 | 0.96 | 0.44 | $9.1 \pm 0.5$ | | $7.2 \pm 0.7$ | $6.6 \pm 0.5$ | $33 \pm 18$ | 1.0 | 1.1 | $< 39\ 10^{-15}$ |
| **TRANSIENT SOURCES** | | | | | | | | | | |
| IGR J16465−4507 | 0.39 | 4.3 | $60 \pm 10$ | 0.46 | $7.0 \pm 0.5$ | $6.5 \pm 2.0$ | $< 60$ | 2.1 | 2.8 | $18\ 10^{-15}$ |
| IGR J17544−2619 | 0.91 | 61 | $1.8 \pm 0.3$ | | $5.9 \pm 0.6$ | $3.8 \pm 0.5$ | $< 35$ | 5.5 | 6.1 | $< 17\ 10^{-14}$ |

The column densities are larger than the galactic absorption by factors of 4 to 100 except for IGR J17544-2619 (González-Riestra et al. 2004). The depth of the Iron edge is fully compatible with the absorbing column density (requiring a slight over or under abundance in four sources).

A normalisation constant was introduced in the model to account for source variability between the XMM-Newton observations and the average source flux measured by INTEGRAL. This constant is compatible with the typical variability observed in those sources. In the case of IGR J16479-4514 and the two transient sources the normalisation constant is large illustrating the strong variability of those sources on short time scales.

The continuum parameters are constrained in a narrow range with typical values found in X-ray pulsars (Nagase 2002).

### 3.3.2. Soft excess

Significant soft X-ray (0.5–2 keV) excesses (listed in Table 4) are found above the low energy extrapolation of the absorbed continuum in five sources. This emission was modeled with a blackbody emission modified by the fixed galactic absorption (the data are not good enough to determine a temperature). Except for IGR J16318-4848, soft X-ray excesses are detected in all sources with absorbing column densities in excess of $10^{23}$ atom cm$^{-2}$. This is a detection bias as weak soft X-ray excesses cannot be detected if the primary continuum is not absorbed.

Soft X-ray excesses have been resolved in high resolution spectra of supergiant HMXB, especially during eclipse, and have been interpreted as fluorescent and recombination lines and/or scattering in the outer parts of the systems (van der Meer et al. 2004; Sako et al. 2002).

The soft excesses observed in our sources are probably of similar nature, however excesses in low resolution spectra could also be represented by partial covering or hot absorber (e.g. Kuulkers 2005) models. In all sources featuring a soft X-ray excess, we have tried an alternate model based on a partial covering absorber.

In three sources, the soft X-ray excess could be mostly explained by partial covering of the intrinsic absorption: (1) In IGR J17252-3616, a covering factor of $0.995 \pm 0.002$ (Zurita Heras et al. 2005) could explain satisfactorily the soft X-ray excesses. (2) In IGR J16320-4751, a covering factor of $0.998 \pm 0.002$ could explain most of the excess. In that case, a small excess ($F_{0.5-2keV} = 5\ 10^{-15}$ erg cm$^{-2}$ s$^{-1}$) and galactic absorption ($N_H$=1.1 $10^{22}$ atom cm$^{-2}$) lower than the value derived from (Dickey & Lockman 1990) are however required to obtain a good fit of the data. (3) In IGR J17597-2201, a covering factor of $0.90 \pm 0.02$ could represent the X-ray spectrum without any soft excess component ($\chi^2_\nu = 1.0$). In this case, the resulting intrinsic absorbing column density $N_H = (2.70 \pm 0.15)\ 10^{22}$ atom cm$^{-2}$ differs significantly from the value listed in Table 4.

Partial covering opens the possibility to observe a Compton reflection continuum at high energy in the form of a hard energy tail or of an additional flat low energy continuum. There is, however, no evidence for a high energy tail and the spectral shape of the soft excesses do not correspond to what would be expected from Compton reflection.

In two sources, the soft X-ray excess cannot be accounted for with a simple partial covering absorber model:

(1) In IGR J16465-4507, the soft X-ray excess is very large and a partial covering model increases the $\chi^2$ by 13 for 29 d.o.f. (2) In IGR J16393-4641 partial covering cannot explain the observed spectrum, a soft excess remains needed (Bodaghee et al. 2005).

The observed soft X-ray excesses could therefore be explained by various spectral models. Better spectral resolution and statistics would be needed to disentangle them. It however seems likely that the excesses observed in HMXB during eclipse could also explain the excesses detected when most of the continuum emission is absorbed. This interpretation also suggests that the absorbing matter is located close to the compact object.

#### 3.3.3. Fe $K\alpha$ line

The centroid of the Fe $K\alpha$ line, compatible with 6.4 keV, and the width of the lines, compatible with zero, in all cases indicate that the fluorescence lines are emitted in gas that is not strongly ionized.

The apparent Fe K$\alpha$ line equivalent width is strongly variable from source to source (between less than 100 eV to more than 2 keV). However, when compared to the continuum corrected for the effect of the intrinsic photoionisation absorption the equivalent width reduces to 30 to 90 eV in all intrinsically absorbed sources. This indicates that fluorescence could originate from the same gas configuration among the studied sources with the gas surrounding the X-ray source.

### *3.4. Pulsations*

Hard X-ray pulsation as a general characteristic of new persistent INTEGRAL sources has been reported by Walter (2004). Pulsation has been reported in detailed studies of several of our sample sources (Bodaghee et al. 2005; Zurita Heras et al. 2005; Lutovinov et al. 2005b; Hill et al. 2005). No pulsation has been found in IGR J16318-4848.

Here, we report on the remaining individual sources of our sample. A summary of the pulsation periods is given in Table 6. Pulsations were also searched for below 1.5 keV in sources featuring a soft X-ray excesses to disentangle independent soft X-ray excess from partial covering absorber models. The data are unfortunately not good enough to reach a definite conclusion.

#### 3.4.1. IGR J16418-4532

Removing the periods with strong background flares resulted in 10.5 ksec of good EPIC data. A 30 sec resolution lightcurve was extracted. During the first half of the observation the source featured 3 short and strong flares reaching about 2 count s$^{-1}$ while the averaged count rate is about 0.2 count s$^{-1}$ for most of the observation. To search for a period in the quiescent state, intervals of time affected by flares were removed from the dataset which resulted in a continuous 9 ksec lightcurve. We searched for a period by folding the data through ranges of periods and compared the results with the ones obtained from the background lightcurve (Fig. 5).

A period of $1246 \pm 100$ sec is present in the data. The probability of chance detection can be estimated as below $10^{-3}$. The pulse fraction (Fig. 5) is $64 \pm 10\%$ (2–10 keV).

The source is too faint to search for a period with ISGRI and folding the ISGRI 15–30 keV lightcurve of the source obtained on revolution 37 (MJD 52671.08-52674.07) using a period of 1246 sec did not provide any significant result.

#### 3.4.2. IGR J16479-4514

The XMM-Newton observation of IGR J16479-4514 was affected by a very strong and variable background. The low source count rate when compared to the strong background is such that the lightcurve is completely dominated by the background variations. No period could be searched for.

We also searched a 100 sec resolution ISGRI lightcurve of revolution 100 (MJD 52859.48-52862.47), when the source was bright, but no pulsation was found.

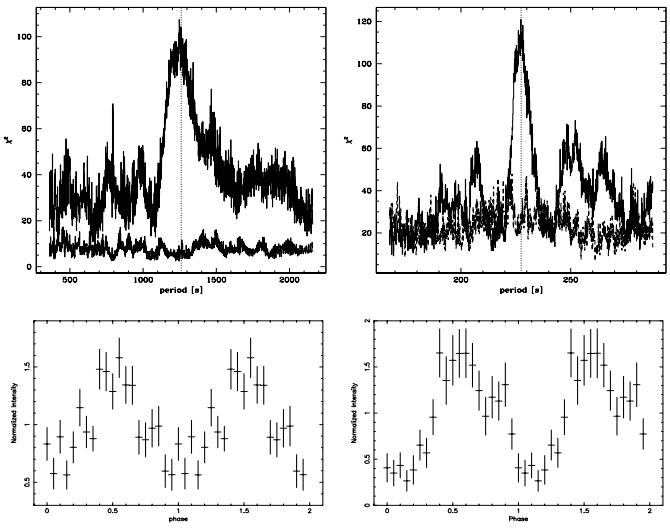


**Fig. 5.** XMM EPIC pn $\chi^2$ periodogram (lower curve is derived from the background) and folded lightcurve for IGR J16418-4532 (left) and IGR J16465-4507 (right).

#### 3.4.3. IGR J16465-4507

A 10 sec resolution EPIC (2–10 keV) lightcurve was extracted. The source count rate is very low (0.2 count s$^{-1}$). A period of 227±5 sec is found in the lightcurve and absent from the background (Fig. 5). The probability of chance detection can be estimated as below $10^{-3}$. The pulse fraction (Fig. 5) is 80±16%. A lightcurve folded with the same

period was extracted at low energy (0.4–1.5 keV) to study the strong soft X-ray excess found in this source but the number of counts was too low to reach any conclusion.

We also searched a 10 sec time bin ISGRI lightcurve of revolution 232, when the source was bright, but no pulsation was found.

EPIC pulse phase spectra have been built for the pulse (0.38–0.92) and the interpulse (0.92–0.38) phase regions. The spectra do not show significant spectral shape variations and could be fitted with the parameters listed in Table 4 besides the change in continuum normalisation ($\chi^2_\nu = 1.05$).

#### 3.4.4. IGR J17544-2619

The XMM-Newton observation was presented by González-Riestra et al. (2004). No pulsation was detected but the source featured a number of short flares. During the 3 INTEGRAL revolutions when the source was bright, the ISGRI lightcurve shows intense variability with count rate increasing from $0 \pm 15$ to $80 \pm 15$ count $s^{-1}$ ($\approx$ 1 Crab) in 300 sec (15–30 keV). Figure 6 shows the strong source activity that occured during revolution 113 (MJD 52898.36-52901.35) just before the XMM-Newton observation. Study of those flares did not reveal any periodicity.

#### 3.4.5. IGR J17597-2201

The XMM-Newton observation of IGR J17597-2201 was affected by on-board buffer overflow due to high background and to the strength of the source, generating an instrumental periodicity of 192 sec. The EPIC pn lightcurve suggests a period of 1800 sec that is however not significant. Nothing could be found in the ISGRI data.

### *3.5. Infrared Photometry*

We have collected (see Table 5) JHK magnitudes available from the 2MASS catalogue (Cutri et al. 2003) for the candidate stellar counterparts (see Sect. 3.1), and in some cases additional BRI magnitudes from the USNO and GSC catalogues (these data were collected through the VizieR service (Ochsenbein et al. 2000).

In order to derive an upper limit on the reddening, we fitted these data with a reddened blackbody model following a procedure detailed in Filliatre & Chaty (2004). The temperature of the black-body was fixed to 20000 K to insure that only the Rayleigh-Jeans part of the spectrum contributes in the available spectral band. If the star is intrinsically cooler or if it harbors any additional infrared contribution (from dust/disk), the absorption must be lower.

We checked that the normalizations resulting from the spectral fits are consistent with the luminosity of a bright blue star given a distance range of 1-10 kpc. In the case of IGR J16320-4751, we were unable to derive reasonable fits. Possible problems may include strong departures from the blackbody model and photometric errors. The upper limit on the reddening obtained for IGR J16318-4848 is fully in agreement with the value derived by Filliatre & Chaty (2004).

The reddening upper limits were converted to $N_H$ according to Predehl & Schmitt (1995) and listed in Table 6. These upper limits are consistent with the galactic interstellar absorption in the direction of the sources and significantly smaller than the amount of absorption derived from the X-ray data excepting for IGR J17597-2201 and IGR J17544-2619. Such conclusions, already derived for IGR J16318-4848 (Walter et al. 2003b; Filliatre & Chaty 2004) and IGR J16320-4751 (Rodriguez et al. 2003), indicate that, excepting for IGR J17597-2201 and IGR J17544-2619, the absorbing matter is not interstellar but concentrated close to the X-ray sources.

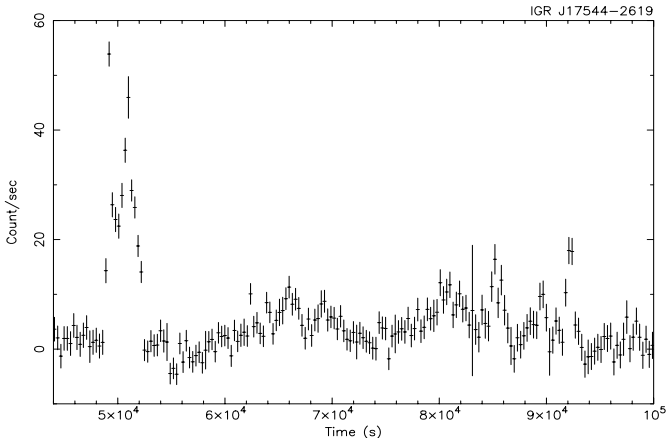


**Fig. 6.** INTEGRAL/ISGRI 15–30 keV lightcurve of IGR J17544-2619

## 4. Discussion

Among the unidentified sources detected by INTEGRAL in the galactic plane, XMM-Newton observations could be obtained for 10 objects. Eight sources appear to be persistent, two are transient.

Using the precise positions provided by XMM-Newton, we found bright infrared candidate counterparts in the 2MASS survey images for all sources. The upper limits on the absorption derived from the available photometry are consistent with the galactic interstellar absorption and smaller than the absorption derived from the X-ray data for eight sources. In those sources the additional absorption of the X-ray sources is local to the compact source and not of interstellar origin. More precisely the absorbing matter is located close enough to the source so that dust could not form.

In our sample, seven sources are persistent and feature absorbing column densities much larger than the galactic value. Those sources are discussed in Sect. 4.2 to 4.4. The three sources that do not share those properties are discussed in Sect. 4.1.

**Table 5.** Counterpart photometry. JHK magnitudes are from the 2MASS catalogue. BRI magnitudes are from the USNO and GSC catalogue (obtained through *Vizier*) and from Filliatre & Chaty (2004) for IGR J16318-4848.

| Counterpart | B | R | I | J | H | K |
|---|---|---|---|---|---|---|
| 16314831-4849005 | $25.4 \pm 1.0$ | $17.7 \pm 0.1$ | $16.1 \pm 0.5$ | $10.16 \pm 0.02$ | $8.33 \pm 0.03$ | $7.19 \pm 0.02$ |
| 16320175-4752289 | | | | $14.08 \pm 0.10$ | $13.03 \pm 0.05$ | $10.99 \pm 0.03$ |
| 16390535-4642137 | | | | $14.63 \pm 0.06$ | $13.32 \pm 0.04$ | $12.78 \pm 0.04$ |
| 16415078-4532253 | | | | $13.87 \pm 0.05$ | $12.31 \pm 0.04$ | $11.48 \pm 0.03$ |
| 16480656-4512068 | | 18.4 | 16.7 | $12.95 \pm 0.03$ | $10.83 \pm 0.02$ | $9.80 \pm 0.02$ |
| 17251139-3616575 | | | | $14.23 \pm 0.03$ | $11.81 \pm 0.03$ | $10.67 \pm 0.02$ |
| 17594556-2201435 | | | | $14.87 \pm 0.07$ | $13.44 \pm 0.07$ | $12.95 \pm 0.07$ |
| 18024194-2017172 | | | | $12.72 \pm 0.04$ | $11.91 \pm 0.04$ | $11.47 \pm 0.03$ |
| 180242.0-201720.2 | 17.5 | 15.5 | 14.2 | $12.87 \pm 0.04$ | $13.30 \pm 0.04$ | $11.75 \pm 0.03$ |
| 16463526-4507045 | $15.2 \pm 0.3$ | $13.2 \pm 0.3$ | $11.7 \pm 0.3$ | $10.54 \pm 0.03$ | $10.08 \pm 0.03$ | $9.84 \pm 0.02$ |
| 17542527-2619526 | 14.2 | $11.5 \pm 0.4$ | 10.4 | $8.79 \pm 0.02$ | $8.31 \pm 0.03$ | $8.02 \pm 0.03$ |

**Table 6.** Properties of the newly discovered INTEGRAL sources that have been observed with sensitive X-ray instruments. $N_{\rm H}^{\rm gal}$ is the galactic column in the source direction (Dickey & Lockman 1990). $N_{\rm H}^{\rm E_{B-V}}$ is the maximum absorption derived from the infrared photometry. $N_{\rm H}$ is the measured intrinsic X-ray absorbing column density. $P_{\rm spin}$ is the spin period in sec and $P_{\rm orb}$ the orbital period in days.

| Source | Region | $P_{\rm spin}$ [s] | $N_{\rm H}$ | $N_{\rm H}^{\rm gal}$ | $N_{\rm H}^{\rm E_{B-V}}$ | SP. T. | $P_{\rm orb}$ [d] |
|---|---|---|---|---|---|---|---|
| | | | [$10^{22}$ atom cm$^{-2}$] | | | | |
| **PERSISTENT SOURCES** | | | | | | | |
| IGR J16318−4848 | Nor | | 193 | 2.1 | <4.2 | sgB[e][1] | |
| IGR J16320−4751 | Nor | 1300[2] | 18 | 2.1 | | Early type[8] | 8.99 |
| IGR J16393−4641 | Nor | 912[3] | 24 | 2.2 | <2.7 | | |
| IGR J16418−4532 | Nor | 1246 | 10 | 2.0 | <3.6 | | |
| IGR J16479−4514 | Nor | | 8 | 2.1 | <4.8 | Early type[8] | |
| IGR J17252−3616 | GC | 414[4] | 15 | 1.5 | <5.3 | Early type[8] | 9.72[4,6] |
| IGR J17597−2201 | GC | | 5 | 1.2 | <2.9 | Late type[8] | |
| IGR J18027−2016 | GC | 139[5] | 9 | 1.1 | <2.1 | sgOB[5] | 4.57[5] |
| **TRANSIENT SOURCES** | | | | | | | |
| IGR J16465−4507 | Nor | 228 | 60 | 1.6 | <1.0 | sgB[7] | |
| IGR J17544−2619 | GC | | 2 | 1.4 | <2.5 | sgB[8] | 165 |

References: [1]Filliatre & Chaty (2004); [2]Lutovinov et al. (2005b) ; [3]Bodaghee et al. (2005); [4]Zurita Heras et al. (2005); [5]Hill et al. (2005); [6]Markwardt & Swank (2003); [7]Smith (2004); [8]Chaty et al (in prep.)

### *4.1. Transient or unabsorbed sources*

IGR J17544-2619 is probably a long period (165 d) system flaring at periastron passage. The system did not show any enhanced absorption and shares the properties of typical Be systems. During flares, the source flux became 100 times brighter than the typical flux observed in the persistent sources. This suggests accretion events reaching the Eddington limit typically observed in Roche-lobe overflow systems when the compact object reaches the periastron of an eccentric orbit. The early spectral type (Chaty et al, in prep.) of the infrared counterpart we suggest confirms the HMXB nature of the source.

IGR J16465-4507 is a transient X-ray pulsar featuring huge absorbing column density (when active). The companion of IGR J16465-4507 is a supergiant massive star (Smith 2004). This object could be a long orbital period system similar to IGR J17544-2619.

IGR J17597-2201 is a persistent source that is not strongly absorbed (the additional column density is compatible with the upper limit on the infrared reddening). This system has been proposed to be a LMXB (Lutovinov et al. 2005a) which is in agreement with the late spectral type of the infrared counterpart we have proposed (Chaty et al, in prep.).

### *4.2. Persistent intrinsically absorbed sources*

The seven persistent absorbed sources in our sample are bright ($> 10^{-10}$ erg s$^{-1}$ cm$^{-2}$) above 10 keV but weak enough in the keV range to have remained largely unnoticed in previous X-ray galactic plane surveys. In some cases, they could have been missed also because of their variability on time scales of hours to days.

A major step forward in understanding these systems has come from the detection of X-ray pulsations in the source light curves. Pulse periods ranging from 139 to 1300 sec have been determined for five of the seven sources. No pulsation was found from IGR J16479-4514 and in IGR J16318-4848. In the former object, the presence of a pulsar is not excluded as the XMM-Newton and ISGRI data, that were of too low quality to allow any period detection, are compatible with a pulsed fraction of 100% for a period of 1 ksec. In the latter source, either the pulse fraction is small (<10%), or the spin period is very long ($P_s$>5 ksec).

Known HMXBs accreting pulsars with pulse periods exceeding 100 seconds fall into two distinct groups according to the nature of their companion stars. The Be binary systems with orbital periods above 100 days and the supergiant systems with shorter orbital periods. In supergiant systems, Waters & van Kerkwijk (1989) have suggested that the long spin periods resulting from the propeller effect (Illarionov & Sunyaev 1975) during the post SN evolution could remain during the high-mass X-ray binary phase of the system almost independently of the orbital period.

Among the persistent INTEGRAL sources, estimates of the orbital period are only available for four systems: 4.57 d for IGR J18027−1455 (Hill et al. 2005), 8.99 d for IGR J16320-4751, 9.7 d for IGR J17252−3616 (Markwardt & Swank 2003) and 13 d for IGR J19140+0951 (Corbet et al. 2004) that are therefore very probably supergiant systems. Two additional persistent sources of our sample have spin periods consistent with such systems. Those sources being persistent they are unlikely to be Be systems and likely supergiant as well.

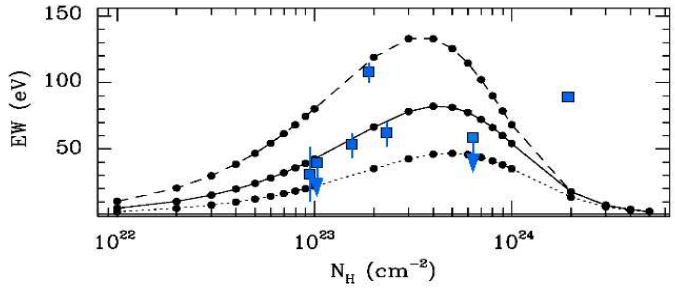


**Fig. 7.** The Fe K$\alpha$ equivalent width calculated with reference to the unabsorbed continuum (and corrected for the peculiar Iron abundances when needed) plotted against the absorbing column density. The curves show the prediction of a spherical distribution of matter around the X-ray source for different Fe abundances (from Matt 2002).

The observed X-ray spectral shape clearly point to a transmission geometry where the compact source is embedded in dense material (a reflection geometry cannot explain the spectra). When compared to the continuum flux corrected for the photoelectric absorption, the strength of the Fe fluorescence line varies in a narrow range (30–90 eV) indicating that a very significant fraction of the solid angle around the X-ray sources is filled with cold matter. The relation between the Fe K$\alpha$ equivalent width and the absorbing column density could help understanding the geometry of the cold dense matter surrounding the X-ray sources. Our data, corrected for the peculiar Fe abundances when needed, are displayed in Fig. 7 together with the results of simulations obtained by Matt (2002) for a spherical shell geometry. Except for IGR J16318-4848, which displays an excess of absorption on the line of sight, all sources are compatible with a spherical distribution of dense gas around the X-ray sources.

The excess of absorption on the line of sight in IGR J16318-4848 could be related to the absence of soft X-ray excess in that source (Sect. 3.3.2) and to the B[e] type companion. In this source most of the absorption could be related to matter located far away from the neutron star, e.g. the cold circum-stellar matter responsible for the B[e] low ionization spectral line, that contributes less to the fluorescence.

The picture emerging of these observations is that of a neutron star (or a black hole in some cases), orbiting constantly in dense material expelled from a supergiant stellar companion. Spectral identification of the infrared counterparts is on-going. 5 out the 7 counterparts show early spectral type or evidence for a high-mass, confirming their HMXB nature (Table 6). Recent observations of the highly-absorbed persistent source IGR J19140+0951 (Rodriguez et al. 2005) are compatible with the above picture.

### 4.3. Galactic distribution

When compared to known HMXBs detected by INTEGRAL, the density of new bright INTEGRAL sources from the catalogue of Bird et al. (2004) peaks in the galactic bulge and in the Norma arm (Walter et al. 2004) regions (Fig. 8). The number of new bright sources detected in the Norma region is significantly higher than the number of new bright sources found in the Scutum arm with a chance probability to be identical lower than 0.1% (the two regions have similar exposure in the images used by Bird et al. (2004)). Interestingly, Bronfman et al. (2000) reported that the Norma arm is currently the region of the galaxy with the highest OB star formation rate.

Hipparcos observations of supergiant OB systems suggest that those systems have peculiar tangent velocities (corrected for the differential galactic rotation) above 60 km $s^{-1}$ (Chevalier & Ilovaisky 1998). With an age since SN explosion of few $10^6$ years, supergiant HMXB systems could have reached locations as distant as 0.1 kpc from their birth location. The new sources in the Norma region are distributed within 2 degrees of the galactic plane. Such narrow distribution could be kept only if the source's distance is higher than 2 kpc. The spread of the Norma source distribution with galactic longitude (about 10 degrees) in-

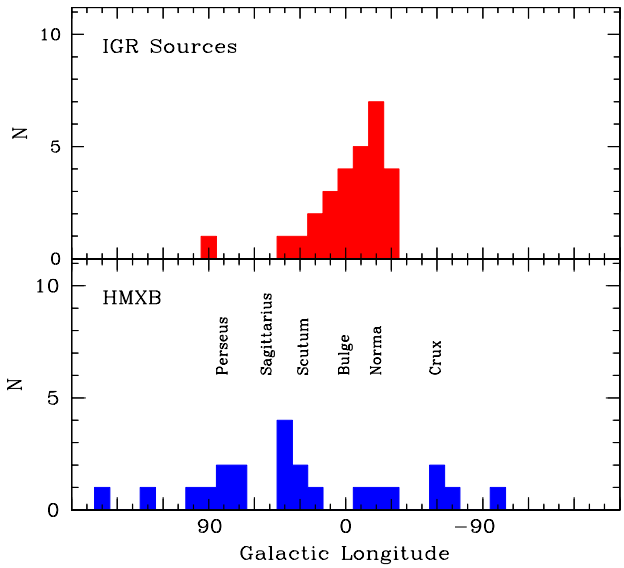


**Fig. 8.** Galactic longitude distribution of new bright INTEGRAL sources and of known HMXBs detected by INTEGRAL (according to Bird et al. 2004).

dicates that these sources most likely did not originate from a single location in the Norma arm.

If the distance to the sources is between 5 and 10 kpc, the luminosities that could be inferred from the infrared photometry, 0.3–10 $\times$ $10^5$ $L_\odot$, is in good agreement with the expectations for 15 to 30 $M_\odot$ companions. IGR J16318-4848 is significantly brighter in the infrared, however, sgB[e] stars are known to have infrared excesses of several magnitudes (Zickgraf et al. 1992).

### 4.4. Geometry

In HMXB, the absorbing column density expected from a spherically symetric stellar wind (terminal velocity $V_W \approx$ 1000 km $s^{-1}$) of the companion (of radius $R_C \approx 10^{12}$ cm) can be evaluated as

$$N_H \approx \frac{\dot{M}}{4\pi R_C V_W m_H} \approx 2 \times 10^{22} \text{atom cm}^{-2} \frac{\dot{M}}{10^{-6} M_\odot yr^{-1}}.$$

This is too small to account for the observation unless the strongly absorbed systems feature extreme mass loss rates, small wind velocities or tidal accretion streams (Blondin et al. 1991).

For small orbital radii, the Stomgren sphere around the X-ray source ($R_S \approx R_C$) will efficiently photoionize the stellar wind such that the acceleration of the wind will be very much reduced. Reduction of the wind velocity by a factor of 5 could increase the absorbing column density to more than $10^{23}$ atom $cm^{-2}$ (Blondin 1994) forming an accretion wake/torus of dense material surrounding the compact object. In the absence of eclipse, for a face-on orbit and a relatively low X-ray luminosity ($\approx 10^{36}$ erg $s^{-1}$), the compact source could remain occulted by this shadow wind for a large fraction of the orbit. In eclipsing systems like IGR J17252-3616 or IGR J18027-2016 larger variations of the absorbing column density are expected.

The compact object should have an important impact on the wind flow creating inhomogeneities that could be responsible for the strong variability observed on time scales of the order of a fraction of the orbital period. Negueruela (1998) have shown that systems with small orbits, accreting from dense regions of a perturbed disk, will feature X-ray outbursts. Negueruela (2004) suggested a relation between fast transient HMXB systems and high absorption which could indicate a different dynamic of the stellar wind than in the persistent systems.

It is interesting to note that within the proposed geometry, soft X-ray excesses emitted close to the neutron star (surface, accretion flow) would be completely absorbed and therefore not detected. The soft X-ray excesses observed in some of our sources are very weak with $F^{SE} \approx 10^{-4} F_{2-100}$ and compatible with the expectation from X-ray reprocessing in larger photoionised shells (Hickox et al. 2004; Schulz et al. 2002).

In sgB[e] system, like IGR J16318-4848 (Filliatre & Chaty 2004) or CI Cam (Hynes et al. 2002) dense equatorial wind components have been observed. Models of B[e] systems predict the possible co-existence of a rapid highly ionised polar wind with a slow dense, low ionized, equatorial component with an extension of 10–20 stellar radii and a thickness of up to 1 stellar radius/$10^{24}$ $cm^{-2}$ (Stee 1998). In IGR J16318-4848, the low ionisation of Iron is compatible with a size of the fluorescence region of the order of $10^8$ km which was also found to be compatible with the absence of delay between Fe line and continuum flux variations observed at one occasion (Walter et al. 2003b). We therefore suggest that the compact object orbits within the dense wind component of that system explaining the excess of absorbing matter on the line of sight and the absence of a soft X-ray excess.

## 5. Conclusions

Among the 10 unidentified INTEGRAL sources with XMM observations we have found that:

- All sources are detected below 10 keV.
- Candidate infrared counterparts have been found for all sources. Their reddening is compatible with the expectation from interstellar absorption.
- IGR J17597-2201 is probably a LMXB with little or no intrinsic absorption. IGR J17544-2619 is a long period (165 d) transient (probably a Be system) without strong intrinsic absorption. IGR J16465-4507 is a highly absorbed supergiant transient system.
- The other 7 sources are persistent, intrinsically absorbed (0.8–19.3 $10^{23}$ $cm^{-2}$) and very likely supergiant systems. Long pulse periods (139–1300 s) have been found in 5 of these sources, with large pulse fractions. These are X-ray pulsars. One source (IGR J16318-

4848) does not feature a strong pulsation or has a period longer than 2–5 ksec. In these sources, a transmission geometry is likely with the region emitting fluorescence lines related to the absorbing material.
– Dense shadow wind flows could explain the observed X-ray absorption. Such absorption could be persistent for face-on orbits. The very strong absorption observed in IGR J16318-4848 is probably related to a more extended dense stellar wind.
– Previously, only 10 supergiant HMXB were known in the Galaxy (Liu et al. 2000). If a significant fraction of the new sources detected by INTEGRAL are absorbed supergiant wind accretors, as suggested here, then the number of supergiant HMXB could be 2–3 times higher.
– The density of new bright INTEGRAL sources is significantly enhanced in the direction of the inner Norma arm of the galaxy. As many systems are HMXB, a burst of stellar formation may have occurred recently in that region.

With the accumulation of exposure time and the increased sensitivity that will result from an extended mission lifetime, INTEGRAL is very likely to further increase the number of known persistent (i.e. supergiant) HMXB systems. Extrapolating the log N-log S of the unidentified sources predicts the possible detection of up to a hundred supergiant HMXB systems in the galaxy during the next years by INTEGRAL. Identification of these sources will require an intense follow-up programme with XMM-Newton and other missions.

*Acknowledgements.* Based on observations obtained with the ESA science missions INTEGRAL and XMM-Newton. The INTEGRAL and XMM-Newton instruments and data centers were directly funded by ESA member states and the USA (NASA).

## References

Apparao, K. M. V. 1994, Space Science Reviews, 69, 255
Augello, G., Iaria, R., Robba, N. R., et al. 2003, ApJ, 596, L63
Bird, A. J., Barlow, E. J., Bassani, L., et al. 2004, ApJ, 607, L33
Blondin, J. M. 1994, ApJ, 435, 756
Blondin, J. M., Stevens, I. R., & Kallman, T. R. 1991, ApJ, 371, 684
Bodaghee, A., Walter, R., Zurita Heras, J. A., et al. 2005, A&A, in press
Bronfman, L., Casassus, S., May, J., & Nyman, L.-Å. 2000, A&A, 358, 521
Chevalier, C. & Ilovaisky, S. A. 1998, A&A, 330, 201
Corbet, R., Barbier, L., Barthelmy, S., et al. 2005, American Astronomical Society Meeting Abstracts, 207,
Corbet, R. H. D., Hannikainen, D. C., & Remillard, R. 2004, The Astronomer's Telegram, 269, 1
Courvoisier, T. J.-L., Walter, R., Beckmann, V., et al. 2003, A&A, 411, L53
Cutri, R. M., Skrutskie, M. F., van Dyk, S., et al. 2003, VizieR Online Data Catalog, 2246, 0
Dickey, J. M. & Lockman, F. J. 1990, ARA&A, 28, 215
Filliatre, P. & Chaty, S. 2004, ApJ, 616, 469
González-Riestra, R., Oosterbroek, T., Kuulkers, E., Orr, A., & Parmar, A. N. 2004, A&A, 420, 589
Gros, A., Goldwurm, A., Cadolle-Bel, M., et al. 2003, A&A, 411, L179
Hickox, R. C., Narayan, R., & Kallman, T. R. 2004, ApJ, 614, 881
Hill, A., Walter, R., Knigge, C., et al. 2005, A&A, in press
Hynes, R. I., Clark, J. S., Barsukova, E. A., et al. 2002, A&A, 392, 991
Illarionov, A. F. & Sunyaev, R. A. 1975, A&A, 39, 185
Jansen, F., Lumb, D., Altieri, B., et al. 2001, A&A, 365, L1
Kuulkers, E. 2005, in AIP Conf. Proc. 797: Interacting Binaries: Accretion, Evolution, and Outcomes, 402
Labanti, C., Di Cocco, G., Ferro, G., et al. 2003, A&A, 411, L149
Lebrun, F., Leray, J. P., Lavocat, P., et al. 2003, A&A, 411, L141
Liu, Q. Z., van Paradijs, J., & van den Heuvel, E. P. J. 2000, A&AS, 147, 25
Lubinski, P., Chernyakova, M., Kretschmar, P., et al. 2004, ISDC Newsletter, 16
Lund, N., Budtz-Jørgensen, C., Westergaard, N. J., et al. 2003, A&A, 411, L231
Lutovinov, A., Revnivtsev, M., Molkov, S., & Sunyaev, R. 2005a, A&A, 430, 997
Lutovinov, A., Rodriguez, J., Revnivtsev, M., & Shtykovskiy, P. 2005b, A&A, 433, L41
Markwardt, C. B. & Swank, J. H. 2003, The Astronomer's Telegram, 179
Mas-Hesse, J. M., Giménez, A., Culhane, J. L., et al. 2003, A&A, 411, L261
Matt, G. 2002, MNRAS, 337, 147
Matt, G. & Guainazzi, M. 2003, MNRAS, 341, L13
Morrison, R. & McCammon, D. 1983, ApJ, 270, 119
Murakami, H., Dotani, T., & Wijnands, R. 2003, IAU Circ., 8070, 3
Nagase, F. 2002, Journal of Astrophysics and Astronomy, 23, 59
Negueruela, I. 1998, A&A, 338, 505
Negueruela, I. 2004, in The Many Scales of the Universe - JENAM 2004 Astrophysics Reviews". Kluwer Academic Publishers, eds. J. C. del Toro Iniesta et al.
Ochsenbein, F., Bauer, P., & Marcout, J. 2000, A&AS, 143, 23
Patel, S. K., Kouveliotou, C., Tennant, A., et al. 2004, ApJ, 602, L45
Predehl, P. & Schmitt, J. H. M. M. 1995, A&A, 293, 889
Revnivtsev, M. G., Sazonov, S. Y., Gilfanov, M. R., & Sunyaev, R. A. 2003, Astronomy Letters, 29, 587
Rodriguez, J., Cabanac, C., Hannikainen, D. C., et al. 2005, A&A, 432, 235

Rodriguez, J., Tomsick, J. A., Foschini, L., et al. 2003, A&A, 407, L41
Sako, M., Kahn, S., Paerels, F., et al. 2002, in High-resolution X-ray Spectroscopy Workshop with XMM-Newton and Chandra, edited by Branduardi-Raymont G., http://www.mssl.ucl.ac.uk/~gbr/rgs_workshop/
Schartel, N., Ehle, M., Breitfellner, M., et al. 2003, IAU Circ., 8072, 3
Schulz, N. S., Canizares, C. R., Lee, J. C., & Sako, M. 2002, ApJ, 564, L21
Smith, D. M. 2004, The Astronomer's Telegram, 338
Stee, P. 1998, A&A, 336, 980
Strüder, L., Briel, U., Dennerl, K., et al. 2001, A&A, 365, L18
Sugizaki, M., Mitsuda, K., Kaneda, H., et al. 2001, ApJS, 134, 77
Turner, M. J. L., Abbey, A., Arnaud, M., et al. 2001, A&A, 365, L27
Ubertini, P., Lebrun, F., Di Cocco, G., et al. 2003, A&A, 411, L131
van der Meer, A., Kaper, L., di Salvo, T., Méndez, M., & van der Klis, M. 2004, in Revista Mexicana de Astronomia y Astrofisica Conference Series, 213
van Paradijs, J. 1983, High-mass X-ray Binaries (Cambridge Astrophysics Series, Cambridge, MA: Cambridge University Press)
van Paradijs, J. 1995, in *X-ray Binaries*, edited by Lewin, W.H.G., van Paradijs, J., van den Heuvel, E.P.J., Cambridge University Press, 536
Vedrenne, G., Roques, J.-P., Schönfelder, V., et al. 2003, A&A, 411, L63
Walter, R. 2004, in AAS/High Energy Astrophysics Division Meeting 8, 33.01
Walter, R., Courvoisier, R., Foschini, L., et al. 2004, in Proceedings of the 5th INTEGRAL workshop, 16-20 February 2004, Munich, Germany (ESA-SP-552), Vol. 552, 417–421
Walter, R., Favre, P., Dubath, P., et al. 2003a, A&A, 411, L25
Walter, R., Rodriguez, J., Foschini, L., et al. 2003b, A&A, 411, L427
Warwick, R. S., Norton, A. J., Turner, M. J. L., Watson, M. G., & Willingale, R. 1988, MNRAS, 232, 551
Waters, L. B. F. M. & van Kerkwijk, M. H. 1989, A&A, 223, 196
Winkler, C., Courvoisier, T. J.-L., Di Cocco, G., et al. 2003, A&A, 411, L1
Zickgraf, F.-J., Stahl, O., & Wolf, B. 1992, A&A, 260, 205
Zurita Heras, J. A., de Cesare, G., Walter, R., et al. 2005, A&A, in press

# Third part

# Other Contributions to *INTEGRAL* Science

# Chapter 10
# Other Contribution to the *INTEGRAL* LMXB Monitoring programme

In this chapter, we describe our contribution to the LMXB monitoring programme that is performed with the *INTEGRAL* mission. First, we briefly describe the sample of the selected LMXB that we monitor. Then, we present in detail the early efforts put in place to study the variability of the galactic X-ray sources detected by the ISGRI and JEM-X instruments.

This study was performed in the early days of the mission (2002–2003), particularly during the first two announcements of opportunities periods, AO1 and AO2, so we present preliminary results in this thesis, particularly the first light curves.

The LMXB monitoring programme is part of the core programme whose aim and structure has been presented in Sect. 5.1.4. Only CP data were used for this investigation.

## 10.1 The sample of monitored sources

The two most common categories of X-ray binary sources, LMXB and HMXB, are studied separately. In our case, we concentrated our effort on the former group. The LMXB selected for the *INTEGRAL* monitoring programme were chosen in the catalogue of Liu et al. (2001). Furthermore, only the sources that would be in the FCFOV during the observations of the galactic centre and galactic plane were selected. A further selection was done as sources were distributed within the different *INTEGRAL*-related teams. At the end, our sample represented in total 78 sources that are listed in Table 10.1.

**Table** 10.1: LMXB sample of the *INTEGRAL* monitoring programme. **C.O.**: compact object. In case of a black hole the means of the identification is specified (d=dynamical measurements; s,l=spectra and light-curve similar to known black holes). **Type**: A=atoll, B=burst, D=dipper, G=globular cluster, P=pulsar, T=transient, U=ultrasoft, Z=Z source; **fx**=average or minimum observed flux in 2–10 keV range in microjanksy; **fmax**=max observed flux or average outburst flux in $\mu$j, in the 2–10 keV range. If fmax is present then fx is the minimum flux; **DE** = Deep Exposure, if $*$ then the source will be observed also in the GCDE.

| Name | l | b | C.O. | Type | fx | fmax | Vmag | DE |
|---|---|---|---|---|---|---|---|---|
| 0620-003 (N Mon 1975) | 209.9 | -6.5 | BH(d) | TU | <0.02 | 50000 | 11.2 | |
| 0918-549 | 275.8 | -3.8 | | | 10 | | 21 | |
| 0921-630 | 281.8 | -9.3 | | D | 3 | | 15.3 | |
| 1009-45 (XN Vel 1993) | 275.8 | 9.3 | BH | TU | | 800 | 14.7 | |
| 1124-684(N Mus 1991) | 295.3 | -7.0 | BH(d) | TU | <4 | 3000 | 13.6 | |
| 1354-645 (Cen X-2) | 309.9 | -2.7 | BH | TU | 5 | 120 | 16.9 | |
| 1524-617 (TrA X-1) | 320.3 | -4.4 | BH | TU | <5 | 950 | | |
| 1543-475 | 330.9 | 5.4 | BH | TU | 1 | 15000 | 14.9 | * |
| 1543-624 | 321.7 | -6.3 | | | 35 | | | |
| 1556-605 | 324.1 | -5.9 | | | 16 | | 18.6 | |
| 1617-155 (Sco X-1) | 359.0 | 23.7 | | Z | 14000 | | 12.2 | |
| 1624-490 | 334.9 | -0.2 | | D | 55 | | | * |
| 1630-472 (Nor X-1) | 336.9 | 0.2 | BH | TUD | <2 | 1400 | | * |
| 1632-477 | 336.8 | -0.3 | | | 13 | | | * |
| 1642-455(GX 340+0) | 339.5 | 0.0 | | Z | 500 | | | * |
| 1702-363 (GX349+2) | 349.1 | 2.7 | | Z | 825 | | 18.6 | * |
| 1705-250 (N Oph 1977) | 358.5 | 9.0 | BH(d) | T | 2 | 3600 | 15.9 | * |
| 1708-408 | 346.3 | -0.9 | | | 32 | | | * |
| 1711-339 | 352.0 | 2.7 | | T | 16 | 130 | | * |
| 1716-249 (XN Oph 1993) | 0.1 | 6.9 | BH | T | | 1500 | 16.65 | * |
| 1724-356 | 352.2 | 0.4 | | | 32 | | | * |
| 1728-169 (GX 9+9) | 8.5 | 9.0 | | A | 300 | | 16.8 | * |
| 1730-220 | 4.4 | 5.8 | | T | <10 | 130 | | * |
| 1730-312 | 356.6 | 0.9 | BH(s,l) | T | | 900 | | * |
| 1732-273 | 0.1 | 2.5 | | TU | <5 | 50 | | * |
| 1734-292 | 358.8 | 1.3 | | | 3.4 | | | * |
| 1735-28 | 359.5 | 1.5 | | T | <0.4 | 565 | | * |
| 1736-297 | 358.6 | 0.7 | | | 2 | | | * |
| 1737-282 | 359.9 | 1.2 | | | 3 | | | * |
| 1737-31 | 357.6 | -0.0 | BH(s,l) | T | | 26 | | * |
| 1739-278 | 0.6 | 1.1 | BH(s,l) | T | | 860 | 23.2 | * |
| 1739-304 | 358.3 | -0.2 | | | 9 | | | * |
| 1740-294 (GX X-4) | 359.3 | 0.0 | | T(?) | | 30 | | * |
| 1741-322 | 357.1 | -1.6 | | TU | 2 | 770 | | * |

**Table** 10.1: *continued.*

| Name | l | b | C.O. | Type | fx | fmax | Vmag | DE |
|---|---|---|---|---|---|---|---|---|
| 1741.2-2859 | 359.7 | 0.1 | | | 1.5 | 300 | | * |
| 1742-326 | 356.7 | -1.9 | | | <2 | 3 | | * |
| 1742.2-2857 | 359.9 | 0.0 | | | 0.1 | | | * |
| 1742.5-2845 | 0.1 | 0.0 | | | 0.15 | 26 | | * |
| 1742.5-2859 | 359.9 | -0.0 | | | 1 | 5 | | * |
| 1742.7-2902 | 359.9 | -0.1 | | | 0.2 | | | * |
| 1742.8-2853 | 0.0 | -0.0 | | | 0.2 | | | * |
| 1742.9-2849 | 0.1 | -0.0 | | | 0.2 | | | * |
| 1742.9-2852 | 0.0 | -0.0 | | | 0.2 | | | * |
| 1743.1-2843 | 0.2 | -0.0 | | | 0.5 | 12 | | * |
| 1743.1-2852 | 0.1 | -0.1 | | | 0.2 | | | * |
| 1744-265 (GX3+1) | 2.2 | 0.7 | | BA | 400 | | | * |
| 1744-299 | 359.2 | -0.8 | | | 6 | | | * |
| 1744-361 | 354.1 | -4.1 | | T | <25 | 275 | | * |
| 1745-203 | 7.7 | 3.7 | | GT | <0.1 | 180 | | * |
| 1746-331 | 356.8 | -2.9 | BH | U | 26 | | | * |
| 1746.7-3224 | 357.5 | -2.6 | | | 0.1 | | | * |
| 1747-313 | 358.5 | -2.1 | | GT | 1.5 | 20 | | * |
| 1749-285 (GX+1.1,-1.0) | 1.1 | -1.0 | | T | | 60 | | * |
| 1755-338 | 357.2 | -4.8 | BH | DUT | | 100 | 18.5 | * |
| 1758-205 (GX9+1) | 9.0 | 1.1 | | A | 700 | | | * |
| 1758-250 (GX5-1) | 5.0 | -1.0 | | Z | 1250 | | | * |
| 1803-245 | 6.1 | -1.9 | | T | <2 | 1000 | | * |
| 1813-140 (GX17+2) | 16.4 | 1.2 | | ZB | 700 | | 17.5 | * |
| 1822-000 | 29.9 | 5.7 | | | 25 | 62 | 22 | * |
| 1822-371 | 356.8 | -11.2 | | D | 10 | 25 | 15.3-16.3 | * |
| 1846-031 | 29.9 | -0.9 | BH | TU | | 300 | | * |
| 1918+146 | 49.2 | 0.4 | | T | <5 | 45 | | |
| 1957+115 | 51.3 | -9.3 | | U | 30 | | 18.7 | |
| 2000+251 (XN Vul 1988) | 63.3 | -2.9 | BH(d) | TU | <0.5 | 11000 | 18.9 | |
| 2023+338 (V 404 Cyg) | 73.1 | -2.0 | BH(d) | TU | 0.4 | 20000 | 12.7 | |
| 2142+380 (Cyg X-2) | 87.3 | -11.3 | | ZB | 450 | | 14.7 | |
| 2318+620 | 112.5 | 1.2 | | | 2.4 | | | |
| J0422+32 (XN Per 1992) | 165.8 | -11.9 | BH(d) | T | | 3000 | 13.2 | |
| J1755-324 | 358.0 | -3.6 | BH | T | | 180 | | * |
| J1856+053 | 38.2 | 1.2 | BH | T | | 70 | | |
| J1859+226 | 54.0 | 8.6 | BH | T | | 600 | 15.31 | |
| J2012+381 | 75.4 | 2.2 | BH | TU | | 160 | 21.33 | * |
| 1516-569 (Cir X-1) | 322.1 | 0.0 | NS | TBA | 5 | 3000 | 21.4 | |
| 1758-258 | 4.5 | -1.3 | BH(s) | U | 20 | | | * |
| J1748-288 | 0.6 | -0.2 | BH | T | 640 | | | * |
| RX J17457-2904 | 359.8 | -0.1 | | | | 9.00 | | |
| SAX J1744-2916 | 359.6 | -0.0 | | | | 8.00 | | * |
| XTE J1739-302 | 358.2 | 0.5 | | | | 70.00 | | * |

The final LMXB selection gathers together sources with noticeable differences: neutron star or black hole as the compact object, Atoll or Z class, presence of jets, presence of a spin period, etc. The aim of this program is to study a wide sample of LMXB on a long-term basis with the same instruments and in the same energy ranges. This allows to address general questions without interpolation and wrong comparison, such as the average spectra of LMXB, the difference between BH and NS, the presence of a hard tail emission, the range of luminosities, the presence of bursts, etc.

## 10.2 The long-term monitoring : preliminary results

Two years of *INTEGRAL* core programme data were analysed with OSA 3.0 until the imaging level. The long-term monitoring was done with the ISGRI and JEM-X instruments. This covered the period between MJD 52650–53100. The total amount of data was huge. Therefore, a clear strategy had to be defined, as several attempts were not possible. Indeed, it was computer time consuming and a lot of disk space was necessary. Besides, decisions about several scientific points needed to be done.

### IBIS/ISGRI

A decision regarding the number of energy bands and their values had to be made. The final choice was to extract images in 7 energy bands: 20–40 keV, 40–60 keV, 60–80 keV, 80–100 keV, 100–150 keV, 150–300 keV, and 300–500 keV. This way, the hard X- and $\gamma$-ray spectral bands were fully covered by the most sensitive range of ISGRI.

OSA offers several modes for detecting sources and extracting their fluxes. Should the extraction for the monitored sources be forced even if it means extracting the background when the source is not present? Or should the programme be left free to extract values only when a source is detected, thus not giving values for every monitored source? Moreover, the image cleaning depends on the number of sources that are searched. All bright sources detected in the FOV have to be cleaned, otherwise ghosts remain in the sky image. Therefore, when monitoring the sample of selected LMXB, several other sources were also monitored "serendipitously". A catalogue with all bright sources plus all the selected LMXB was thus used. The choice was to force the extraction at the source position given in the catalogue.

The analysis was carried out until the IMA step. In 2002 and 2003, the OSA software was still quite unstable. Moreover, it could not manage hundreds of pointings within the same observation group (OG), because crashes were happening too frequently. Since OSA cannot go back, these crashes were definitive and the analysis had to be started all over again. Therefore, the decision was taken to analyse each pointing individually, *i.e.* within its own OG. In case of failure, only that single pointing analysis would be affected. This way, most of the analysis would go until the end, while just a few cases would crash, require further investigation, and running the analysis again if a solution was found.

Each analysis ends with one file (`isgri_sky_ima.fits`) containing four images per energy band : INTENSITY, VARIANCE, SIGNIFICANCE, and RESIDUAL, and one associated file (`isgri_sky_res.fits`) containing the list of sources detected with their found position (`RA_FIN,DEC_FIN`), the extracted flux and its associated error (`FLUX,FLUX_ERR`), and its significance (`DETSIG`) as main information. Unfortunately, all the values are spread in a

hierarchical complex structure. There is no easy way to see the main behaviour of one source, thus requiring new scripts.

The first step was to write tools that would automatise the work needed to study the behaviour of one source. The basic structure of *INTEGRAL* data products is organised by pointings (*i.e.* ScW). Therefore, the relevant information should be sought in each ScW, and then re-organised per source : one file for each and every source would be created and all relevant information stored in it. The following columns would be available :

- the science window number (`ScW`);
- the start time (`TimeStart`) and the stop time (`TimeStop`) of the given pointing;
- the found position in the equatorial coordinate system (`RA_FIN,DEC_FIN`);
- the off-axis angle of the source within the ISGRI FOV (`ANGLE`);
- the average flux of the source per ScW (`FLUXn`) and its error (`F_ERRn`) for each energy band (`n=1,2,..,7`); and
- the detection significance (`DETSIGn`) also for each energy band.

The tool was developed as `perl` script and made extensive use of `FTOOLS` commands.

The first script creates one file per source listed in the input catalogue. For each ScW, the second script selects all the sources of our sample that are located within the ScW FOV. It reads all the information present in the OSA result files, *i.e.* all the results for each source listed in the file `isgri_sky_res.fits` without considering if every detected source is part of our sample. Afterwards, it cross-checks both lists (sample and results) and prints only the information relative to the list of sources selected. No specific task is done for the other detected sources. The goal being to create a light curve of the source, a line was added to the output file every time the source crossed the FOV. It often happened that the source was not detected, either because the analysis crashed and no result file was created, or because the file was empty. To discriminate between these 3 situations, a default value was written for the special cases in each column instead of a value read in the result file :

- -101: the source was not detected in this ScW, so only an upper limit was extracted;
- -111: the analysis crashed; and
- -222: the result file was empty.

This way, it was possible to handle the crashes while building a light curve.

The time scale would be the ScW, *i.e.* one point per $\sim$2 ks. The time used would be the mean between the beginning (`TimeStart`) and the end of the pointing (`TimeStop`) without considering the effects that dead times or good time intervals could have. The off-axis angle of the source in the FOV was important. In the early days of the mission, during the calibration phase, it was noted that the flux of the Crab was varying according to its position in the FOV, meaning that the origin of these variations was instrumental. The off-axis angle was calculated with help of the spacecraft pointing direction (`RA_SCX,DEC_SCX`)

$(\mathrm{ra}_1, \mathrm{dec}_1)$ and the source position $(\mathrm{ra}_2, \mathrm{dec}_2)$. It comes from a simple scalar product :

$$x_1 = cos(\mathrm{dec}_1) * cos(\mathrm{ra}_1) \tag{10.1}$$
$$y_1 = cos(\mathrm{dec}_1) * sin(\mathrm{ra}_1) \tag{10.2}$$
$$z_1 = sin(\mathrm{dec}_1) \tag{10.3}$$
$$x_2 = cos(\mathrm{dec}_2) * cos(\mathrm{ra}_2) \tag{10.4}$$
$$y_2 = cos(\mathrm{dec}_2) * sin(\mathrm{ra}_2) \tag{10.5}$$
$$z_2 = sin(\mathrm{dec}_2) \tag{10.6}$$
$$\mathrm{off-axis\ angle} = arccos(x_1 * x_2 + y_1 * y_2 + z_1 * z_2) \tag{10.7}$$

As the extraction was forced at each source position listed in the input catalogue irrespective of its presence, many "spurious detections" occurred. These could be tracked as, in these cases, the significance was well below $3\sigma$. When checking the images, it appeared that detections with a significance lower than $4\sigma$ were apparently background features. Thus, flux values had to be discarded, and upper flux limits had to be calculated. The VARIANCE map is linked to the background level, and the values are in counts$^2$ s$^{-2}$. Therefore, the $3\sigma$ flux upper limit ($F_{3\sigma}$) at the source location was simply estimated from the variance map ($variance_{\mathrm{src}}$) as:

$$F_{3\sigma} = 3 \times \sqrt{(variance_{\mathrm{src}}(x, y))} \tag{10.8}$$

where $(x, y)$ was the source location in the image coordinate system.

### Of the importance of the off-axis angle

The deconvolution and the image cleaning are complex tasks. Strong background structures remain in the image after the cleaning, especially at the border[16]. These background regions introduced "artificial" detections of sources due to high background features located at the same place. Therefore, these sources were significantly detected with high fluxes. As this effect is strongly increasing with the off-axis angle, it could be minimised by choosing to plot only fluxes when the source was located within a certain radius.

To illustrate this effect, we show an example with the LMXB GX 339-4. We plot the light curve in 4 energy bands selecting either all the pointings with an off-axis angle lower than 12$^o$ (see Fig. 10.1) or selecting all the pointings (see Fig. 10.2). In the second image, we clearly see the important amount of unuseful data we would add if no screening is done.

### The light curves

Most of the LMXB are not powerful emitters in the $\gamma$-ray domain. Their emission is usually detected up to a few tens of keV in the hard X-ray domain. A few examples are shown : Crab (see Fig. 10.3), 4U 1630-47 (see Fig. 10.4), Sco X-1 (see Fig. 10.5), GX 5-1 (see Fig. 10.6), and 3A 1822-371 (see Fig. 10.7).

[16] An example of such a structure is the one called the "chessboard pattern".

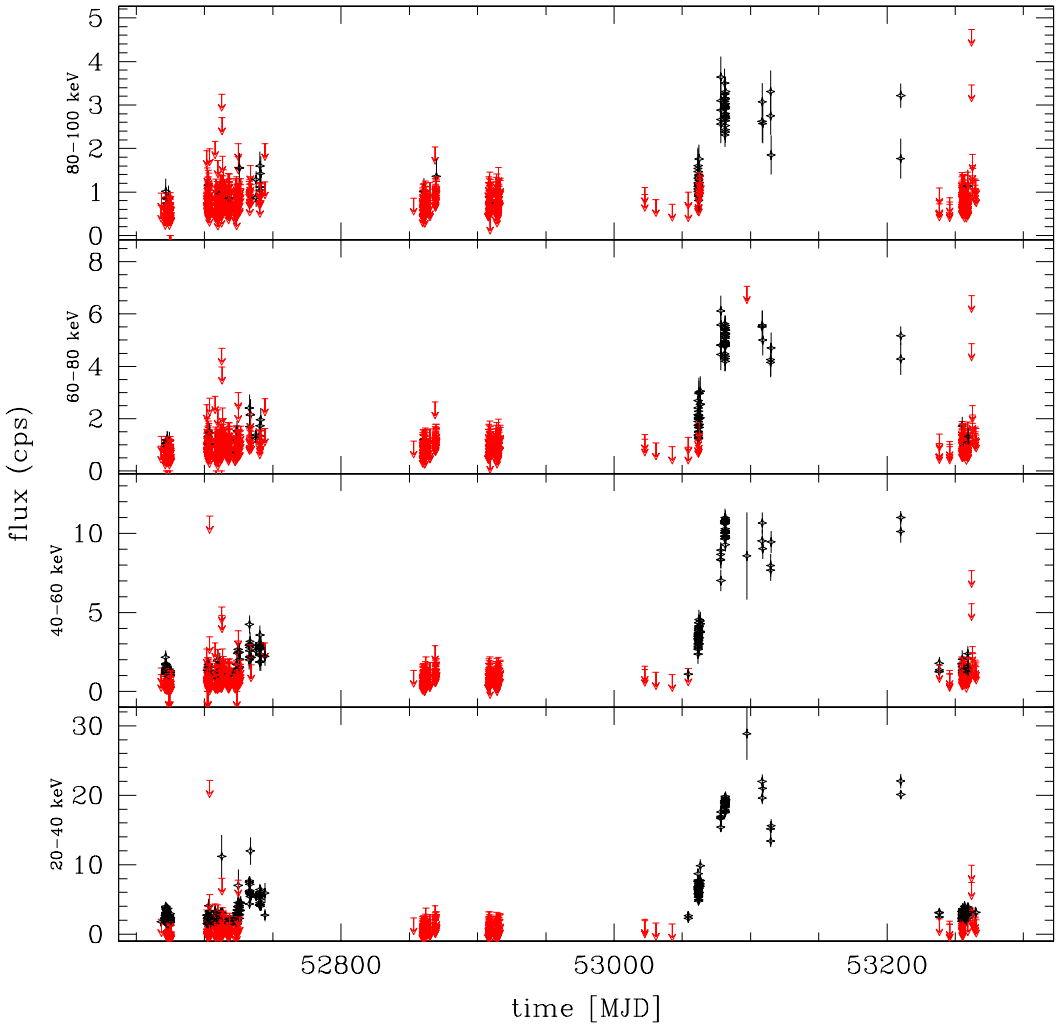


**Figure** *10.1: ISGRI light curve of GX 339-4 during the first two years of the CP. Only pointings with the source within 12° of the FOV centre are plotted.*

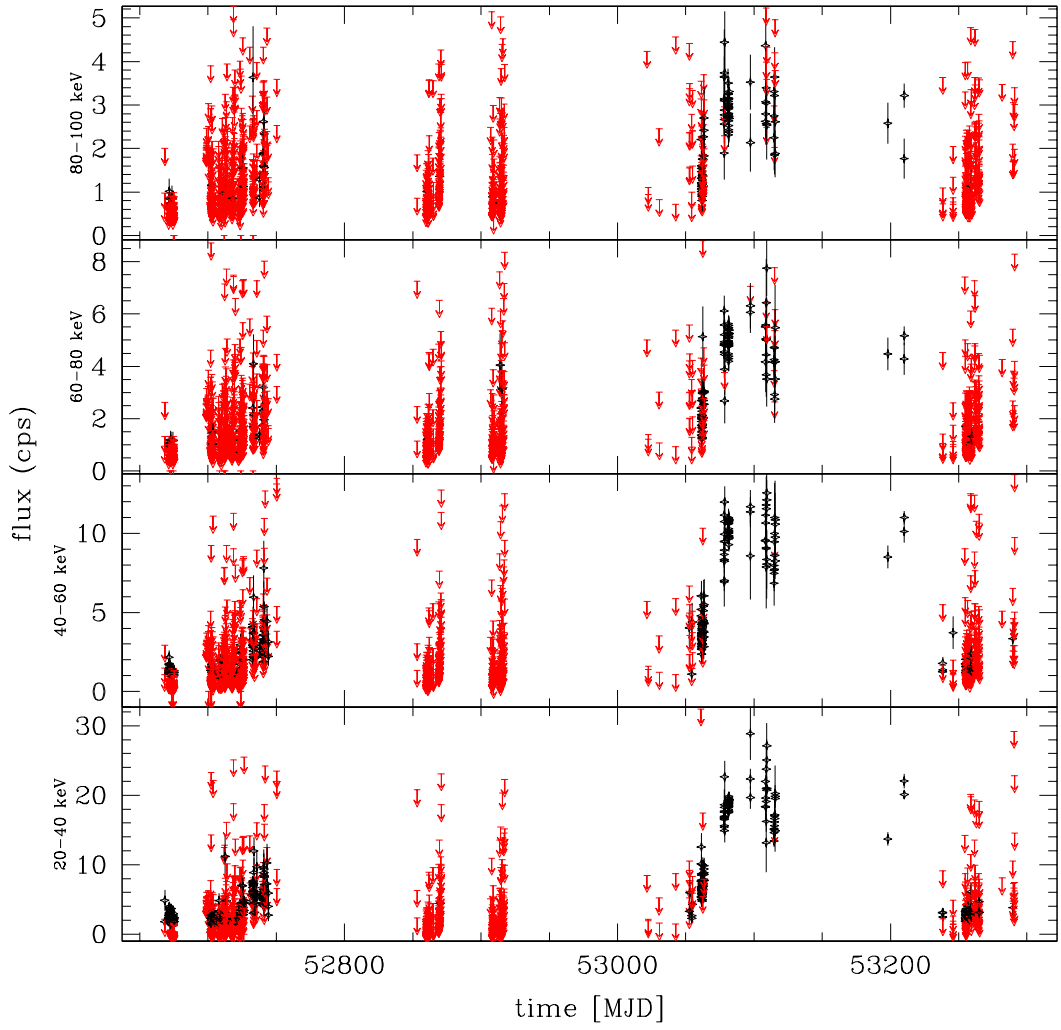


**Figure** *10.2: ISGRI light curve of GX 339-4 during the first two years of the CP. All the pointings are selected.*

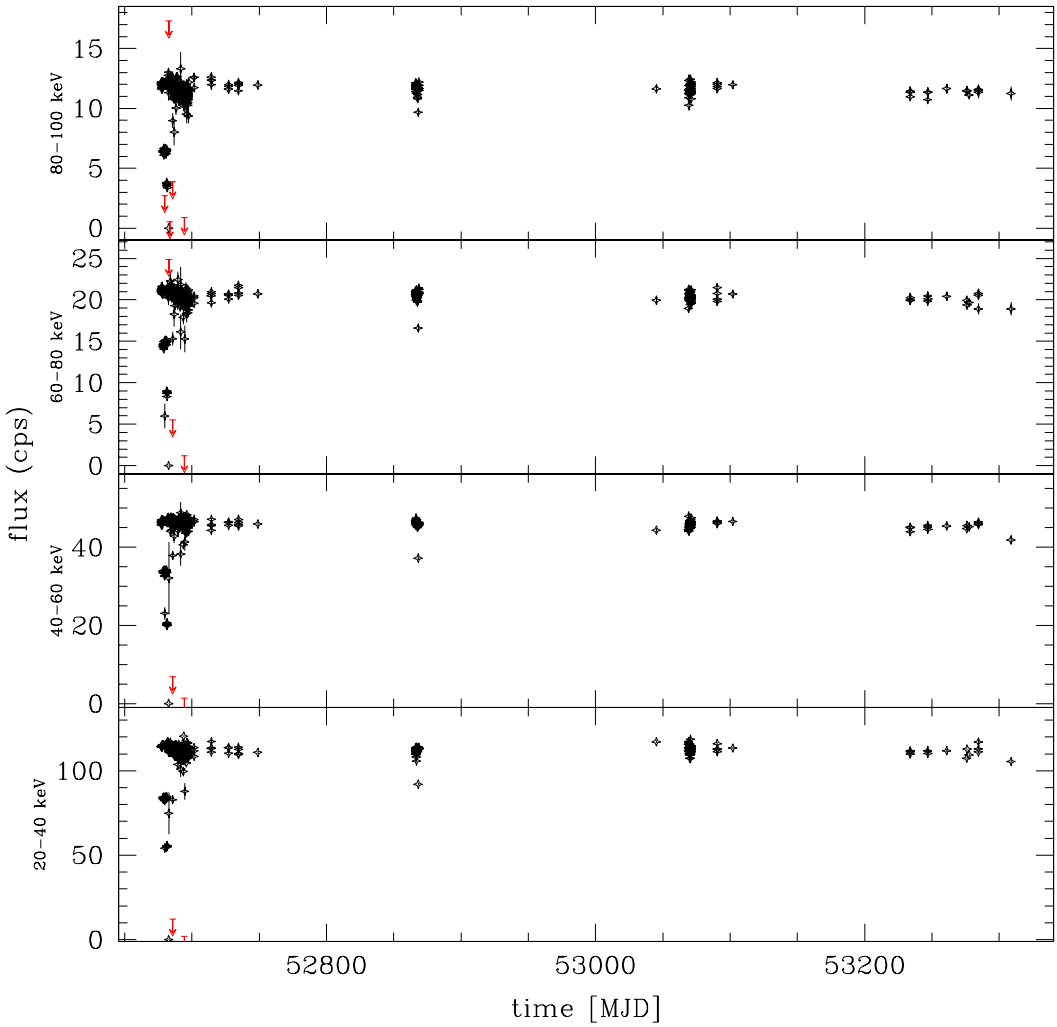


**Figure** *10.3: ISGRI light curve of the Crab.*

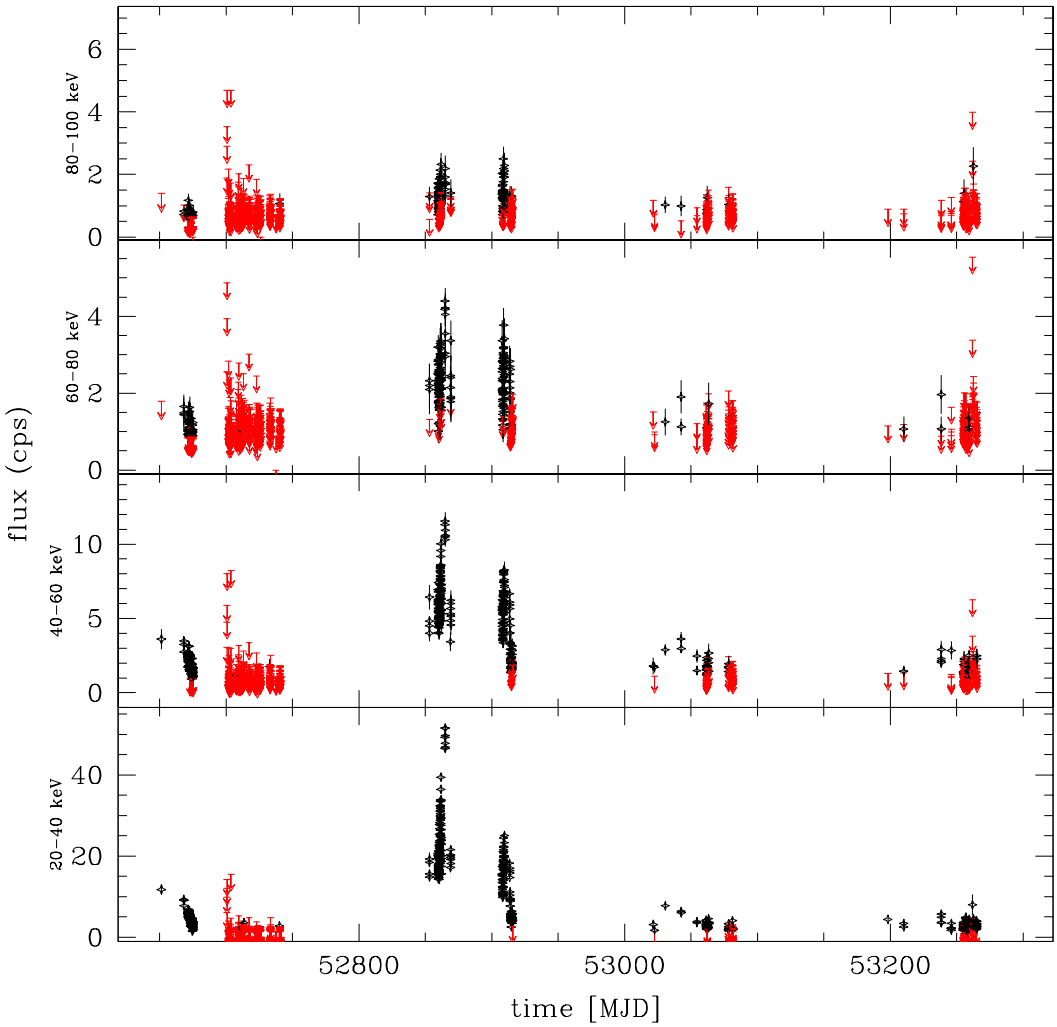


**Figure** *10.4: ISGRI light curve of 4U 1630-47.*

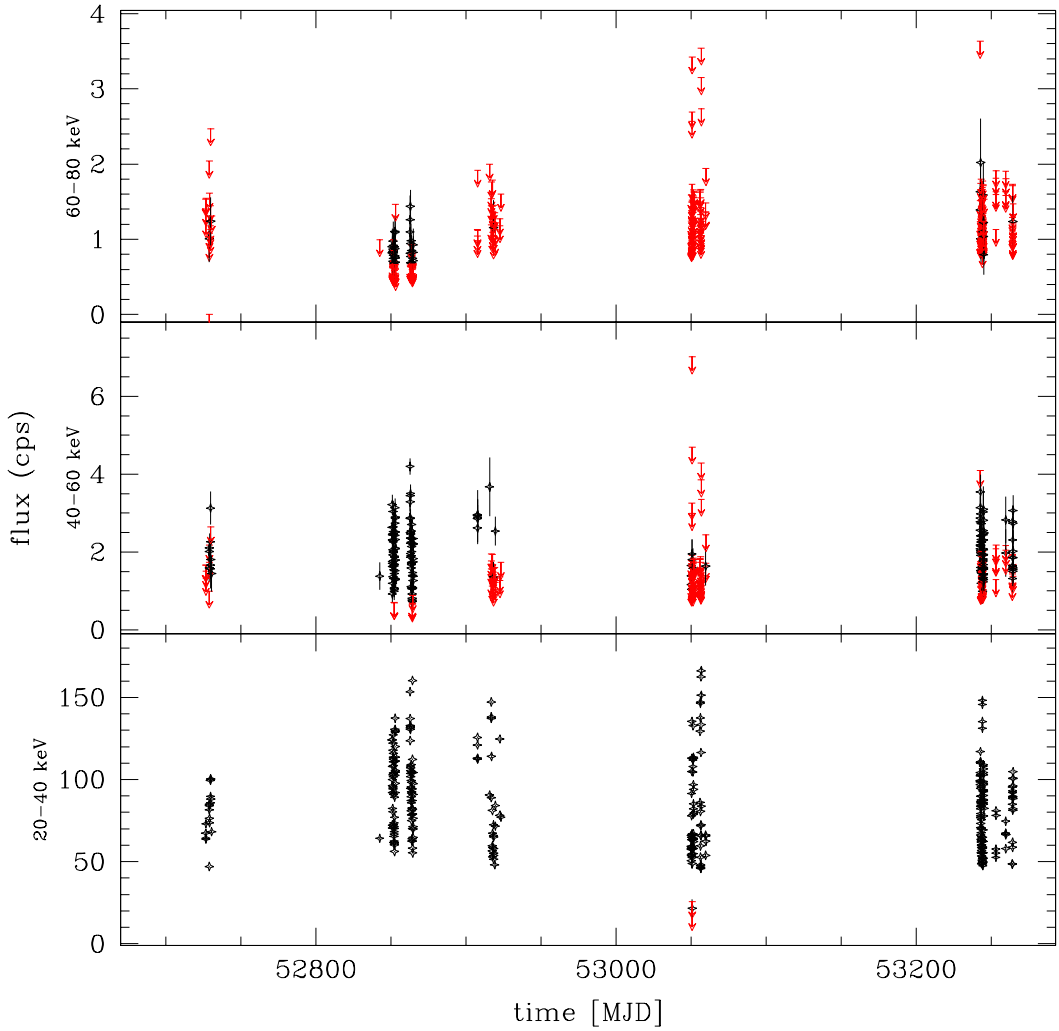


**Figure** *10.5: ISGRI light curve of Sco X-1.*

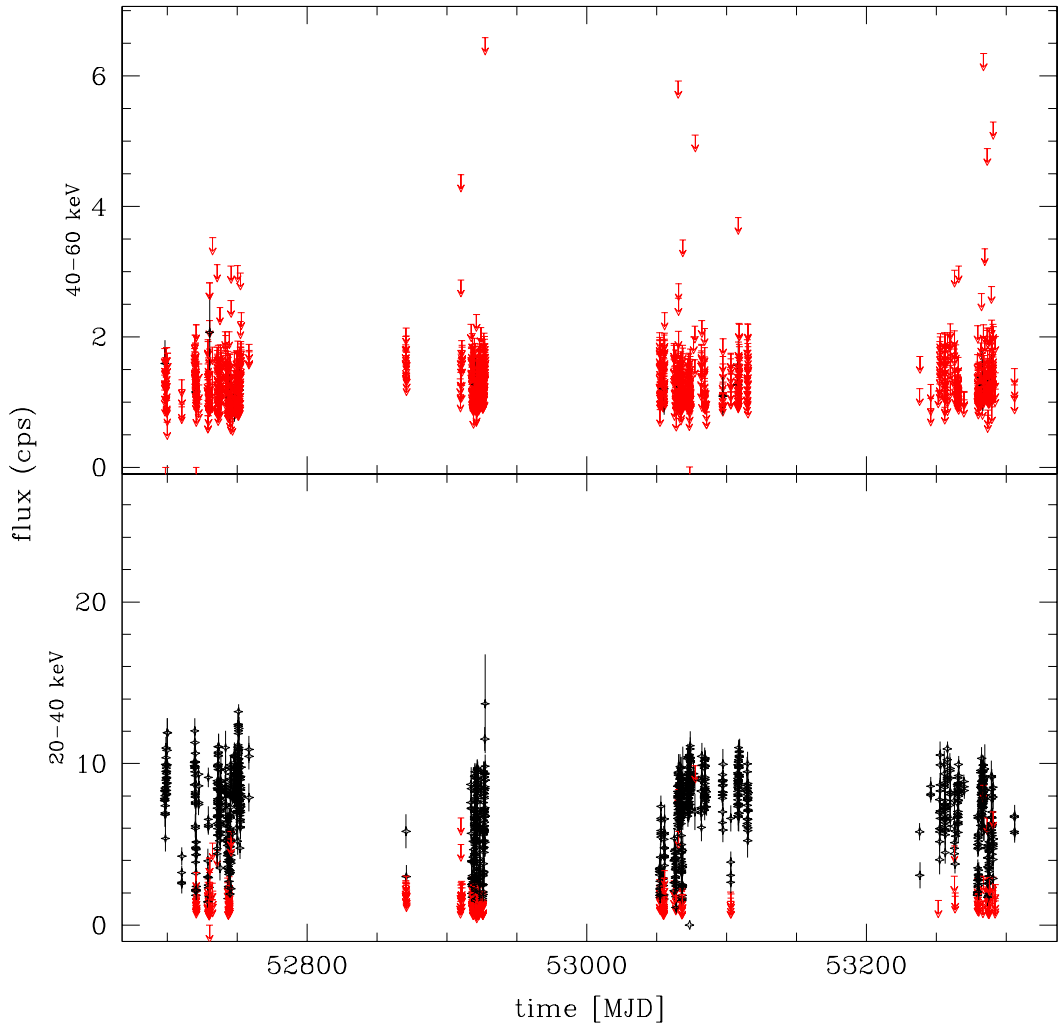


**Figure** *10.6: ISGRI light curve of GX 5-1.*

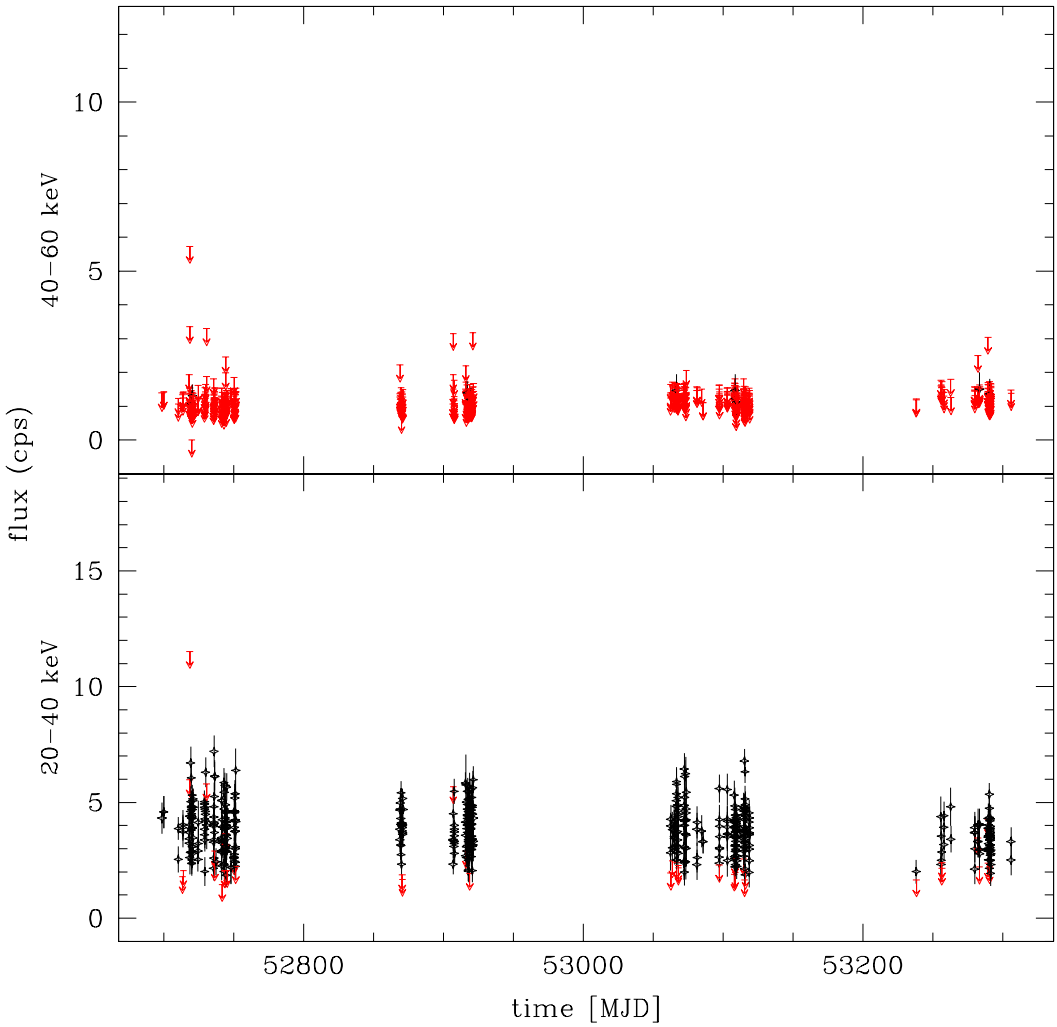


**Figure** *10.7: ISGRI light curve of 3A 1822-371.*

**JEM-X**

The same effort was also undertaken for JEM-X, allowing the monitoring to go down to 3 keV. An other specific `perl` script was written to extract the fluxes, as the organisation in the JEM-X files is different from that of ISGRI. The images per pointings are listed in the file `jmx2_sky_ima.fits`. For each energy band, there are an INTENSITY and a VARIANCE images. The results for all the detected sources are listed inside the file `jmx2_srcl_res.fits`. As for ISGRI, one output file per source was created. The information stored was almost the same as in ISGRI, except there was only one significance value per source, and not one per energy band. The off-axis angle was not reported either. Unfortunately, the relatively bad quality of JEM-X analysis performance at the beginning of the mission did not allow us to make much use of the JEM-X data. Most of the efforts were therefore put into ISGRI.

## 10.3 Conclusions

The quality of the first versions of OSA (up to version 3.0) was not sufficient to get a trustful flux extraction. The light curves were not reliable : long-term variability, short outbursts, flux values, etc were influenced by many external factors. Thus, the scientific output was very limited. However, it gave us a first taste of the possibilities of ISGRI and JEM-X. For instance, we were able to list which sources were bright enough to be persistently detected by *INTEGRAL*. It also showed that OSA needed important improvements before further analysis could be carried out.

Even if the direct scientific impact of this work was rather low, it allowed me to better understand the *INTEGRAL* data analysis, which proved very useful for other studies presented in my thesis. The first results of this LMXB monitoring programme are presented in two papers : one in the special *Astronomy&Astrophysics* issue dedicated to the *INTEGRAL* mission (Paizis et al. 2003) and the other one in the proceedings of the 5th *INTEGRAL* workshop held in Munich (Paizis et al. 2004).

In the current version of OSA, a specific tool (`src_collect`) is able to performs the extraction of average fluxes per ScW, for a given source.

This work is still going on under the supervision of A. Paizis. Currently, the data base is composed of $\sim$ 15 000 ScW. Light curves for all the bright sources were extracted. Individual studies and sample studies are going on. For example, with help of colour-colour diagrams or colour-intensity diagrams, they are looking if it is possible to disentangle the population of NS and BH in the in the hard X-rays.

# Chapter 11
# In the shift...

In this chapter, we describe our contribution to the daily monitoring of the X/$\gamma$-ray sky done by *INTEGRAL*. It is mandatory for the ISDC to follow the observations in real time and to react to extraordinary events occurring at a specific moment.

All the public, private and CP observations are immediately analysed in real time in order to detect any extraordinary event : gamma-ray burst (GRB), new X/$\gamma$-ray source, outburst of a known source, etc. If something interesting happens and if necessary, a world-wide announcement is sent.

## 11.1 The barn

The ISDC is the centre in charge to collect and archive all the science data accumulated by the *INTEGRAL* satellite. As the X/$\gamma$-ray sky is highly variable and the events at these energies can be very short in time, it was decided to process all the data as soon as possible once sent on Earth and forwarded to ISDC. The *barn* is the physical place at ISDC where the daily monitoring is done.

There are two aspects in the monitoring : one technical and one scientific. The technical follow-up is done by the operators that check :

- we are receiving the data;
- the data are correctly processed through the different pipelines;
- the technical parameters of the instruments (temperatures, voltages, etc) are within their limits on a daily-basis;
- they keep contact with the operation centre; and
- they track any technical problem, and alert the people in charge of the instrument showing the problem when necessary.

The scientific aspect of the monitoring is done by all the scientists working at the ISDC. On a 3-days shift basis (as the lapse of one revolution), everybody goes to the barn in order to :

- monitor the instruments on a short 3-hours basis : shadowgrams, count rates, etc;

- detect any new bright source in the sky;
- alert the community in case of any new GRB in the FOV of IBIS;
- monitor any SPI ACS trigger that would be a potential GRB, and alert the group that does triangulation with other spacecrafts in order to localise them;
- detect any outburst or extraordinary variability of any known source; and
- write the end of revolution report.

In case of something interesting happens, there is a procedure to alert the competent people and, sometimes, a world-wide announcement is sent. Evidently, if something happens during a private observation, the people contacted are the Principal Investigator (PI) of that specific observation. The rate of shifts is of three every four months.

Once all the necessary data are received and stored, they go through a set of pipelines that transform them from raw data to processed data. A set of tools has been created in order to ease the job of the Scientist on Duty (Scody). There are two main tasks that the Scody shares : the monitoring of the instruments (shadowgrams of IBIS and JEM-X, image shots of OMC, detector plane of SPI, all the count rates, the telemetry rate) that is done with help of the Interactive Operation Status Monitoring (IOSM). As the operations are currently nominal, that part does not take long anymore.

As the time scale of X/$\gamma$-ray events is an important aspect of the monitoring, the data are not processed with the normal science analysis package OSA, but with a reduced version of it called the Interactive Quick Look Analysis (IQLA). The monitoring is done at a ScW basis, so no SPI images are processed. No specific job is done for OMC. Standard pipelines have been created that process the data and create images for ISGRI and JEM-X (1 or 2) in two energy bands : 20–60 keV and 60–200 keV, and 3–10 keV and 10–30 keV, respectively. There are approximately 3 hours between the data acquisition on-board and the time it is sent and processed, and the images appear in the screen. Therefore, we monitor the X/$\gamma$-ray sky in Near-Real Time (NRT).

A third software package is used to trigger the GRB, and is independent of the IQLA. The *INTEGRAL* Burst Alert System developed jointly between the ISDC and the CNR-Milano looks for any short trigger that looks like a GRB in real time. Indeed, for GRB, each second counts. Follow-up at other wavelengths (UV,OPT,IR) needs to be done as quick as possible.

The shift allows to broaden the current knowledge of everyone on the X/$\gamma$-ray sky. Once in front of the screen, the scody is confronted with any kind of source, not only the specific sources we study.

## 11.2 The external announcements

During my shifts, apart from the normal emission of the sources populating the X/$\gamma$-ray sky, a few events happened that were worth an announcement to the community.

There are a few *on-line* services that allow to spread information in short notice :

- the International Astrophysics Union Circular (IAUC);

- the Astronomer's Telegram (ATel), whose purpose is to report and comment upon new astronomical observations of transient sources.; and
- the Gamma-ray burst Coordinate Network (GCN) maintained by the Heasarc (High-Energy Astrophysics Archive). It is specific to GRB.

*INTEGRAL* has joined the GCN service. All groups interested in GRB detected by *INTEGRAL* can have access to them through the GCN website :

`http://gcn.gsfc.nasa.gov/`.

The ATel are favoured as this service is free of charge. Everybody can have access to it and post any new information about a flaring/outbursting source :

`http://www.astronomerstelegram.org/`.

During my period of shifts (2003–2005), three ATel and one GCN were sent.

**ATel#248** *The LMXRB GX354-0 is flaring in the hard X-rays*, J.A. Zurita Heras (ISDC Geneva), A. Bazzano (IASF Roma), S. Brandt (DSRI Copenhagen), A. Domingo (LAEFF Madrid), C. Winkler (ESA/ESTEC Noordwijk), S. Grebenev (IKI Moscow); March 9, 2004

GX 354-0 (also known as 4U 1728-34) was monitored by *INTEGRAL* as part of the GCDE almost continuously in February–March 2004. Over that period the source flux measured by IBIS/ISGRI between 20–60 keV featured a smooth increase with a maximum flux of 0.2 Crab measured on February 24. The source flux then decreased by a factor of 5 on a time scale of one week. Below 10 keV the flux measured by JEM-X increased by a factor larger than 6 continuously on a time scale of 3 weeks. The flux at 2004-03-08 UTC measured by JEM-X in the 3–10 keV band was 0.5 Crab.

This outburst was confirmed by (Markwardt & Swank 2004) (ATel#255) with RXTE PCA observations that detected a peak flux of 385 mCrab on March 10.04 and a decrease down to normal value a few days later (120 mCrab on March 19.76).

**ATel#331** *INTEGRAL detects increased activity from 4U 0115+63*, J.A. Zurita Heras (ISDC, Versoix), S.E. Shaw (Southampton; ISDC, Versoix), I. Kreykenbohm (IAA, Tubingen), P. Kretschmar (ISDC, Versoix; MPE, Garching), D. Gotz (IASF, Milano), S. Mereghetti (IASF, Milano), A. Lutovinov (IKI, Moscow), G. Palumbo (Bologna), T. Oosterbroek (ESTEC, Noordwijk), C. Budtz-Jorgensen (DSRI, Copenhagen), P. Ubertini (IASF, Roma); September 13, 2004

During a GPS on September 12, 2004, the *INTEGRAL* $\gamma$-ray observatory detected the high mass X-ray binary 4U 0115+63. Increased activity was first noticed by the IBAS gamma-ray burst detection software at 14:53 UTC, leading to the generation of three alerts (1978-79-80). The source was visible in the ISGRI field of view until 16:24 UTC.

The source was also visible in the JEM-X X-ray monitor in one Science Window (2 ks observation starting at 15:31 UTC) leading to the following estimated fluxes:

JEM-X: 3–10 keV$\sim$500 mCrab; 10–30 keV$\sim$750 mCrab; and

ISGRI: 20–60 keV∼400 mCrab; 60–200 keV∼25 mCrab.

Those values corresponded to an increase of a factor 10 to the fluxes reported in Atel#326 from Lutovinov et al. 14 days earlier.

Spectral extraction was possible from the JEM-X observation. No cyclotron line features were seen, although only a 2 ks observation was available for JEM-X in this preliminary analysis.

Pulsed analysis of the ISGRI data, in the 15–40 keV band, clearly showed a periodic signal of 3.614±0.003 s, which is in agreement with published values and identified the flux as being from the associated pulsar, PSR B0115+63.4.

**ATel#367** *Outburst from EXO 2030+375 detected with INTEGRAL*, D. Gotz (IASF, Milano), J.A. Zurita Heras (ISDC, Geneva), C. Winkler (ESTEC), N. Gehrels (NASA/GSFC), S. Martinez-Nuñez (Valencia), A. Bazzano (IASF, Roma), Alexander Lutovinov (IKI, Moscow); December 15, 2004

The HMXB pulsar EXO 2030+375 was observed by *INTEGRAL* during a GPS on December 14, 2004, from 10:46:43 to 14:29:08 UTC. The 20–60 keV flux averaged on single pointings of 2200 s increased from 93 to 214 mCrab. EXO 2030+375 was in the JEMX FOV during one pointing and was detected with average fluxes of 45 and 69 mCrab in the 3–10 keV and 10–31 keV bands.

At 11:46:25 UTC the source did show a 450 s long outburst detected by the *INTEGRAL* Burst Alert System. Its pulse peak spectrum was characterised by a power-law with a photon index of 3.2±0.4 and a flux of $5\,10^{-9}$ ergs cm$^{-2}$ s$^{-1}$ in the 20–40 keV band corresponding to about 0.6 Crab. The 42 s characteristic pulsations were clearly detected.

In the last pointing, the source was still brightening, reaching the highest level ever observed by *INTEGRAL*.

**GCN#4007** *Possible GRB 050922 detected by INTEGRAL*, D.Gotz, S.Mereghetti (IASF, Milano) S. Shaw, N. Mowlavi, M. Beck, J.A. Zurita Heras (ISDC, Versoix) and J. Borkowski (CAMK, Torun) on behalf of the IBAS Localization Team; September 22, 2005

A possible GRB triggered IBAS at 13:43:18 UT with coordinates (J2000)

R.A. = 271.1541

Dec. = -32.0235

with an uncertainty of 3.5′ radius (90% confidence level).

The trigger significance was below the threshold for automatic alert delivery.

A preliminary analysis showed a spectrum consistent with an X-ray flash and a fluence (20–200 keV) was $10^{-7}$ ergs cm$^{-2}$. However, due to the position in the galactic bulge and the soft spectrum, we could not exclude that the trigger was due to an non-catalogued Galactic source.

*Swift* triggered a ToO observation at the same position at 15:21:21 UTC (Kennea et al. 2005) (GCN#4014). They did not detect any point source with a 90% confidence level upper limit of the 0.5–10 keV flux of $3\,10^{-14}$ ergs cm$^{-2}$ s$^{-1}$ with XRT.

# Fourth part

# Quantitative Assessment of Accretion in the Universe

# Chapter 12
# ENERGETIC CONTRIBUTION FROM ACTIVE GALACTIC NUCLEI AND NUCLEOSYNTHESIS

This thesis was started before the launch of the *INTEGRAL* satellite. The first year of this thesis was partly spent on another question more general and not specifically linked to *INTEGRAL*. Meanwhile some questions concerning the possibility of *INTEGRAL* were addressed with the help of the simulator, we looked for the importance of photons produced by the two main physical mechanisms in action in the Universe except for the Big-Bang: gravitation and nucleosynthesis. Based on simple hypotheses, we could derive the ratio of energies radiated by each phenomena. This little study is presented in this chapter.

## 12.1 Scientific paper published in AA

We present the paper published in A&A.

A&A 411, 71–76 (2003)
DOI: 10.1051/0004-6361:20031334


Astronomy & Astrophysics

# Ratio of energies radiated in the universe through accretive processes and nucleosynthesis

J. A. Zurita Heras[1,2], M. Türler[1,2], and T. J.-L. Courvoisier[1,2]

[1] INTEGRAL Science Data Centre, ch. d'Écogia 16, 1290 Versoix, Switzerland
[2] Observatoire de Genève, ch. des Maillettes 51, 1290 Sauverny, Switzerland

Received 8 July 2002 / Accepted 30 July 2003

**Abstract.** We present here a new determination of the ratio of energies radiated by active galactic nuclei and by stars and discuss the reasons for the apparently conflicting results found in previous studies. We conclude that the energy radiated by accretion processes onto super massive black holes is about 1 to 5% of the energy radiated by stars. We also estimate that the total mass accreted on average by a super massive black hole at the centre of a typical $10^{11}\,M_{\odot}$ galaxy is of about $7 \times 10^{7}\,M_{\odot}$.

**Key words.** galaxies: active – stars: evolution

## 1. Introduction

The universe is composed of various objects with a wide variety of emission processes. However, photons have three main origins: the big bang as the source of the cosmic microwave background (CMB), nuclear reactions in stars and gravity through accretion onto compact objects, especially super massive black holes (SMBH). Currently (at $z \simeq 0$), the ratio of the number of photons of CMB and stellar origin in the universe is of the order of 400. It is more difficult to estimate the ratio of the nuclear energy radiated by stars and the gravitational energy radiated by active galactic nuclei (AGN). Several recent studies have shown that the energy released by nucleosynthesis is evolving with cosmic time (Madau et al. 1996, 1998; Trentham et al. 1999; Somerville et al. 2001). It further seems that the star formation history roughly matches the evolution of energy release through accretion onto black holes (Dunlop 1998; Franceschini et al. 1999), since both processes peak around $z \sim 2$. It is therefore possible to relate both phenomena and to estimate the energy ratio radiated by AGN and by stars over the history of the universe.

The determination of this ratio has been addressed several times in the literature. Dunlop (1998) constructed two models of the radio luminosity function of a sample of radio-loud quasars (RLQ), the first only considering luminosity evolution and the second combining luminosity and density evolution. He then related this luminosity to the mass accreted onto the central black hole and compared these curves with the star formation history. The two curves appear to be correlated, suggesting that when $1\,M_{\odot}$ is accreted by a SMBH in a radio loud quasar, $10^{7}\,M_{\odot}$ are used in the star formation process. Based on this relation, Courvoisier (2001) derived a ratio of the energy radiated by RLQ and stars of $E_{\rm RLQ}/E_{\rm stars} \sim 10^{-5}$ by assuming an accretion efficiency of 10 % for the RLQ and a stellar population made of 10 solar mass stars each radiating $4 \times 10^{52}$ ergs over their lifetime. Rather than considering only radio loud AGN, Franceschini et al. (1999) use the 0.5−2 keV X-ray emission as a measure of the energy radiated by AGN. They find that when $1\,M_{\odot}\,{\rm yr}^{-1}\,{\rm Mpc}^{-3}$ is absorbed for star formation, the 0.5−2 keV volume emissivity from AGN is $2.4 \times 10^{40}\,{\rm ergs\,s}^{-1}\,{\rm Mpc}^{-3}$. Considering that type I and II AGN bolometric luminosity is 250 times the 0.5−2 keV luminosity and a stellar radiative efficiency of 0.001, Franceschini et al. (1999) finally obtain $L_{\rm bol(AGN)}/L_{\rm bol(SFR)} \sim 0.1$.

A different approach was followed by Fabian & Iwasawa (1999). Their estimate of this ratio is based on relations linking the bulge mass of a galaxy to both the mass of its central black hole and of its stars. They obtained a value of ∼0.2 for the ratio of the energy radiated by accretion processes and by stars, when assuming an accretion efficiency of 10% for the AGN and the fact that one tenth of the stellar mass is used for nuclear fusion with an efficiency of 0.6%.

Finally, Elvis et al. (2002) estimated that AGN contribute by at least 7% to the total luminosity of the universe as derived from the diffuse background from submillimeter to ultraviolet wavelengths. They obtained this result by first deriving a lower limit of the AGN X-ray emission from the X-ray background (XRB) and by applying a bolometric correction determined with the average spectral energy distribution of quasars.

The aim of this study is to compare the various studies described above and to derive a new estimate of the ratio of gravitational energy released around SMBH to the energy released

*Send offprint requests to*: J. A. Zurita Heras,
e-mail: Juan.Zurita@obs.unige.ch

by nuclear fusion in stars. We first derive the radiation energy density due to stars in Sect. 2, then the corresponding value for accretion by SMBH based on the XRB in Sect. 3. The obtained ratio is compared with previous studies in Sect. 4, where we try to identify the origin of the discrepancies.

## 2. Energy radiated by stars

To estimate the energy radiated by stars in the universe we need to know both the energy release of a typical stellar population and the overall star formation history. Below, we start with the calculation of the stellar energy release, while the evolution of the star density will be described in Sect. 2.2.

### 2.1. Stellar energy release

We use the *Starburst 99*[1] models of Leitherer et al. (1999) to determine the typical stellar energy release. These models predict the spectrophotometric evolution of starburst galaxies between $10^6$ and $10^9$ years after the onset of star formation based on the stellar evolution models of the Geneva group (Schaller et al. 1992; Charbonnel et al. 1993; Schaerer et al. 1993a,b; Meynet et al. 1994). They consider the atmosphere models of Lejeune et al. (1997) and those of Schmutz et al. (1992) when the mass loss becomes important. A simple black body is used for cool stars with additional nebular continuum including free-free interactions below 912 Å and free-bound interactions above. These models have been computed with the isochrone synthesis method and are optimized for massive stars.

Since we are only interested in the total energy release of a typical population of stars during its whole life, we only consider the instantaneous star formation models of Leitherer et al. (1999) because in this case most of the energy is released before $10^9$ years. To assess the effect of changing the power-law index $\alpha$ of the initial mass function (IMF) of the stars we consider both a Salpeter IMF ($\alpha = 2.35$) and a steeper Scalo IMF ($\alpha = 3.3$). In both cases, the cutoff masses are chosen as $M_{\rm low} = 1\,M_\odot$ and $M_{\rm up} = 100\,M_\odot$. The effect of changing the metallicity $Z$ is taken into account by considering four different metallicities: $Z = 0.040, 0.020(= Z_\odot), 0.008$ and 0.001, but without chemical evolution in the models. As an example, we show in Fig. 1 the evolution of the bolometric luminosity of a $10^6\,M_\odot$ star cluster formed instantaneously with a solar metallicity ($Z = 0.020$) according to the model of Leitherer et al. (1999). We extrapolate the bolometric luminosity from $10^9$ to $10^{10}$ years with a power-law in order to include the energy radiated during the final stages of stellar activity. This extrapolation is in good agreement with the earlier study of Charlot & Bruzual (1991).

The total energy radiated by a $10^6\,M_\odot$ star cluster is obtained by integrating the bolometric luminosity over time. The results are presented in Table 1 for the instantaneous stellar formation law, four different metallicities, and two different IMF. Since the bolometric luminosity is dominated by the energy radiated by the most massive stars, the flatter powerlaw index $\alpha$ of the Salpeter IMF provides a higher energy release than the Scalo IMF until $\sim 10^8$ years. Afterwards, the radiated energy being provided by less massive stars, a Scalo IMF gives more energy. Globally, the difference between the total energy radiated by a cluster of stars for a Scalo or a Salpeter IMF is quite small. On the other hand, the effect of increasing the metallicity is to decrease the stellar energy release. This effect can be understood as being due to an increase of stellar opacity with metallicity (Mowlavi et al. 1998). A quick comparison with

[1] http://www.stsci.edu/science/starburst99/

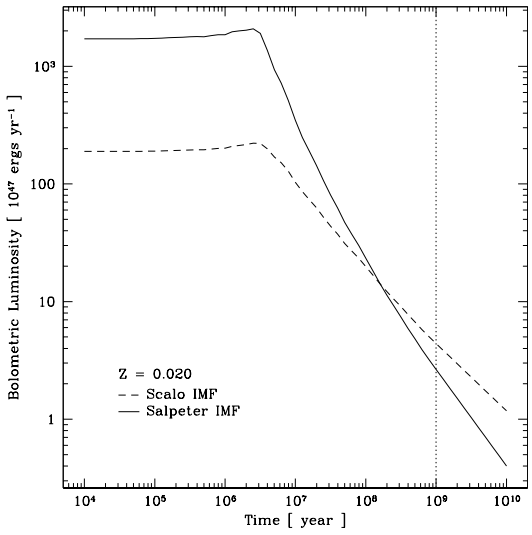


**Fig. 1.** Evolution of the bolometric luminosity of a $10^6\,M_\odot$ star cluster formed instantaneously with a metallicity $Z = 0.020$ according to the model of Leitherer et al. (1999). The solid line is for a Salpeter IMF ($\alpha = 2.35$) and the dashed line is for a Scalo IMF ($\alpha = 3.3$). Only stars in the mass range between 1 and $100\,M_\odot$ are considered. Beyond $10^9$ years (dotted line), the model data have been linearly extrapolated up to $10^{10}$ years.

**Table 1.** Energy radiated per unit of solar mass by stars $(E_{\rm rad}/M_\odot)_{\rm stars}$ and the corresponding energy density $U_{\rm stars}$ for different metallicities $Z$ and for a Salpeter ($\alpha = 2.35$) or a Scalo ($\alpha = 3.3$) IMF. The last column shows the corresponding energy density ratio radiated by AGN and by stars.

| $Z$ | $\alpha_{\rm IMF}$ | $(E_{\rm rad}/M_\odot)_{\rm stars}$ | $U_{\rm stars}$ | $U_{\rm AGN}/U_{\rm stars}$ |
|---|---|---|---|---|
| | | $10^{51}$ ergs $M_\odot^{-1}$ | $10^{60}$ ergs Mpc$^{-3}$ | $(10^{-2})$ |
| 0.001 | 2.35 | 4.16 | 1.29 | 2.8 |
| | 3.3 | 4.69 | 3.33 | 1.1 |
| 0.008 | 2.35 | 3.46 | 1.07 | 3.4 |
| | 3.3 | 3.39 | 2.40 | 1.5 |
| 0.020 | 2.35 | 3.09 | 0.96 | 3.8 |
| | 3.3 | 2.92 | 2.07 | 1.8 |
| 0.040 | 2.35 | 2.33 | 0.72 | 5.1 |
| | 3.3 | 1.71 | 1.21 | 3.0 |

Courvoisier (2001) shows that the values in Table 1 are consistent with his rough estimation that stars radiate $\sim 10^{51}$ ergs $M_\odot^{-1}$ over their entire lives.

### 2.2. Evolution of the stellar density

Madau et al. (1996) first computed the star formation as a function of redshift. Since then, several authors have added new points to his diagram of the star formation rate (SFR) per unit of comoving volume as a function of the redshift. Different tracers have been used to derive the SFR, but now, it is common to use galaxy luminosities at different wavelengths. They can be converted into stellar formation rates using stellar population and galaxy spectral models, stellar formation scenarios and various IMF. Madau et al. (1998) propose conversion factors from luminosity to star formation rates ($L_{\rm UV} = C \cdot SFR$) with different values of $C$ for a Salpeter IMF and a Scalo IMF. Somerville et al. (2001) compiled all the observations made in this way and present a homogeneous table of the comoving SFR density data for different cosmological models and a Salpeter IMF. Figure 2 shows those data in the case of an Einstein-de Sitter cosmology and a Salpeter IMF. We calculate the stellar density $\rho_{\rm stars}$ by integrating the star formation rate $\dot{\rho}_{\rm stars}$ over the whole cosmic time:

$$\rho_{\rm stars} = \int \dot{\rho}_{\rm stars}\, {\rm d}t. \qquad (1)$$

If we consider a Friedman cosmological model, a flat universe, $q_0 = 0.5$, and $H_0 = 50\ {\rm km\,s^{-1}\,Mpc^{-1}}$, Eq. (1) becomes:

$$\rho_{\rm stars} = \int_{z_{\rm max}}^{0} \dot{\rho}_{\rm stars}(z) \frac{{\rm d}z}{H_0 (1+z)^{2.5}}. \qquad (2)$$

With $z_{\rm max} = 5.5$ and $\dot{\rho}_{\rm stars}(z)$ being the solid line adjusted to the data points of Fig. 2, we obtain:

$$\rho_{\rm stars} = 3.1 \times 10^8\ M_\odot\,{\rm Mpc^{-3}}. \qquad (3)$$

This value is an average over the star formation history. Using the conversion factors given by Madau et al. (1998) and the table of Somerville et al. (2001), we deduce a different stellar density if we consider a Scalo IMF. Thus, for a Scalo IMF, an Einstein-de Sitter cosmology and $H_0 = 50\ {\rm km\,s^{-1}\,Mpc^{-1}}$, we get:

$$\rho_{\rm stars} = 7.1 \times 10^8\ M_\odot\,{\rm Mpc^{-3}} \qquad (4)$$

which is about twice the value for the Salpeter IMF. These results are only very weakly dependent on the cosmological model. Indeed, if we consider a ΛCDM cosmological model ($\Omega_0 = 0.3, \Omega_\Lambda = 0.7$) and calculate $\rho_{\rm stars}$, we find a difference that is negligible (∼0.2%) for both a Salpeter and a Scalo IMF compared to our previous values.

### 2.3. Energy density of the stellar radiation field

Having obtained the energy radiated by stars (see Table 1, Col. 3) and the star density for a Salpeter IMF (see Eq. (3)) and for a Scalo IMF (see Eq. (4)), we calculate the energy density due to stars as

$$U_{\rm stars} = \rho_{\rm stars} \cdot \left(\frac{E_{\rm rad}}{M_\odot}\right)_{\rm stars}\ {\rm ergs\,Mpc^{-3}}. \qquad (5)$$

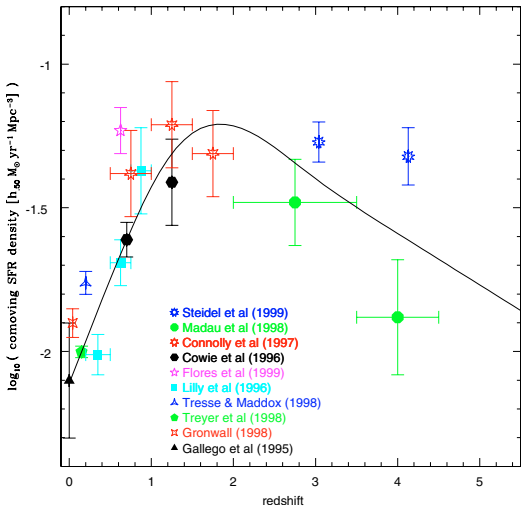


**Fig. 2.** Evolution of the comoving SFR density for an Einstein-de Sitter cosmology and a Salpeter IMF from the data in Table A2 of Somerville et al. (2001). The solid line is a cubic spline matching as well as possible the observational constraints.

The obtained values are reported in the fourth column of Table 1. Since $U_{\rm stars}$ is proportional to $\rho_{\rm stars}$ and $E_{\rm rad}({\rm stars})$, we note that $U_{\rm stars}$ decreases when $Z$ increases following the $E_{\rm rad}({\rm stars})$ behavior and increases when the IMF slope is steeper.

## 3. Energy radiated by active galactic nuclei

To estimate the energy radiated by AGN, we use the observed X-ray background (XRB). This is motivated by the growing evidence that the XRB is emitted by discrete sources that are mainly AGN as proposed by Setti & Woltjer (1989). By adding the contribution of type I and II AGN, the observed XRB spectrum can indeed be well reproduced (Comastri et al. 1995; Gilli et al. 1999, 2001). Furthermore, it seems that the contribution of both massive X-ray binaries and supernovae to the XRB is negligible (Natarajan & Almaini 2000). The emission from the hot interstellar medium is also small compared to the AGN contribution (Comastri et al. 1995). It is therefore possible to calculate the energy density in the AGN radiation field, $U_{\rm AGN}$, from the observed XRB spectrum. Fabian & Iwasawa (1999) give the following analytic parametrisation that describes well the spectral energy distribution of the XRB as observed by HEAO-2 and ASCA for soft and hard X-rays:

$$I(E) = 9E^{-0.4} \exp(-E/50_{\rm keV})\ {\rm keV cm^{-2} s^{-1} sr^{-1} keV^{-1}}. \qquad (6)$$

To relate this spectrum to the bolometric intensity of AGN, we use the mean ratio from the 2−10 keV intensity to the bolometric intensity derived by Fabian & Iwasawa (1999):

$$L_{[2-10\,{\rm keV}]}/L_{\rm bol}\,({\rm RQQ}) = 3.3\%. \qquad (7)$$

This ratio is based on a compilation of spectral energy distributions of radio-quiet quasars (RQQ) by Elvis et al. (1994),

which can be considered to be representative for the average emission of unobscured AGN. We further assume Fabian & Iwasawa (1999)'s hypothesis that the unobscured emission $E\,I(E)$ of AGN down to 2 keV can be considered as constant with a value of 38 keV cm$^{-2}$ s$^{-1}$ sr$^{-1}$ which is the XRB intensity at 30 keV. We then calculate the 2−10 keV intensity of AGN as being 61 keV cm$^{-2}$ s$^{-1}$ sr$^{-1}$. From this last value and Eq. (7), we derive the bolometric intensity of AGN and we calculate the energy density of the AGN radiation field as

$$U_{\rm AGN} = 3.7 \times 10^{58}\ {\rm ergs\,Mpc^{-3}}. \quad (8)$$

## 4. Discussion

We have independently determined the energy densities emitted both by stars and AGN in the universe. The obtained ratio $U_{\rm AGN}/U_{\rm stars}$ is given in the last column of Table 1 for two IMF and four different metallicities. We note that all values are between $10^{-2}$ and $5 \times 10^{-2}$. They slightly depend on the IMF slope and on the metallicity. Moreover, the choice of the cosmological model has a negligible effect as mentioned at the end of Sect. 2.2. This ratio is expected to remain rather constant with cosmic time because the star formation history is similar to the AGN luminosity evolution towards higher redshifts (Dunlop 1998; Franceschini et al. 1999).

### 4.1. Comparison between the different approaches

Our results differ by several orders of magnitude from other estimations of the energy ratio radiated by AGN and by stars. The different results extend from $10^{-5}$ (Courvoisier 2001) to $10^{-1}$ (Fabian & Iwasawa 1999; Franceschini et al. 1999; Elvis et al. 2002) through $4 \times 10^{-2}$ (this work). We cannot directly compare these values, because each study is based on a different approach to the problem; sometimes observational and sometimes approximative with the mass to energy conversion derived according to an efficiency $\varepsilon_{\rm rad}$ through $E_{\rm rad} = \varepsilon_{\rm rad} Mc^2$.

Fabian & Iwasawa (1999) consider a typical galaxy and the contribution to the flux radiated both by the stars and the black hole hosted in this galaxy. They implicitly assume all galaxies with a black hole to host an AGN. However, the presence of a black hole does not mean that this galaxy is active. Some galaxies might have had an active phase, but are currently quiescent. Taking their ratio is equivalent to considering that every galaxy is currently active and contributes to the radiated energy of AGN. This leads to overestimate the energy radiated by AGN and thus to an overestimation of the AGN-to-star radiation ratio.

Franceschini et al. (1999) tackles the problem from the observational point of view starting with the energy radiated by the stars and the AGN to find a link between both phenomena. This approach is motivated by the apparent similarity between the cosmic evolution of the SFR and the AGN activity. In Courvoisier (2001), the sample of these active galaxies is based only on a radio survey. Therefore, this selection results in a sample of radio-loud galaxies which are only a small fraction of the whole AGN population. This leads to an underestimation of the accretion rate per unit of volume because there are many radio-quiet quasars that contribute to the energy radiated by accretion processes that are not taken into account. The use of the 0.5−2 keV volume emissivity by Franceschini et al. (1999) allows one to include all AGN because they all radiate in the X-rays (Comastri et al. 1995; Gilli et al. 1999; Miyaji et al. 2000; Pompilio et al. 2000; Gilli et al. 2001) while only including a negligible contribution of other objects like star clusters or massive X-ray binaries (Gilli et al. 1999; Natarajan & Almaini 2000; Gilli et al. 2001).

Elvis et al. (2002) also consider the AGN emission based on the XRB. However, they compare it to the total luminosity of the universe that is estimated from the diffuse background from submillimeter to UV wavelengths rather than only the stellar luminosity.

We conclude that the various studies mentioned above actually measure different quantities. Therefore, it is not possible to compare directly the values obtained by different groups.

### 4.2. Comparison between the different parameter values

In addition to the differences in the approaches and the measured quantities pointed out above, various studies use different values for the same parameters. The stellar efficiency $\varepsilon_{\rm rad}$ used by Fabian & Iwasawa (1999) is 0.0006, but it is of 0.001 in Franceschini et al. (1999). Similarly, the ratio of the 2−10 keV luminosity to the bolometric luminosity of the AGN is used in Fabian & Iwasawa (1999) and in this work, while Franceschini et al. (1999) consider instead the 0.5−2 keV flux to derive a bolometric luminosity. Using the spectrum of Eq. (6), we can convert their bolometric correction to the one based on the 2–10 keV flux. Thus, we derive that their bolometric correction differs from the 3.3% value of Fabian & Iwasawa (1999) by a factor of 3. It seems therefore that there is an accumulation of different factors explaining the diverging results in the literature. By taking the values of $\varepsilon_{\rm rad} = 0.0006$ and $L_{[2-10\,{\rm keV}]}/L_{\rm bol} = 3.3\%$ from Fabian & Iwasawa (1999) and repeating the calculation of Franceschini et al. (1999), we obtain a value of ∼0.053 for the ratio $L_{\rm bol(AGN)}/L_{\rm bol(SFR)}$, which tends to the value of 0.04 we obtain in this work for a solar metallicity and a Salpeter IMF.

In order to explicitly calculate $U_{\rm stars}$ as defined here from the study of Elvis et al. (2002), we first subtract the quasar contribution to the total luminosity of the universe they give to get only the stellar background. We then obtain that $6.6 \times 10^{59}$ ergs Mpc$^{-3}$ are radiated by stars which is quite similar to our result (see Table 1). Therefore, keeping their value of $U_{\rm AGN}$, we estimate the ratio $U_{\rm AGN}/U_{\rm stars} \sim 0.067$ that becomes ∼0.046 if we use the energy radiated by stars obtained in our study for a Salpeter IMF and a solar metallicity (see Table 1) instead of theirs. If we compare this to our results, we note that a difference also resides in the value of $U_{\rm AGN}$. Considering Elvis et al. (2002)'s values of 48 keV cm$^{-2}$ s$^{-1}$ sr$^{-1}$ at 30 keV for the XRB instead of 38 keV cm$^{-2}$ s$^{-1}$ sr$^{-1}$ and their correction of a factor 1.6 to the bolometric correction, we recalculate our value of $U_{\rm AGN}$ applying the same method as seen previously in Sect. 3. We find that the AGN emitted energy density of

Elvis et al. (2002) is 1.5 times higher than ours. With this new derivation of $U_{\rm AGN}$, we calculate a ratio $U_{\rm AGN}/U_{\rm stars} \sim 0.031$ for a Salpeter IMF and a solar metallicity that is a factor 2 lower than their value of 0.067. The difference comes from a lower $U_{\rm AGN}$ and a higher $U_{\rm stars}$, both effects combining to give a ratio twice lower.

Finally, it is worth noting that recent observations by Sarzi et al. (2001) lead to a smaller ratio of the central black hole mass to the host bulge mass than the value used by Fabian & Iwasawa (1999). By using their new result of $M_{\rm BH}/M_{\rm bulge} \simeq 0.002$ the ratio $E_{\rm AGN}/E_{\rm stars}$ found by Fabian & Iwasawa (1999) would have been of ∼0.07 instead of ∼0.2.

### 4.3. Relation between RLQ radio luminosity and AGN bolometric luminosity

Franceschini et al. (1999) and Courvoisier (2001) compared the star formation rate to the accretion history based on the observation either in the X-ray band or in the radio band. Every AGN is responsible for the X-ray emission but only a subset of AGN has a significant radio emission. Therefore, we easily get a link between these two classes of objects. When 1 $M_\odot\,{\rm yr}^{-1}\,{\rm Mpc}^{-3}$ is used by the star formation, $2.4{\times}10^{40}\,{\rm ergs\,s}^{-1}\,{\rm Mpc}^{-3}$ are emitted by the AGN in the 0.5−2 keV band and $10^{-7}\,M_\odot\,{\rm yr}^{-1}\,{\rm Mpc}^{-3}$ is accreted onto the central black hole of a RLQ. If we transform the 0.5−2 keV luminosity into the bolometric luminosity using $L_{[0.5-2\,{\rm keV}]}/L_{\rm bol}({\rm AGN}) \sim 1.25\%$ derived from Eqs. (6) and (7) and if we consider an accretion efficiency onto the black hole of 10%, we obtain that $3.4\times10^{-4}\,M_\odot\,{\rm yr}^{-1}\,{\rm Mpc}^{-3}$ is accreted by the AGN for a SFR of 1 $M_\odot\,{\rm yr}^{-1}\,{\rm Mpc}^{-3}$. Therefore, we can compare the luminosity of both the RLQ and the AGN as we get $\sim10^4$ of difference between them. When 1 $\,{\rm erg\,s}^{-1}\,{\rm Mpc}^{-3}$ is radiated by the RLQ at 2.7 GHz, the complete population of AGN radiates about 3400 times more.

Furthermore, we can reconsider the method used by Courvoisier (2001) to determine $U_{\rm AGN}/U_{\rm stars}$. We have seen that we cannot directly compare his result to the others since they are not considering the same family of objects. Instead of using the analysis of RLQ by Dunlop (1998), we recalculate the ratio of Courvoisier (2001) using the analysis of the XRB of Franceschini et al. (1999). Therefore, we obtain a value of $E_{\rm AGN}/E_{\rm stars} \sim 0.015$ between the energies radiated by AGN and stars instead of RLQ and stars. This value becomes ∼0.020 if we use our result of the energy radiated by stars for a Salpeter IMF and a solar metallicity (see Table 1). The initial inconsistency of a factor of a thousand has been reduced to only a factor of 2 between this last estimate and the one in Table 1.

### 4.4. Mass accreted by supermassive black holes

Based on our previous results we can estimate the total mass accreted by SMBH. If we consider a galaxy with a mass of $10^{11}\,M_\odot$ in stars, we can estimate the energy radiated by those stars from the value in Table 1 for a Salpeter IMF and a solar metallicity. Using the corresponding ratio of the AGN-to-stars energy release, we can then derive the energy radiated by the SMBH. By further assuming an accretion efficiency of 10%, we obtain that the total mass accreted by the SMBH is $6.5\times10^7\,M_\odot$. In general, the typical mass accreted by a SMBH in a galaxy can be calculated according to

$$M_{\rm AGN}^{\rm accr}(M_\odot) = 2.2\times10^7 \left(\frac{0.1}{\varepsilon}\right)\left(\frac{E_{\rm AGN}/E_{\rm stars}}{0.04}\right) \times\left(\frac{M_{\rm Gal}}{10^{11}\,M_\odot}\right)\left(\frac{(E_{\rm rad}/M_\odot)_{\rm stars}}{10^{51}\,{\rm ergs}\,M_\odot^{-1}}\right). \quad (9)$$

We can also estimate this mass starting from the link given in the previous subsection. We have seen that when 1 $M_\odot$ of material is converted into stars, $3.4\times10^{-4}\,M_\odot$ is accreted onto SMBH. If we consider again a galaxy with a mass of $10^{11}\,M_\odot$ in stars, we estimate that $3.4\times10^7\,M_\odot$ is accreted onto the SMBH that is half of our previous estimate. This difference by a factor of 2 is the same as for the ratio $E_{\rm AGN}/E_{\rm stars}$ mentioned in Sect. 4.3.

## 5. Conclusion

We derived the relative contribution of AGN and stars to the radiation energy density of the universe. The results are given for different IMF and metallicities of the stellar population. The obtained values for the energy ratio released by AGN and stars are all between 0.01 and 0.05. In the case of a Salpeter IMF and solar metallicity we obtain a ratio of 0.04. This result cannot be compared directly with previous studies because the approaches as well as the values of some parameters used in the calculation differ from one study to the other. Actually, when using similar parameters and appropriate correction factors it seems that all previous studies do converge to values between 0.02 and 0.07 for the ratio of energy radiated by AGN and stars.

Since the CMB energy density is about ∼0.2 $\,{\rm eV\,cm}^{-3}$, the energy density due to stars is of the order of $10^{60}\,{\rm ergs\,Mpc}^{-3} \sim 0.02\,{\rm eV\,cm}^{-3}$ and the AGN related radiation energy density is of about $8\times10^{-4}\,{\rm eV\,cm}^{-3}$, the general picture resulting from this work is that the CMB contributes 10 times more than stars and 250 times more than AGN to the local energy density of background photons.

We also estimate that RLQ contribute about 3400 times less than the whole AGN family to the total accretion power in the universe and that the cumulated mass accreted on average by a SMBH is of about $6.5\times10^7\,M_\odot$.

*Acknowledgements.* We thank G. Meynet for useful discussions on star formation related issues.

## References

Charbonnel, C., Meynet, G., Maeder, A., Schaller, G., & Schaerer, D. 1993, A&AS, 101, 415

Charlot, S., & Bruzual, A. G. 1991, ApJ, 367, 126

Comastri, A., Setti, G., Zamorani, G., & Hasinger, G. 1995, A&A, 296, 1

Courvoisier, T. J.-L. 2001, in Quasars, AGNs and Related Research Across 2000, Conference on the occasion of L. Woltjer's 70th birthday, held in Rome, Italy, 3–5 May 2000, ed. G. Setti, & J.-P. Swings (Springer), 155

Dunlop, J. S. 1998, in Observational Cosmology with the New Radio Surveys, ASSL, 226, 157
Elvis, M., Risaliti, G., & Zamorani, G. 2002, ApJ, 565, L75
Elvis, M., Wilkes, B. J., McDowell, J. C., et al. 1994, ApJS, 95, 1
Fabian, A. C., & Iwasawa, K. 1999, MNRAS, 303, L34
Franceschini, A., Hasinger, G., Miyaji, T., & Malquori, D. 1999, MNRAS, 310, L5
Gilli, R., Risaliti, G., & Salvati, M. 1999, A&A, 347, 424
Gilli, R., Salvati, M., & Hasinger, G. 2001, A&A, 366, 407
Leitherer, C., Schaerer, D., Goldader, J. D., et al. 1999, ApJS, 123, 3
Lejeune, T., Cuisinier, F., & Buser, R. 1997, A&AS, 125, 229
Madau, P., Ferguson, H. C., Dickinson, M. E., et al. 1996, MNRAS, 283, 1388
Madau, P., Pozzetti, L., & Dickinson, M. 1998, ApJ, 498, 106
Meynet, G., Maeder, A., Schaller, G., Schaerer, D., & Charbonnel, C. 1994, A&AS, 103, 97
Miyaji, T., Hasinger, G., & Schmidt, M. 2000, A&A, 353, 25
Mowlavi, N., Meynet, G., Maeder, A., Schaerer, D., & Charbonnel, C. 1998, A&A, 335, 573
Natarajan, P., & Almaini, O. 2000, MNRAS, 318, L21
Pompilio, F., La Franca, F., & Matt, G. 2000, A&A, 353, 440
Sarzi, M., Rix, H., Shields, J. C., et al. 2001, ApJ, 550, 65
Schaerer, D., Charbonnel, C., Meynet, G., Maeder, A., & Schaller, G. 1993a, A&AS, 102, 339
Schaerer, D., Meynet, G., Maeder, A., & Schaller, G. 1993b, A&AS, 98, 523
Schaller, G., Schaerer, D., Meynet, G., & Maeder, A. 1992, A&AS, 96, 269
Schmutz, W., Leitherer, C., & Gruenwald, R. 1992, PASP, 104, 1164
Setti, G., & Woltjer, L. 1989, A&A, 224, L21
Somerville, R. S., Primack, J. R., & Faber, S. M. 2001, MNRAS, 320, 504
Trentham, N., Blain, A. W., & Goldader, J. 1999, MNRAS, 305, 61

# Fifth part

# Conclusions

# Chapter 13
# CONCLUSIONS

In this chapter, we present the final conclusion of four years of work at the ISDC. This will be done in the real chronological order I have done my work, *i.e.* the inverse order in comparison with the chapters of my thesis. I will go from the biggest to the smallest, from large sample of sources to the individual sources.

## 13.1 Accretion in the Universe

Based on the simple hypothesis that the star formation rate and the emission due to accretion processes in the Universe are similar, there is the possibility to compare the importance of each radiation in the frame of the Universe.

Accretion gives rise to the most powerful events in the Universe, *i.e.* the AGN. However it is not the most energetic contributor. We have seen that in fact, it is the less powerful than the stars with a ratio of $E_{\rm AGN}/E_{\rm stars} = 0.02 - 0.07$. In the order, we find the CMB with $\sim$0.2 eV cm$^{-3}$, followed by the stars with $\sim$0.02 eV cm$^{-3}$, and finally the accretion in AGN with $\sim$0.0008 eV cm$^{-3}$. The low-energy photons dominate the population of cosmic background photons.

Besides, as the population of radio-loud quasars is a small fraction of the AGN family, their power emission represents also a tiny fraction of the global AGN emission, less than $10^{-3}$.

Finally, the average mass accreted onto a SMBH is of the order of $\sim 6.5\,10^7$ M$_\odot$.

## 13.2 LMXB monitoring

The LMXB monitoring did not result in much science as, in 2002–2003, the knowledge about the performance of the instruments was still under debate. The variability observed in the light curves was not reliable as it was linked to the position of the source in the FOV.

However, it shows the promising possibilities of long-term coverage of a very large sample of sources that can be studied uniformly with the same instruments.

Otherwise, it was a great opportunity to improve my knowledge on data analysis, on computing languages, and discover a new family of objects, as at that time I was more focused on AGN. Finally, I finished to work with their *big cousin*, the HMXB.

## 13.3 The family of IGR sources

The IGR sources are bright hard X-rays sources that were unknown or poorly studied with previous high energy missions. The combination of *XMM-Newton* and *INTEGRAL* analysis were useful to understand the nature of the detected objects. The *XMM-Newton* observations of three IGR sources of our sample (IGR J16418−4532, IGR J16479−4514 and IGR J17597−2201) were perturbed by background activity. The following results were found during our studies :

1. For the 6 sources of our *XMM-Newton* programme, we present new X-ray locations with an accuracy of $4''$ that are compatible with the *INTEGRAL* position. This will help to localise the optical counterpart in catalogues or/and in new spectroscopic observations;
2. Seven sources have a persistent emission and show a strong local absorption. When the data quality is high enough, the 6.4 keV iron emission line is detected. For 5 sources, we also find pulsations that range from 139 s to 1302 s. We know the orbital periods for 3 systems that are comprised between 5–10 d. These systems are apparently HMXB accreting from the stellar wind of a supergiant companion. The compact object is deeply embedded in the stellar wind. The matter distribution is compatible with a spherical geometry and the cold iron is located $\sim 10^8$ km from the X-ray source. This is probably the case of IGR J16318−4848, IGR J16320−4751, IGR J16393−4643, IGR J16418−4532, IGR J16479−4514, IGR J17252−3616, and IGR J18027−2016;
3. Three sources are transients. IGR J17544−2619 is probably a Be system with an orbital period of 165 d without intrinsic absorption. IGR J16465−4507 is a HMXB that is highly absorbed with a sgB supergiant companion (Negueruela et al. 2005a). The nature of IGR J16358−4726 is still a mystery. Nevertheless, most of its characteristics tend to classify it as a transient HMXB with strong absorption. Its pulsation of 5880 s would be the longest one detected in accreting pulsars;
4. IGR J17597−2201 is probably a LMXB without absorption as already proposed by Lutovinov et al. (2005a);
5. A soft excess is detected in the highly absorbed HMXB. This is common in this category of objects (Hickox et al. 2004), e.g. Vela X-1 or 4U 1700-377;
6. IGR J17252−3616 and IGR J18027−2016 are eclipsing systems; and
7. the population of HMXB with supergiant significantly increases with the discovery of these new IGR sources. Around ten were previously known.

In this thesis, we present only 11 IGR sources, but currently, there are around 100 sources that have been detected with *INTEGRAL*. The combination of multi-wavelength observations helps to elucidate the nature of the new X-ray sources. The future is open to further individual studies that will help to improve the knowledge of X-ray binaries in term of populations and general features.

*Sometimes, this thesis should be concluded and there we are.*

# BIBLIOGRAPHY

Augello, G., Iaria, R., Robba, N. R., et al. 2003, ApJ, 596, L63

Belloni, T., Homan, J., Casella, P., et al. 2005, A&A, 440, 207

Bildsten, L., Chakrabarty, D., Chiu, J., et al. 1997, ApJS, 113, 367

Bird, A. J., Barlow, E. J., Bassani, L., et al. 2004, ApJ, 607, L33

Bodaghee, A., Walter, R., Zurita Heras, J. A., et al. 2005, A&A, in press

Bulik, T., Gondek-Rosińska, D., Santangelo, A., et al. 2003, A&A, 404, 1023

Comastri, A., Setti, G., Zamorani, G., & Hasinger, G. 1995, A&A, 296, 1+

Combi, J. A., Ribó, M., Mirabel, I. F., & Sugizaki, M. 2004, A&A, 422, 1031

Corbet, R., Barbier, L., Barthelmy, S., et al. 2005a, The Astronomer's Telegram, 649, 1

Corbet, R. H. D. 1984, A&A, 141, 91

Corbet, R. H. D. 1986, MNRAS, 220, 1047

Corbet, R. H. D., Markwardt, C. B., & Swank, J. H. 2005b, ApJ, in press

Courvoisier, T. J.-L. 2001, in Quasars, AGNs and Related Research Across 2000. Conference on the occasion of L. Woltjer's 70th birthday, held in Rome, Italy, 3-5 May 2000. Giancarlo Setti and Jean-Pierre Swings (eds.). Springer. p. 155., 155+

Courvoisier, T. J.-L., Walter, R., Beckmann, V., et al. 2003a, A&A, 411, L53

Courvoisier, T. J.-L., Walter, R., Rodriguez, J., Bouchet, L., & Lutovinov, A. A. 2003b, IAU Circ., 8063, 3

Dickey, J. M. & Lockman, F. J. 1990, ARA&A, 28, 215

Dunlop, J. S. 1998, in ASSL Vol. 226: Observational Cosmology with the New Radio Surveys, 157+

Ebisawa, K., Bourban, G., Bodaghee, A., Mowlavi, N., & Courvoisier, T. J.-L. 2003, A&A, 411, L59

Elvis, M., Risaliti, G., & Zamorani, G. 2002, ApJ, 565, L75

Fabian, A. C. & Iwasawa, K. 1999, MNRAS, 303, L34

Filliatre, P. & Chaty, S. 2004, ApJ, 616, 469

Franceschini, A., Hasinger, G., Miyaji, T., & Malquori, D. 1999, MNRAS, 310, L5

Giacconi, R., Gursky, H., Paolini, F. R., & Rossi, B. B. 1962, Phys. Rev. Lett., 9, 439

Gilli, R., Risaliti, G., & Salvati, M. 1999, A&A, 347, 424

Gilli, R., Salvati, M., & Hasinger, G. 2001, A&A, 366, 407

González-Riestra, R., Oosterbroek, T., Kuulkers, E., Orr, A., & Parmar, A. N. 2004, A&A, 420, 589

Gonzalez-Riestra, R., Santos-Lleo, M., Tomas, L., & Perez-Martinez, R. 2003, IAU Circ., 8202, 2

Grebenev, S. A., Lutovinov, A. A., & Sunyaev, R. A. 2003, The Astronomer's Telegram, 192, 1

Gros, A., Goldwurm, A., Cadolle-Bel, M., et al. 2003, A&A, 411, L179

Hickox, R. C., Narayan, R., & Kallman, T. R. 2004, ApJ, 614, 881

Hill, A. B., Walter, R., Knigge, C., et al. 2005, A&A, 439, 255

Horne, J. H. & Baliunas, S. L. 1986, ApJ, 302, 757

House, L. L. 1969, ApJS, 18, 21

in't Zand, J. & et al. 2004, in ESA SP-552: 5th INTEGRAL Workshop on the INTEGRAL Universe, 427–+

in't Zand, J. J. M. 2005, A&A, 441, L1

Jansen, F., Lumb, D., Altieri, B., et al. 2001, A&A, 365, L1

Jonker, P. G. & van der Klis, M. 2001, ApJ, 553, L43

Kallman, T. R., Palmeri, P., Bautista, M. A., Mendoza, C., & Krolik, J. H. 2004, ApJS, 155, 675

Kennea, J. A., Burrows, D. N., & Gehrels, N. 2005, GRB Coordinates Network, 4014, 1

King, A. 1995, X-ray binaries (Cambridge Astrophysics Series, Cambridge, MA: Cambridge University Press, |c1995, edited by Lewin, Walter H.G.; Van Paradijs, Jan; Van den Heuvel, Edward P.J.), 419–456

Kouveliotou, C., Patel, S., Tennant, A., et al. 2003, IAU Circ., 8109, 2

Kuiper, L., Hermsen, W., Cusumano, G., et al. 2001, A&A, 378, 918

Kuulkers, E., , & . 2006, in preparation

Labanti, C., Di Cocco, G., Ferro, G., et al. 2003, A&A, 411, L149

Leahy, D. A., Darbro, W., Elsner, R. F., et al. 1983, ApJ, 266, 160

Lebrun, F., Leray, J. P., Lavocat, P., et al. 2003, A&A, 411, L141

Leitherer, C., Schaerer, D., Goldader, J. D., et al. 1999, ApJS, 123, 3

Liu, Q. Z., van Paradijs, J., & van den Heuvel, E. P. J. 2000, A&AS, 147, 25

Liu, Q. Z., van Paradijs, J., & van den Heuvel, E. P. J. 2001, A&A, 368, 1021

Lomb, N. R. 1976, Ap&SS, 39, 447

Lund, N., Budtz-Jørgensen, C., Westergaard, N. J., et al. 2003, A&A, 411, L231

Lutovinov, A., Revnivtsev, M., & Molkov, S. 2003a, The Astronomer's Telegram, 178, 1

Lutovinov, A., Revnivtsev, M., Molkov, S., & Sunyaev, R. 2005a, A&A, 430, 997

Lutovinov, A., Rodrigues, J., Budtz-Jorgensen, C., Grebenev, S., & Winkler, C. 2004, The Astronomer's Telegram, 329, 1

Lutovinov, A., Rodriguez, J., Revnivtsev, M., & Shtykovskiy, P. 2005b, A&A, 433, L41

Lutovinov, A., Walter, R., Belanger, G., et al. 2003b, The Astronomer's Telegram, 155, 1

Lutovinov, A. et al. 2004, Proceedings of the 5th INTEGRAL workshop, ESA-SP552, 253

Madau, P., Ferguson, H. C., Dickinson, M. E., et al. 1996, MNRAS, 283, 1388

Malizia, A., Bassani, L., di Cocco, G., et al. 2004, The Astronomer's Telegram, 227, 1

Markwardt, C. B. & Swank, J. H. 2003, The Astronomer's Telegram, 156, 1

Markwardt, C. B. & Swank, J. H. 2004, The Astronomer's Telegram, 255, 1

Mas-Hesse, J. M., Giménez, A., Culhane, J. L., et al. 2003, A&A, 411, L261

Matt, G. 2002, MNRAS, 337, 147

Matt, G. & Guainazzi, M. 2003, MNRAS, 341, L13

Molkov, S., Mowlavi, N., Goldwurm, A., et al. 2003, The Astronomer's Telegram, 176, 1

Nagase, F. 1989, PASJ, 41, 1

Negueruela, I., Smith, D., Reig, P., Chaty, S., & Torrejon, J. M. 2005a, Proceedings of "The X-ray Universe 2005", astro-ph/0511088, ESA-SP 604

Negueruela, I., Smith, D. M., & Chaty, S. 2005b, The Astronomer's Telegram, 429, 1

Orlandini, M. 2004, in To appear in the proceedings of AGILE Science Workshop No. 4: X-Ray and gamma-ray astrophysics of galactic sources, Rome, Italy, 11-13 Jun 2003

Paizis, A., Beckmann, V., Courvoisier, T. J.-L., et al. 2003, A&A, 411, L363

Paizis, A. et al. 2004, Proceedings of the 5th INTEGRAL workshop, ESA-SP552, 229

Pandey, M., Manchanda, R., Rao, A. P., Durouchoux, P., & Ishwara-Chandra, C. H. 2005a, submitted to A&A, astroph/0509645

Pandey, M., Rao, A. P., Manchanda, R., Durouchoux, P., & Ishwara-Chandra, C. H. 2005b, submitted to A&A, astroph/0512060

Patel, S. K., Kouveliotou, C., Tennant, A., et al. 2004, ApJ, 602, L45

Patel, S. K., Zurita Heras, J. A., & others. 2006, in prep.

Press, W. H. & Rybicki, G. B. 1989, ApJ, 338, 277

Revnivtsev, M., Lutovinov, A., & Ebisawa, K. 2003a, The Astronomer's Telegram, 131, 1

Revnivtsev, M., Tuerler, M., Del Santo, M., et al. 2003b, IAU Circ., 8097, 2

Revnivtsev, M. G. 2003, Astronomy Letters, 29, 644

Revnivtsev, M. G., Sunyaev, R. A., Varshalovich, D. A., et al. 2004, Astronomy Letters, 30, 382

Rodriguez, J., Bodaghee, A., Kaaret, P., et al. 2006, MNRAS, 366, 274

Rodriguez, J., Cabanac, C., Hannikainen, D. C., et al. 2005, A&A, 432, 235

Rodriguez, J., Foschini, L., Courvoisier, T. J.-L., & Hannikainen, D. 2003a, The Astronomer's Telegram, 194, 1

Rodriguez, J., Tomsick, J. A., Foschini, L., et al. 2003b, A&A, 407, L41

Scargle, J. D. 1982, ApJ, 263, 835

Schartel, N., Ehle, M., Breitfellner, M., et al. 2003, IAU Circ., 8072, 3

Sguera, V., Barlow, E. J., Bird, A. J., et al. 2005, A&A, 444, 221

Shakura, N. I. & Sunyaev, R. A. 1973, A&A, 24, 337

Somerville, R. S., Primack, J. R., & Faber, S. M. 2001, MNRAS, 320, 504+

Stephen, J. B., Bassani, L., Molina, M., et al. 2005, A&A, 432, L49

Sunyaev, R. A., Grebenev, S. A., Lutovinov, A. A., et al. 2003, The Astronomer's Telegram, 190, 1

Takeuchi, Y., Koyama, K., & Warwick, R. S. 1990, PASJ, 42, 287

Tauris, T. M. & van den Heuvel, E. P. J. 2005, Formation and Evolution of Compact Stellar X-ray Sources (Compact Stellar X-Ray Sources, eds. W.H.G. Lewin and M. van der Klis, Cambridge University Press), in press

Tawara, Y., Yamauchi, S., Awaki, H., et al. 1989, PASJ, 41, 473

Tomsick, J. A., Lingenfelter, R., Corbel, S., Goldwurm, A., & Kaaret, P. 2004, The Astronomer's Telegram, 224, 1

Tomsick, J. A., Lingenfelter, R., Walter, R., et al. 2003, IAU Circ., 8076, 1

Ubertini, P., Lebrun, F., Di Cocco, G., et al. 2003, A&A, 411, L131

Vedrenne, G., Roques, J.-P., Schönfelder, V., et al. 2003, A&A, 411, L63

Verbunt, F. & van den Heuvel, E. P. J. 1995, X-ray binaries (Cambridge Astrophysics Series, Cambridge, MA: Cambridge University Press, |c1995, edited by Lewin, Walter H.G.; Van Paradijs, Jan; Van den Heuvel, Edward P.J.), 457–494

Walter, R., Bodaghee, A., Barlow, E. J., et al. 2004, The Astronomer's Telegram, 229, 1

Walter, R., Rodriguez, J., Foschini, L., et al. 2003, A&A, 411, L427

Walter, R., Zurita Heras, J. A., Bassani, L., et al. 2005, submitted to A&A

Warwick, R. S., Norton, A. J., Turner, M. J. L., Watson, M. G., & Willingale, R. 1988, MNRAS, 232, 551

White, N. E., Nagase, F., & Parmar, A. N. 1995, X-ray binaries (Cambridge Astrophysics Series, Cambridge, MA: Cambridge University Press, |c1995, edited by Lewin, Walter H.G.; Van Paradijs, Jan; Van den Heuvel, Edward P.J.), 1–57

Wijnands, R. 2003, The Astronomer's Telegram, 191, 1

Winkler, C., Courvoisier, T. J.-L., Di Cocco, G., et al. 2003, A&A, 411, L1

Zurita Heras, J. A., de Cesare, G., Walter, R., et al. 2005, A&A, in press

Zurita Heras, J. A., Türler, M., & Courvoisier, T. J.-L. 2003, A&A, 411, 71

Zurita Heras, J. A. & Walter, R. 2004, The Astronomer's Telegram, 336, 1

# Chapter 14
# Acknowledgments

*This is the end, my friend....*

Finally, after four years of procastinating... I mean... of hard work, this thesis is over. Can't believe it! When my advisor asked me to start to write it last July, I just thought : "what will I put in it?" And he warned me : "Writing is like bleeding." Might be in other words but the meaning was this one. Indeed, it took me awhile to start to write it. I took a bit of time of thinking and the quietness (and sun) of *España* in October to really find the inspiration. At the end, it was not so hard. I found the experience quite exciting, even funny. I even discovered the ISDC by night. A bit scary, no soul living around...

The thesis is over and throughout the process, many people have been involved in some ways in it. I would like to thank them before closing this manuscript. So in the desorder....

First, Roland Walter. He came one day asking me if I wanted "to go to Madrid at the ESAC to the *XMM-Newton* Analysis Workshop the next week". No time to think, I just jumped on the opportunity. I think this has been a turning point in my thesis. Also, even if he is a quite secret guy, he is always open to my questions.

My advisor Thierry Courvoisier. Even if he prefers to work on extragalactic sources, he always kept an eye on my work. I found his door always open for my questions. He has been supportful throughout all my thesis, particularly when writing it.

My acknowledgements goes also to Diana Hannikainen and Georges Meynet that have accepted to be part of my jury. They did a great job reading my thesis and giving me corrections and feedback.

Very important, Sandrine Deluit with who I shared the office for so many years. The pain, the job, the fun. You are a great friend. It was good to have you in the worst moments. Know you are happy in Toulouse.

Jean-Christophe Leyder for the energy, for working until 11pm, for reading my thesis. Was a nightmare to go through all your corrections. You were always disturbing me. It is great you were in the mountain skiing when I had to finish to write this piece of document. And for many more....

Mark Gaber, the quiet cheerful Canadien. You make me discover I like programming. Thanks to teach me perl, to always help me with programming problems. Was great to be there for your weeding. Many thanks. You will be a great father. Never stop to do bicycle.

Simona Soldi, I like when you speak in Italian. Thanks to come the "Permutation city" exposition with me. Give up Inter, there is only one Real.

Patrick Eggenberger and Marc Cherix, for all the time spent at Les Gravines. It was not good for our thesis, but so funny!

Arash Bodaghee, thanks for the music. Good luck for your last year.

Thanks to Isabelle Lecoeur, Franca Costa and Marie-Claude Bernasconi, the beautiful ladies of ISDC. Fortunately, you are here to lighten our hearts. We are too many guys in science.

Nami Mowlavi, for his kindness, to make life on shift a bit easier.

Everybody at ISDC... Nicolas Produit for his help with ISGRI analysis, Jérome Rodriguez (thanks for reading my thesis and giving me comments, and in general taking time to respond to my questions when I had some), Daniel Rychick for the help with computers and else, Nicolas Morisset, Marc Tuerler, Stéphane Paltani (running is not so bad), Christel, Dominique (both of you, good luck with your thesis), Piotr (interesting discussion, keep your smile even if the Crab spectrum makes jumps!),

I mean, everybody at ISDC : THANKS!

Gerald Bourban, good officemate, bit too short, good luck for the last line!

Stefania Carpano and Marina Kaufman Bernardo for Dublin and El Escorial. So much fun. With you the conferences became like holidays. Good luck with your post-docs!!

Because it was funny, the football teams from the Observatory and the ISDC : Axel, Christel, Fabian, Simon, Dave, Jake, Pepe, Arash, Simona, Patrick, etc. Everybody! Hope it will continue.

Life is not only work, but also fun. So necessary to have some when doing a PhD. And there, I must warmly thanks :

Rafa, the guy that knows everything I liked/hated/suffered/appreciated in this thesis. Thanks for everything, for Morrocco, for the salsa, but for listening. Have fun in Paris or in Mars!

Eva, the lovely Eva! Thanks for being my friend. *Viva Barcelona.*

Pablo, you have too much energy!

Najat, Bruxelles is too far!

Fred, it is always very fruitful to talk with you, guy!

Xavier, you never call but you always answer.

Anne-Gaëlle, Arianne, Marie, Laure, Pika, Binh, Fabienne, Pierric, everybody from the Tiger team, for the volley. Thanks Laure for the days at Les Diablerrets, it helped me to finish the thesis.

Sylvain, for Rollo, for the PhD comic, for much more!

Fanny, for everything you organised so well, for the garden party.

Damien, Gil, JP, Nath, Michael, Lalya, Chiara for the funny days in physics, for the dance, for the parties.

And a few words in spanish for the family, the most important...

*Muchas gracias a mis padres, ahora os toca a vosotros de disfrutar!*

*mi hermano Javier, por todo lo bueno y la malo!*

*Mari y mis tíos Paca y Rafael, muchas gracias!*

*Marga, Eugenio, tía Consuelo y la pequeñita Marina, gracias por todo, por las vacaciones. Besos!*

*A todos por todas partes : Pili, Eva, ....*

There is much more in my heart.

I have no strength left to write more. So...
My only friend, the end.....

# Sixth part

# Appendices

# Appendix A
# List of Publications

## 2003

- Zurita Heras, J. A., Türler, M. & Courvoisier, T. J.-L., 2003, *Ratio of energies radiated in the universe through accretive processes and nucleosynthesis*, Astronomy & Astrophysics, **411**, 71-76
- Paizis, A., Beckmann, V., Courvoisier, T. J.-L., Vilhu, O., Lutovinov, A., Ebisawa, K., Hannikainen, D., Chernyakova, M., Zurita Heras, J. A., Rodriguez, J., Zdziarski, A. A., Bazzano, A., Kuulkers, E., Oosterbroek, T., Frontera, F., Gimenez, A., Goldoni, P., Santangelo, A., Palumbo, G. G. C., 2003, *First INTEGRAL observations of eight persistent neutron star low mass X-ray binaries*, Astronomy & Astrophysics, **411**, L363-L367

## 2004

- A. Paizis, T.J.-L. Courvoisier, O. Vilhu, M. Chernyakova, T. Tikkanen, A. Bazzano, V. Beckmann, J. Chenevez, M. Cocchi, K. Ebisawa, R. Farinelli, F. Frontera, A. Gimenez, P. Goldoni, D. Hannikainen, E. Kuulkers, N. Lund, T. Oosterbroek, S. Piraino, J. Rodriguez, A. Santangelo, R. Walter, A. A. Zdziarski, J. A. Zurita Heras, 2004, *The INTEGRAL LMXRB monitoring programme*, Proceedings of the 5th INTEGRAL workshop, **ESA-SP552**, 229-236
- S. E. Shaw, N. Mowlavi, K. Ebisawa, A. Paizis, J. Rodriguez, J. Zurita, R. Walter, M. Turler, J. Soldan, A. Sauvageon, N. Produit, K. Pottschmidt, P. Meynis, L. Martins, L. Lerusse, I. Kreykenbohm, P. Kretschmar, P. Haymoz, P. Favre, P. Dubath, S. Deluit, T.J.-L. Courvoisier, M. Chernyakova, A. Bodaghee, V. Beckmann, 2004, *Scientific Performance of the ISDC Quick Look Analysis*, Proceedings of the 5th INTEGRAL workshop, **ESA-SP552**,
- J.A. Zurita Heras, A. Bazzano, S. Brandt, A. Domingo, C. Winkler, S. Grebenev, 2004, *The LMXRB GX354-0 is flaring in the hard X-rays*, ATel 248
- J.A. Zurita Heras, S.E. Shaw, I. Kreykenbohm, P. Kretschmar, D. Gotz, S. Mereghetti, A. Lutovinov, G. Palumbo, T. Oosterbroek, C. Budtz-Jorgensen, P. Ubertini, 2004, *INTEGRAL detects increased activity from 4U 0115+63*, ATel 331

- D. Gotz, J.A. Zurita Heras, C. Winkler, N. Gehrels, S. Martinez-Nuñez, A. Bazzano, A. Lutovinov, 2004, *Outburst from EXO 2030+375 detected with INTEGRAL*, ATel 367

## 2005

- Zurita Heras, J. A., de Cesare, G., Walter, R., Bodaghee, A., Bélanger, G., Courvoisier, T.J.-L., Shaw, S.E., Stephen, J.B., 2005, *IGR J17252−3616: an accreting pulsar observed by INTEGRAL and XMM-Newton*, Astronomy & Astrophysics, in press
- Bodaghee, A., Walter, R., Zurita Heras, J. A., Bird, A.J., Courvoisier, T.J.-L., Malizia, A., Terrier, R., Ubertini, P., 2005, *IGR J16393-4643: a new heavily-obscured X-ray pulsar*, Astronomy & Astrophysics, in press
- Walter, R., Zurita Heras, J. A., Bassani, L., Bazzano A., Bodaghee, A., Dean, A., Dubath, P., Parmar, A., Ubertini, P., 2005, *XMM-Newton and INTEGRAL observations of new absorbed super-giant high-mass X-ray binaries*, submitted to Astronomy & Astrophysics
- D.Gotz, S.Mereghetti, S. Shaw, N. Mowlavi, M. Beck, J.A. Zurita Heras, J. Borkowski on behalf of the IBAS Localization Team, 2005, *Possible GRB 050922 detected by INTEGRAL*, GCN 4007

## 2006

- Patel, S. K., Zurita Heras, J. A., del Santo, M., Finger, M., Kouveliotou, K., Ubertini, P., Walter, R., Woods, P., Wilson, C. A., Wachter, S., Eichler, D., Bazzano, A., 2006, *Exploring the Nature of IGR J16358-4726*, in preparation, to be submitted to the Astrophysical Journal